

This item was submitted to [Loughborough's Research Repository](#) by the author.  
Items in Figshare are protected by copyright, with all rights reserved, unless otherwise indicated.

## Thermodynamic and parametric optimisation of collision/reaction cells in plasma-source mass spectrometry

PLEASE CITE THE PUBLISHED VERSION

PUBLISHER

© Matthew A. Dexter

PUBLISHER STATEMENT

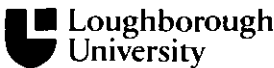
This work is made available according to the conditions of the Creative Commons Attribution-NonCommercial-NoDerivatives 4.0 International (CC BY-NC-ND 4.0) licence. Full details of this licence are available at: <https://creativecommons.org/licenses/by-nc-nd/4.0/>

LICENCE

CC BY-NC-ND 4.0

REPOSITORY RECORD

Dexter, Matthew A.. 2019. "Thermodynamic and Parametric Optimisation of Collision/reaction Cells in Plasma-source Mass Spectrometry". figshare. <https://hdl.handle.net/2134/34294>.



University Library

Author/Filing Title .....DEXTER.....

Class Mark .....T.....

Please note that fines are charged on ALL  
overdue items.

FOR REFERENCE ONLY





**Thermodynamic and Parametric Optimisation of  
Collision/Reaction Cells in Plasma Source Mass Spectrometry**

by


**Matthew A. Dexter**

**A Doctoral Thesis**

**Submitted in partial fulfilment of the requirements for the award of the degree of  
Doctor of Philosophy of Loughborough University**

**September 2003**

**© Matthew A. Dexter, 2003.**

 <b>Loughborough University</b> Reading Library	
Date	June 04
Class	
Acc No.	040294621

## **Abstract**

Inductively coupled plasma mass spectrometry (ICP-MS) is an established technique for elemental analysis. Collision/reaction cell ICP-MS is a recently established variation of the technique that facilitates the determination of elements suffering from spectral interference.

Two distinct collision cell ion energy effects have been identified: the ion kinetic energy effect (IKEE) and kinetic energy discrimination (KED). IKEE influences the reactivity of the cell by altering the ion energy. Slowing ions by increasing the potential difference between the hexapole pole bias and plasma increases the rate of exothermic reactions in the cell. KED excludes slow, cell-formed ions from the mass analyser by the use of an appropriate potential difference between the quadrupole and hexapole pole biases.

The role of adventitious water in the collision cell gases has been investigated by the deliberate addition of water and deuterium oxide to helium cell gas. Protons from this water contributed to the levels of proton containing polyatomic ions ubiquitous to ICP-MS spectra but did not result in the occurrence of additional species. The addition of water to a reactive helium/hydrogen mixture in the cell did not greatly influence the levels of interference or analyte ions observed.

A helium/hydrogen collision cell gas mixture has been identified that facilitated the determination of Si by attenuating the coincident spectral interferences. Stable Si solutions were achieved by the use of a fluoroboric-boric acids matrix.

Various methods to narrow the ion energy distribution were explored. Helium as a collision cell gas and a variety of plasma screen modifications were considered. These techniques varied the median potential of the distribution but did not significantly affect the width of the distribution.

### **Acknowledgements**

The author would like to thank the Analytical Division of the Royal Society of Chemistry and the EPSRC for provision of his studentship, Thermo Electron for the provision of the VG PQ ExCell instrument and use of the clean room at Winsford and the Valid Analytical Measurement programme of the Department of Trade and Industry for financial support of the research group.

I am grateful to all those at Thermo Electron in Winsford who have supported this work, particularly Jonathan Batey, Jenny Godfrey, Simon Nelms, Phil Shaw and Bill Spence.

I am indebted to Barry Sharp, my supervisor, for all of his support and guidance over the last six years, I am extremely grateful to him. I would also like to thank the other members of the Atomic Spectroscopy Research Group: Helen Reid, Chris Ingle, Petra Appelblad, Abdulaziz Bashammakh, Mark Landon and Peter Winship. Thanks also to the Radiochemistry Research Group for providing such pleasant and friendly company whilst I worked in their laboratory and to Linda Sands, Sonia Wilson, Jill Thorley, David Wilson and Stuart Pinkney for all their help.

I am especially grateful to my friends and family for keeping me happy and helping me to preserve what little sanity I may have, particularly Andrew Akehurst, Ruth Bedford, Jamie Beaumont, Gareth Edwards, Cat Jones, Jude Lynn, Miles Trumper and Chris Wallis.

Finally, I would like to thank John 'Doc' Houlding and the late Barry Long for imbuing me with the love of science that set me on this path.

## Contents

<b>Abstract</b> .....	<b>ii</b>
<b>Acknowledgements</b> .....	<b>iii</b>
<b>Contents</b> .....	<b>iv</b>
<b>List of Tables</b> .....	<b>vi</b>
<b>List of Figures</b> .....	<b>viii</b>
<b>Glossary of Abbreviations</b> .....	<b>xi</b>
 <b>Chapter One – Introduction</b> .....	<b>1</b>
<b>1.0 Introduction</b> .....	<b>2</b>
1.1 <i>Principles of Plasma Source Mass Spectrometry</i> .....	3
1.2 <i>Interferences</i> .....	8
1.2.1 Desolvation .....	11
1.2.2 Cool Plasma .....	13
1.2.3 Increased Resolution .....	15
1.2.4 Mixed Gas Plasmas .....	17
1.2.5 Collision/Reaction Cells.....	20
 <b>Chapter Two – Collision/reaction Cell ICP-MS</b> .....	<b>22</b>
<b>2.0 Collision/Reaction Cell ICP-MS</b> .....	<b>23</b>
2.1 <i>Instrumentation</i> .....	24
2.2 <i>Reactions in the Collision/Reaction Cell</i> .....	29
2.2.1 Kinetics.....	33
2.2.2 Preparation of the ‘Thermoli’ Ion-Molecule Reaction Database .....	36
2.3 <i>Collision/Reaction Cell Gases</i> .....	41
2.3.1 Ammonia.....	42
2.3.2 Helium.....	45
2.3.2.1 Helium and the Role of Adventitious Water .....	46
2.3.2.2 Noise Reduction in Isotope Ratio Studies .....	47
2.3.2.3 Helium as an Inert ‘Buffer’ in Conjunction with a Reactive Gas .....	52
2.3.2.4 Energy Discrimination of Polyatomic Ions .....	52
2.3.3 Hydrogen.....	55
2.3.4 Methane.....	61
2.3.5 Oxygen .....	63
2.3.6 Other Gases .....	68
2.3.7 Summary .....	74
2.4 <i>Performance Optimisation Methods</i> .....	77
2.4.1 Multi-element Optimisation Indicators .....	77
2.4.2 Ion Energy Techniques.....	80
2.5 <i>Determination of Silicon</i> .....	83
2.5.1 Determination of Si by Collision Cell ICP-MS .....	86
2.5.2 Determination of Si by Dynamic Reaction Cell ICP-MS .....	88



<b>Chapter Three – Determination of Silicon .....</b>	<b>83</b>
<b>3.0 Determination of Silicon .....</b>	<b>92</b>
3.1 <i>Instrumentation and General Experimental</i> .....	92
3.2 <i>Experimental</i> .....	93
3.2.1 Preliminary Work – Si in a Water Matrix.....	93
3.2.2 Si in an Aqueous Fluoroboric-boric Acids Matrix .....	95
3.3 <i>Results and Discussion</i> .....	96
3.3.1 Preliminary Work – Si in a Water Matrix.....	96
3.3.2 Si in an Aqueous Fluoroboric-boric Acids Matrix.....	103
3.4 <i>Summary</i> .....	109
<b>Chapter Four – The Role of Water in the Collision Cell Gas.....</b>	<b>111</b>
<b>4.0 The Role of Water in the Collision Cell Gas.....</b>	<b>112</b>
4.1 <i>Thermodynamics</i> .....	112
4.2 <i>Experimental</i> .....	113
4.3 <i>Results and Discussion</i> .....	115
4.4 <i>Summary</i> .....	126
<b>Chapter Five – Ion Energy Effects .....</b>	<b>127</b>
<b>5.0 Ion Energy Effects.....</b>	<b>128</b>
5.1 <i>Experimental</i> .....	128
5.1.1 Instrumentation and Optimisation .....	128
5.1.2 Materials and Reagents .....	133
5.1.3 Methodology .....	133
5.1.3.1 Collision Cell Effects .....	133
5.1.3.2 Ion Energy Effects.....	135
5.2 <i>Reactions and Thermodynamics</i> .....	139
5.3 <i>Results and Discussion</i> .....	144
5.3.1 Ion Energy Effects in Collision/reaction Cells .....	144
5.3.1.1 Use of Oxygen as a Cell Gas .....	144
5.3.1.2 Use of Helium/hydrogen as a Cell Gas .....	150
5.3.1.3 Energy Distribution in the Ion Beam .....	152
5.3.1.4 Ion Energy, Reactivity and Species Selectivity.....	155
5.3.1.5 Influence of the Plasma Screen on IKEE.....	168
5.3.2 Ion Energy Distribution.....	177
5.3.2.1 Effect of the Collision/reaction Cell.....	179
5.3.2.2 Effect of ‘Active’ Plasma Screen Use.....	192
5.3.2.3 Effect of Plasma Screen Grounding.....	196
5.3.2.4 Use of Different Cones and Tuning for Plasma Screen Use.....	212
5.3.2.5 Summary .....	216
<b>Conclusion.....</b>	<b>218</b>
<b>References.....</b>	<b>222</b>
<b>Appendices.....</b>	<b>231</b>
<b>Appendix 1 – Extracts from the “Thermoli” Ion-Molecule Reaction Database.....</b>	<b>232</b>
<b>Appendix 2 – Professional Development.....</b>	<b>239</b>
<b>Appendix 3 – Publications and Conference Contributions.....</b>	<b>241</b>

## List of Tables

Table	Caption	Page
1.1	A selection of common spectral interferences	10
1.2	Selected analytes with their first ionisation potentials (IP)	15
1.3	Resolution necessary to resolve some common interferences	16
1.4	Some isobaric interferences which cannot be resolved with current technology	17
2.1	Proprietary names for collision/reaction cells	25
2.2	Names for collision/reaction cells used in the titles of articles and frequency of use	26
2.3	General and specific examples of gas-phase reactions of each type	33
2.4	Interference ions commonly encountered in ICP-MS, as featured in the 'Thermoli' database	37
2.5	Reactions between $\text{NO}^+$ or $\text{Ar}_2\text{H}^+$ and helium: an extract from the 'Thermoli' database	38
2.6	All reactions with $\text{ArH}^+$ listed in the 'Thermoli' database	39
2.7	Influence of helium flow on mass bias at various masses.	51
2.8	Selected isobaric interferences on a range of metals in seawater	54
2.9	Interferences resolved using methane by Chen and Jiang	62
2.10	Spectral interferences to P and S determination	65
2.11	Reactions between $\text{P}^+$ , $\text{S}^+$ and polyatomic ions in the $m/z$ 31-36 range with $\text{O}_2$	65
2.12	Some significant oxide interferences to noble metal analysis	66
2.13	Principal argon- and calcium-based spectral interferences to Fe isotopes	69
2.14	Kinetic and thermodynamic data for reactions of the form shown in Equation 2.29	72
2.15	Gases used in collision/reaction cell ICP-MS to determine analytes suffering isobaric interference	75
2.16	The 'key players': ions for which the signals vary most over the helium/hydrogen flow rates studied	78
2.17	Isobaric interferences with silicon	84
2.18	Resolution required for isobaric interferences with Si	85
2.19	Effect of different gases on the determination of Si (at $m/z$ 28) by ICP-CC-MS	86
3.1	Instrumental parameters used for Si experiments	94
3.2	Background signal, analyte sensitivity, theoretical detection limits and background equivalent concentrations for Si at $m/z$ 28 with varying helium and hydrogen flows	97
3.3	Summarised results of torch box argon flushing experiments. Counts recorded are for deionised water at $m/z$ 28	106
4.1	Reactions between selected argon-based ions and helium or water with $\Delta H_r \leq +1$ eV	113
4.2	Plasma, ion optic and acquisition parameters used	114
4.3	Hydroxy and deuterioxy species in the region $m/z$ 17-22	120
4.4	Source of protons in various polyatomic species	123

<b>Table</b>	<b>Caption</b>	<b>Page</b>
5.1	Plasma parameters used	128
5.2	Acquisition parameters used	134
5.3	$m/z$ monitored in each $m/z$ set	135
5.4	Combinations of collision cell gas flow rates, $V_H$ settings and plasma screen use used	136
5.5	Cone and extraction potential combinations used	138
5.6	Proposed reactions for thermodynamic evaluation of a collision/reaction cell for ICP-MS	140
5.7	Reactions between metal cations and oxygen or water forming $MO^+$ selected for use in the study of collision/reaction cell reactivity	142
5.8	Possible reactions for the formation of $MO^+$ ( $M = Ce, Cr, Ti, V$ ) and $H_3O^+$ and for the removal of $Ar^+$ and $Ar_2^+$	144
5.9	Isotopic abundances of Ni and Zn calculated for 20 ng ml <sup>-1</sup> single-element solutions. Data were acquired with helium+hydrogen 1.0+1.7 ml min <sup>-1</sup> in the collision cell.	151
5.10	Specified parameters for a simple electronic model of an ICP-MS system	196
5.11	Potentials and currents on the plasma screen grounds and the plasma potential for the various plasma screen grounding patterns of the circuit in Figure 5.31 as modified by Figure 5.32	201
5.12	Normalised $CeO^+/Ce^+$ and $Ba^{++}/Ba^+$ levels for standard plasma, wire ground plasma screen, rf ground plasma screen and combined rf and wire ground plasma screen	205
5.13	Normalised $CeO^+/Ce^+$ and $Ba^{++}/Ba^+$ levels for standard plasma, wire ground plasma screen, dc ground plasma screen, rf ground plasma screen and divided ground plasma screen	208
5.14	Energy distribution median potentials and half-widths for standard plasma, wire grounded plasma screen, rf grounded plasma screen, dc grounded plasma screen and divided ground plasma screen.	209
5.15	Experimentally determined median potentials and plasma potentials from electronic modelling for standard plasma, wire grounded plasma screen, dc grounded plasma screen, rf grounded plasma screen and divided ground plasma screen	210
A1.1	Reactions between interference ions and helium, neon, argon or krypton with reaction enthalpy $\leq +1$ eV	232
A1.2	Reactions between interference ions and hydrogen with reaction enthalpy $\leq +1$ eV	234
A1.3	Reactions between interference ions and water with reaction enthalpy $\leq +1$ eV	237

## List of Figures

Figure	Caption	Page
1.1	Schematic of a typical ICP-MS instrument with a quadrupole mass analyser	3
1.2	An illustration of the ICP torch and vacuum interface region: axial and radial cross-sections	4
1.3	The basic layout of a quadrupole mass analyser	7
1.4	Schematic representation of a cryogenic desolvation system	12
2.1	A generalised schematic of a collision/reaction cell inductively coupled plasma mass spectrometer	27
2.2	Typical reaction coordinate for an exothermic ion-neutral reaction	30
2.3	Reaction coordinate for the gas phase reaction shown in Equation 2.1	31
2.4	Semilogarithmic graphs of ion signal at a particular $m/z$ against collision/reaction cell gas flow rate for a contamination-free blank and a blank with moderate contamination present	35
3.1	Semilogarithmic graph of counts at $m/z$ 28 for deionised water against helium flow	98
3.2	Determination of Si in water at $m/z$ 28: calibration curve and repeat readings of a sample of semiconductor grade water	99
3.3	Signal recorded at $m/z$ 28 for a range of Si standards in water with a trace of hydrofluoric acid	100
3.4	Day one: calibration curves for Si at $m/z$ 28 and Zr at $m/z$ 92	103
3.5	Day two: calibration curve for Si at $m/z$ 28	104
3.6	Day three: calibration curve for Si at $m/z$ 28	104
3.7	Illustration of a design for a torch bonnet system to envelop the plasma in an argon atmosphere	107
3.8	Calibration curves for Si at $m/z$ 28 and W at $m/z$ 182	108
3.9	Calibration curve for Si at $m/z$ 28	109
4.1	Expected patterns of peaks for $XH^+$ on $D_2O - H_2O$ plots	117
4.2	Expected pattern of peaks for $XH_2^+$ on $D_2O - H_2O$ plots	118
4.3	$D_2O - H_2O$ plots for the $m/z$ region 14–45	119
4.4	$D_2O - H_2O$ plots for the $m/z$ region 81–84	122
4.5	Ratio of signals 'wet'/'dry' with helium+hydrogen $1.0+1.7 \text{ ml min}^{-1}$ in the cell for a multi-element standard and a 2 % nitric acid blank	124
5.1	Diagrammatic representation of the 'active' plasma screen apparatus	130
5.2	Diagram of the mounting disc used to connect the braid to the grounded side of the rf coil and the disc <i>in situ</i>	131
5.3	Diagrammatical representation of wire ground and rf ground plasma screen and dc ground and rf ground plasma screen	132
5.4	Variation in selected analyte oxide signals with $V_Q$ and $V_H$ . Collision cell gas oxygen.	146
5.5	Variation in the $VO^+/V^+$ ratio with $V_Q - V_H$ for a range of $V_Q$ values and $V_H$ values. Collision cell gas oxygen.	148
5.6	Variation in $In^+$ signal with $V_Q - V_H$ . Collision cell gas oxygen.	149
5.7	'Stopping curves' and ion beam energy distributions for $^{115}In^+$ with and without the use of a plasma screen. No collision cell gas.	153
5.8	Variation in $^{115}In^+$ signal and $^{156}(CeO)^+/^{140}Ce^+$ with $V_H$ .	156

Figure	Caption	Page
	Helium+hydrogen cell gas.	
5.9	Variation in $^{115}\text{In}^+$ signal with $V_Q - V_H$ at a range of $V_H$ values.	157
	Helium+hydrogen cell gas	
5.10	Variation in $^{80}(\text{Ar}_2)^+$ signal with $V_Q - V_H$ at a range of $V_H$ values.	159
	Collision cell gases helium+hydrogen and helium.	
5.11	Variation in $^{67}(\text{VO})^+ / ^{51}\text{V}^+$ and $^{156}(\text{CeO})^+ / ^{140}\text{Ce}^+$ with $V_Q - V_H$ at a range of $V_H$ values. Collision cell gases helium+hydrogen.	162
5.12	Variation in $^{68}(\text{CrO})^+ / ^{52}\text{Cr}^+$ and $^{144}(\text{TeO})^+ / ^{128}\text{Te}^+$ with $V_Q - V_H$ at a range of $V_H$ values. Collision cell gases helium+hydrogen.	164
5.13	Variation in $^{21}(\text{H}_3\text{O})^+ / ^{36}\text{Ar}^+$ with $V_Q - V_H$ at a range of $V_H$ values. Collision cell gases helium+hydrogen and helium.	166
5.14	Variation in $^{80}(\text{Ar}_2)^+$ signal with $V_Q - V_H$ at $V_H$ values of +2, +4 and +6 V for helium+hydrogen collision cell gas flows of 1.0+1.0, 1.0+1.7 and 1.0+2.5 ml min <sup>-1</sup>	167
5.15	Variation in $^{115}\text{In}^+$ signal with $V_Q - V_H$ at various $V_H$ values; without and with plasma screen. Collision cell gases helium+hydrogen.	169
5.16	Variation in $^{80}(\text{Ar}_2)^+$ signal with $V_Q - V_H$ at a range of $V_H$ values; without and with plasma screen. Collision cell gas helium+hydrogen.	171
5.17	Variation in $^{156}(\text{CeO})^+ / ^{140}\text{Ce}^+$ with $V_Q - V_H$ at a range of $V_H$ values; without and with plasma screen. Collision cell gas helium+hydrogen.	173
5.18	Variation in $^{144}(\text{TeO})^+ / ^{128}\text{Te}^+$ with $V_Q - V_H$ at a range of $V_H$ values; without and with plasma screen. Collision cell gas helium+hydrogen.	174
5.19	Variation in $^{21}(\text{H}_3\text{O})^+ / ^{36}\text{Ar}^+$ with $V_Q - V_H$ at a range of $V_H$ values; without and with plasma screen. Collision cell gas helium+hydrogen.	176
5.20	Illustrative ion energy distributions: analyte ion and interference ion energy distributions separated and analyte ion and interference ion energy distributions overlap	178
5.21	Maxwell distributions of speeds and energies in the plasma	180
5.22	Distributions of speeds and energies at the skimmer orifice	182
5.23	Distributions of speeds and energies of ions exiting the collision cell	185
5.24	Normalised $V_Q$ stopping curves and energy distributions for $\text{In}^+$ with helium+hydrogen cell gas with and without plasma screen use	187
5.25	Normalised $\text{In}^+$ energy distributions with and without plasma screen use with 3.0 ml min <sup>-1</sup> helium or no gas	189
5.26	Normalised $\text{In}^+$ energy distributions with and without plasma screen use with 6.0 ml min <sup>-1</sup> helium or no gas in the collision cell	190
5.27	Normalised $V_H$ stopping curves and ion energy distributions for $\text{In}^+$ with standard plasma, grounded plasma screen and -1.5 V 'active' plasma screen with helium+hydrogen cell gas	193
5.28	Variation in normalised $^{67}(\text{VO})^+ / ^{51}\text{V}^+$ level with $V_H$ for standard plasma, grounded plasma screen and -1.5 V active plasma screen with helium+hydrogen 1.0+1.7 ml min <sup>-1</sup>	194
5.29	Simple electronic model of an ICP-MS system	197
5.30	Waveforms of the applied rf and plasma potential in the electronic model shown in Figure 5.29	198
5.31	A simple electronic model of an ICP-MS system including a plasma screen	200

<b>Figure</b>	<b>Caption</b>	<b>Page</b>
5.32	Modified plasma screen circuit	201
5.33	Normalised $\text{In}^+$ stopping curves and energy distributions for standard plasma, wire grounded plasma screen, rf grounded plasma screen and combined wire and rf grounded plasma screen	203
5.34	$\text{In}^+$ stopping curves for standard plasma, wire grounded plasma screen, rf grounded plasma screen, dc grounded plasma screen and divided ground plasma screen	208
5.35	Circuit used to ascertain the frequency dependence of the divided ground plasma screen	211
5.36	Frequency dependence of current in the circuit shown in Figure 5.35	212
5.37	Normalised $\text{In}^+$ stopping curves for standard plasma, standard tuned plasma screen and retuned plasma screen	213
5.38	Normalised $\text{In}^+$ stopping curves and energy distributions for standard cones, $\text{X}_i$ cones and standard sample cone with trial skimmer cone under $-566 \text{ V}$ and $-200 \text{ V}$ extraction conditions	215

### **Glossary of Abbreviations**

ac	Alternating current
ArM <sup>+</sup>	An argon-metal ion
ArX <sup>+</sup>	An argon-based polyatomic ion
BEC	Background equivalent concentration
CID	Collision-induced dissociation
dc	Direct current
DL	Detection limit
DRC	Dynamic Reaction Cell
HPLC	High performance liquid chromatography
i.d.	Inside diameter
ICP	Inductively coupled plasma
ICP-AES	Inductively coupled plasma atomic emission spectroscopy
ICP-CC-MS	Collision cell ICP-MS
ICP-DRC-MS	Dynamic Reaction Cell ICP-MS
ICP-MCMS	Multicollector ICP-MS
ICP-MS	Inductively coupled plasma mass spectrometry
ICP-QMS	Quadrupole ICP-MS
ICP-SFMS	Sector field ICP-MS
IKEE	Ion kinetic energy effect
IP	Ionisation potential
<i>k</i>	Rate constant
<i>k<sub>B</sub></i>	Boltzmann constant
KED	Kinetic energy discrimination
<i>m</i>	Atomic/molecular mass
<i>m/z</i>	Mass-to-charge ratio
<i>m/Δm</i>	See Section 1.2.3
M <sup>+</sup>	A metal ion
M <sup>++</sup>	A divalent metal ion
MH <sup>+</sup>	A metal hydride ion
MO <sup>+</sup>	A metal oxide ion
MOH <sup>+</sup>	A metal hydroxide ion

$MX^+$	A metal-based polyatomic ion
o.d.	Outside diameter
ppm	Parts per million
rf	Radiofrequency
$S/B$	Signal-to-background ratio
$S/N$	Signal-to-noise ratio
$T$	Temperature
TIMS	Thermal ionisation mass spectrometry
$V_H$	(Collision cell) hexapole bias potential
$V_Q$	(Mass analyser) quadrupole bias potential
$\Delta H_r$	Reaction enthalpy



# **Chapter One**

## **Introduction**

## **1.0 Introduction**

Inorganic mass spectrometry has its origins in the early twentieth century. In 1912, Thomson obtained mass spectra of several atmospheric gases and, in 1913, he discovered the 20 u and 22 u isotopes of neon using mass spectrometry.<sup>1</sup> A variety of mass spectrometers and ion sources were developed over the course of the century including arc and spark spectrometries, thermal ionisation mass spectrometry (TIMS), secondary ion mass spectrometry (SIMS) and glow discharge mass spectrometry (GDMS).

The inductively coupled plasma (ICP) had been used as an excitation source for atomic emission spectroscopy (ICP-AES) for almost two decades when, in 1980, Houk and others<sup>2</sup> coupled an ICP to a mass spectrometer. ICP-MS is now accepted as a powerful technique for the determination of trace elements. ICP-MS has been used in the analysis of a wide range of samples, of biological, geological, environmental and other origins. The desirable characteristics of ICP-MS include a dynamic range of more than eight orders of magnitude and detection limits as low as 1 pg ml<sup>-1</sup> for many elements.<sup>3</sup> ICP-MS, like other mass spectrometries, permits the determination of isotopes and isotope ratios in addition to elemental determination. ICP-MS requires only simple sample preparation compared with that required for other techniques such as TIMS.

ICP-MS is a relatively interference-free technique, it does however suffer spectral interference from monatomic and polyatomic ions, particularly at the lower end of the mass range. Much of the continuing development of ICP-MS has been concerned with methods to prevent or resolve these interferences; several methods are discussed later in this chapter. Collision/reaction cell ICP-MS is one technique for reducing this interference problem. The development of a greater understanding of the processes occurring in collision/reaction cells and their analytical benefits are the subject of this thesis.

## 1.1 Principles of Plasma Source Mass Spectrometry

An inductively coupled plasma mass spectrometer consists of an atmospheric argon plasma source coupled, *via* an interface, to a mass analyser and detector located in a vacuum chamber. The basic layout of a typical ICP-MS instrument is depicted in Figure 1.1.

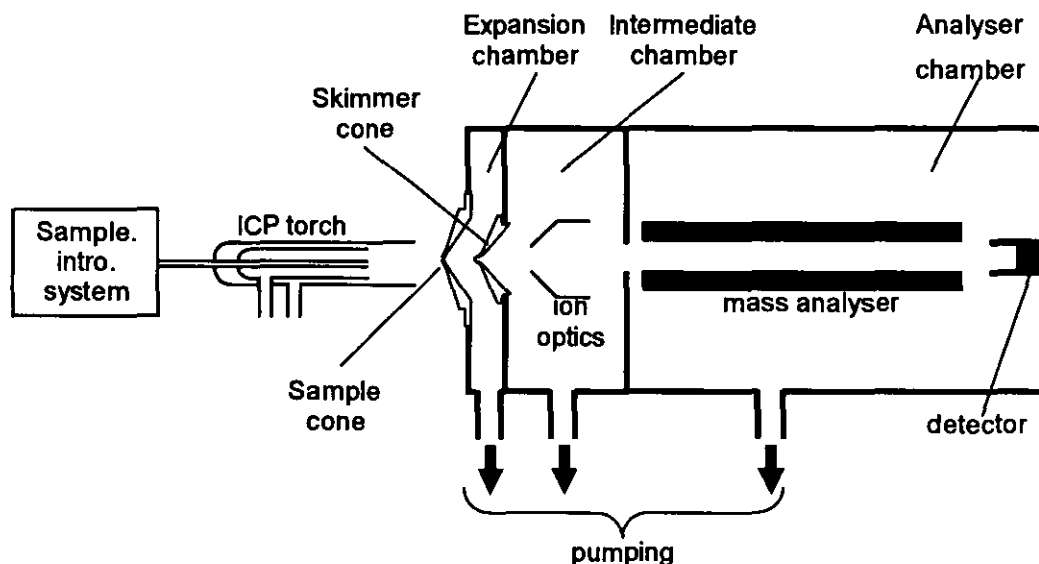


**Figure 1.1** – Schematic of a typical ICP-MS instrument with a quadrupole mass analyser.

The descriptions of the component parts of an ICP-MS instrument which follow relate to a standard quadrupole mass analyser instrument operated under standard conditions. (More than 90 % of ICP-MS instruments feature quadrupole mass analysers.)<sup>4</sup> Several possible variations from these standard conditions are discussed in Sections 1.2.1 – 1.2.5 below.

The argon ICP acts as an effective ion source, vaporising, atomising and ionising the sample.<sup>3</sup> The majority of elements are more than 90 % ionised<sup>5</sup> during their 2–3 ms transit time<sup>3</sup> in the plasma. The plasma is formed by three concentric argon flows formed and directed by the silica ICP torch. The energy is supplied by a 1 – 2 kW 27 or 40 MHz rf power supply.<sup>3</sup> A high voltage electric discharge is used to trigger the formation of the plasma. Current from the rf generator is transferred to the plasma by a three-turn

water-cooled load coil which encircles the end of the torch. The magnetic field from the current in the load coil induces a current in the argon, forming the plasma.<sup>3</sup>

The basic layout of the different argon flows in the ICP torch is depicted in Figure 1.2. Virtually all ICP-MS systems employ Fassel-type torches.<sup>6</sup> Such torches have an internal diameter of 18 mm and use approximately  $15 \text{ l min}^{-1}$  argon gas to form the plasma. The innermost flow in the torch, called the injector or nebuliser flow, consists of  $0.4 - 1.0 \text{ l min}^{-1}$  argon and carries the sample mist from the sample introduction/nebulisation system. The injector flow is surrounded by an intermediate or auxiliary flow of  $0.5 - 1.0 \text{ l min}^{-1}$  argon, introduced tangentially to the torch, to promote plasma formation and stability. The outermost gas flow, called the main or cool flow, consists of  $12 - 14 \text{ l min}^{-1}$  argon, which is tangentially introduced to the torch. This flow constitutes the bulk of the plasma.<sup>6</sup>

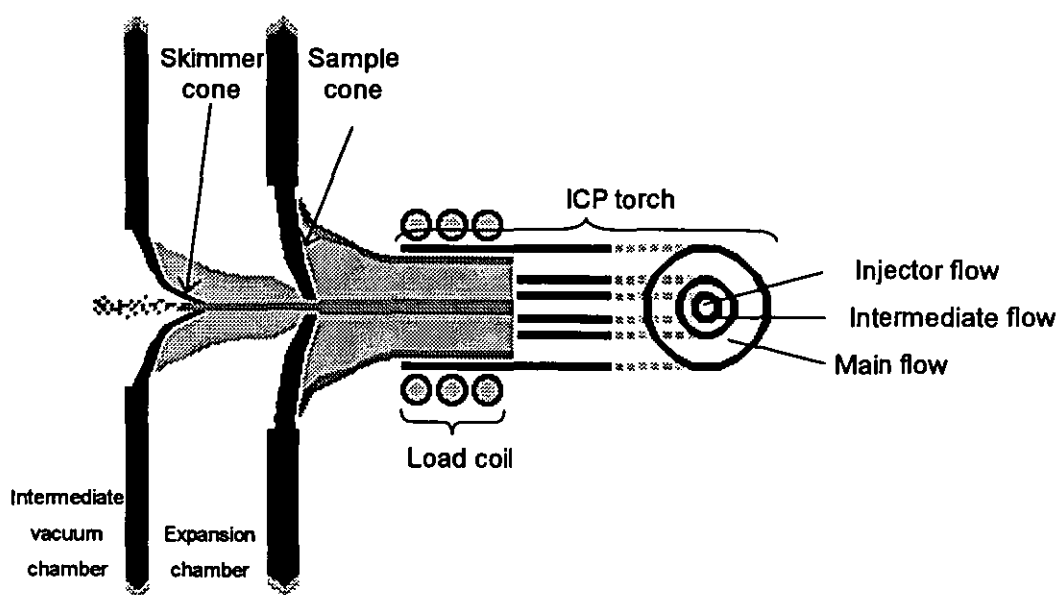


**Figure 1.2** – An illustration of the ICP torch and vacuum interface region: axial and radial cross-sections

The outer tube of the plasma torch extends approximately 2 cm beyond the ends of the inner two tubes. This portion of the torch is surrounded by the load coil and is the location of the plasma. The plasma fills this end portion of the torch without touching it

and extends beyond the end of the torch; it has a classical flame shape. The body of the plasma has an annular shape with the injector flow running through the centre.<sup>3</sup>

The effectiveness of the ICP as a monatomic ion source is due to the high temperatures and high electron number density of the plasma. The gas kinetic and electron temperatures are 4500 – 8000 K and 8000 – 10 000 K respectively, the electron number density is  $1-3 \times 10^{15} \text{ cm}^{-3}$ . The electron number density is 1000 times higher in the ICP than in combustion flames, minimising ionisation related interference by maximising the extent of ionisation. Ions formed in the ICP have an ion kinetic energy spread of several electronvolts.<sup>3</sup>

By capacitive coupling with the load coil, the plasma develops a non-zero potential.<sup>5</sup> This results in an arc, called the 'secondary discharge', forming between the ICP and the electrically grounded sample cone.<sup>5</sup> In some cases, the secondary discharge can contribute to wide energy distributions and elevated levels of divalent ions.<sup>5</sup>

The tip of the plasma strikes the sample cone, which samples the central channel of the plasma. The sample cone is usually made of nickel and has an orifice at its tip with a diameter of *circa* 1 mm.<sup>3</sup> The sampled plasma undergoes supersonic expansion in the low pressure expansion chamber (*ca.* 2 mbar).<sup>3</sup> The plasma expands behind the sample cone, forming a free jet within which the pressure may be lower than the background pressure.<sup>3,5</sup> The free jet is divided into three distinct regions, a well characterised 'zone of silence', which is surrounded by a poorly characterised shock wave with higher density than within the zone of silence called the 'barrel shock'. The zone of silence terminates in a 'Mach disc', perpendicular to the jet axis, which is followed by a further shockwave.<sup>3,5</sup>

The expanding plasma is sampled several millimetres into the expansion chamber and within the zone of silence by a second nickel cone, known as the 'skimmer cone'. Behind the skimmer, the beam enters a lower pressure intermediate vacuum chamber ( $10^{-3}$ – $10^{-5}$  mbar).<sup>3</sup> In this chamber, space charge effects have an important influence on ion motion. The cations in the plasma beam are mutually repelled by electrostatic interactions and, due to momentum considerations, lighter ions are deflected more than

Ion optics consist of different metal elements to which dc potentials are applied, many different designs are used in the different instruments.<sup>7</sup> These elements can be conical, cylindrical or plate structures, with axial symmetry.<sup>5,6</sup> Varying the potentials applied to the different lens elements alters the trajectories of ions within the ion optics allowing the ion beam to be focussed.<sup>5</sup>

Two named combinations of lens elements that have been used in ICP-MS systems are the Einzel lens and the Bessel box.<sup>6,7</sup> An Einzel lens consists of three consecutive cylindrical lens elements to each of which different potentials can be applied.<sup>7</sup> A Bessel box consists of a cylindrical or 'barrel' lens element with a plate lens, containing an axial aperture, at each end of the cylinder. A small circular lens element, called the 'photon stop' is located in the centre of the Bessel box on its axis. The photon stop prevents the transmission of photons from the plasma reaching the detector and contributing to the background signal. The other lens elements deflect the ion beam around the photon stop.<sup>7</sup>

During or following passage through the series of ion optical elements, the ion beam exits the intermediate vacuum chamber and enters the higher vacuum analyser chamber ( $10^{-6} - 10^{-7}$  mbar).<sup>3</sup>

The ion optics direct the focussed ion beam into the quadrupole mass analyser. The quadrupole consists of four rods with circular or hyperbolic cross-sections. Combinations of dc and radiofrequency (rf) ac potential are applied to these rods, allowing ions of different mass-to-charge ratio ( $m/z$ ) a stable path through the quadrupole to the detector with ions of other  $m/z$  being rejected from the quadrupole. Variation of the applied potentials with time allows the detection of ions of different  $m/z$ . Figure 1.3 shows the basic layout of a quadrupole mass analyser.

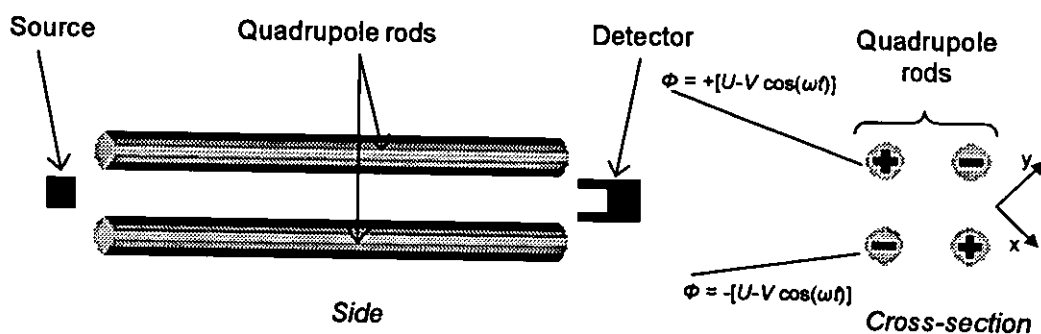


**Figure 1.3** – The basic layout of a quadrupole mass analyser. The mathematical expressions are described in the text.

The rod pairs carry a combination of dc and ac potentials,<sup>8</sup>  $\Phi$ , as described in Equation 1.1. Opposite rods bear the same potential and adjacent rods opposite potentials, as shown in Figure 1.3.

$$\Phi = \pm[U - V \cos(\omega t)]$$

**Equation 1.1**

In Equation 1.1,  $\Phi$  is the total potential applied to the rods,  $U$  the dc potential,  $V$  the zero-to-peak amplitude of the ac component,  $\omega$  the angular frequency ( $\omega = 2\pi f$  where  $f$  is the frequency) and  $t$  is time.

If axes are defined as  $x$  and  $y$  as in Figure 1.3 and  $z$  parallel to the rods, then the motion of ions in the  $x$ - $y$  plane as contributed to by the electric field are described by the Mathieu equation (Equation 1.2).<sup>8</sup> The velocity of ions parallel to the  $z$ -axis is unaffected by the fields.<sup>8</sup>

$$\frac{d^2 u}{d x^2} + [a_u - 2q_u \cos(\omega t)]u = 0$$

**Equation 1.2**

In the Mathieu equation,  $u$  represents the  $x$ - or  $y$ -axes and  $a_u$  and  $q_u$  the Mathieu parameters in direction  $u$ . The expressions for the Mathieu parameters are shown, for a monovalent ion, in Equations 1.3 and 1.4.<sup>8</sup> ( $e$  is the charge on an electron,  $m$  the mass of the ion and  $r_0$  the radius of the multipole.)

$$a_u = \frac{8eU}{mr_0^2\omega^2}$$

**Equation 1.3**

$$q_u = \frac{4eV}{mr_0^2\omega^2}$$

**Equation 1.4**

For a particular quadrupole,  $r_0$  and  $\omega$  are usually constant leaving  $U$ ,  $V$  and  $m$  as the only variables. Ions oscillate in the  $x$ - $y$  plane and provided  $u < r_0$  the ions have a stable path through the cell. (If  $u \geq r_0$ , the ions hit the rods.) The  $a$ - $q$  stability regions in the  $x$  and  $y$  directions overlap to give a triangular  $a$ - $q$  region within which the ions have stable passage through the quadrupole.<sup>8</sup> The  $U$  and  $V$  values represented by  $a$  and  $q$  respectively vary with ion mass. Thus for different  $U$  and  $V$  values, different masses have stable paths through the quadrupole. If a suitably high  $U/V$  ratio is selected, then a narrow range of masses has stable passage and the quadrupole acts as a mass analyser; by increasing  $U$  and  $V$  in proportion so  $U/V$  is constant, successive higher mass ions can be determined.<sup>8</sup> If a lower  $U/V$  (or  $a/q$ ) is selected then a larger range of masses have stable passage through the cell and if  $U = 0$  (i.e. rf-only operation) a very wide range of ions have stable transit.<sup>8</sup> Ions stably transmitted by the quadrupole are measured, as pulses or current, by a suitable ion detector.<sup>3</sup>

## **1.2 Interferences**

Elemental mass spectra are very simple; each element has a unique 'fingerprint' of ten or fewer isotopes. 95 % of all elements have seven or fewer natural isotopes and 61 % three or fewer.<sup>9</sup> Background count levels in ICP-MS are generally very low,<sup>3</sup> typically less than 10 counts  $s^{-1}$ . ICP-MS systems do however suffer from two distinct forms of interference: non-spectral interference, usually termed matrix effects, and spectral interference.

Non-spectral matrix effects are due to interactions in the system between analyte ions and high concentrations of matrix constituents from the sample. Matrix effects usually



produce a suppression of analyte signals although signal enhancement can also occur,<sup>6</sup> for example the presence of 1000  $\mu\text{g ml}^{-1}$  aluminium resulted in approximately 60 % suppression of the Zn, Sr, Y, Mo and Sb signals but 60 % enhancement of the Mg signal.<sup>10</sup> Matrix effects are very general, although the effects are more noticeable with low mass analytes and with high mass matrix ions.<sup>6</sup> Matrix effects are principally due to the influence of ions from the matrix on the ion beam in the mass spectrometer. The high level of matrix ions present causes an increase in space charge, *i.e.* the charge density of the ion beam is higher and so more scattering and loss of ions due to electrostatic repulsion occurs.<sup>6</sup>

Various strategies exist for controlling matrix effects including matrix separation by sample pre-treatment or sample introduction methods, optimisation of plasma conditions to minimise signal suppression, the use of internal standards and mathematical correction.<sup>6,10</sup>

Spectral interferences occur when two or more ions of the same nominal mass-to-charge ratio ( $m/z$ ) are present. These interferences, termed isobars, can be further divided into elemental (or monatomic) and molecular (or polyatomic) ion interferences. For elemental quantification, the majority of the elemental isobar interferences can be avoided by judicious selection of isotopes free from these interferences. Other methods must be adopted where monoisotopic elements or particular isotopes are to be determined.

Several different types of polyatomic ions can be identified: argon-based ions ( $\text{ArX}^+$ ), metal oxides, hydroxides and other polyatomic metal ions ( $\text{MO}^+$ ,  $\text{MOH}^+$ ,  $\text{MX}^+$ ) and species derived from atmospheric gases and the sample solvent.<sup>6,11</sup> Divalent metal ions ( $\text{M}^{++}$ ) also occur. The majority of argon-based and atmospheric gas or sample solvent derived polyatomic ions occur below  $m/z$  82, with many of these ions occurring in all background spectra. By contrast, metal-based polyatomic ions can occur throughout the mass spectrum and the presence of particular ions depends on the composition of the sample matrix.<sup>6,11</sup> Examples of common spectral interferences are given in Table 1.1.

**Table 1.1 – A selection of common spectral interferences (Data from May and Wiedermeyer<sup>11</sup> and Rosman and Taylor<sup>9</sup>)**

Analyte		Monatomic	Polyatomic interferences		
Isotope	Abundance (%)	Interferences	Argon-based	Metal-based	Gas/solvent-based
<sup>28</sup> Si	92.21				<sup>14</sup> N <sub>2</sub> <sup>+</sup> , <sup>12</sup> C <sup>16</sup> O <sup>+</sup>
<sup>32</sup> S	95.02				<sup>16</sup> O <sub>2</sub> <sup>+</sup>
<sup>40</sup> Ca	96.97	<sup>40</sup> Ar <sup>+</sup>			
<sup>54</sup> Fe	5.82	<sup>54</sup> Cr <sup>+</sup>	<sup>40</sup> Ar <sup>14</sup> N <sup>+</sup>		<sup>37</sup> Cl <sup>16</sup> OH <sup>+</sup>
<sup>56</sup> Fe	91.66		<sup>40</sup> Ar <sup>16</sup> O <sup>+</sup>		
<sup>64</sup> Zn	48.89			<sup>48</sup> Ti <sup>16</sup> O <sup>+</sup>	
<sup>75</sup> As	100		<sup>40</sup> Ar <sup>35</sup> Cl <sup>+</sup>		
<sup>80</sup> Se	49.82		<sup>40</sup> Ar <sub>2</sub> <sup>+</sup>		
<sup>87</sup> Rb	27.83	<sup>87</sup> Sr			
<sup>107</sup> Ag	51.8			<sup>91</sup> Zr <sup>16</sup> O <sup>+</sup>	
<sup>109</sup> Ag	48.2			<sup>92</sup> Zr <sup>16</sup> OH <sup>+</sup>	

Polyatomic ions can be divided into two groups based on their manner of formation.<sup>12</sup> One group, which includes metal oxides, hydroxides and divalent cations and ions derived from atmospheric gases and the sample solvent, are formed by the ionisation of incompletely atomised neutral species (e.g. MO) in the ICP. The second group of ions, which consists of argon-based ions, are formed by reactions between neutral Ar and X<sup>+</sup> in the secondary discharge (X includes H, C, N, O, S, Ar).

A number of different methods exist for resolving spectral interferences. These approaches include prevention the formation of the polyatomic ions by the use of sample desolvation, mixed gas plasmas or cool plasma techniques and chemical or spectral resolution of the interference ions by the use of collision/reaction cells or higher resolution mass spectrometers respectively. These techniques are discussed in Sections 1.2.1 – 1.2.5 below.

### 1.2.1 Desolvation

The majority of isobaric interferences contain either oxygen or hydrogen from the sample solvent, thus if this matrix is removed the corresponding interferences will be reduced.<sup>13</sup> At the simplest level, the use of cooled spray chambers, which is now standard for many ICP-MS systems, reduces the water loading of the plasma and thus the level of oxide and hydroxide ions detected.<sup>14</sup> Desolvation of the sample prior to the ICP will further reduce the solvent load of the plasma.

Desolvation systems consist of a heated tube followed by either a condenser<sup>13,15,16</sup> or a membrane separator.<sup>16</sup> A coiled tube with alternately heated and cryogenically cooled sections may be connected after the initial desolvation system and before the ICP.<sup>16-18</sup>

Typically, the heated tube is held at approximately 150 °C. At this temperature, water droplets in the aerosol rapidly evaporate, 90 % of the radius change occurs within the first 100 ms.<sup>16</sup> The much drier aerosol and water vapour then enters the cooled section of tubing, or a membrane separator. In the condenser, the water vapour condenses onto the sides of the tube, which are maintained at *ca.* 0 °C, and the condensate runs into a pumped drain, the dried aerosol enters the ICP injector flow.<sup>16</sup> Using this technique, interferences due to rare earth oxide and hydroxide ions were reduced to less than one tenth of normal levels.<sup>16</sup>

In a membrane separator, the aerosol and water vapour stream enter a tube of semi-permeable membrane, such as Teflon. This membrane is enclosed in a solid tube through which a counter current of argon 'sweep gas' is passed. The water concentration gradient across the membrane causes the diffusion of water vapour into the sweep gas. Membrane separators remove 99 % of the solvent from the aerosol flow.<sup>16-18</sup>

Experimental cryogenic desolvation systems have been reported in the literature.<sup>16</sup> Cryogenic desolvation systems have been used to further desolvate the argon aerosol output of heater-condenser desolvation systems. The devices consisted of a coil of copper tubing alternate semicircles of which were electrically heated to 140 °C and cooled to -80 °C in a bath of absolute ethanol. To minimise heat transfer between

semicircles, the copper tube was discontinuous, with poorly conducting plastic joints between. This system is represented schematically in Figure 1.4.

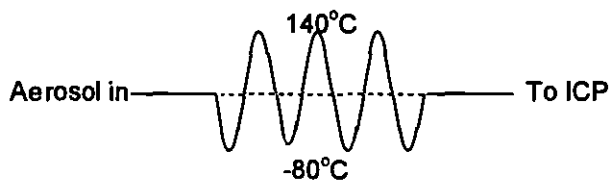


**Figure 1.4** – Schematic representation of a cryogenic desolvation system

The sequential heating and cooling of cryogenic desolvation was found to have reduced the solvent level in the output aerosol to such low levels that different plasma conditions were not necessary for non-aqueous solvents, and polyatomic interferences such as  $\text{ArO}^+$ ,  $\text{ClO}^+$  and  $\text{ArCl}^+$  were reduced by several orders of magnitude.<sup>16</sup> However, when cryogenic desolvation was used, analyte sensitivity was halved and detection limits were at least doubled for almost all analytes.<sup>16</sup> The sample uptake and washout times were also distinctly increased due to the longer aerosol path.<sup>17</sup>

When standard flow nebulisers are used to aspirate samples in organic solvents, it is usually necessary to use desolvation to prevent carbon deposits forming on the sample cone.<sup>16</sup>

A number of difficulties are encountered when desolvation systems are employed. Desolvation systems have only a limited ability to handle dissolved solids so many more difficult matrixes may be beyond their scope. Due to the variety of materials used in desolvation systems, new elemental contamination can easily enter the system. For example, Cu from the copper coils of cryogenic desolvation systems has been observed.<sup>17</sup>

The principal problem with desolvation systems is that whilst they greatly reduce interference ions originating in the sample matrix they do not have any effect on interferences derived solely from the plasma, such as  $\text{Ar}^+$  and  $\text{Ar}_2^+$ , or those derived from entrained air, such as  $\text{N}_2^+$  and  $\text{O}_2^+$ .

### 1.2.2 Cool Plasma

The term 'cool' or 'cold' plasma is used to describe a number of techniques where the forward power of the plasma is reduced and a grounded metal cylinder (the 'shield' or 'screen') inserted between the plasma and the coil. A balanced load rf coil can also be used instead of the shield. The reduced power results in a lower temperature in the central channel and the shield prevents the dc potential of the coil transferring to the plasma and thus prevents or minimises the formation of a secondary discharge.<sup>19-24</sup>

For cool plasma techniques the plasma is operated at lower power, *ca.* 650 W, with an increased gas flow in the central channel, lowering the temperature in the central channel. The lower temperature simplifies the mass spectrum, as it no longer provides sufficient energy for the formation of divalent cations or metal oxides. As the power to the plasma drops, the secondary discharge appears to increase,<sup>20</sup> (although it is possible that the discharge effects are not increased but are more visible in the lower energy environment of the cool plasma). This increase in secondary discharge results in an increase in the formation of  $\text{Ar}^+$ ,  $\text{H}^+$  and  $\text{O}^+$ . The secondary discharge is an electrical arc formed by the discharge of the plasma to the grounded sample cone.<sup>25</sup> The secondary discharge can be prevented by removing the potential difference between the plasma and the cone. The plasma potential derived from the interaction between the rf coil and the plasma. If a grounded metal cylinder (with a narrow gap along its length) is inserted between the plasma torch and the rf coil, the plasma is shielded from the potential of the coil, preventing the secondary discharge and therefore minimising  $\text{ArX}^+$  formation.<sup>20</sup>

A balanced load rf coil prevents secondary discharge as this coil geometry does not produce a dc potential in the plasma. A balanced load coil has opposite potentials applied to each end with a virtual ground point in the centre of the coil. Thus the net potential applied to the plasma is nil.<sup>22</sup>

When cool plasma with shield is used, the spectrum for clean solutions changes from one dominated by peaks from  $\text{Ar}^+$ ,  $\text{ArH}^+$ ,  $\text{C}^+$ ,  $\text{N}^+$  and  $\text{O}^+$  to one with only a small number of molecular ion peaks.<sup>19</sup> The most prominent peak is  $\text{NO}^+$  with further small peaks due to  $\text{O}^+$ ,  $\text{OH}^+$ ,  $\text{H}_2\text{O}^+$  and  $\text{H}_3\text{O}^+$ . The usual background ions are essentially replaced by  $\text{NO}^+$ .

Cool plasma prevents the formation of many interference ions, including divalent metal ions and many metal oxide, hydroxide, argon-based and atmospheric gas or solvent derived ions, producing a much simpler background spectrum free from many of the interferences present with normal plasma.<sup>21,22,24,26</sup> Cool plasma enables the determination of elements such as K, Ca and Fe which suffer from severe isobaric interference in normal plasma.<sup>21,22,26</sup>

Unfortunately, the universal application of cool plasma techniques is prevented by two major problems. Firstly, the lack of power in the plasma prevents the ionisation of those elements with first ionisation potentials greater than that of the neutral precursor to the predominant spectral feature,  $\text{NO}^+$  (9.27 eV). Such elements are only ionised to a minimal extent and so cannot be determined.<sup>20</sup> Table 1.2 lists a selection of elements that can be determined using cool plasma techniques and a selection of those which, owing to their high ionisation potential, cannot. Secondly, the technique does not work with more complex matrixes, as the low power plasma is unable to sufficiently atomise the matrix. For example, the determination of Fe in rice flour by cool plasma techniques was hindered by serious spectral interference from  $\text{CaO}^+$  and  $\text{CaOH}^+$ .<sup>26</sup> The technique is thus restricted to samples where the matrix has been removed and to 'clean' samples, such as mineral acids.<sup>21</sup>

**Table 1.2** – *Selected analytes with their first ionisation potentials (IP). Analytes with  $IP < IP(NO)$  can be determined using cool plasma techniques, those with  $IP > IP(NO)$  cannot.*

Species	IP/eV
K	4.3
Al	6.0
Ca	6.1
Fe	7.9
NO	9.27
Zn	9.4
As	9.8
Se	9.8
I	10.5

The use of plasma shield with a standard power plasma has been reported.<sup>12</sup> In this combination, the shield prevented the occurrence of secondary discharge and the full power plasma prevented the suppression of analytes but only the argon-based interferences formed in the secondary discharge were removed. Metal monoxide ions and cations of atmospheric gases, formed in the plasma, were observed at higher levels than in the unshielded plasma. The use of the plasma shield with normal rf power still resulted in a lowering of the central channel temperature and therefore a decrease in the degree of ionisation of high IP elements. Thus, the sensitivity and detection limits of these elements were poorer than under normal conditions.

### 1.2.3 Increased Resolution

The absolute mass, and therefore  $m/z$ , is different for each cation species with the same nominal mass ( $m/z$ ), for example the masses of  $^{40}\text{Ca}^+$  and  $^{40}\text{Ar}^+$  are 39.962 590 7 u and 39.962 383 u respectively.<sup>7</sup> The difference in mass between two ions of the same nominal mass is greater between a monatomic ion and a polyatomic ion than between two different monatomic ions, e.g. the mass difference  $^{38}\text{ArH}^+ - ^{39}\text{K}^+$  is 0.006 849 u whereas  $^{40}\text{Ca} - ^{40}\text{Ar}$  is just 0.000 208 u.<sup>7</sup> Therefore, if sufficient mass resolution is available to separate ions of the same nominal mass, analytes can be determined away from any potential interference ions.

Mass resolution is usually expressed in the form  $m/\Delta m$  where  $m$  and  $(m + \Delta m)$  are the masses of two closely spaced peaks of equal intensity and the valley between the two peaks is 10 % or less of the height of the peaks.<sup>7</sup> The majority of ICP-MS instruments, more than 90 %, feature a quadrupole mass analyser (ICP-QMS).<sup>3,4</sup> The resolution of commercially available quadrupole mass spectrometers is up to 150 ( $m/\Delta m$ ).<sup>27</sup> However, as shown in Table 1.3, the minimum resolution required to resolve many analytes and interferences is considerably higher than this.

**Table 1.3 – Resolution ( $m/\Delta m$ ) necessary to resolve some common interferences<sup>7</sup>**

Analyte	Interference	Minimum resolution
<sup>39</sup> K	<sup>38</sup> ArH <sup>+</sup>	5700
<sup>51</sup> V	<sup>35</sup> Cl <sup>16</sup> O <sup>+</sup>	2600
<sup>52</sup> Cr	<sup>40</sup> Ar <sup>12</sup> C <sup>+</sup>	2400
<sup>56</sup> Fe	<sup>40</sup> Ar <sup>16</sup> O <sup>+</sup>	2500
<sup>63</sup> Cu	<sup>40</sup> Ar <sup>23</sup> Na <sup>+</sup>	2800
<sup>75</sup> As	<sup>40</sup> Ar <sup>35</sup> Cl <sup>+</sup>	7800
<sup>80</sup> Se	<sup>40</sup> Ar <sub>2</sub> <sup>+</sup>	9700

To achieve higher resolutions mass spectrometers with magnetic and electrostatic sectors have been developed. These spectrometers, usually called sector-field mass spectrometers (ICP-SFMS), have other benefits over quadrupole mass analysers in addition to higher resolution. When operated in low resolution mode ( $m/\Delta m$  300 – 400), ICP-SFMS has very high sensitivity which, combined with very low background levels, enables the determination of uninterfered elements with lower detection limits than ICP-QMS.<sup>28</sup> An increase in mass resolution results in a decrease in sensitivity. A change in resolution ( $m/\Delta m$ ) from 400 to 3000 decreases sensitivity to 10 % of its initial value and further increase in resolution to 12 000 lowers sensitivity to just 2 % of its level at  $m/\Delta m$  400.<sup>29</sup>

The widespread adoption of ICP-SFMS in preference to ICP-QMS is unlikely for several reasons. Currently available instrumentation has a maximum resolution ( $m/\Delta m$ ) in the order of 10 000 and so cannot resolve all isobaric interferences, particularly those



between elemental isobars.<sup>4</sup> Examples of some of the important interferences that cannot be resolved by current instruments are shown in Table 1.4.

**Table 1.4 – Some isobaric interferences which cannot be resolved with current technology<sup>7,30</sup>**

Analyte	Interference	Min. resolution ( $m/\Delta m$ )
<sup>40</sup> Ca	<sup>40</sup> Ar <sup>+</sup>	193 000
<sup>129</sup> I	<sup>129</sup> Xe <sup>+</sup>	600 000
<sup>90</sup> Sr	<sup>90</sup> Y <sup>+</sup>	150 000

ICP-SFMS instruments are more complicated than ICP-QMS instruments to operate and thus require more operator expertise, increasing the cost of analysis. Ultimately, ICP-SFMS instruments are much less common than ICP-QMS instruments, due to the much higher cost of the instrument itself – ICP-SFMS instruments are two to three times more expensive than ICP-QMS instruments.<sup>7</sup>

#### 1.2.4 Mixed Gas Plasmas

The argon ICP is particularly suitable for elemental mass spectrometry as it has a high gas kinetic temperature, electron temperature and electron density that, combined with a residence time of several milliseconds, effectively vaporises, atomises and ionises the sample.<sup>3,31</sup> The introduction of gases other than argon to the plasma modifies the physical characteristics of the plasma and therefore the analytical performance of the plasma, varying analyte sensitivity and the nature and level of polyatomic interferences. Other gases can be introduced to any or all of the argon flows comprising the plasma – the injector flow, intermediate (or auxiliary) flow or the main (or cool) flow – at different levels up to 100 % of the flow.<sup>31</sup>

The addition of 5 – 10 % nitrogen to the outer flow of the plasma raised the gas kinetic temperature by approximately 1000 K; it also raised the electron density of the plasma and produced a narrowing of the central channel.<sup>31</sup> This resulted in up to four-fold enhancement of analyte sensitivity and a reduction in the level of polyatomic ions: oxides, hydroxides and argon-based. The addition of nitrogen to any argon flow adversely affected the determination of Si due to greatly elevated levels of N<sub>2</sub><sup>+</sup>.<sup>31</sup>

1 % nitrogen in the main flow of the plasma reduced the signals for  $^{35}\text{Cl}^{16}\text{O}^+$  and  $^{40}\text{Ar}^{35}\text{Cl}^+$  by more than two orders of magnitude but had little effect on analyte sensitivity. These effects combine to halve the detection limits (DLs) for the interfered isotopes  $^{51}\text{V}$  and  $^{75}\text{As}$ .<sup>32</sup>

Up to 10 % oxygen in the outer flow of the plasma had a similar effect to low levels of nitrogen. The addition of oxygen elevated the gas kinetic temperature; the maximum temperature occurred at 8 – 10 % oxygen. Oxygen in the outer flow also resulted in a narrowing of the central channel and a reduction in argon-based interferences.<sup>31</sup>

The ionisation of elements with high ionisation potentials (IPs), such as I, was enhanced by the introduction of 20 % helium in the main and intermediate flows. Such ionisation enhancement improved analyte sensitivity and therefore reduced DLs for high IP elements. For example, the DL for  $^{127}\text{I}$  (IP 10.4 eV) was observed to lower to  $6\text{ pg ml}^{-1}$  from  $400\text{ pg ml}^{-1}$  with the argon plasma. No significant variation in the extent of ionisation occurred for lower IP elements. The use of helium in the plasma caused a significant reduction in analyte dynamic range, to as little as one or two orders of magnitude in some cases.<sup>31</sup>

Nitrogen- or oxygen-only main flows resulted in considerable reduction in the gas kinetic temperature, 1200 K in the case of nitrogen. To restore the gas kinetic and electron temperatures for the molecular gas main flow plasmas to similar levels to a 1.2 kW argon plasma required a power of 2.5 kW. When both the injector and main flows were nitrogen or oxygen (the intermediate flow alone was argon), the levels of argon-based ions were, as might be expected, significantly reduced but the levels of oxide ions were considerably increased – especially with oxygen. Under these conditions, the DLs of low IP elements (less than 6 eV) were improved but those for high IP elements (greater than 6 eV) were increased.<sup>31</sup>

The effect of adding low flows of other gases to the argon in the injector or intermediate flows was more dependent on the gas used than the effect of adding them to the main flow. Addition of 16.7 % helium or hydrogen to the injector flow increased the gas kinetic temperature by 1500 – 2000 K due to their greater thermal conductivity and lower

viscosity than argon. Similar addition of nitrogen produced a decrease in the gas kinetic temperature. The effect of the three gases on the electron temperature was slightly different. Helium produced no change in the electron temperature, hydrogen raised it by almost 1500 K and use of nitrogen lowered it by 3000 – 5000 K.<sup>31,33</sup>

The analytical benefits of nitrogen in the injector flow are the reduction of argon-based and chlorine-based interferences and considerable reduction in the level of oxide ions. For example, 20 % nitrogen in the injector flow reduced  $\text{LaO}^+$  to minimal levels and considerably reduced  $\text{ArO}^+$ ,  $\text{ArOH}^+$ ,  $\text{Ar}_2^+$ ,  $\text{ClO}^+$  and  $\text{ArCl}^+$ .<sup>31</sup> With only 3 % nitrogen in the injector flow, no reduction in oxide levels was observed. The levels of  $^{35}\text{Cl}^{16}\text{O}^+$  and  $^{40}\text{Ar}^{35}\text{Cl}^+$  were dramatically reduced, halving the DLs for  $^{51}\text{V}$  and  $^{75}\text{As}$  in a chloride matrix.<sup>32</sup>

Inclusion of a few  $\text{ml min}^{-1}$  xenon to the injector flow resulted in a several-hundred fold reduction in the signals due to  $^{14}\text{N}_2^+$ ,  $^{14}\text{N}_2\text{H}^+$ ,  $^{14}\text{N}^{16}\text{O}^+$ ,  $^{40}\text{Ar}^{14}\text{N}^+$  and  $^{40}\text{Ar}^{16}\text{O}^+$  but a less than twenty-fold reduction in the signals of the interfered isotopes  $^{28}\text{Si}$ ,  $^{29}\text{Si}$ ,  $^{30}\text{Si}$ ,  $^{54}\text{Fe}$  and  $^{56}\text{Fe}$ , thereby improving DLs for those analytes.<sup>31</sup> Perhaps the most well known use of mixed gas plasmas is the use of a few percent oxygen in the injector flow to facilitate the analysis of samples in organic solvents by preventing the deposition of carbon on the sample cone.<sup>23,31</sup>

Mixed gas plasmas generally have higher temperatures than equivalent argon plasmas, resulting in higher degrees of ionisation and therefore higher analyte sensitivity, they also generate lower levels of many polyatomic ions (although levels of some polyatomic ions are increased).<sup>31</sup> Mixed gas plasmas can be used to lower running costs where the gas used is cheaper than the argon it replaces.<sup>33</sup>

The use of mixed gas plasmas is discouraged by the apparently empirical way in which appropriate conditions are selected, particularly the selection of the gas used and which flow it is added to. The selection of appropriate plasmas is confused by the same gas having different effects on the plasma properties when added to different flows. Mixed gas plasmas cannot readily be used in conventional argon ICP-MS instruments as the provision of additional mass flow controllers for the added gas is required as (particularly

when large helium flows are employed) are modifications to the torch, load coil, rf impedance matching network and extraction chamber pumping conductance. Ignition problems are also an issue for high molecular gas plasmas, these are formed by first igniting an argon plasma and then gradually replacing argon with the desired gases.<sup>31</sup>

### 1.2.5 Collision/Reaction Cells

The techniques discussed above remove spectral interference at various stages in the ICP-mass spectrometer. Desolvation removes the precursors to some interferences prior to the plasma. Cool plasma and mixed gas plasmas modify the plasma conditions to prevent the formation of certain polyatomic ions. High resolution mass spectrometers do not prevent the formation of interference ions, instead the analyte and interference ions are spectrally resolved. Collision/reaction cell ICP-MS uses a vessel filled with a low pressure of a reactive gas to reactively remove or 'chemically resolve' spectral interferences.

A collision/reaction cell consists of an enclosed multipole (quadrupole, hexapole or octopole) ion guide located within the evacuated part of the ICP-MS instrument. The enclosed multipole is filled with a low pressure of a reactive gas. Gas phase reactions occur within the cell which remove the interference ions from the ion beam prior to the mass analyser.<sup>7,34</sup>

A range of different gases can be used in collision/reaction cells to attenuate polyatomic ions by reactions in the cell. Perhaps the two most frequently used gases in collision/reaction cells are ammonia and hydrogen.<sup>35</sup> These two gases can be used to attenuate most argon-based polyatomic ions, amongst others, and thereby facilitate the determination of analyte ions with which the polyatomic ions interfere. For example, hydrogen<sup>34,35</sup> or ammonia<sup>36</sup> have both been used to reactively attenuate the  $^{38}\text{ArH}^+$  interference, by the reactions given in Equations 1.5 and 1.6 respectively.



**Equation 1.5**



**Equation 1.6**

Since  $^{39}\text{K}^+$  reacts with neither hydrogen<sup>34,37</sup> nor ammonia<sup>38</sup> to any significant extent in the cell, the reactive removal of  $\text{ArH}^+$  left the K signal with much lower levels of interference and therefore permitted its determination. Using ammonia, K could be determined with a detection limit<sup>34,36</sup> of  $1 \text{ pg ml}^{-1}$ .

One of the key capabilities of collision/reaction cell ICP-MS is the determination of ions suffering spectral interference from elemental isobars, which cannot be spectrally resolved by ICP-DFMS. A wide range of different gases can be used in the collision/reaction cell, each gas having different reactivity and so providing a wide range of different reaction possibilities.

An example of the use of different gases to chemically resolve interferences is the use of chloromethane,<sup>39</sup> fluoromethane<sup>40</sup> or nitrous oxide<sup>39</sup> to facilitate the determination of  $^{87}\text{Sr}$  in the presence of  $^{87}\text{Rb}^+$ . In this case, rather than attenuating  $^{87}\text{Rb}^+$ , Sr was removed from the interference and determined *via* the  $\text{SrCl}^+$ ,  $\text{SrF}^+$  or  $\text{SrO}^+$  signals. Without the use of sample pre-treatment to separate Sr from rubidium in the sample, collision/reaction cell ICP-MS appears to be the only ICP-MS technique available for determining  $^{87}\text{Sr}$ . ICP-DFMS cannot be used to spectrally resolve  $^{87}\text{Sr}$  and  $^{87}\text{Rb}^+$  as the resolution required for this is  $286\,000 (m/\Delta m)$ ,<sup>39</sup> far in excess of that available. Nor can cool plasma techniques be used to prevent the formation of  $\text{Rb}^+$  as the ionisation potentials of Rb and Sr are similar, 4.18 eV and 5.70 eV respectively.

Collision/reaction cell ICP-MS is further explored in Chapter Two. The different types of instrumentation available, the properties of reactions occurring in the cell, non-reactive effects of collision/reaction cell use and the many different applications of collision/reaction cells to chemically resolve analytes and spectral interferences using different gases heretofore reported in the literature are discussed.

## **Chapter Two**

### **Collision/reaction Cell ICP-MS**

## 2.0 Collision/Reaction Cell ICP-MS

The development of collision/reaction cells in ICP-MS begins with collision cells used to elucidate structure in organic mass spectrometry. Tandem mass spectrometry (MS/MS), as collision cell organic mass spectrometry is usually known, generally utilises three quadrupole mass analysers in succession to further fragment molecular 'parent' ions and collect the mass spectrum of the 'daughter' ion products.<sup>8,41</sup> The mass spectrum of the daughter ions can then be used to determine the structure of the parent ion and therefore part of the structure of the analyte. The first quadrupole is used to select the parent ion. The second quadrupole is operated as an rf-only ion guide and is filled with helium. The parent ions collide with helium in the second quadrupole (the collision cell) and are fragmented, a process called collision-induced dissociation (CID). The third quadrupole is the mass analyser associated with the detector.<sup>8,41</sup>

Although the basic form of collision/reaction cells in ICP-MS is the same as that of the collision cell in MS/MS, *viz.* an enclosed gas filled multipole ion guide, the purpose of collision/reaction cells in elemental mass spectrometry is distinctly different from that of the collision cell in elemental mass spectrometry. Rather than pre-filtering and admitting ions of a single mass to charge ratio ( $m/z$ ) to the cell, as in MS/MS, the entire ion beam is introduced to the cell in collision/reaction cell ICP-MS. Polyatomic ions formed in the ICP, unlike the large molecular ions in MS/MS, tend to be scattered more than they are fragmented by collisions with unreactive gases in the cell, so reactive gases and ion-molecule chemistry are preferred over CID. The principal reason for using collision/reaction cells in ICP-MS and collision cells in MS/MS are fundamentally different. In ICP-MS, the collision/reaction cell is used to remove spectral interferences to aid the determination of (usually monatomic) analytes, *i.e.* to simplify the mass spectrum, whereas the collision cell in MS/MS is used to fragment a polyatomic ion and generate a range of ions of different  $m/z$ , *i.e.* to convert a single peak into a more complex spectrum.

In what can be considered to be the first report of collision/reaction cell ICP-MS in the literature, Douglas<sup>42</sup> described the coupling of an ICP source to the triple quadrupole

mass spectrometer used in MS/MS. A small quantity of air was bled into the middle, rf-only, quadrupole and the first and third quadrupoles were synchronously scanned 16 u apart.  $\text{Ce}^+$  and  $\text{Tb}^+$  reacted with oxygen in the air filled collision cell, elevating the observed levels of  $\text{CeO}^+$  and  $\text{TbO}^+$ .

Rowan and Houk<sup>43</sup> and, several years later, Eiden *et al.*<sup>30</sup> presented custom built collision/reaction cell ICP-MS systems with an rf-only quadrupole and octopole respectively as the collision/reaction cell ion guide. Rowan and Houk<sup>43</sup> showed that collision/reaction cell ICP-MS could be used to chemically resolve isobaric interference; they reported the use of xenon to attenuate  $^{40}\text{Ar}^{14}\text{N}^+$  and  $^{40}\text{Ar}^{16}\text{O}^+$  and thereby facilitate the determination of  $^{54}\text{Fe}$  and  $^{56}\text{Fe}$  respectively. The instrument was also used with methane to ameliorate the determination of  $^{75}\text{As}$  and  $^{80}\text{Se}$  by attenuating  $\text{ArCl}^+$  and  $\text{Ar}_2^+$  respectively. Eiden *et al.*<sup>30</sup> reported that low pressure hydrogen ( $\sim 10^{-5}$  mbar) in the cell reduced  $\text{Ar}^+$  and  $\text{ArH}^+$  to the level of the general background. These effects are discussed in more detail in the appropriate sub-section of Section 2.3.

Shortly after the publication of Eiden *et al.*,<sup>30</sup> the first commercial collision/reaction cell systems were launched. These first systems, together with currently available instrumentation are discussed in Section 2.1 below.

This chapter discusses various aspects of collision/reaction cell ICP-MS: the instrumentation available, the nature, kinetics and thermodynamics of reactions in the cell and the effects (reactive or otherwise) of various gases in the cell.

## **2.1 Instrumentation**

In the late 1990s, collision/reaction cell ICP-MS instruments were produced by three different manufacturers; the Platform ICP (Micromass, Manchester), the VG PQ ExCell (Thermo Electron, Winsford, Cheshire) and the ELAN 6100 DRC (PerkinElmer SCIEX, Concord, ON, Canada). Subsequently Agilent Technologies (Paulo Alto, CA, USA) offered the 7500c and Thermo Electron and PerkinElmer produced seconded generation instruments, the X7 and the ELAN DRC<sup>plus</sup> respectively. The proprietary names for the collision/reaction cells are given in Table 2.1.



***Table 2.1 – Proprietary names for collision/reaction cells.***

<b>Manufacturer</b>	<b>Name of collision/reaction cell</b>
Agilent	Octopole Reaction System
Micromass	HEX
PerkinElmer	Dynamic Reaction Cell
Thermo Electron	Collision Cell Technology

The collision/reaction cells in the various systems are all different. The most functionally significant differences are between the bandpass filtered quadrupole ‘Dynamic Reaction Cell’ of the PerkinElmer instruments and the rf-only hexapole or octopole cells in the other instruments.

Due to the infancy of the technique, no single generic name has yet been settled on. The various names used in the titles of articles in the literature together with the frequency of use of each name are given in Table 2.2.

**Table 2.2 – Names for collision/reaction cells used in the titles of articles and frequency of use (up to July 2003). A – review articles only, B – articles featuring bandpass scanned quadrupole cells and C – articles featuring rf-only hexapole and octopole cells.**

Name	Frequency of use (%) <sup>*</sup>			
	Total	A	B	C
Collision/reaction cells	1.8	50		
Reaction cells and collision cells	1.8	50		
Dynamic Reaction Cell (DRC)	37		68	
Hexapole collision cell	14			33
Reaction cell	12.8		19	4.2
Collision and reaction cell	3.5			8.3
Collision/reaction cell	3.5			8.3
Hexapole	3.5			8.3
Hexapole collision and reaction cell	3.5			8.3
Tuneable bandpass reaction cell	3.5		6.5	
Bandpass reaction cell	1.8		3.2	
HEX	1.8			4.2
Hexapole collision/reaction cell	1.8			4.2
Hexapole ion optics	1.8			4.2
Octopole collision cell	1.8			4.2
Octopole reaction cell	1.8			4.2
Octopole Reaction System	1.8			4.2
Quadrupole reaction cell	1.8		3.2	
Rf-only collision and reaction cell	1.8			4.2

<sup>\*</sup> Due to rounding, columns do not total to 100 %

Given the wide range of different names used in the literature with little consistency, three terms have been selected and are used as follows herein:

Collision/reaction cell ICP-MS – for the technique in general

Dynamic Reaction Cell ICP-MS – for bandpass scanned quadrupole cells  
(ICP-DRC-MS)

Collision cell ICP-MS – for rf-only hexapole and octopole cells  
(ICP-CC-MS)

The basic layouts of all collision/reaction cell ICP-MS systems are very similar. The general layout of collision/reaction cell ICP-mass spectrometers is shown schematically in Figure 2.1. The collision/reaction cell consists of an enclosed multipole located within the mass spectrometer vacuum chambers. Ions are formed in the plasma (on the left of Figure 2.1) and sampled into the mass spectrometer *via* the two-stage sample cone and skimmer cone interface (described in more detail in Section 1.1). On entering the spectrometer, the ion beam starts to expand due to space charge. The expansion is reversed by a series of ion optics; these differ in design in the various instruments. The ion beam then enters the collision/reaction cell where various collision and reaction related processes, which are described later in this chapter, occur. Ions exiting the cell are refocused by further ion optics of various designs before entering the quadrupole mass analyser.

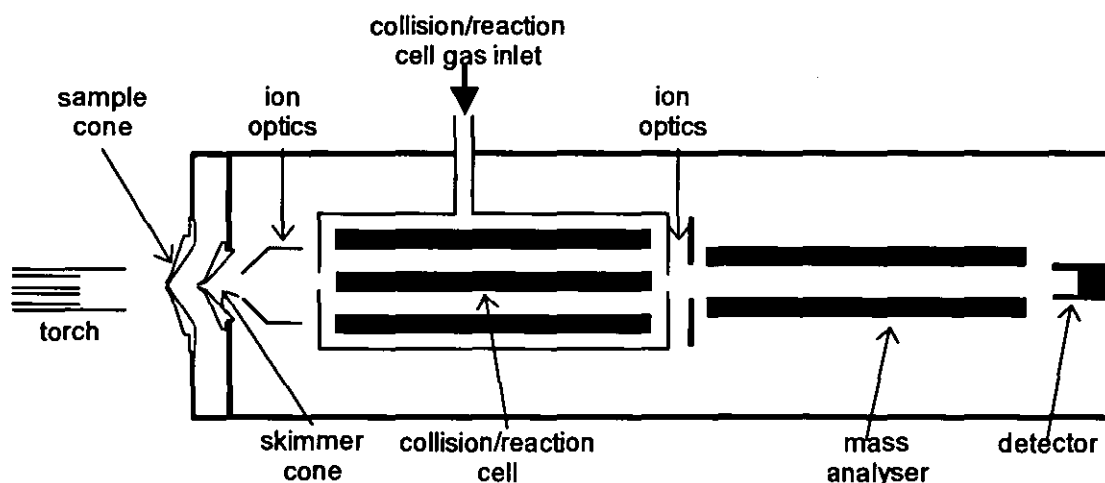


**Figure 2.1** – A generalised schematic of a collision/reaction cell inductively coupled plasma mass spectrometer.

If, as in Figure 2.1, there is an unobstructed linear path from the plasma to the detector then high-energy photons contribute to the background registered by the detector.<sup>7</sup> Different methods are employed in the various instruments to obstruct the linear path.<sup>41</sup> In the ELAN, the linear geometry shown in Figure 2.1 is maintained, with the inclusion of a 'shadow stop' just behind the skimmer cone to stop photons. The shadow stop consists of a small metal disc located on the instrument axis. The ExCell has the plasma,

cones and cell on one axis with the quadrupole and detector on a second parallel axis, thereby preventing photons from reaching the detector. The ion path is maintained by a chicane or deflector lens between the collision cell exit and the quadrupole. In the Platform and the 7500c, photons are excluded without additional ion optic elements by slanting the collision cell multipole away from the plasma-cone axis.<sup>41</sup>

The enclosure containing the collision/reaction cell multipole is virtually complete in the ELAN, ExCell and 7500c with openings only for the entry and egress of the ion beam.<sup>41</sup> (The ELAN also features mechanical vents for rapidly evacuating the cell; these are closed when collision/reaction cell gases are in use.)<sup>44</sup> The hexapole ion guide of the Platform is only partially enclosed.<sup>41</sup>

The collision cells in the ExCell and Platform contain rf-only hexapole ion guides and the collision cell of the 7500c contains an rf-only octopole ion guide. These higher order multipoles, especially when operated in an rf-only manner, have a wide potential well and a broad (and ill defined) stability region. They are therefore able to better contain ions scattered by collisions and to transmit ions of a wide range of  $m/z$  simultaneously.<sup>41</sup> The Dynamic Reaction Cell of the ELAN contains a bandpass filtered quadrupole. The potential well of the quadrupole is well defined and narrow. The stability region is also well defined and its width can be varied.<sup>44</sup> In the ELAN, the stability region is controlled by the 'RPa' and RPq' variables, which are proportional to the Mathieu parameters  $a$  and  $q$ ; thus the range of stable  $m/z$  (relative to the analyte  $m/z$ ) can be altered.<sup>41</sup> By careful selection of suitable 'RPa' and 'RPq' values, the  $m/z$  range transmitted can be arranged to prevent the observation of cell-formed polyatomic ions. For a cell-formed polyatomic ion to be observed, both the reactant and product ions must have  $m/z$  simultaneously within the stability region. The nature and operation of quadrupole mass analysers is discussed in more detail in Section 1.1 above.

The Dynamic Reaction Cell of the second generation ELAN DRC<sup>plus</sup> contains four electrodes in addition to the four rods of the quadrupole.<sup>41,45</sup> The electrodes are in between and parallel to the quadrupole rods. These additional electrodes are used to introduce an axial field gradient through the cell of  $0.2 \text{ V cm}^{-1}$ . The axial field gradient gently accelerates ions through the cell, typically transferring less than 0.1 eV to the ions.

This acceleration has a number of beneficial effects. Where ions are thermalised, they possess only random, Brownian, motion so ion transmission relies on the gas flow through the cell. The axial field gradient draws these thermalised ions through the cell, increasing the count rate and sensitivity recorded. The axial field also reduces analysis time by reducing stabilisation time for the two quadrupoles.<sup>41,45</sup>

## ***2.2 Reactions in the Collision/Reaction Cell***

Ions entering the collision cell encounter a body of relatively static atoms and/or molecules. Collisions are likely between the ions and atoms/molecules as ions accelerated by the lenses have a high velocity parallel to the multipole axis and the collision cell gas possesses only the low random speed of thermal energy ( $3k_{\text{B}}T/2 = 0.04 \text{ eV}$  at 298 K). Many of these collisions result in reactions.

Reactions in the collision/reaction cell occur in a low pressure, high-energy gas-phase environment and so proceed in a somewhat different manner to conventional solution-based chemistry. One of the most distinct differences is the absence of any solvation spheres; ionic and neutral species are present in their 'bare' form. The absence of solvation spheres greatly reduces the activation energy as it removes the need for the solvation spheres to interact before any reaction can occur. In reactions not featuring high energy intermediates or transition states, ion-neutral reactions are believed to occur with zero activation energy.<sup>46</sup> A typical example of a reaction coordinate for an exothermic ion-neutral reaction is shown in Figure 2.2.<sup>46</sup>

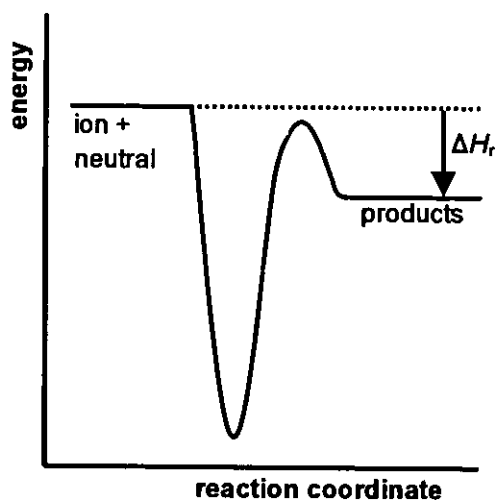
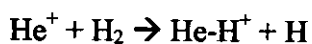


**Figure 2.2** – Typical reaction coordinate for an exothermic ion-neutral reaction.

In some cases, reactions proceed *via* a high energy intermediate or transition state and therefore require activation energy, for example:



$$\Delta H_r = -8.3 \text{ eV}$$

**Equation 2.1**

This reaction proceeds *via* two intermediates,  $\text{He}^+ \cdot \text{H}_2$  and  $\text{He-H}_2^+$ . The former of the two intermediates has a high formation enthalpy. A representation of the reaction coordinate for this reaction (Equation 2.1) is shown in Figure 2.3.

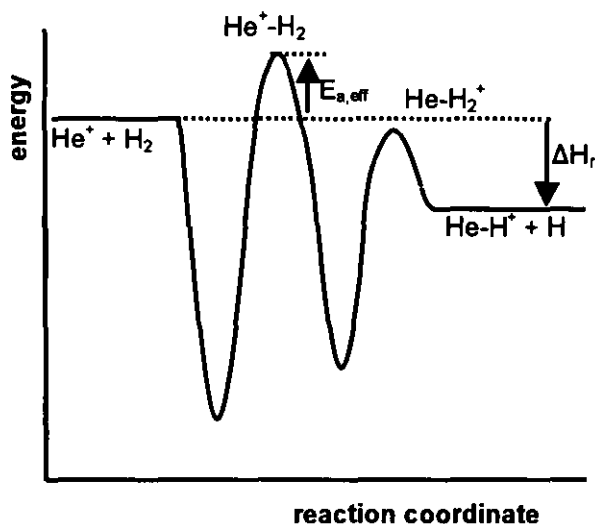


**Figure 2.3** – Reaction coordinate for the gas phase reaction shown in Equation 2.1.

Due to the large range of species present in the collision cell, it is difficult to predict the outcome of reaction sequences occurring therein. Frequently, authors have made use of thermodynamic<sup>44,47</sup> or kinetic<sup>37,44,48</sup> data to predict or explain reactions occurring in the cell. Considerable thermodynamic data suitable for this purpose are available, detailing the formation enthalpies for many gaseous ionic and neutral species. Most of these data have been collated by Lias *et al.*<sup>49</sup> A large number of rates of reaction are available in the literature;<sup>50-53</sup> although considerable gaps exist in the literature as the earlier work, tabulated by Anicich,<sup>50-52</sup> was intended for modelling of gas phase reactions in space. This deficiency is being resolved by ongoing work by Koyanagi and others<sup>54-57</sup> with an ICP source-single ion flow tube (SIFT) mass spectrometer which enables the rapid determination of many bimolecular gas phase reactions with analytical importance.

Kinetic data currently available, *e.g.* in Anicich,<sup>52</sup> are for thermal conditions and so can be used only as a rough guide if non-thermal conditions are used. In accordance with Le Chatelier's principle, in non-thermal conditions such as high kinetic energy ion beams, the rate of endothermic reactions is increased and the rate of exothermic reactions is decreased compared to those for thermal conditions.<sup>58</sup>

In general, the rate constants tabulated in Anicich<sup>52</sup> for reactions with reactive gases commonly used in collision cells, such as ammonia, hydrogen and methane, fall into two

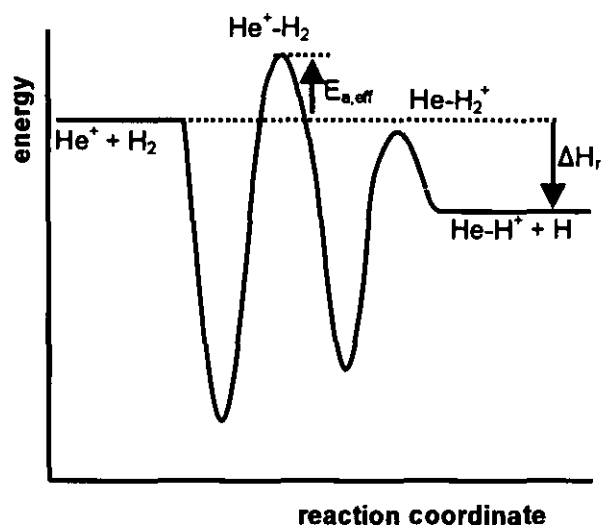


**Figure 2.3** – Reaction coordinate for the gas phase reaction shown in Equation 2.1.

Due to the large range of species present in the collision cell, it is difficult to predict the outcome of reaction sequences occurring therein. Frequently, authors have made use of thermodynamic<sup>44,47</sup> or kinetic<sup>37,44,48</sup> data to predict or explain reactions occurring in the cell. Considerable thermodynamic data suitable for this purpose are available, detailing the formation enthalpies for many gaseous ionic and neutral species. Most of these data have been collated by Lias *et al.*<sup>49</sup> A large number of rates of reaction are available in the literature;<sup>50-53</sup> although considerable gaps exist in the literature as the earlier work, tabulated by Anicich,<sup>50-52</sup> was intended for modelling of gas phase reactions in space. This deficiency is being resolved by ongoing work by Koyanagi and others<sup>54-57</sup> with an ICP source-single ion flow tube (SIFT) mass spectrometer which enables the rapid determination of many bimolecular gas phase reactions with analytical importance.

Kinetic data currently available, *e.g.* in Anicich,<sup>52</sup> are for thermal conditions and so can be used only as a rough guide if non-thermal conditions are used. In accordance with Le Chatelier's principle, in non-thermal conditions such as high kinetic energy ion beams, the rate of endothermic reactions is increased and the rate of exothermic reactions is decreased compared to those for thermal conditions.<sup>58</sup>

In general, the rate constants tabulated in Anicich<sup>52</sup> for reactions with reactive gases commonly used in collision cells, such as ammonia, hydrogen and methane, fall into two



groups,  $k = 10^{-9} - 10^{-10} \text{ cm}^3 \text{ s}^{-1}$  and  $10^{-12} - 10^{-15} \text{ cm}^3 \text{ s}^{-1}$ . Those in the former group are likely to be observed in the cell; those in the latter group are unlikely to proceed to a discernible extent.<sup>54,59</sup>

It is possible to readily determine the enthalpy of reaction for a given species from the formation enthalpy data available using Equation 2.2; or, for a charge transfer reaction, from the first ionisation potentials of the neutral species, using Equation 2.3.

$$\Delta H_r^\circ = \sum \Delta H_f^\circ(\text{products}) - \sum \Delta H_f^\circ(\text{reactants})$$

**Equation 2.2**

$$\Delta H_r^\circ = \text{IP}_{(\text{product ion})} - \text{IP}_{(\text{reactant ion})}$$

**Equation 2.3**

Reactions can occur if they are thermodynamically allowed, *i.e.* if they are thermoneutral or exothermic. Reactions that are slightly endothermic may also occur if the particles involved have sufficient kinetic energy upon impact. It is believed<sup>30</sup> that resonant reactions (thermoneutral reactions) are the most likely to produce stable products as any molecular product of a strongly exothermic reaction will possess a large quantity of vibrational energy that is likely to break the covalent bonds of the molecule.

Reactions in the collision cell fall into a small number of categories:<sup>38,59</sup> condensation, association, collisional dissociation, charge transfer, proton transfer, and small atom (especially hydrogen atom) transfer.

Condensation reactions feature the addition of atoms to the ion, together with a rearrangement in the way the charge is held by the ion. In association reactions, the colliding species are joined by any of the various possible bonding modes of differing bond strengths. In collisional dissociation, collision with a neutral atom/molecule fractures the molecular ion into two, or more, parts. Collisional dissociation reactions are considered to be rare and of little analytical importance,<sup>30</sup> they are included here as they have been shown to occur in other, similar, systems<sup>60</sup> and so cannot be overlooked.

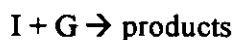
Proton, charge and hydrogen atom transfer reactions are frequently exothermic or mildly endothermic and proceed at a fast rate, almost equal to the rate of collision. They are, thus, the most common collision cell reactions. Transfer reactions are particularly useful for removing polyatomic interferences. General and specific examples of each reaction type are shown in Table 2.3.

**Table 2.3** – (i) General and (ii) specific examples of gas-phase reactions of each type. (In (i), X, Z = general atoms/molecules, G = gas (atoms or molecules); in (ii) reaction enthalpies shown were calculated using data in Lias et al.<sup>49</sup> and Equation 2.2)

Reaction type	Example	$\Delta H_r^\circ/\text{eV}$
<i>(i) General examples:</i>		
Condensation	$\text{XO}^+ + \text{GO} \rightarrow \text{XO}_2^+ + \text{G}$	-
Association	$\text{X}^+ + \text{G} \rightarrow \text{X.G}^+$	-
Collisional dissociation	$\text{XZ}^+ + \text{G} \rightarrow \text{X}^+ + \text{Z} + \text{G}$	-
Proton transfer	$\text{XH}^+ + \text{G} \rightarrow \text{X} + \text{GH}^+$	-
Charge transfer	$\text{X}^+ + \text{G} \rightarrow \text{G}^+ + \text{X}$	-
Hydrogen atom transfer	$\text{X}^+ + \text{GH} \rightarrow \text{XH}^+ + \text{G}$	-
<i>(ii) Specific examples:</i>		
Condensation	$\text{CeO}^+ + \text{O}_2 \rightarrow \text{CeO}_2^+$	-3.1
Association	$\text{Ar}^+ + \text{He} \rightarrow \text{Ar.He}^+$	-0.03
Collisional dissociation	$\text{Ar}_2^+ + \text{He} \rightarrow \text{Ar} + \text{Ar}^+ + \text{He}$	+1.3
Proton transfer	$\text{ArH}^+ + \text{H}_2 \rightarrow \text{H}_3^+ + \text{Ar}$	-0.5
Charge transfer	$\text{Ar}^+ + \text{H}_2 \rightarrow \text{H}_2^+ + \text{Ar}$	-0.33
Hydrogen atom transfer	$\text{Ar}^+ + \text{H}_2 \rightarrow \text{ArH}^+ + \text{H}$	-1.53

### 2.2.1 Kinetics

Reactions in the collision/reaction cell take the form of a bimolecular elementary reaction,<sup>38</sup> as shown in Equation 2.4. I is a mono- or polyatomic ion, an atom or a molecule. G is the collision/reaction cell gas. Since plasma source mass spectrometry is a cation detection system, the effect of only those reactions featuring a cation can be observed (*i.e.* I is a mono- or polyatomic ion).



**Equation 2.4**

Bimolecular elementary reactions have second order rate laws,<sup>61</sup> viz. Equation 2.5.

$$v = -k[I][G]$$

**Equation 2.5**

In Equation 2.5,  $v$  is the reaction rate,  $k$  the rate constant for a given temperature and  $[I]$  and  $[G]$  are the reactant concentrations. For gas phase reactions, the conventional units are  $\text{mol cm}^{-3} \text{s}^{-1}$  for  $v$ ,  $\text{mol}^{-1} \text{cm}^3 \text{s}^{-1}$  for  $k$  and  $\text{mol cm}^{-3}$  for  $[I]$  and  $[G]$ . Equation 2.5 can be integrated with respect to time to give Equation 2.6, where the subscript  $t$  denotes 'at time  $t$ ' and the subscript 0 denotes 'at time 0'.<sup>61</sup>

$$kt = \frac{1}{[G]_0 - [I]_0} \ln \left( \frac{[G]_t/[G]_0}{[I]_t/[I]_0} \right)$$

**Equation 2.6**

Since the gas concentration is so much greater than the concentration of the reactant ions, i.e.  $[G]_0 \gg [I]_0$ , it can be assumed that  $[G]_t = [G]_0$ ; the integrated rate law shown in Equation 2.6 can therefore be reduced to the linear form given in Equation 2.7.

$$\ln[I]_t = -kt[G]_0 + ([I]_0 kt - \ln[I]_0)$$

**Equation 2.7**

Thus, a plot of  $\ln[I]_t$  versus  $[G]_0$  will be linear. The observed signal for  $I$  is directly proportional to  $[I]_t$  and  $[G]_0$  is directly proportional to collision/reaction cell gas flow rate. A semilogarithmic plot of ion signal against collision/reaction cell gas flow rate will, therefore, also be linear provided only one reaction is occurring at the  $m/z$  monitored. Kinetic theory can therefore be used to determine if a moderate level of contamination by a particular analyte is present in the blank.

Tanner and Baranov<sup>48</sup> showed that a graph of signal for a blank at a particular  $m/z$ , on a logarithmic scale, against collision/reaction cell gas flow rate, on a linear scale, could be used to ascertain if moderate levels of contamination were present. The differing rates of reduction in signal of the contaminant and the interference ions as the gas flow is increased would produce two distinct lines, of different gradients and intercepts. (In Equation 2.7, the gradient depends on the rate constant,  $k$ , and the intercept on both  $k$  and the concentration of the reactant ion entering the cell.) Since the two ions are isobaric, their lines are superimposed with the signals summed; on a semilogarithmic graph of signal *versus* gas flow rate they will therefore appear as a curve. Thus the presence of moderate levels of contamination at a given  $m/z$  will be indicated by a curve, such as that shown in Figure 2.4(ii), whereas the absence of contamination will be demonstrated by a linear relationship, such as that shown in Figure 2.4(i).

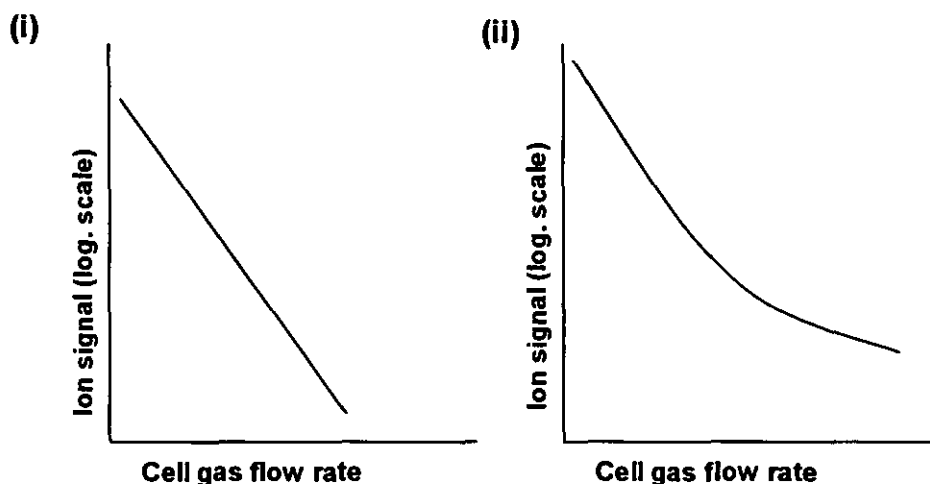


**Figure 2.4** – Semilogarithmic graphs of ion signal at a particular  $m/z$  against collision/reaction cell gas flow rate for (i) a contamination-free blank and (ii) a blank with moderate contamination present.

It is possible, with a little extra information, to estimate the level of contamination from a graph such as Figure 2.4(ii) by determining the  $y$ -intercept of a tangent to the high gas flows portion of the curve. The value of the  $y$ -intercept is approximately equal to the signal, at the gas flow represented by the  $y$ -axis. Thus if the sensitivity of the contaminant at that gas flow is known, its concentration can be estimated by dividing the value of the  $y$ -intercept by the sensitivity.

### 2.2.2 Preparation of the 'Thermoli' Ion-Molecule Reaction Database

Available kinetic and thermodynamic data are not presented in the most useful form for selecting collision/reaction cell gases. Kinetic data are arranged by reactant ion in Anicich<sup>52</sup> and more recently determined rate constants are variously arranged across several publications,<sup>54-57</sup> thus hindering location of the desired data, especially for data associated with reactions to form a particular product. Thermodynamic data are less accessible than kinetic data. The extensive data collated by Lias *et al.*<sup>49</sup> are presented as formation enthalpy data for the various ions and neutral species. This data must be used in Equation 2.2 (p32) to calculate the reaction enthalpy and therefore if the reaction is likely to proceed.

In order to facilitate the selection of suitable gases for chemically resolving interferences, an extensive database of ion-molecule reactions has been prepared, with kinetic and thermodynamic data included where available. This database has been named 'Thermoli'.

The kinetic<sup>52</sup> and thermodynamic<sup>49</sup> data available for gas-phase ion-molecule reactions relate to thermal conditions. Conditions in the collision/reaction cells are more energetic than thermal conditions. The thermal data cannot therefore be directly applied to reactions occurring in the collision/reaction cell although they can be used as a useful guide to probable effects in the cell.

The 'Thermoli' database was initially developed B. L. Sharp and C. P. Ingle at Loughborough University. A list of 42 interference ions commonly encountered in ICP-MS was produced; this is given in Table 2.4.

**Table 2.4 – Interference ions commonly encountered in ICP-MS, as featured in the ‘Thermoli’ database.**

<i>m/z</i> *	Species	<i>m/z</i> *	Species	<i>m/z</i> *	Species
13	CH <sup>+</sup>	32	O <sub>2</sub> <sup>+</sup>	52	ArC <sup>+</sup>
15	NH <sup>+</sup>	33	O <sub>2</sub> H <sup>+</sup>	54	ArN <sup>+</sup>
16	NH <sub>2</sub> <sup>+</sup>	34	O <sub>2</sub> H <sub>2</sub> <sup>+</sup>	56	ArO <sup>+</sup>
17	OH <sup>+</sup>	37	Cl <sup>+</sup>	56	CaO <sup>+</sup>
18	H <sub>2</sub> O <sup>+</sup>	38	HCl <sup>+</sup>	57	ArOH <sup>+</sup>
19	H <sub>3</sub> O <sup>+</sup>	40	Ar <sup>+</sup>	62	NO <sub>3</sub> <sup>+</sup>
24	C <sub>2</sub> <sup>+</sup>	41	ArH <sup>+</sup>	69	Ba <sup>++</sup>
28	CO <sup>+</sup>	42	ArH <sub>2</sub> <sup>+</sup>	70	ArNO <sup>+</sup>
28	N <sub>2</sub> <sup>+</sup>	44	CO <sub>2</sub> <sup>+</sup>	72	ArS <sup>+</sup>
29	HCO <sup>+</sup>	44	N <sub>2</sub> O <sup>+</sup>	75	ArCl <sup>+</sup>
29	COH <sup>+</sup>	44	SiO <sup>+</sup>	80	Ar <sub>2</sub> <sup>+</sup>
30	NO <sup>+</sup>	46	NO <sub>2</sub> <sup>+</sup>	81	Ar <sub>2</sub> H <sup>+</sup>
31	NOH <sup>+</sup>	47	HNO <sub>2</sub> <sup>+</sup>	82	Ar <sub>2</sub> H <sub>2</sub> <sup>+</sup>
31	HNO <sup>+</sup>	51	ClO <sup>+</sup>	239	UH <sup>+</sup>

\* major isotope

A database was then created, with the assistance of the author, of all possible reactions between the various ions listed in Table 2.4 and helium. Every combination of atoms and the ionic charge were listed as potential products, however unlikely such combinations may be, to ensure that all possible reaction pathways were included. Reaction enthalpies were included for all reactions where sufficient data were available. The enthalpies were calculated using Equation 2.2 (p32) and the formation enthalpies listed in Lias *et al.*<sup>49</sup> An extract from this database, for the reactant ions NO<sup>+</sup> and Ar<sub>2</sub>H<sup>+</sup>, is shown in Table 2.5.

**Table 2.5** – Reactions between  $\text{NO}^+$  or  $\text{Ar}_2\text{H}^+$  and helium: an extract from the 'Thermoli' database. (Reaction enthalpy ( $\Delta H_r$ ) data from Lias et al.<sup>49</sup>)

Reactant			Products†	$\Delta H_r$
Ion $m/z^*$	Ion†	Gas		/eV
30	$\text{NO}^+$	He	$\text{He}^+$ , NO	+15.30
30	$\text{NO}^+$	He	He, $\text{N}^+$ , O	+11.80
30	$\text{NO}^+$	He	He, N, $\text{O}^+$	+10.90
30	$\text{NO}^+$	He	$\text{HeN}^+$ , O	+11.60
30	$\text{NO}^+$	He	HeN, $\text{O}^+$	
30	$\text{NO}^+$	He	$\text{HeO}^+$ , N	+10.90
30	$\text{NO}^+$	He	HeO, $\text{N}^+$	
30	$\text{NO}^+$	He	$\text{HeNO}^+$	
81	$\text{Ar}_2\text{H}^+$	He	$\text{He}^+$ , $\text{Ar}_2\text{H}$	
81	$\text{Ar}_2\text{H}^+$	He	$\text{He}^+$ , Ar, Ar, H	
81	$\text{Ar}_2\text{H}^+$	He	He, $\text{Ar}^+$ , Ar, H	
81	$\text{Ar}_2\text{H}^+$	He	He, Ar, Ar, $\text{H}^+$	
81	$\text{Ar}_2\text{H}^+$	He	$\text{He}^+$ , ArH, Ar	
81	$\text{Ar}_2\text{H}^+$	He	He, $\text{ArH}^+$ , Ar	
81	$\text{Ar}_2\text{H}^+$	He	He, ArH, $\text{Ar}^+$	
81	$\text{Ar}_2\text{H}^+$	He	$\text{HeH}^+$ , Ar, Ar	
81	$\text{Ar}_2\text{H}^+$	He	HeH, $\text{Ar}^+$ , Ar	
81	$\text{Ar}_2\text{H}^+$	He	$\text{HeH}^+$ , $\text{Ar}_2$	
81	$\text{Ar}_2\text{H}^+$	He	HeH, $\text{Ar}_2^+$	
81	$\text{Ar}_2\text{H}^+$	He	$\text{HeArH}^+$ , Ar	
81	$\text{Ar}_2\text{H}^+$	He	$\text{HeArH}$ , $\text{Ar}^+$	
81	$\text{Ar}_2\text{H}^+$	He	$\text{HeAr}^+$ , Ar, H	
81	$\text{Ar}_2\text{H}^+$	He	HeAr, $\text{Ar}^+$ , H	
81	$\text{Ar}_2\text{H}^+$	He	HeAr, Ar, $\text{H}^+$	
81	$\text{Ar}_2\text{H}^+$	He	$\text{HeAr}_2^+$ , H	
81	$\text{Ar}_2\text{H}^+$	He	$\text{HeAr}_2$ , $\text{H}^+$	
81	$\text{Ar}_2\text{H}^+$	He	$\text{HeAr}_2\text{H}^+$	

\* major isotope

† '+' - monovalent cation, '2' - diatomic in preceding atom.

Further development of the database was by the author alone. The 'Thermoli' database was extended to incorporate all possible reactions between the ions listed in Table 2.4 and neon, argon or krypton with reaction enthalpy data included where available. In a similar fashion, hydrogen and water were added to the database. The addition of reactions between hydrogen or water and the ions listed in Table 2.4 more than doubled the size of the database as the diatomic hydrogen and triatomic water had many more possible reaction products than the monatomic gases already in the database. Further additions of reactions to the database were on an individual reaction, rather than systematic, basis.

The database was modified to facilitate its use. The 'products' field was separated into 'product ion' and 'neutral products' fields and the mass of the major isotope of the product ion included. Rate constant data, where available, were also added to the database. Appropriate citations for the kinetic and thermodynamic data associated with each reaction were also included. All reactions listed in the 'Thermoli' database with  $\text{ArH}^+$  as a reactant are shown in Table 2.6.

*Table 2.6 – All reactions with  $\text{ArH}^+$  listed in the 'Thermoli' database.*

Reactant			Product		Neutral	$\Delta H_r$	$k$	References for:	
$m/z^*$	Ion†	Gas†	$m/z^*$	ion†	product(s)†	/eV	/cm <sup>3</sup> s <sup>-1</sup>	$\Delta H_r$	$k$
41	ArH+	He	4	He+	ArH				
41	ArH+	He	40	Ar+	HeH				
41	ArH+	He	5	HeH+	Ar	+2.00		49	
41	ArH+	He	4	He+	H, Ar	+14.80		49	
41	ArH+	He	1	H+	He, Ar	-9.80		49	
41	ArH+	He	40	Ar+	He, H	+6.00		49	
41	ArH+	He	44	HeAr+	H	+6.00		49	
41	ArH+	He	1	H+	HeAr	-9.80		49	
41	ArH+	He	45	HeArH+					
41	ArH+	H2	2	H2+	ArH				
41	ArH+	H2	40	Ar+	H3				
41	ArH+	H2	3	H3+	Ar	-0.54	6.3E-10	49	52
41	ArH+	H2	2	H2+	H, Ar	+5.67		49	
41	ArH+	H2	1	H+	H2, Ar	-9.75		49	
41	ArH+	H2	40	Ar+	H2, H	+6.01		49	
41	ArH+	H2	42	H2Ar+	H	+5.98		49	
41	ArH+	H2	1	H+	ArH2	-9.75		49	
41	ArH+	H2	43	H3Ar+					
41	ArH+	H2	40	Ar+	H, H, H	+10.53		49	
41	ArH+	H2	1	H+	Ar, H, H	+8.36		49	
41	ArH+	H2	41	ArH+	H, H	+4.52		49	
41	ArH+	H2	1	H+	HAr, H				
41	ArH+	H2O	18	H2O+	ArH				
41	ArH+	H2O	18	H2O+	Ar, H	+2.86		49	
41	ArH+	H2O	40	Ar+	H2O, H	+6.01		49	
41	ArH+	H2O	1	H+	H2O, Ar	+3.85		49	
41	ArH+	H2O	19	H3O+	Ar	-3.37		49	
41	ArH+	H2O	40	Ar+	H3O				
41	ArH+	H2O	17	OH+	H, ArH				
41	ArH+	H2O	1	H+	OH, ArH				
41	ArH+	H2O	1	H+	H, OH, Ar	+9.02		49	
41	ArH+	H2O	40	Ar+	H, OH, H	+11.18		49	



Reactant			Product		Neutral	$\Delta H_r$	$k$	References for:	
$m/z^*$	Ion†	Gas†	$m/z^*$	ion†	product(s)†	/eV	/cm <sup>3</sup> s <sup>-1</sup>	$\Delta H_r$	$k$
41	ArH+	H2O	17	OH+	H, Ar, H	+8.42		49	
41	ArH+	H2O	1	H+	H, H, O, Ar	+13.45		49	
41	ArH+	H2O	40	Ar+	H, H, O, H	+15.62		49	
41	ArH+	H2O	16	O+	H, H, Ar, H	+13.48		49	
41	ArH+	H2O	42	ArH2+	OH				
41	ArH+	H2O	17	OH+	ArH2				
41	ArH+	H2O	42	ArH2+	H, O				
41	ArH+	H2O	16	O+	H, ArH2				
41	ArH+	H2O	1	H+	O, ArH2				
41	ArH+	H2O	43	ArH3+	O				
41	ArH+	H2O	16	O+	ArH3				
41	ArH+	H2O	59	H2OArH+					
41	ArH+	H2O	1	H+	HOArH				
41	ArH+	H2O	58	HOArH+	H				
41	ArH+	H2O	1	H+	OArH, H				
41	ArH+	H2O	57	OArH+	H, H				
41	ArH+	H2O	1	H+	OAr, H, H				
41	ArH+	H2O	56	OAr+	H, H, H	+12.80		49	
41	ArH+	Ne	20	Ne+	ArH				
41	ArH+	Ne	40	Ar+	NeH				
41	ArH+	Ne	21	NeH+	Ar				
41	ArH+	Ne	20	Ne+	H, Ar	+11.81		49	
41	ArH+	Ne	1	H+	Ne, Ar	-9.75		49	
41	ArH+	Ne	40	Ar+	Ne, H	+6.01		49	
41	ArH+	Ne	60	NeAr+	H	+5.98		49	
41	ArH+	Ne	1	H+	NeAr	-9.75		49	
41	ArH+	Ne	61	NeArH+					
41	ArH+	Ar	40	Ar+	ArH				
41	ArH+	Ar	40	Ar+	H, Ar				
41	ArH+	Ar	1	H+	Ar, Ar	0.00		49	
41	ArH+	Ar	80	Ar2+	H	+6.01		49	
41	ArH+	Ar	1	H+	Ar2	-9.75		49	
41	ArH+	Ar	81	Ar2H+		+6.01		49	
41	ArH+	Kr	84	Kr+	ArH				
41	ArH+	Kr	40	Ar+	KrH				
41	ArH+	Kr	85	KrH+	Ar				
41	ArH+	Kr	84	Kr+	H, Ar	+4.25		49,62	
41	ArH+	Kr	1	H+	Kr, Ar	-9.75		49,62	
41	ArH+	Kr	40	Ar+	Kr, H	+4.25		49,62	
41	ArH+	Kr	124	KrAr+	H	+5.98		49,62	
41	ArH+	Kr	1	H+	KrAr	-9.75		49,62	
41	ArH+	Kr	125	KrArH+					

\* major isotope

† '+' – monovalent cation, '2' – diatomic in preceding atom.

Table 2.6 shows that for some ions exothermic reaction pathways appear to exist for all of the gases listed in 'Thermoli'. In the case of  $\text{ArH}^+$ , exothermic reaction pathways are generally those producing neutral noble gas species, as the high ionisation potentials of the noble gases mean that large amounts of energy are required to ionise them.

To allow rapid identification of suitable reactions in the 'Thermoli' database and to simplify its use, an interface was created using Microsoft® Access 2000 software. The interface presents the reactions and associated data in an easy to use format and a similar format suitable for printing. The interface includes additional functionality, allowing the database to be searched for reactant or product ion formula or  $m/z$ . The search can be refined to specify a particular reactant gas and/or a maximum reaction enthalpy for the reactions identified.

Potential future developments of 'Thermoli' include the inclusion of potential reactions with analyte ions and the inclusion of reactions with further gases, such as ammonia. For reference purposes, Appendix 1 to this thesis lists all reactions in the 'Thermoli' database with reaction enthalpies of +1 eV or less.

### 2.3 Collision/Reaction Cell Gases

The specific chemistry occurring in the collision/reaction cell is highly dependent on the cell gases used. The use of various gases, individually and in mixtures, has been reported including ammonia,<sup>36,38,44,48,63-86</sup> carbon monoxide,<sup>80,83</sup> chloromethane,<sup>39</sup> fluoromethane,<sup>40</sup> helium,<sup>35,38,58,59,82,87-109</sup> hydrogen,<sup>7,30,35,37,45,59,82,89,93,95-121</sup> methane,<sup>39,43,80,82,121-128</sup> neon,<sup>40,63</sup> nitrous oxide,<sup>39,85,121</sup> oxygen<sup>30,42,80,121,129-132</sup> and xenon.<sup>43,58</sup> These gases have been used to chemically resolve a range of analytes and isobaric interferences.

In general, hydrogen, helium or mixtures thereof are used in collision cells unless the specific chemistry of another gas is required. In Dynamic Reaction Cells, ammonia is the preferred gas although methane and oxygen are also frequently used for their specific chemistries and a range of other gases have been employed for their specific chemistries too. The difference in preferred gases is an artefact of the different modes of operation of collision cells and Dynamic Reaction Cells. In the non-scanning collision cells, the

preferred gas is the lightest and least reactive possible to adequately attenuate the interference<sup>30</sup> as heavier and more reactive gases produce high background spectra.<sup>44</sup> The bandpass mass filtering ability of the Dynamic Reaction Cell means that highly reactive gases such as ammonia can readily be used in the cell as mass filtration can be used to prevent the production of new background ions.

The various analytical results and other effects of using different gases and combinations of gases are discussed below and summarised in Table 2.15 (p75).

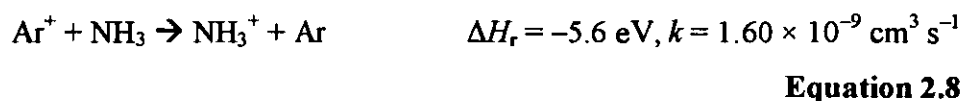
### 2.3.1 Ammonia

Ammonia is a highly reactive gas that is frequently used in collision/reaction cells. It is occasionally used in collision cells<sup>85,86</sup> and is the most frequently reported gas used in dynamic reaction cells.<sup>36,38,44,48,63-84</sup> Unlike other reactive gases used in collision/reaction cells, ammonia frequently acts as a ligand, forming complexes with elemental ions.<sup>44,69</sup> This ligation may cause high background levels in non-filtered multipole cells<sup>44</sup> but the effect is filtered out by the bandpass of DRC so the gas can readily be used therein. Due to interaction between the different complexation reactions, plots of signal *versus* gas flow have a complex shape, for example nickel.<sup>44</sup> The reactions between  $\text{Ni}^+$  and ammonia form a range of nickel-ammonia complexes,  $\text{Ni}(\text{NH}_3)_{1-4}^+$ . The signal for  $\text{Ni}^+$  decreases linearly with increasing flow rate, those for  $\text{Ni}(\text{NH}_3)^+$  and  $\text{Ni}(\text{NH}_3)_2^+$  increase rapidly on initial introduction of gas, then decrease at a similar rate to the  $\text{Ni}^+$  signal.  $\text{Ni}(\text{NH}_3)_3^+$  also increases rapidly on initial introduction of gas, before reaching a constant level.  $\text{Ni}(\text{NH}_3)_4^+$  only appears at higher flow rates, gradually increasing with flow rate thereafter.

Spence *et al.*<sup>86</sup> explored the formation of ammonia based complexes or clusters of a wide range of elements using 1 % ammonia in helium and ICP-CC-MS. Many of the elements tested – 30 out of 72 – formed  $\text{MNH}_3^+$  as their main cluster, with a further 21, mostly non-metals, forming no cluster ions at all. The remainder of the elements tested formed  $\text{MNH}^+$  or  $\text{MNH}_2^+$  as their main cluster ion. Without the use of kinetic energy discrimination (see Section 2.4.2 below), more than 40 % of the elements tested had 99 % or more of the total signal for the element (including all identified cluster ion signals) as

the atomic ion ( $M^+$ ). Almost 70 % of the elements tested had more than 95 % of their total signals as the  $M^+$  signal. The elements with the lowest proportion of their total signal present as the atomic ion signal correlated reasonably well with the elements with the highest M-N bond enthalpies. Kinetic energy discrimination, with a +1 V 'potential barrier' was used to reduce the signals for the clusters without dramatically affecting the sensitivity of the atomic ion. For example, kinetic energy discrimination reduced the main Y-ammonia clusters to less than 5 % of their level with no energy discrimination whilst maintaining more than 95 % of the  $M^+$  signal. The formation of complexes when ammonia is used can therefore be controlled even in ICP-CC-MS.

Ammonia is used to reduce a number of significant polyatomic ions such as the argon-based ions  $Ar^+$ ,  $ArC^+$ ,  $ArN^+$  and  $ArO^+$  without greatly attenuating the isobaric analyte ions –  $^{40}Ca$ ,  $^{52}Cr$ ,  $^{54}Fe$  and  $^{56}Fe$  respectively.<sup>65,67,68,70,71,74,78,79,84,133</sup> It has also been used to facilitate the determination of As and V in a chloride matrix by attenuating the  $ArCl^+$  and  $ClO^+$  interferences.<sup>66,71,73,75,78,79</sup> In order to determine Ca at  $m/z$  40, the  $^{40}Ar^+$  interference must be greatly reduced. Ammonia successfully reduces this signal by the fast, highly specific, exothermic charge transfer reaction shown in Equation 2.8 that can reduce the  $^{40}Ar^+$  signal by nine orders of magnitude.<sup>48</sup>



The analogous reaction for Ca, shown in Equation 2.9, is endothermic and not observed. Thus the  $^{40}Ca^+$  signal is reduced only minimally, due to collisional scattering, permitting the determination of Ca by its major isotope.



The use of ammonia to ameliorate the determination of two other analytes with argon-based interferences is more problematic.  $^{75}As$  and  $^{80}Se$  are interfered with by  $^{40}Ar^{35}Cl^+$  and  $^{40}Ar_2^+$  respectively.  $^{75}As$  is the only naturally occurring isotope of arsenic. Arsenic is a biologically active element, with several toxic species.<sup>94</sup> It is therefore

desirable to determine As in a wide range of biological and environmental samples, such as seawater, which typically contains 1 – 2 ng ml<sup>-1</sup> As and approximately 2 % chloride,<sup>94</sup> and botanical samples, such as the fungus *Ganoderma lucidum* used in traditional Chinese medicine where As is present at tens of ng g<sup>-1</sup> levels.<sup>66</sup> The use of ammonia to facilitate the determination of As is not usually possible as, although ArCl<sup>+</sup> is greatly reduced by reaction with ammonia, so is As<sup>+</sup>.<sup>82</sup> Instead of ammonia, methane is usually used for the determination of arsenic by ICP-DRC-MS.<sup>82</sup> In a recent paper, Chan and Lo<sup>66</sup> reported the determination of As in digested plant samples by ICP-DRC-MS using ammonia. A low flow rate was used to minimise reactive loss of As in this work, together with a high 'RPq' value to prevent the observation of NiNH<sub>3</sub><sup>+</sup>. ('RPq' is related to the *q* Mathieu parameter.)

The alternative method of determining an analyte as a polyatomic product ion has also been used with ammonia, for the measurement of Cu in a high titanium matrix<sup>76</sup> and Ti and Zn in sulfuric acid.<sup>72</sup> The determination of Cu in a high titanium matrix, such as coal fly ash, is problematic due to interference by TiO<sup>+</sup> on both Cu isotopes, <sup>47</sup>Ti<sup>16</sup>O<sup>+</sup> on <sup>63</sup>Cu and <sup>49</sup>Ti<sup>16</sup>O<sup>+</sup> and <sup>47</sup>Ti<sup>18</sup>O<sup>+</sup> on <sup>65</sup>Cu.<sup>76</sup> The use of a variety of different gases to reactively remove the TiO<sup>+</sup> interference was investigated by Liu and Jiang.<sup>76</sup> They found that NH<sub>3</sub>, CH<sub>4</sub>, O<sub>2</sub> and N<sub>2</sub>O were all ineffective at removing the TiO<sup>+</sup> interference without unduly reducing the Cu signal. However, when ammonia was employed, most of the Cu<sup>+</sup> signal was transferred to Cu(NH<sub>3</sub>)<sub>2</sub><sup>+</sup> by the clustering reaction:



**Equation 2.10**

Thus, Cu was determined *via* the Cu(NH<sub>3</sub>)<sub>2</sub><sup>+</sup> ion, with <sup>65</sup>Cu(<sup>14</sup>NH<sub>3</sub>)<sub>2</sub><sup>+</sup> (*m/z* 99) as the preferred isotope, avoiding the <sup>97</sup>Mo<sup>+</sup> interference on <sup>63</sup>Cu(<sup>14</sup>NH<sub>3</sub>)<sub>2</sub><sup>+</sup>.

Kawabata *et al.*<sup>72</sup> developed a method for the determination of Ti and Zn in concentrated sulfuric acid. Specifications for high-purity sulfuric acid for use in semiconductor manufacture are limited by detection ability, due to sulfur-based spectral interferences hindering the determination of many elements by ICP-MS.<sup>72</sup> <sup>48</sup>Ti is interfered with by <sup>32</sup>S<sup>16</sup>O<sup>+</sup> and <sup>64</sup>Zn by both <sup>32</sup>S<sub>2</sub><sup>+</sup> and <sup>32</sup>S<sup>16</sup>O<sub>2</sub><sup>+</sup>. Ti and Zn react with ammonia in the DRC

forming  $\text{TiNH}(\text{NH}_3)_3^+$  and  $\text{Zn}(\text{NH}_3)_3^+$ , thereby enabling the interference-free determination at  $m/z$  114 and 115 respectively with detection limits well below the lowest concentration guidelines produced. Similarly, Spence *et al.*<sup>86</sup> used 1 % ammonia in helium to determine  $^{48}\text{Ti}$  in 1 % sulfuric acid by ICP-CC-MS. Ti was determined as  $^{114}(\text{TiNH}(\text{NH}_3)_3)^+$  with a detection limit of 21  $\text{pg ml}^{-1}$ .

Ammonia has also been used in ICP-CC-MS to determine  $^{51}\text{V}$  in a sodium chloride matrix and to determine Cr in a matrix containing chloride or carbon.<sup>86</sup> 1 % ammonia in helium was used to attenuate the  $^{51}(\text{ClO})^+$  background from 20 000  $\text{counts s}^{-1}$  to less than 100  $\text{counts s}^{-1}$  for a 1200  $\text{mg ml}^{-1}$  sodium chloride solution and thereby facilitate the determination of  $^{51}\text{V}$  in that matrix. The background equivalent concentration was reduced by more than two orders of magnitude. This method could also be used to determine  $^{51}\text{Cr}$  in isotope tracer experiments, for example in red blood corpuscle studies. 1 % ammonia in helium was also used to determine  $^{52}\text{Cr}$  and  $^{53}\text{Cr}$  in a high chloride (0.2 %) and carbon (0.06 %) matrix by attenuating  $^{40}\text{Ar}^{12}\text{C}^+$  and  $^{37}\text{Cl}^{16}\text{O}^+$  interferences.

A summary of the analyses performed using ammonia is given in the appropriate column of Table 2.15 below.

### 2.3.2 Helium

Helium has been used as a collision/reaction cell gas in a particularly diverse range of roles compared to other gases. In early work with collision cells helium was used alone to perform chemistry in the cell,<sup>87</sup> although it is now believed that the effects observed were due to adventitious water in the system.<sup>38,82,88</sup> Helium has also been used as a buffer, alone to reduce noise in isotope ratio studies or enhance sensitivity by collisional focussing and together with a reactive gas such as hydrogen.<sup>35,58,86,89-92,96,105,106,108</sup> Helium alone has also been used for removal of polyatomic ions by kinetic energy discrimination methods.<sup>93-95</sup>

### 2.3.2.1 Helium and the Role of Adventitious Water

Early work by Turner *et al.*<sup>87</sup> used helium alone in a collision cell to attenuate the argon-based ions  $\text{Ar}_2^+$ ,  $\text{ArCl}^+$ ,  $\text{ArO}^+$  and  $\text{Ar}^+$  to enable the determination of  $^{80}\text{Se}$ ,  $^{75}\text{As}$ ,  $^{56}\text{Fe}$  and  $^{40}\text{Ca}$  respectively. Background equivalent concentrations were less than  $2 \text{ ng ml}^{-1}$ . It is believed<sup>38,82,88</sup> that these results were due to the presence of adventitious water in the cell.

A recent publication<sup>88,134</sup> explored the role of water in helium collision cell ICP-MS. Mass spectra for a cobalt solution under two different conditions were compared. The two conditions were helium in the collision cell and deliberately wetted (by wet filter paper in a side-arm in the gas line) helium at the same flow rate. The addition of water had a dramatic effect on the argon-based  $^{40}\text{Ar}^{16}\text{O}^+$  and  $^{40}\text{Ar}_2^+$ , the former was reduced to less than one third of its value under drier conditions and the latter to less than 0.5 % of its 'dry' value. In contrast, the  $^{59}\text{Co}$  signal was more than two-thirds of its 'dry' value.

A further experiment showed that variation in levels of adventitious water could considerably alter the chemistry in the cell. Two  $m/z$ , 59 and 80, were monitored for a cobalt solution while the helium flow rate was gradually increased. The helium was delivered *via* a 10 m length of polytetrafluoroethylene (PTFE) tubing, and the experiment conducted twice, upon the initial introduction of helium and following several hours of flushing. When  $3.0 \text{ ml min}^{-1}$  He was initially introduced to the cell,  $^{59}\text{Co}^+$  was attenuated by two orders of magnitude and  $^{40}\text{Ar}_2^+$  by four orders. Following flushing, the same flow rate caused much less attenuation: one order of magnitude for  $^{40}\text{Ar}_2^+$  and less than one order for  $^{59}\text{Co}^+$ . This change in reactivity was due to differing levels of water in the cell gas. PTFE tubing is water permeable, permitting water to diffuse into the gas line. This level was much higher initially, due to gradual build up over time, than after several hours flushing, when a steady state had developed.

The role of adventitious water in collision cell ICP-MS is further explored in Chapter Four below. A number of papers have been published after that work,<sup>95,106</sup> these are discussed following that work.

### 2.3.2.2 Noise Reduction in Isotope Ratio Studies

Becker and co-workers<sup>89,90,92,97</sup> explored the use of helium in a collision cell to reduce noise in isotope ratio studies. Isotope ratios are used in a number of different fields, principally for monitoring long-lived radionuclides, environmental and geochronological studies, and isotope dilution or tracer experiments for biological/medical purposes.<sup>89</sup> Due, in part, to its speed and sensitivity, ICP-MS is widely used to determine isotope ratios.<sup>91</sup> The use of ICP-MS to determine isotope ratios is also favoured by the simple sample preparation procedures necessary.<sup>90</sup> TIMS, an alternative technique for determining isotope ratios, frequently gives better precision than ICP-MS techniques, but the laborious sample preparation necessary for TIMS discourages its use. Very high precision is required for isotope ratio studies. The best precision is achieved using multicollector ICP-MS (ICP-MCMS) as simultaneous collection of the data cancels out temporal effects. Sector-field ICP-MS (ICP-SFMS) is also widely used for isotope ratios as the higher resolution settings can be used to resolve interferences. Quadrupole ICP-MS is a cheaper and more available technique<sup>3</sup> than ICP-SFMS or ICP-MCMS so its use for isotope ratio studies is desirable.

The use of collision cell ICP-MS can result in enhancement of analyte sensitivity due to a range of related effects.<sup>90,91</sup> Ions, with several electronvolts of energy from the plasma, colliding with the thermal collision cell gas atoms transfer a proportion of their kinetic energy to the gas and are thereby reduced in energy. Multiple collisions result in considerable reduction in the kinetic energy of the ions. These lower energy ions are then much better contained within the rf multipole, increasing transmission of ions to the mass analyser and therefore increasing the sensitivity of the technique.<sup>91</sup> This effect is termed 'collisional focussing'.<sup>91</sup> 10 ml min<sup>-1</sup> helium in the hexapole collision cell of a Platform ICP-MS instrument (Micromass Ltd, Manchester) reduced the median ion energy to 0.9 eV from 3.3 eV with no gas in the cell.<sup>91</sup> Collisional focussing increased transmission of ions to the mass analyser increasing the sensitivity of the technique.

One difficulty encountered when measuring isotope ratios by quadrupole ICP-MS is the peak tailing of high abundance isotopes overlapping adjacent isotope peaks, introducing positive bias to them.<sup>91</sup> The tailing of peaks over adjacent  $m/z$  is termed 'isotopic



abundance sensitivity' and is reported as the ratio of peak tail intensity at mass  $m \pm x$  to the analyte sensitivity at mass  $m$ . (Values are typically quoted for  $x = 1$  and are dimensionless.)<sup>91</sup>

Boulyga and Becker<sup>91</sup> studied the effect of helium in a collision cell on isotopic abundance sensitivity, with reference to the  $^{175}\text{Lu}$  isotope ( $m = 174.94$  u). Compared with no gas in the cell,  $10 \text{ ml min}^{-1}$  helium reduced the peak tail at  $m - 1.5$  u by three orders of magnitude. As is generally found for quadrupole ICP-MS, tailing was more pronounced on the low mass side of the peak than on the high mass side.

Improved isotopic abundance sensitivity is particularly useful when measuring small signals in the presence of much larger signals at a similar  $m/z$ , for example the radionuclide  $^{236}\text{U}$  in the presence of the highly abundant  $^{238}\text{U}$  (99.27 %)<sup>9</sup> for  $^{236}\text{U}/^{238}\text{U}$  isotope ratios. Introduction of  $10 \text{ ml min}^{-1}$  to the cell improved the  $((m - 1)/m)$  isotopic abundance sensitivity of the  $^{236}\text{U}/^{238}\text{U}$  ratio, from  $2.3 \times 10^{-5}$  with no gas in the cell to  $6.3 \times 10^{-8}$  at  $10 \text{ ml min}^{-1}$  helium.<sup>91</sup> Helium in a 'Platform' ICP-CC-MS system has been used to determine U and Os isotope ratios.<sup>90,92</sup>

$^{236}\text{U}$  (half-life  $2.3416 \times 10^7$  years) has been used as a tracer of nuclear fallout in environmental samples.<sup>90</sup>  $^{236}\text{U}$  is formed in nuclear reactors by the  $^{235}\text{U}(n, \gamma)^{236}\text{U}$  reaction, it does not occur naturally. If elevated levels of  $^{236}\text{U}$  are present in environmental samples, showing that uranium of nuclear reactor origin is present, the  $^{236}\text{U}/^{238}\text{U}$  ratio will become elevated enabling the contaminated areas to be identified and the  $^{236}\text{U}$  level quantified. Boulyga *et al.*<sup>90</sup> used ICP-CC-MS with helium to determine  $^{236}\text{U}/^{238}\text{U}$  ratios in soil samples from the Ukraine and Belarus, in the area surrounding the Chernobyl nuclear power plant. In all of the locations studied  $^{236}\text{U}$  was present, with the level of contamination decreasing with depth over the top 20 cm of soil with only naturally abundant U below that depth. The  $^{236}\text{U}/^{238}\text{U}$  levels recorded were in very good agreement with the values recorded by ICP-SFMS. The two techniques, ICP-CC-MS and ICP-SFMS, gave very similar precisions.

Determination of Os isotope ratios is necessary for Re/Os dating of minerals.<sup>92</sup> The long-lived radioisotope  $^{187}\text{Re}$  (half-life  $4.23 \times 10^{10}$  years) undergoes  $\beta^-$  decay to form stable  $^{187}\text{Os}$ . Thus the level of  $^{187}\text{Os}$  relative to other isotopes and the level of Re can be used to ascertain the age of the mineral. Boulyga *et al.*<sup>92</sup> used ICP-MCMS, ICP-DFMS and ICP-CC-MS with helium to determine Os isotope ratios in refined Os metal enriched in  $^{187}\text{Os}$ . Mathematical correction was used to correct for low levels of Pt, W and Ir interferences. The isotope ratios for the  $^{187}\text{Os}$  enriched samples for the other isotopes over  $^{187}\text{Os}$  (i.e.  $^{18x}\text{Os}/^{187}\text{Os}$ ) were, for ratios over  $2 \times 10^{-4}$ , in good agreement between the three techniques – ICP-CC-MS, ICP-SFMS and ICP-MCMS. ICP-MCMS gave the best precision, 0.02 – 0.06 % for ratios over  $2 \times 10^{-4}$ ; ICP-SFMS gave slightly poorer precision, 0.06 – 0.21 % for the same ratios, and ICP-CC-MS gave the poorest precision, 0.19 – 0.55 %.  $^{184}\text{Os}/^{187}\text{Os}$  was below  $10^{-6}$  in all samples; the  $^{184}\text{Os}$  signal in ICP-SFMS and ICP-CC-MS was too low for the ratio to be measured.  $^{186}\text{Os}/^{187}\text{Os}$  was  $1.6 \times 10^{-4}$  in one sample and around  $7 \times 10^{-5}$  in the other samples. For the other ratio below  $2 \times 10^{-4}$ ,  $^{186}\text{Os}/^{187}\text{Os}$ , ICP-MCMS gave the best precision, 0.7 – 0.8 %, with the other two techniques having similar precisions to each other, 2.5 – 4.6 % for ICP-SFMS and 3.1 – 6.9 % for ICP-CC-MS.

ICP-CC-MS has been shown to be a valid method for determining isotope ratios where the cell has been used purely to reduce ion energy by collisional processes, without any reactive effects occurring. The use of ICP-CC-MS to determine isotope ratios where chemical resolution is also used is discussed elsewhere in Section 2.3, in the sub-section for the appropriate reactive gas.

### Mass Bias

'Mass bias' or variation in analyte response with  $m/z$ , is an important factor in isotope ratio studies. At low mass, mass bias can cause considerable variation in analyte sensitivity over the small mass range of 1 – 2 u typical of isotope ratios, causing a large error in the accuracy of the ratio, for example, 5 % mass bias per mass unit (MB) has been observed<sup>96</sup> for  $^{25}\text{Mg}/^{26}\text{Mg}$ . Even at higher masses, where mass bias is much less pronounced (MB of 0.7 % has been seen for  $^{203}\text{Tl}/^{205}\text{Tl}$ ),<sup>96</sup> mass bias can introduce considerable error. Mass bias is mathematically corrected for in isotope ratio studies.

An isotope ratio for an internal standard of known isotopic abundance is studied and the mass bias in that measurement determined. The mass bias in the isotope ratio of interest is then calculated using one of a range of possible models and is mathematically corrected for.<sup>135</sup>

Mass bias is caused by a number of different effects in the mass spectrometer including detector 'dead time', focussing effects from the ion lenses and 'space charge' effects in the interface region.<sup>96</sup> Mass bias varies with operating conditions such as nebuliser gas flow rate, torch position and rf power but is not time independent in ICP-MS.<sup>96</sup> Detector dead time affects mass bias by registering fewer counts than actually occur for large signals. Focussing effects result from the ion energy dependence of lens focussing, where the ion lenses will more efficiently focus ions of either lower kinetic energy (and therefore mass) or higher kinetic energy (and so mass) depending on the settings adopted. 'Space charge' effects occur in the interface region as the electrons are separated from the ions to leave an ion beam and at other points where the ion beam is narrowly focussed. Within the dense positive cloud of the ion beam, the ions are mutually repelled, with momentum considerations causing the lighter ions to be dispersed to a greater extent than the heavier ones.<sup>96</sup> The use of a pressurised collision/reaction cell provides an additional source of mass bias that depends on gas type<sup>58</sup> and flow rate.<sup>96-98</sup>

The use of helium in a collision cell results in collisional focussing which leads to an enhancement in the sensitivity of high mass isotopes whereas low mass isotopes are deflected off course and rejected from the cell by a process called 'collisional scattering'. Thus, the gas filled cell increases the mass dependence of sensitivity, resulting in an increase in mass bias.<sup>97</sup> Mass bias is also affected by the lowered energy of ions exiting the cell, as ion optics are ion kinetic energy dependent.<sup>97</sup> The use of a reactive gas has a considerable effect on space charge effects within the multipole in the cell as, for example, hydrogen reactively removes argon-based ions from the system, reducing the positive charge density of the ion beam and so influencing space charge effects.<sup>97</sup> The rate of reaction of different isotopes of an ion are different due to the mass dependence of collisional kinetic energy loss in the cell. The use of gases other than helium, particularly heavier gases such as xenon, results in significantly different mass bias as the effect of the changed mass of the gas and changed reactivity alters ion

focussing and space charge effects.<sup>58,98</sup> Similarly, changing gas flows alters the collision rate in the cell and therefore changes mass bias effects.<sup>96-98</sup>

Xie and Kerrich<sup>96,98</sup> explored the influence of a helium/hydrogen collision cell on mass bias. The use of collision cell gas caused an increase in mass bias at low mass (from 5 to 10 % MB for <sup>25</sup>Mg/<sup>26</sup>Mg) and a decrease at high mass (MB changed from 0.7 % with no gas to 0.1 % with gas for <sup>203</sup>Tl/<sup>205</sup>Tl). Increasing the helium flow rate from 2.5 to 5.0 ml min<sup>-1</sup> caused mass bias at low mass to increase significantly with only minimal increase at higher masses, as is shown in Table 2.7.

**Table 2.7 – Influence of helium flow on mass bias at various masses.<sup>96</sup> Hydrogen flow rate 2.8 ml min<sup>-1</sup> throughout. (MB = mass bias per mass unit)**

Helium flow rate/ml min <sup>-1</sup> :	2.5	5.0
	MB (%)	
<sup>25</sup> Mg/ <sup>26</sup> Mg	7.48	10.55
<sup>86</sup> Sr/ <sup>88</sup> Sr	1.02	2.03
<sup>203</sup> Tl/ <sup>205</sup> Tl	0.10	0.11

The variation in mass bias due to collision cell effects reported by Xie and Kerrich<sup>96</sup> was much smaller than some of the effects that had previously been reported with variation in ion lens tuning. This lead the authors to conclude,<sup>96</sup> somewhat controversially,<sup>97,98</sup> that the use of a collision cell with helium/hydrogen and variation in the flow rates used did not introduce any additional mass bias. As discussed above, theoretically the use of collision cells influences mass bias in various ways and the data presented by Xie and Kerrich<sup>96</sup> show that the use of a collision cell does distinctly influence mass bias.<sup>96-98</sup> The complex interaction of the factors causing mass bias means that the experimental parameters may be optimised so MB is very similar whether a collision cell is used or not and is also minimally affected by alteration of gas flows.<sup>97</sup> This does not however indicate that the use of a collision cell does not influence mass bias, only that the influence of the collision cell on mass bias is of a similar magnitude to the influence of other parameters.

### 2.3.2.3 Helium as an Inert 'Buffer' in Conjunction with a Reactive Gas

The most widely reported use of helium in collision/reaction cell ICP-MS is as an inert 'buffer' in conjunction with a reactive gas. The reactive gas used with helium was most frequently hydrogen<sup>35,59,89,96,99-109</sup> although ammonia<sup>86</sup> or hydrogen with xenon<sup>58</sup> has also been reported.

The principal reasons for using helium 'buffer' gas are related to the loss of ion energy resulting from non-reactive collisions in the collision/reaction cell. The most widely presented argument for the use of a 'buffer' gas is 'collisional focussing' although collisional cooling of ions also promotes reactions in the cell. The use of an inert 'buffer' gas improves transmission of ions through the cell by slowing the ions by non-reactive collisions; the slower ions are then better focussed towards the axis of the collision/reaction cell multipole.<sup>35,58,86,96,105,106,108</sup> In addition, the reduction in ion energy caused by helium 'buffer' gas promotes reactivity in the cell. This enhancement in reactivity reduces the level of reactive gas necessary to achieve the same reduction in polyatomic ions as achieved by the reactive gas alone, resulting in less loss of analyte ion sensitivity.<sup>35</sup> For example, transmission of  $^{115}\text{In}^+$  was increased by one third when a 1:1 mixture of helium and hydrogen was used instead of hydrogen alone (at the same total flow rate);  $\text{Ar}^+$  and  $\text{Ar}_2^+$  were attenuated by four orders of magnitude in both cases.<sup>59</sup>

### 2.3.2.4 Energy Discrimination of Polyatomic Ions

The Agilent 7500c ICP-CC-MS, with its octopole collision cell, has been used with helium to remove polyatomic ions formed in the plasma and interface region (hereafter abbreviated to plasma-formed polyatomic ions) by energy discrimination methods.<sup>93-95</sup>

Polyatomic ions are much larger than monatomic ions of similar mass. Therefore, polyatomic ions experience more collisions in the cell than monatomic ions of similar mass and hence lose more energy. When the pole bias potential on the cell octopole ( $V_O$ ) is set less negative than the pole bias potential on the quadrupole mass analyser ( $V_Q$ ) (i.e.  $V_Q - V_O$  is positive) then a 'potential barrier' is introduced between the cell and the mass analyser which the slower ions, such as the polyatomic ions retarded by larger numbers of collisions in the cell, cannot overcome.

Yamada *et al.*<sup>95</sup> collected  $V_Q$  'stopping curves' with no collision cell gas employed and with 7 ml min<sup>-1</sup> helium in the cell. Stopping curves are collected by scanning the potential applied to an ion optic element so that gradually more of the ions are excluded as they have insufficient energy to overcome the potential; they thus supply information on ion energy distribution. Examples of stopping curves can be seen in Chapter Five below. With no gas in the cell, the stopping curves for  $^{56}(\text{ArO})^+$ ,  $^{59}\text{Co}^+$ ,  $^{80}(\text{Ar}_2)^+$  and  $^{89}\text{Y}^+$  all centred about +4 V  $V_Q$ ; approximately half of each of the signal present at the most negative  $V_Q$  could still be observed +4 V. When 7 ml min<sup>-1</sup> helium was introduced, the  $^{59}\text{Co}^+$  and  $^{89}\text{Y}^+$  curves centred *circa* -14 V  $V_Q$  (+1 V  $V_Q - V_O$ ) whilst those of  $^{56}(\text{ArO})^+$  and  $^{80}(\text{Ar}_2)^+$  centred several volts lower, *ca.* -17 V  $V_Q$  (-2 V  $V_Q - V_O$ ). ( $V_Q - V_O$  is linearly related to ion energy, but due to the influence of other ion optic elements is not directly equivalent.) The stopping curves showed that the higher collision rate of polyatomic ions resulted in their losing more energy than monatomic ions of similar mass.

The energy discrimination effect described above has been used to determine  $^{75}\text{As}$  ( $^{40}\text{Ar}^{35}\text{Cl}^+$  interference)<sup>94</sup> and a range of other metals (interferences argon-, calcium- or chlorine-based)<sup>93</sup> in seawater. Yamada *et al.*<sup>95</sup> also found that energy discrimination could be used to reduce the level of  $\text{CeO}^+$  ions detected. An energy barrier of  $V_Q - V_O = +1$  V and 5 ml min<sup>-1</sup> helium reduced the level of  $^{156}(\text{CeO})^+ / ^{140}\text{Ce}^+$  by approximately one order of magnitude to 0.001 compared with 0.01 with no gas in the cell. Without energy discrimination ( $V_Q - V_O = -5$  V) 5 ml min<sup>-1</sup> had no effect on the  $\text{CeO}^+ / \text{Ce}^+$  level.

Nakazato *et al.*<sup>94</sup> used HPLC coupled to ICP-CC-MS using helium to determine As speciation in seawater. Unfortunately, the multipole bias potentials were not given, but the authors described an energy discrimination-type mechanism. The  $^{40}\text{Ar}^{35}\text{Cl}^+$  signal decreased rapidly as the helium flow increased; the  $^{75}\text{As}$  signal decreased much less rapidly. The BEC minimised at 6 ml min<sup>-1</sup> helium, with a value of 0.1 ng ml<sup>-1</sup>, this compared favourably to a BEC of tens of ng ml<sup>-1</sup> with no gas in the cell.

ICP-CC-MS with helium was used by Prange and co-workers<sup>93</sup> to determine a range of metals in seawater, all of which suffer from argon-metal diatomic ion and other spectral interferences caused by the complex inorganic matrix. A range of these interferences are shown in Table 2.8.

**Table 2.8 – Selected isobaric interferences on a range of metals in seawater<sup>93</sup>**

Analyte isotope	Interference
<sup>51</sup> V	<sup>35</sup> Cl <sup>16</sup> O <sup>+</sup> , <sup>37</sup> Cl <sup>14</sup> N <sup>+</sup> , <sup>40</sup> Ar <sup>11</sup> B <sup>+</sup>
<sup>52</sup> Cr	<sup>40</sup> Ar <sup>12</sup> C <sup>+</sup> , <sup>35</sup> Cl <sup>16</sup> OH <sup>+</sup> , <sup>37</sup> Cl <sup>14</sup> NH <sup>+</sup>
<sup>58</sup> Ni	<sup>23</sup> Na <sup>35</sup> Cl <sup>+</sup> , <sup>42</sup> Ca <sup>16</sup> O <sup>+</sup>
<sup>59</sup> Co	<sup>24</sup> Mg <sup>35</sup> Cl <sup>+</sup> , <sup>23</sup> Na <sup>35</sup> Cl <sup>+</sup>
<sup>63</sup> Cu	<sup>40</sup> Ar <sup>23</sup> Na <sup>+</sup> , <sup>40</sup> Ca <sup>23</sup> Na <sup>+</sup>
<sup>64</sup> Zn	<sup>40</sup> Ar <sup>24</sup> Mg <sup>+</sup> , <sup>40</sup> Ar <sup>23</sup> NaH <sup>+</sup> , <sup>32</sup> S <sup>16</sup> O <sub>2</sub> <sup>+</sup>
<sup>75</sup> As	<sup>40</sup> Ar <sup>35</sup> Cl <sup>+</sup> , <sup>40</sup> Ca <sup>35</sup> Cl <sup>+</sup>
<sup>98</sup> Mo	<sup>40</sup> Ar <sup>23</sup> Na <sup>35</sup> Cl <sup>+</sup>

A potential barrier ( $V_Q - V_O$ ) of approximately +1 V was used to minimise background levels and maximise analyte sensitivity. The authors presented three possible arguments to explain the attenuation of polyatomic ions by helium in this case: reactions with water and other impurities, collision-induced dissociation (CID) and energy discrimination.<sup>93</sup>

The possibility of water and other impurities removing the polyatomic ions by reaction was presented as one potential cause of the attenuation, but was not further considered.<sup>93</sup>

CID was described as a possible effect to reduce the levels of polyatomic ions with low binding (or bond dissociation) energies, such as ArNa<sup>+</sup> and ArMg<sup>+</sup> (both 0.2 eV)<sup>93</sup>. CID only occurred where the binding energy of the ion colliding with helium atoms was lower than the centre-of-mass energy available in the collision. The centre-of-mass energy available in collisions between helium and the polyatomic ions under the collision cell conditions used was estimated to be 1 eV. There was some evidence that CID did occur in the system, in addition to other means of attenuating the polyatomic ions. When the helium flow was increased, the signal for the ArNa<sup>+</sup> ion at  $m/z$  63 decreased more rapidly than the polyatomic ions at  $m/z$  51 and 52 that have binding energies similar to or

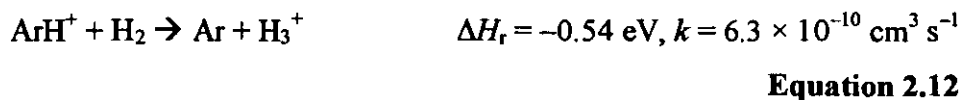
higher than the 1 eV centre-of-mass energy available<sup>93</sup> (around 0.8 eV and 1.8 eV for ArB<sup>+</sup> and ArC<sup>+</sup> respectively).<sup>136</sup>

The majority of the reduction in backgrounds was attributed to energy discrimination, although no exploration of this phenomenon or of the effect of reactions with water *etc.* was undertaken.<sup>93</sup> By the use of 5 ml min<sup>-1</sup> helium in the cell, with  $V_Q - V_O \approx 1$  V, the analytes listed in Table 2.8 were determined in a ten-fold diluted sea water standard reference material. The data were in good agreement with the certified values; except for V and As, the values were 89–107 % of the certified value. (The values for V and As were 127 and 121 % of the certified values respectively). Detection limits for all of the analytes listed above were in the range 1 – 15 pg ml<sup>-1</sup>; in some cases these values were lower, and at worse were an order of magnitude higher, than those for ultra-pure water with no gas in the cell.

### 2.3.3 Hydrogen

Hydrogen is one of the most frequently used gases in collision cells,<sup>7,30,35,37,59,89,93,95-117</sup> it has also been used in Dynamic Reaction Cells.<sup>45,82,118-121</sup> Due to its widespread use, a range of different effects have been observed.

The use of hydrogen in collision/reaction cells considerably reduces the <sup>40</sup>Ar<sup>+</sup> signal, allowing the determination of Ca by its principal isotope, <sup>40</sup>Ca (97 %). Determining Ca *via* <sup>40</sup>Ca greatly improves the instrumental sensitivity for Ca compared with determination *via* <sup>42</sup>Ca (0.64 %)<sup>11</sup> or <sup>44</sup>Ca (2.06 %)<sup>11</sup> in conventional quadrupole ICP-MS. For example, Boulyga *et al.*<sup>112</sup> used helium/hydrogen in ICP-CC-MS to determine Ca *via* <sup>40</sup>Ca with a detection limit of 42 pg ml<sup>-1</sup>. One possible pathway for the reaction between Ar<sup>+</sup> and hydrogen is:<sup>37</sup>





Eiden *et al.*<sup>30</sup> showed that the use of *circa*  $1.3 \times 10^{-5}$  mbar hydrogen in collision cell ICP-MS reduced the  $^{40}\text{Ar}^+$  signal by more than six orders of magnitude, to general background levels. This is consistent with kinetic studies,<sup>137</sup> which have shown that hydrogen reacts with  $\text{Ar}^+$   $10^6$  times faster than it does with the majority of other ions. The thermal rate constant ( $k$ ) for the reaction between  $\text{Ar}^+$  and hydrogen is more than an order of magnitude greater than those between metal cations and hydrogen.<sup>52</sup>

Much of the research using hydrogen in a collision/reaction cell has focussed on the attenuation of argon-based ions containing atoms of atmospheric gas or sample solvent origin, such as  $\text{ArC}^+$ ,  $\text{ArN}^+$ ,  $\text{ArO}^+$ ,  $\text{ArCl}^+$  and  $\text{Ar}_2^+$  (collectively referred to as  $\text{ArX}^+$ ).<sup>7,35,59,82,89,99,100,103-111,114-116,119,121</sup> Hydrogen has also been used to facilitate the determination of a range analytes by attenuating argon-metal ions ( $\text{ArM}^+$ ), for example,  $\text{ArNi}^+$  and  $\text{ArCr}^+$ .<sup>106,120</sup> The attenuation of a range of atmospheric gas- and solvent-based ions to permit the determination of  $^{31}\text{P}$  and the attenuation of a range of diatomic metal cations to permit the determination of the radioisotope  $^{226}\text{Ra}$  have also been accomplished by use of hydrogen in a collision cell ICP-MS system.<sup>102,117</sup>

Whilst hydrogen reacts very well with  $\text{Ar}^+$  and a wide range of polyatomic ions, it has been shown to react with very few elemental ions in the collision/reaction cell. Eiden *et al.*<sup>30,37</sup> studied the reactivity of hydrogen with 43 different elemental ions. Only six of these elemental ions reacted with hydrogen to a significant effect;  $\text{N}^+$ ,  $\text{O}^+$ ,  $\text{Si}^+$ ,  $\text{Cl}^+$ ,  $\text{Ar}^+$  and  $\text{Kr}^+$ .  $\text{Si}^+$  is the only one of the six ions regularly determined using ICP-MS. The determination of Si using hydrogen in ICP-CC-MS is discussed in Section 2.5 below.

A large number of elemental ions do not react with hydrogen to any significant extent. (Eiden *et al.*<sup>30,37</sup> defined ions as not reacting with hydrogen to a significant extent if  $\text{MH}^+/\text{M}^+$  was less than 1 % if  $\text{M}^+$  or  $\text{MH}^+$  did not suffer from isobaric interference or less than 10 % where isobaric interference occurred.) The 37 elements identified as not reacting with hydrogen are  $\text{Na}^+$ ,  $\text{Mg}^+$ ,  $\text{Al}^+$ ,  $\text{K}^+$ ,  $\text{Ca}^+$ ,  $\text{Sc}^+$ ,  $\text{Ti}^+$ ,  $\text{V}^+$ ,  $\text{Cr}^+$ ,  $\text{Mn}^+$ ,  $\text{Fe}^+$ ,  $\text{Co}^+$ ,  $\text{Ni}^+$ ,  $\text{Cu}^+$ ,  $\text{Zn}^+$ ,  $\text{Ga}^+$ ,  $\text{As}^+$ ,  $\text{Se}^+$ ,  $\text{Rb}^+$ ,  $\text{Sr}^+$ ,  $\text{Y}^+$ ,  $\text{Zr}^+$ ,  $\text{Mo}^+$ ,  $\text{Rh}^+$ ,  $\text{Ag}^+$ ,  $\text{Cd}^+$ ,  $\text{In}^+$ ,  $\text{Sb}^+$ ,  $\text{I}^+$ ,  $\text{Xe}^+$ ,  $\text{Cs}^+$ ,  $\text{Ba}^+$ ,  $\text{Tl}^+$ ,  $\text{Pb}^+$ ,  $\text{Bi}^+$ ,  $\text{Th}^+$  and  $\text{U}^+$ .

Hydrogen (in some cases with helium 'buffer' gas) has been successfully used to attenuate a variety of  $\text{ArX}^+$  ions and thereby permit the determination of isobaric monatomic ions. Attenuation of  $^{40}\text{Ar}^{12}\text{C}^+$ ,  $^{40}\text{Ar}^{14}\text{N}^+$ ,  $^{40}\text{Ar}^{16}\text{O}^+$ ,  $^{40}\text{Ar}^{35}\text{Cl}^+$  and  $^{40}\text{Ar}_2^+$  to facilitate the determination of  $^{52}\text{Cr}$  (83.76 %),  $^{54}\text{Fe}$  (5.82 %),  $^{56}\text{Fe}$  (91.66 %),  $^{75}\text{As}$  (100 %) and  $^{80}\text{Se}$  (49.82 %)<sup>11</sup> respectively using hydrogen (often in conjunction with helium buffer gas) and ICP-CC-MS has been widely reported in the literature.<sup>7,35,59,89,99,100,103-111,114-116</sup> For example, Jakubowski and co-workers<sup>59</sup> reported use of a low flow rate of helium (3 ml min<sup>-1</sup>) together with up to 10 ml min<sup>-1</sup> hydrogen in a Platform ICP ICP-CC-MS system (Micromass) to successfully attenuate signals from a range of  $\text{ArX}^+$  ions.  $^{40}\text{Ar}^+$  and  $^{40}\text{Ar}_2^+$  were both attenuated by three orders of magnitude and  $^{40}\text{Ar}^{16}\text{O}^+$  was attenuated 30-fold, thus facilitating the determination of  $^{40}\text{Ca}$ ,  $^{80}\text{Se}$  and  $^{56}\text{Fe}$  respectively. Further work by Jakubowski and others<sup>114</sup> used 6 ml min<sup>-1</sup> hydrogen alone in the same system. Reduction in the signals due to  $^{40}\text{Ar}^{16}\text{O}^+$ ,  $^{40}\text{Ar}^{14}\text{N}^+$  and  $^{40}\text{Ar}^{12}\text{C}^+$  of more than three orders of magnitude was observed.

Interest in the determination of As and Se by collision/reaction cell ICP-MS has been high. The two elements are of particular interest due to their biological effects. The toxicity of As is well known, as is the variation in its toxicity with chemical form and oxidation state. The precise biological role of Se has been the subject of much recent research.<sup>105</sup>

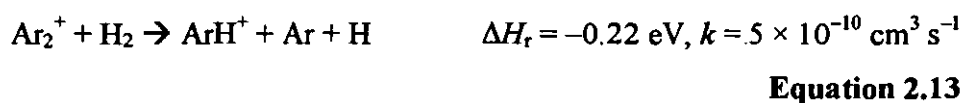
Arsenic exists in various forms in the environment, such as As(III), As(V), monomethylarsenic, dimethylarsenic, arsenobetaine and arsenocholine. The first four species are listed in decreasing order of toxicity; arsenobetaine and arsenocholine are believed to be non-toxic.<sup>109</sup> Determination of the speciation of As in a range of environmental and biological samples is therefore important. One method used to speciate As in aqueous samples is high performance liquid chromatography (HPLC), with an ion exchange column, coupled to ICP-MS.<sup>109</sup>

Arsenic is monoisotopic, its sole isotope ( $^{75}\text{As}$ ) suffering from isobaric interference from  $^{40}\text{Ar}^{35}\text{Cl}^+$  when determined by ICP-MS. This interference presents particular problems for the determination of As in environmental and biological samples as these often contain high levels of chloride, for example, approximately 20 mg ml<sup>-1</sup> in seawater.<sup>94</sup>

The use of hydrogen in ICP-CC-MS reduced the background at  $m/z$  75 for 1 % hydrochloric acid from  $3 \times 10^5$  counts  $s^{-1}$  to  $5 \times 10^3$  counts  $s^{-1}$ , enabling the determination of As with a detection limit of 23  $\mu g\ ml^{-1}$ .<sup>114</sup> The use of a helium/hydrogen mixture attenuated the  $ArCl^+$  signal to permit the determination of As in deionised water with a detection limit of 10  $\mu g\ ml^{-1}$ .<sup>108</sup> A helium/hydrogen mixture has also been used to determine As in seawater.<sup>99</sup>

Xie *et al.*<sup>109</sup> used ion exchange HPLC coupled to helium/hydrogen ICP-CC-MS to develop a method to simultaneously detect As(III), As(V), monomethylarsenic, dimethylarsenic and arsenobetaine. An ammonium nitrate/nitric acid mobile phase was used together with a methacrylate gel based ion exchange column (Micromass). The five As species were all resolved and eluted within 14 minutes. Chloride was co-eluted with As(V) and monomethylarsenic, the resulting  $ArCl^+$  peak was, however, sufficiently attenuated by the helium/hydrogen collision cell that it did not interfere with the analysis. 20  $\mu g\ ml^{-1}$  spike recovery in a river water reference material was generally better than 95 %.

In conventional quadrupole ICP-MS, Se cannot readily be determined *via* the major  $^{80}Se$  isotope (49.7 %) due to the presence of  $^{40}Ar_2^+$ . Se is, therefore, usually determined by the minor  $^{78}Se$  isotope<sup>107</sup> (23.6 %) with a commensurate loss of sensitivity and, therefore, detection limit.  $^{78}Se$  also suffers from interference by  $Ar_2^+$ .<sup>115</sup> The level of  $^{38}Ar^{40}Ar^+$  is however considerably lower than the level of  $^{40}Ar_2^+$ . Collision/reaction cell ICP-MS with hydrogen can be used to improve the determination of  $^{80}Se$  by removing the  $^{40}Ar_2^+$  interference.  $Ar_2^+$  reacts with hydrogen by an exothermic hydrogen-atom transfer reaction, shown in Equation 2.13.<sup>121</sup> The alternative, charge transfer, reaction (Equation 2.14) is strongly endothermic so does not proceed.<sup>121</sup>



Hattendorf and Günther<sup>121</sup> used hydrogen in ICP-DRC-MS to determine Se in nitric acid.  $^{40}\text{Ar}_2^+$  was attenuated to less than  $10^3$  counts  $\text{s}^{-1}$  when  $2.0 \text{ ml min}^{-1}$  hydrogen was introduced to the cell, compared with more than  $10^6$  counts  $\text{s}^{-1}$  with just  $0.1 \text{ ml min}^{-1}$  hydrogen. The  $\text{Ar}_2^+$  signal could not be further reduced, as higher hydrogen flow rates could not be used. At  $2.0 \text{ ml min}^{-1}$  hydrogen, the Se sensitivity at  $m/z$  80 was in excess of  $5000 \text{ counts s}^{-1} \text{ ng}^{-1} \text{ ml}$ .

In biological and other samples, the presence of bromine in the sample presents an additional interference at  $m/z$  80,  $^{79}\text{BrH}^+$ , that is not removed by reaction with hydrogen in the cell.<sup>115</sup> Hinjosa Reyes *et al.*<sup>115</sup> used hydrogen in ICP-CC-MS to determine Se in digests of a range of biological reference materials. Mathematical correction was used to account for the  $^{79}\text{BrH}^+$  interference. The data were in good agreement with the certified values for all of the reference materials tested. (The reference materials used were human serum, freeze dried urine, horse kidney and bovine liver.)

The speciation of Se is of particular interest due to its biological activity. The bioavailability of Se and its toxicity depend on its chemical form.<sup>104</sup> Se is present in a number of proteins in all body tissues as the amino acid selenocysteine.<sup>104</sup> HPLC coupled to ICP-CC-MS using hydrogen or helium/hydrogen has been used to speciate Se in different sample types. Marchante-Gayón and others<sup>104,105</sup> used reversed-phase and ion-pair HPLC coupled to helium/hydrogen ICP-CC-MS to speciate and determine Se in commercial food supplements and human urine. Ion-pair HPLC enabled more Se compounds to be separated than reversed-phase HPLC. The detection limits for Se, determined at  $m/z$  80, were in the range  $30\text{--}200 \text{ pg ml}^{-1}$  in the food supplements and human urine. Mazan *et al.*<sup>107</sup> used HPLC, with a porous graphitic carbon column, coupled to hydrogen ICP-CC-MS to determine selenite (Se(IV)) and selenate (Se(VI)) in water.  $^{40}\text{Ar}_2^+$  was attenuated to give a baseline of less than  $1000 \text{ counts s}^{-1}$  at  $m/z$  80 with detection limits of  $16\text{--}18 \text{ pg ml}^{-1}$  for the two inorganic Se species.

Becker<sup>89,110</sup> reported the use of hydrogen in ICP-CC-MS to determine the radioisotope  $^{79}\text{Se}$  (half-life 65 000 years). A number of different interference ions are present at  $m/z$  79.  $^{39}\text{K}^{40}\text{Ar}^+$ ,  $^{63}\text{Cu}^{16}\text{O}^+$ ,  $^{158}\text{Gd}^{++}$  and  $^{158}\text{Dy}^{++}$  were removed by the use of hydride

generation sample introduction;  $^{38}\text{Ar}^{40}\text{ArH}^+$  was removed by reaction with hydrogen in the collision cell.  $^{79}\text{Se}$  was determined by hydrogen ICP-CC-MS with a detection limit of  $5 \text{ pg ml}^{-1}$ .

Leonhard *et al.*<sup>93</sup> reported the use of hydrogen in ICP-CC-MS to determine a range of elements in seawater (diluted 1:10 with 1 % nitric acid). Seawater is a complex matrix containing high levels of a number of different elements. The complex matrix leads to isobaric interferences existing for many analytes; some examples are listed in Table 2.8 above (p54). The analytes listed in Table 2.8, with the exception of V, Co and Cu for which no data were presented, could be determined at similar levels in seawater with the use of hydrogen ICP-CC-MS and in ultra-pure water by conventional ICP-MS.

Hydrogen has been used in collision/reaction cell ICP-MS to attenuate argon-metal diatomic ions ( $\text{ArM}^+$ ).<sup>106,118,120</sup> For example, the determination of Zr in high Cr matrixes is interfered with by  $\text{ArCr}^+$  ions.<sup>118,120</sup> The use of hydrogen ICP-DRC-MS greatly attenuates the  $\text{ArCr}^+$  interference, to less than 10 counts  $\text{s}^{-1}$  for  $^{90}(\text{ArCr})^+$ , allowing the determination of  $^{90}\text{Zr}$  in  $2 \text{ mg ml}^{-1}$  Cr solutions with an estimated detection limit of  $10 \text{ pg ml}^{-1}$ .<sup>120</sup>  $\text{ArM}^+$  ions can be a particular problem with laser ablation ICP-MS, where a major matrix component can be the source of the interference; the determination of  $^{98}\text{Ru}$  or  $^{100}\text{Ru}$  in nickel,  $^{103}\text{Rh}$  or  $^{105}\text{Pd}$  in copper or  $^{107}\text{Ag}$  in zinc suffer interference from  $^{98}(\text{ArNi})^+$ ,  $^{100}(\text{ArNi})^+$ ,  $^{40}\text{Ar}^{63}\text{Cu}^+$ ,  $^{40}\text{Ar}^{65}\text{Cu}^+$  and  $^{40}\text{Ar}^{67}\text{Zn}^+$  respectively.<sup>106</sup> Mason and Kraan<sup>106</sup> found that the use of  $4 \text{ ml min}^{-1}$  hydrogen in a platform ICP ICP-MS instrument reduced the relative ( $\text{ArM}^+/\text{M}^+$ ) levels of the  $\text{ArM}^+$  ions listed by more than 60 % compared with standard ICP-MS.

The determination of P containing proteins by ICP-MS is hindered by isobaric interference at  $m/z$  31. (The only naturally occurring isotope of P is  $^{31}\text{P}$ .) The interferences;  $^{15}\text{N}^{16}\text{O}^+$ ,  $^{14}\text{N}^{16}\text{OH}^+$  and  $^{12}\text{CH}_3^{16}\text{O}^+$ ; could be readily resolved by ICP-SFMS with a resolution of 4000 ( $m/\Delta m$ ) as they are of sufficiently different mass (30.9950 u, 31.0058 u and 31.0058 u respectively compared with 30.9738 u for  $^{31}\text{P}$ ).<sup>117</sup> Due to its widespread availability and lower cost, determination of  $^{31}\text{P}$  by collision/reaction cell ICP-MS is desirable. Wind *et al.*<sup>117</sup> used hydrogen ICP-CC-MS to determine

phosphorylated proteins via  $^{31}\text{P}$ . The use of hydrogen successfully attenuated the background at  $m/z$  31. The different proteins were separated using coupled HPLC.

Helium/hydrogen ICP-CC-MS has been used to determine  $^{226}\text{Ra}$  in uranium ores, biological and water samples.<sup>102</sup> The radioisotope  $^{226}\text{Ra}$  (half-life 1622 years) features in the uranium decay series and so can be used in the dating of minerals. Ra in drinking water is a radiological hazard and therefore requires monitoring.  $^{226}\text{Ra}$  experiences a number of isobaric interferences:  $^{88}\text{Sr}^{138}\text{Ba}^+$ ,  $^{87}\text{Sr}^{139}\text{La}^+$ ,  $^{86}\text{Sr}^{140}\text{Ce}^+$ ,  $^{40}\text{Ar}_2^{146}\text{Nd}^+$  and  $^{208}\text{Pb}^{18}\text{O}^+$ . Larivière *et al.*<sup>102</sup> used a resin-based cartridge extraction procedure to extract and pre-concentrate Ra in digested uranium ore and lake water samples. This procedure greatly reduced Ba, Ce, La, Nd, Pb, Sr and U levels in the samples, facilitating the determination of  $^{226}\text{Ra}$ . Helium/hydrogen ICP-CC-MS was used to attenuate residual interferences at  $m/z$  226, enabling the determination of  $^{226}\text{Ra}$  in uranium ore and spruce tree reference materials with reasonable agreement between determined and certified values.

Hydrogen, with or without helium buffer gas, has been used in collision/reaction cell ICP-MS to facilitate the determination of a wide range of analytes in a variety of different matrixes. These various applications are summarised in Table 2.15 below.

#### 2.3.4 Methane

The use of methane in collision/reaction cells is widespread in DRC but uncommon in collision cells, owing to the reactivity of the gas. Methane has been used in ICP-DRC-MS to permit the determination of  $^{80}\text{Se}$  (by attenuating  $^{40}\text{Ar}_2^+$ )<sup>80,82,121-127</sup> and other analytes<sup>39,128</sup> whereas the use of methane in ICP-CC-MS has been little reported.<sup>43</sup>

Rowan and Houk,<sup>43</sup> using an early collision cell instrument, observed a reduction in the signals due to  $^{40}\text{Ar}^{35}\text{Cl}^+$  and  $^{40}\text{Ar}_2^+$  at  $m/z$  75 and 80 to the general background level of the spectrum while the sensitivity of the coincident signals for As and Se was 60 % of that observed for the instrument with no gas in the cell. Larsen and co-workers<sup>124,126,127</sup> have used methane in ICP-DRC-MS to determine Se by all of its isotopes, including

isotope ratios featuring  $^{80}\text{Se}$ , although mathematical correction for  $\text{SeH}^+$  was necessary.<sup>126</sup>

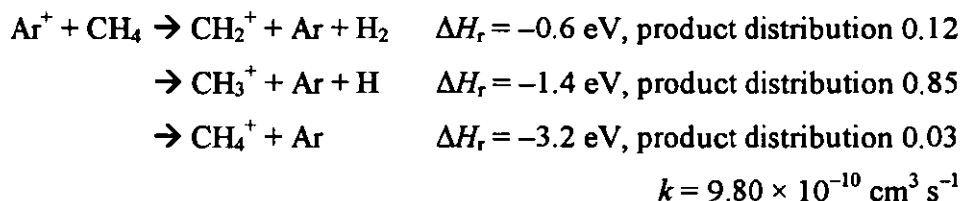
Chen and Jiang<sup>128</sup> used methane to determine Ca, Fe and Zn in digested milk samples by ICP-DRC-MS. Methane reacts with the isobaric interferences detailed in Table 2.9, allowing the determination of Ca, Fe and Zn via  $^{40}\text{Ca}$ ,  $^{56}\text{Fe}$  and  $^{64}\text{Zn}$  with instrumental detection limits of 1, 0.01 and 0.001 ng ml<sup>-1</sup> respectively.

**Table 2.9 – Interferences resolved using methane by Chen and Jiang<sup>128</sup>**

Analyte	Isotope	Interference ion(s)
Ca	$^{40}\text{Ca}$	$^{40}\text{Ar}^+$
Fe	$^{56}\text{Fe}$	$^{40}\text{Ar}^{16}\text{O}^+$ , $^{40}\text{Ca}^{16}\text{O}^+$
Zn	$^{64}\text{Zn}$	$^{48}\text{Ca}^{16}\text{O}^+$ , $^{32}\text{S}^{16}\text{O}_2^+$

Bandura *et al.*<sup>39</sup> used a mixture of nitrous oxide and methane in a DRC instrument to determine  $^{87}\text{Sr}$  as  $^{87}\text{Sr}^{16}\text{OH}^+$ , this method is considered with other applications of  $\text{N}_2\text{O}$  in Section 2.3.6 below.

The major difficulty experienced when using methane in ICP-CC-MS is the general increase in background levels caused by the formation of hydrocarbon ions. These ions include  $^{12}\text{CH}_3^+$  and  $^{12}\text{C}_2\text{H}_5^+$ .<sup>43</sup> They are formed by a series of polymerisation reactions.<sup>48</sup> The reaction sequence is initiated by reactions between two of the most abundant species in the cell,  $\text{CH}_4$  and  $\text{Ar}^+$ :



**Equation 2.15**

Propagation reactions then occur between the hydrocarbon ions and further methane molecules, producing hydrocarbon cations across the mass range. This reaction sequence and therefore the general increase in background is not observed with the DRC as the

bandpass filtering of the cell prevents both the product and reactant ions being stable in the cell simultaneously. Methane is routinely used in ICP-DRC-MS, in place of the generally chosen ammonia, for the determination of arsenic as ammonia and arsenic react together in the cell.<sup>82</sup> Methane is used for the determination of Se in the cell as ammonia reacts only slowly with  $\text{Ar}_2^+$ .

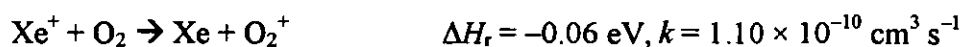
The various applications of methane as a collision/reaction cell gas are summarised in Table 2.15 below.

### 2.3.5 Oxygen

Oxygen has been used as a collision/reaction cell gas since the earliest reports of the technique.<sup>42</sup> The primary type of reaction taking place when oxygen is used is oxidation, usually oxygen atom transfer (Equation 2.16).<sup>30,80,121,129,130</sup> A charge transfer reaction has also been used to remove the  $^{129}\text{Xe}^+$  interference to the determination of  $^{129}\text{I}$  (Equation 2.17).<sup>44,45</sup>



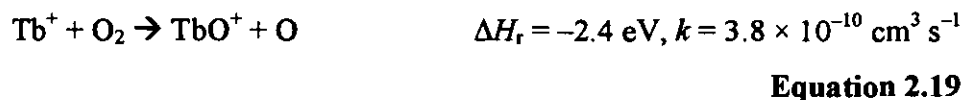
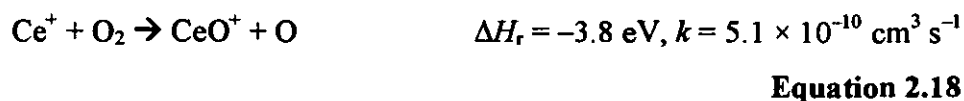
**Equation 2.16**



**Equation 2.17**

In one of the earliest reports of collision/reaction cell ICP-MS; Douglas<sup>42</sup> used the middle quadrupole of an ICP-triple quadrupole mass spectrometer as a collision cell by admitting a limited quantity of air into the vacuum chamber. Only a limited study could be conducted as the first and third quadrupoles were configured to scan a fixed 16 u apart, but this early work showed that  $\text{Ce}^+$  and  $\text{Tb}^+$  could be detected as  $\text{CeO}^+$  and  $\text{TbO}^+$  following reactions in the second quadrupole. The most abundant O-containing gas in air is oxygen ( $\text{O}_2$ ) so it is most likely that the  $\text{CeO}^+$  and  $\text{TbO}^+$  were the result of reactions with oxygen, as shown in Equations 2.18 and 2.19.





Oxygen has been used to determine Se by ICP-DRC-MS.<sup>80,121</sup> The oxygen method contrasts with those methods using ammonia, hydrogen or methane, discussed above, where the  $^{40}\text{Ar}_2^+$  interference was reactively removed, enabling measurement of  $^{80}\text{Se}$  at  $m/z$  80. When oxygen was used to determine Se, an alternative strategy was adopted; formation of a polyatomic ion containing the analyte and measuring this away from the interference. Oxygen reacted with  $\text{Se}^+$ , as shown in Equation 2.20, oxidising  $\text{Se}^+$  to  $\text{SeO}^+$ . Thus  $^{80}\text{Se}$  could be determined as  $^{80}\text{Se}^{16}\text{O}^+$  at  $m/z$  96 away from the spectral interference at  $m/z$  80.



The argon dimer ion also reacted with oxygen, by charge transfer rather than oxygen atom transfer, (Equation 2.21) and so did not interfere at  $m/z$  96.<sup>121</sup>



Hattendorf and Günther<sup>121</sup> used ICP-DRC-MS with oxygen in the reaction cell to determine Se (as  $^{80}\text{Se}^{16}\text{O}^+$ ) in a natural water standard reference material. The value determined was within the confidence range certified, although it was 6.6 % higher than the midpoint value, due to isobaric interference from the minor 96 u isotopes of Mo, Ru or Zr.

Oxygen has also been used to chemically resolve  $^{31}\text{P}$  and  $^{32}\text{S}$  from isobaric polyatomic interferences.<sup>129,130</sup> One preferred method for determining the degree of phosphorylation

of proteins is the use of  $\gamma$ - $^{32}\text{P}$  labelling, with the obvious disadvantages of handling and disposal of radioisotopes. Sector field ICP-MS presents an alternative means of determination, although quadrupole ICP-MS would be a lower cost and more readily accessible method than ICP-SFMS if P were resolved from its interferences. Similar arguments can be presented for the determination of S in proteins. The principal spectral interferences to S and P are shown in Table 2.10.

**Table 2.10 – Spectral interferences to P and S determination (Data from May and Weidermeyer)<sup>11</sup>**

Isotope	Abundance (%)	Interferences
$^{31}\text{P}$	100	$^{14}\text{N}^{16}\text{OH}^+$ , $^{15}\text{N}_2\text{H}^+$ , $^{15}\text{N}^{16}\text{O}^+$ , $^{14}\text{N}^{17}\text{O}^+$ , $^{13}\text{C}^{18}\text{O}^+$ , $^{12}\text{C}^{18}\text{OH}^+$
$^{32}\text{S}$	95.02	$^{16}\text{O}_2^+$ , $^{14}\text{N}^{18}\text{O}^+$ , $^{15}\text{N}^{17}\text{O}^+$ , $^{14}\text{N}^{17}\text{OH}^+$ , $^{15}\text{N}^{16}\text{OH}^+$ , $^{14}\text{N}^{16}\text{OH}_2^+$
$^{33}\text{S}$	0.75	$^{15}\text{N}^{18}\text{O}^+$ , $^{14}\text{N}^{18}\text{OH}^+$ , $^{15}\text{N}^{17}\text{OH}^+$ , $^{16}\text{O}^{17}\text{O}^+$ , $^{16}\text{O}_2\text{H}^+$ , $^{32}\text{SH}^+$
$^{34}\text{S}$	4.21	$^{15}\text{N}^{18}\text{OH}^+$ , $^{16}\text{O}^{18}\text{O}^+$ , $^{17}\text{O}_2^+$ , $^{16}\text{O}^{17}\text{OH}^+$ , $^{33}\text{SH}^+$

Tanner and co-workers<sup>129,130</sup> used oxygen in a Dynamic Reaction Cell system to determine P and S as  $^{31}\text{P}^{16}\text{O}^+$  and  $^{32}\text{S}^{16}\text{O}^+$  at  $m/z$  47 and 48 respectively. (S determination was confirmed by use of  $^{34}\text{S}^{16}\text{O}^+$  at  $m/z$  50.) Details of the relevant reactions are given in Table 2.11. The backgrounds at  $m/z$  31-36 were not transferred with the analyte ions, as the appropriate reactions are either thermodynamically not allowed or kinetically very slow and thus were not observed (see Table 2.11).

**Table 2.11 – Reactions between  $\text{P}^+$ ,  $\text{S}^+$  and polyatomic ions in the  $m/z$  31-36 range with  $\text{O}_2$  (data from ref. <sup>129</sup>)**

Reaction	$\Delta H_r/\text{eV}$	$k_{300}/\text{molecule}^{-1} \text{ cm}^3 \text{ s}^{-1}$
$\text{P}^+ + \text{O}_2 \rightarrow \text{PO}^+ + \text{O}$	-3.10	$5.3 \times 10^{-10}$
$\text{S}^+ + \text{O}_2 \rightarrow \text{SO}^+ + \text{O}$	-0.27	$1.8 \times 10^{-11}$
$\text{CO}^+ + \text{O}_2 \rightarrow \text{CO}_2^+ + \text{O}$	-0.59	$<2 \times 10^{-14}$ (no reaction)
$\text{HCO}^+ + \text{O}_2 \rightarrow \text{COOH}^+ + \text{O}$	+0.14	$<2 \times 10^{-13}$ (no reaction)
$\text{NO}^+ + \text{O}_2 \rightarrow \text{NO}_2^+ + \text{O}$	+2.49	$<1 \times 10^{-11}$ (no reaction)
$\text{NOH}^+ + \text{O}_2 \rightarrow \text{NO}_2\text{H}^+ + \text{O}$	+0.84	n/a
$\text{O}_2^+ + \text{O}_2 \rightarrow \text{O}_3^+ + \text{O}$	+4.43	n/a

By this method, Tanner and co-workers were able to determine P and S as  $^{31}\text{P}^{16}\text{O}^+$  and  $^{32}\text{S}^{16}\text{O}^+$  with detection limits of less than  $50 \text{ pg ml}^{-1}$  in deionised water.<sup>129</sup> The degree of phosphorylation of  $\alpha$ - and  $\beta$ -casein with concentrations in the range  $10 - 1000 \text{ fmol } \mu\text{l}^{-1}$  and 5 – 15 % organic solvent/buffers was measured and shown to be in good agreement with the protein structures.

Detection of the radioisotope  $^{90}\text{Sr}$  by standard ICP-MS requires separation from the isobaric interferences  $^{90}\text{Y}$  and  $^{90}\text{Zr}$  also present in the matrix. Eiden *et al.*<sup>30</sup> used oxygen to determine  $^{90}\text{Sr}$  in the presence of  $^{90}\text{Y}$  and  $^{90}\text{Zr}$ .  $\text{Y}^+$  and  $\text{Zr}^+$  reacted with oxygen in the cell, to produce  $\text{YO}^+$  and  $\text{ZrO}^+$ . Under the same conditions,  $\text{Sr}^+$  did not react. With oxygen in the cell, the background at  $m/z$  90 was indiscernible from adjacent background signals for a  $200 \text{ ng ml}^{-1}$  Y and  $80 \text{ ng ml}^{-1}$  Zr solution.

The increased use of noble metal catalysts, particularly Pt and Rh in catalytic converters for automobile exhaust gases, has increased demand to monitor noble metal levels in a variety of environmental samples.<sup>131,132</sup> ICP-MS is a technique with suitably high sensitivity to determine these metals at appropriately low levels. Determination of the noble metals is, however, hindered by isobaric interference from refractory oxides. Table 2.12 gives details of the refractory oxide interferences for a range of noble metals. The oxide interferences were typically less than 3 % of the analyte signals.

**Table 2.12 – Some significant oxide interferences to noble metal analysis (Data from Ref. 131)**

Noble metal isotope	Relative abundance (%)	Interference	Relative abundance of metal in interference (%)
$^{107}\text{Ag}$	51.84	$^{91}\text{Zr}^{16}\text{O}^+$	11.22
$^{109}\text{Ag}$	48.16	$^{93}\text{Nb}^{16}\text{O}^+$	100.00
$^{197}\text{Au}$	100.00	$^{181}\text{Ta}^{16}\text{O}^+$	99.99
$^{106}\text{Pd}$	27.33	$^{90}\text{Zr}^{16}\text{O}^+$	51.45
$^{108}\text{Pd}$	26.46	$^{92}\text{Zr}^{16}\text{O}^+$	17.15
$^{194}\text{Pt}$	32.90	$^{178}\text{Hf}^{16}\text{O}^+$	27.30
$^{195}\text{Pt}$	33.80	$^{179}\text{Hf}^{16}\text{O}^+$	13.63

ICP-SFMS cannot be used to resolve of these interferences; the small difference in mass between some of the metal analyte ions and their interferences requires resolutions in excess of those attainable in current instrumentation. Amongst the highest resolutions required are those to separate  $^{91}\text{Zr}^{16}\text{O}^+$  and  $^{93}\text{Zr}^{16}\text{O}^+$  from the two Ag isotopes,  $^{107}\text{Ag}$  and  $^{109}\text{Ag}$ . The resolution required in both cases is over 20 000 ( $m/\Delta m$ ).<sup>131,132</sup>

Simpson *et al.*<sup>131,132</sup> used oxygen in ICP-DRC-MS to chemically resolve the noble metals and their refractory oxide interferences. The noble metal ions, including  $\text{Au}^+$ ,  $\text{Ag}^+$ ,  $\text{Pd}^+$  and  $\text{Pt}^+$ , did not appear to react with oxygen as no  $\text{MO}_x^+$  ions were observed. Losses in sensitivity (of less than one order of magnitude) were attributed to collisional scattering. The interferences were entirely removed by further oxidation (Equation 2.22);  $\text{ZrO}^+$ , for example, was oxidised in a stepwise manner to  $\text{ZrO}_2^+$ ,  $\text{ZrO}_3^+$ ,  $\text{ZrO}_4^+$ ,  $\text{ZrO}_5^+$  and  $\text{ZrO}_6^+$ .



**Equation 2.22**

The  $^{91}\text{Zr}^{16}\text{O}^+$  and  $^{93}\text{Nb}^{16}\text{O}^+$  interferences to  $^{107}\text{Ag}$  and  $^{109}\text{Ag}$  were reduced to background levels (less than 10 counts  $\text{s}^{-1}$ ) for a 10 ng  $\text{ml}^{-1}$  Zr and Nb solution, enabling the determination of Ag at either isotope with sub 10 pg  $\text{ml}^{-1}$  estimated detection limits. The Ag isotopic fingerprint was in good agreement with the natural abundance of the isotopes.<sup>131,132</sup> Similarly, oxygen ICP-DRC-MS removed the refractory oxide interferences on Pd,<sup>131</sup> Au and Pt.<sup>132</sup> The isotopic fingerprints of Pd and Pt were in good agreement with natural abundance data. (Au is monoisotopic.)

Thomsen *et al.*<sup>138</sup> used oxygen to determine Cd in the presence of molybdenum and zirconium as the  $\text{MoO}^+$  and  $\text{ZrOH}^+$  interferences were completely removed by oxidation while  $\text{Cd}^+$  did not react.

The determination of the radioisotope  $^{129}\text{I}$  at low levels is of interest to the nuclear industry, for environmental and other monitoring purposes.<sup>139</sup> Due to the long half-life of  $^{129}\text{I}$  ( $1.6 \times 10^7$  years),<sup>139</sup> determination by radiometric methods at suitably low levels is difficult and time consuming. ICP-MS presents a faster alternative method of analysis. The argon gas used to form the ICP invariably contains low levels of xenon. ICP-MS

thus features  $^{129}\text{Xe}^+$  (26.44 % abundant)<sup>9</sup> interference to  $^{129}\text{I}$  determination. Oxygen in a collision/reaction cell system has been shown<sup>30</sup> to remove the  $\text{Xe}^+$  interference by the charge transfer reaction shown in Equation 2.17 above. In contrast to this rapid reaction,  $\text{I}^+$  reacts only very slowly with oxygen.<sup>30,44</sup>  $\text{Xe}^+$  reacts with oxygen 10 000 times faster than  $\text{I}^+$  and the level of  $\text{IO}^+$  formed when oxygen was used in ICP-CC-MS was low, less than 1 %  $\text{IO}^+/\text{I}^+$ .<sup>30</sup>

### 2.3.6 *Other Gases*

In addition to ammonia, helium, hydrogen, methane and oxygen, which were discussed above, the use of a number of other gases in collision/reaction cell ICP-MS has been explored. These gases were selected to perform a specific chemical reaction or were considered in empirical studies to find suitable gases to remove an interference, by exploring the use of a range of different gases. The use of carbon monoxide,<sup>80,83</sup> chloromethane,<sup>39</sup> fluoromethane,<sup>40</sup> neon,<sup>40,63</sup> nitrous oxide<sup>39,85,121</sup> and xenon<sup>43,58</sup> has been reported in the literature.

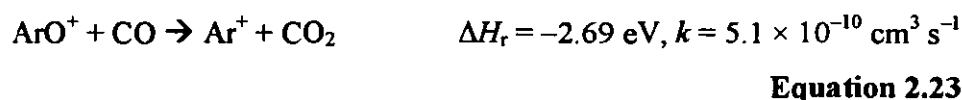
The use of carbon monoxide to facilitate the determination of Fe and Se has been investigated.<sup>80,83</sup> Olesik and co-workers<sup>80</sup> explored the use of a variety of different gases to reduce the  $^{40}\text{Ar}_2^+$  interference on  $^{80}\text{Se}$ . Carbon monoxide (and, separately, ethane) reacted very rapidly with  $\text{Ar}_2^+$ , considerably reducing the level of the interference ion. The gases also reacted rapidly with  $\text{Se}^+$  so were unsuitable for chemically resolving this interference. The other gases explored by the authors were oxygen, ammonia, methane and nitrogen, these are discussed at the appropriate points in this chapter.

Vanhaecke *et al.*<sup>83</sup> successfully used carbon monoxide to enable the determination of Fe isotope ratios featuring  $^{56}\text{Fe}$ . Stable isotope tracers are widely used in human nutrition studies. Determination of Fe in body fluids is complicated by the presence of calcium-based spectral interferences in addition to the argon-based interferences from the ICP. The principal argon- and calcium-based interferences on each of the Fe isotopes are detailed in Table 2.13 (interferences featuring  $^{17}\text{O}$  (0.04 %) have been omitted).

**Table 2.13 – Principal argon- and calcium-based spectral interferences to Fe isotopes<sup>83</sup>**

Isotope	<sup>54</sup> Fe	<sup>56</sup> Fe	<sup>57</sup> Fe	<sup>58</sup> Fe
Natural abundance/%	5.85	91.75	2.12	0.28
Argon-based interference(s)	<sup>40</sup> Ar <sup>14</sup> N <sup>+</sup> <sup>38</sup> Ar <sup>16</sup> O <sup>+</sup> <sup>36</sup> Ar <sup>18</sup> O <sup>+</sup>	<sup>40</sup> Ar <sup>16</sup> O <sup>+</sup>	<sup>40</sup> Ar <sup>16</sup> OH <sup>+</sup> <sup>38</sup> Ar <sup>18</sup> OH <sup>+</sup>	<sup>40</sup> Ar <sup>18</sup> O <sup>+</sup>
Calcium-based interference(s)		<sup>40</sup> Ca <sup>16</sup> O <sup>+</sup>	<sup>40</sup> Ca <sup>16</sup> OH <sup>+</sup>	<sup>40</sup> Ca <sup>18</sup> O <sup>+</sup> <sup>42</sup> Ca <sup>16</sup> O <sup>+</sup>

Carbon monoxide was tested as a possible reaction gas for chemically resolving Fe as kinetic studies<sup>54</sup> suggested they would efficiently remove the <sup>40</sup>Ar<sup>16</sup>O<sup>+</sup> interference, by an oxygen transfer reaction, while not reacting with the Fe<sup>+</sup> analyte:



As predicted, carbon monoxide reactively removed the <sup>40</sup>Ar<sup>16</sup>O<sup>+</sup> interference with only minimal losses of <sup>56</sup>Fe (due to collisional scattering). The signal at *m/z* 56 decreased rapidly on introduction of the gas for a nitric acid solution, while the equivalent signal for an Fe solution decreased only minimally. A 1 µg ml<sup>-1</sup> Ca solution resulted in an elevated blank at all flow rates, compared to the nitric acid blank; the curves for both solutions having very similar shapes. Thus, carbon monoxide does not appear to reactively remove <sup>40</sup>Ca<sup>16</sup>O<sup>+</sup>. In the absence of calcium, carbon monoxide caused an *S/B* improvement of more than two orders of magnitude at *m/z* 54, 56 and 57 – the three most abundant isotopes of Fe. The improvement at *m/z* 58 was limited by nickel contamination. When the calcium matrix was introduced, the improvement in *S/B* was maintained at only *m/z* 54 and 56, with a reduction in the benefit observed at *m/z* 58 and virtually no discernable effect at *m/z* 57. Despite the presence of the calcium-based interferences, <sup>54</sup>Fe/<sup>56</sup>Fe and <sup>57</sup>Fe/<sup>56</sup>Fe were determined with suitably good accuracy and precision. (Confidence

intervals for  $^{54}\text{Fe}/^{56}\text{Fe}$  and  $^{57}\text{Fe}/^{56}\text{Fe}$  were, respectively, half and four times those recorded by ICP-SFMS for the same solution.)

Chloromethane<sup>39</sup> and fluoromethane<sup>40</sup> have been used to determine  $^{87}\text{Sr}$  in the presence of  $^{87}\text{Rb}$ .  $^{87}\text{Sr}$  determination is important for the age determination of rocks. The Rb/Sr levels of a rock can be used to determine its age.  $^{87}\text{Sr}$  undergoes  $\beta^-$  decay to  $^{87}\text{Rb}$  (half-life  $48.8 \times 10^9$  years).<sup>40</sup> Thus, over time the  $^{87}\text{Sr}/^{86}\text{Sr}$  isotope ratio will increase. In order to date a geological system, the  $^{87}\text{Rb}/^{86}\text{Sr}$  (to relate the ratios to the original Rb/Sr concentrations) and  $^{87}\text{Sr}/^{86}\text{Sr}$  ratios for a range of rocks with different Rb/Sr levels within the system are determined and plotted against each other. The gradient of the linear graph is related to the age of the system. As  $^{87}\text{Rb}$  and  $^{87}\text{Sr}$  are isobars, the determination of the ratios is problematic.<sup>40</sup> Thermal ionisation mass spectrometry (TIMS) and multi-collector ICP-MS (ICP-MCMS) are both highly desirable methods for the isotope ratio determination, but TIMS requires considerable sample preparation and ICP-MCMS requires expensive apparatus. ICP-SFMS cannot be used to resolve  $^{87}\text{Rb}$  and  $^{87}\text{Sr}$  due to the extremely high resolution required ( $286\,000\, m/\Delta m$ ).<sup>39</sup>

Bandura *et al.*<sup>39</sup> used chloromethane to chemically resolve  $^{87}\text{Sr}$  and  $^{87}\text{Rb}$ . Sr reacts exothermically with chloromethane, whereas the equivalent chlorine atom transfer reaction for Rb is exothermic:



The use of chloromethane in ICP-DRC-MS enabled the determination of  $^{87}\text{Sr}$  as  $\text{SrCl}^+$ , with virtually no formation of  $\text{RbCl}^+$ .<sup>39</sup> For a  $50\, \text{ng}\, \text{ml}^{-1}$  Rb and Sr solution, Bandura *et al.*<sup>39</sup> showed that, with less than one order of magnitude loss in Rb signal, Sr was converted to  $\text{SrCl}^+$  with less than  $10\, \text{counts}\, \text{s}^{-1}$   $\text{RbCl}^+$  formation (at  $^{85}\text{Rb}^{35}\text{Cl}^+$  – the major isotope). The reaction to form  $\text{SrCl}^+$  was incomplete, less than 10 % of the Sr

converted to  $\text{SrCl}^+$ . Much of the loss was attributed to the low  $q$  parameter used to prevent unwanted reactions between  $\text{Ar}^+$  and chloromethane that form molecular interferences coincident with Rb and Sr isotopes. The  $^{87}\text{SrCl}^+$  signal is split by the two isotopes of Cl,  $^{35}\text{Cl}$  (75.77 %) and  $^{37}\text{Cl}$  (24.23 %), further complicating the determination.

Moens *et al.*<sup>40</sup> explored the use of fluoromethane ( $\text{CH}_3\text{F}$ ) to determine  $^{87}\text{Sr}$  in magmatic rocks. Fluoromethane was used, together with neon buffer gas, in a Dynamic Reaction Cell system to move  $^{87}\text{Sr}$  away from the  $^{87}\text{Rb}^+$  interference:<sup>40</sup>



The analogous reaction for Rb, shown in Equation 2.28, is not observed.



The reaction with  $\text{Sr}^+$  is incomplete, around 80 % of the Sr signal appeared as  $\text{SrF}^+$ . This enabled the determination of the  $^{87}\text{Sr}/^{86}\text{Sr}$  isotope ratio, (as  $\text{SrF}^+$ ) at  $m/z$  106 and 105, with precision close to the counting statistics and only slightly poorer than that observed with determination by TIMS. Fluorine is monoisotopic, so the  $\text{SrF}^+$  signal occurs at a single  $m/z$  for each Sr isotope.

Neon has been used as a buffer in ICP-DRC-MS.<sup>40,63</sup> Moens *et al.*<sup>40</sup> used neon as a buffer gas, in combination with the reactive gas fluoromethane to determine Sr isotope ratios. The role of the buffer gas here is the same as that discussed for helium with reactive gases such as hydrogen, as was discussed in Section 2.3.2.3 above. Neon was selected by the authors in this case as its mass was high enough to provide 'temporal homogenisation' but not so high as to cause large losses of signal through collisional scattering. Temporal homogenisation reduces the noise introduced to the system from the ICP by mixing together ions sampled at slightly different times, smoothing out associated noise, thereby increasing the precision of the isotope ratio measurement.



Bandura *et al.*<sup>63</sup> explored the use of neon in ICP-DRC-MS for the determination of Pb and Ag isotope ratios. The use of DRC has an important (non-reactive) effect on the ion beam. Ion energy is lowered by collisions with the gas; this effect is termed collisional damping. Collisional damping homogenises the ion beam, by mixing ions formed at different times, averaging out noise in the system. The use of neon in DRC approximately halved the noise observed on <sup>107</sup>Ag/<sup>109</sup>Ag measurements.

Nitrous oxide (dinitrogen oxide) has been used as an oxidising agent by several authors to separate a range of different analyte ions from their isobaric interferences; for example, the determination of <sup>56</sup>Fe, <sup>80</sup>Se and <sup>87</sup>Sr as FeO<sup>+</sup>, SeO<sup>+</sup> and SrO<sup>+</sup> away from their respective interferences: ArO<sup>+</sup>, Ar<sub>2</sub><sup>+</sup> Rb<sup>+</sup>.<sup>39,85,121</sup> The generic form of the reaction taking place is given in Equation 2.29, with appropriate kinetic and thermodynamic data for the various reactions given in Table 2.14.



Equation 2.29

Table 2.14 – Kinetic and thermodynamic data for reactions of the form shown in Equation 2.29

M <sup>+</sup>	ΔH <sub>r</sub> /eV	k/cm <sup>3</sup> s <sup>-1</sup>	Notes
Fe <sup>+</sup>	n/a	1.0 × 10 <sup>-10</sup>	
ArO <sup>+</sup>	n/a	n/a	
Se <sup>+</sup>	n/a	6.7 × 10 <sup>-13</sup>	
Ar <sub>2</sub> <sup>+</sup>	-1.6	6.2 × 10 <sup>-10</sup>	Products: <sup>121</sup> 2Ar + N <sub>2</sub> O <sup>+</sup>
Sr <sup>+</sup>	-1.4	n/a	
Rb <sup>+</sup>	+1.4	n/a	

Collision/reaction cell ICP-MS with nitrous oxide has been used to determine <sup>56</sup>Fe as FeO<sup>+</sup> at *m/z* 72; away from the ArO<sup>+</sup> and CaO<sup>+</sup> interferences.<sup>39,85</sup> The conversion to FeO<sup>+</sup> is rapid and exothermic (see Table 2.14). It was not 100 % efficient. The Fe<sup>16</sup>O<sup>+</sup> isotopic fingerprint is correct, confirming the identity of the molecular ions.<sup>39</sup> The background at *m/z* 72 is minimal, CaO<sub>2</sub><sup>+</sup> is not formed to any great extent and <sup>72</sup>Ge<sup>+</sup> reacts with nitrous oxide *via* an oxidation path at a similar rate to the equivalent reaction

for  $\text{Fe}^+$ .<sup>39</sup> Fe in water was determined as  $^{56}\text{Fe}^{16}\text{O}^+$  using  $\text{N}_2\text{O}$  by ICP-CC-MS<sup>85</sup> and ICP-DRC-MS<sup>39</sup> with a DL of  $15 \text{ pg ml}^{-1}$  and BEC of  $2.3 \text{ pg ml}^{-1}$  respectively.

Similarly, nitrous oxide has been used to determine  $^{80}\text{Se}$  as  $^{80}\text{Se}^{16}\text{O}^+$  at  $m/z$  96.<sup>39,85,121</sup> Se can also be determined at  $m/z$  80 using nitrous oxide as  $\text{Ar}_2^+$  is also removed by the gas (see Table 2.14), giving similar detection limits for Se at both  $m/z$  80 and  $m/z$  96.<sup>85</sup> Two potential interferences at  $m/z$  96 are Zr and Mo,<sup>85,121</sup> these are not reactively removed by nitrous oxide.<sup>121</sup> Determination of Se using nitrous oxide will not be possible if high levels of Zr or Mo are present.

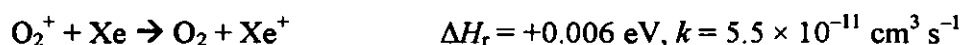
Nitrous oxide has also been used to resolve the  $^{87}\text{Sr}/^{87}\text{Rb}$  interference discussed above.<sup>39</sup> As predicted by the reaction enthalpies (see Table 2.14),  $\text{Sr}^+$  reacted rapidly with nitrous oxide to form  $\text{SrO}^+$  while the reaction with  $\text{Rb}^+$  did not proceed. (The signal for  $50 \text{ ng ml}^{-1}$  Rb at  $^{85}\text{Rb}^{16}\text{O}^+$  was less than  $10 \text{ counts s}^{-1}$  at all nitrous oxide flow rates considered.) Thus ICP-DRC-MS with nitrous oxide can be used to determine  $^{87}\text{Sr}$  as  $^{87}\text{Sr}^{16}\text{O}^+$  at  $m/z$  103; provided that rhodium (monoisotopic,  $^{103}\text{Rh}$ ) is absent from the system. The Rh interference was overcome by introducing methane as a second reaction cell gas, to convert  $\text{SrO}^+$  to  $\text{SrOH}^+$ , as shown in Equation 2.30.



By the use of a mixture of nitrous oxide and methane, effectively complete separation of Sr and Rb was achieved, permitting determination of both  $^{87}\text{Sr}$  and  $^{87}\text{Rb}$ , even in the presence of Rh.<sup>39</sup> A  $50 \text{ ng ml}^{-1}$  Sr and Rb solution gave less than  $1 \times 10^{-4} \text{ counts s}^{-1}$  Sr at  $m/z$  88 and only minimal formation of  $\text{RbO}^+$  or  $\text{RbOH}^+$ , less than 0.01 % of the  $\text{SrOH}^+$  signal.

The use of xenon as a collision cell gas was explored by Rowan and Houk.<sup>43</sup> By the use of  $2.5 \times 10^{-5} \text{ mbar}$  xenon in the collision cell, the signals due to  $^{40}\text{Ar}^{14}\text{N}^+$  and  $^{40}\text{Ar}^{16}\text{O}^+$  were reduced to the level of background noise. The signals due to  $^{54}\text{Fe}$  and  $^{56}\text{Fe}$  retained three quarters of their respective signals when no gas was used. Thus, under the cell condition described, Fe could be determined by either of these isotopes.

Mason *et al.*<sup>58</sup> used low flow rates of xenon combined with higher flow rates of helium for the determination of S and S isotope ratios in natural waters. <sup>32</sup>S/<sup>34</sup>S isotope ratios are useful in biological studies of the sulfur cycle as anaerobic bacterial reactions promote fractionation of these S isotopes.<sup>58</sup> A 1:4 helium:hydrogen mixture was adequate to remove the majority of the N and O based interferences, but the addition of xenon was necessary to attenuate the signal due to O<sub>2</sub><sup>+</sup>. 1:4:0.15 helium:hydrogen:xenon successfully attenuated all interference at *m/z* 32 and 34 allowing the accurate determination of <sup>32</sup>S/<sup>34</sup>S. The S signal was ~ 15 % of that observed with no cell gas used, due to collisional scattering. Such large losses by collisional scatter were due to the low mass of the analyte ions compared with the xenon collision cell gas. The O<sub>2</sub><sup>+</sup> signal was removed by the slightly endothermic charge transfer reaction shown in Equation 2.31.



**Equation 2.31**

The use of helium/hydrogen/xenon in ICP-CC-MS enabled the determination of <sup>32</sup>S and <sup>34</sup>S with detection limits of 48 ng ml<sup>-1</sup> and 25 ng ml<sup>-1</sup> respectively.

A summary of the uses of the various gases in collision/reaction cell ICP-MS, as described above, is given in Table 2.15 below.

### 2.3.7 Summary

A wide range of different gases have been used in collision/reaction cell ICP-MS to determine many elements suffering from isobaric interferences. There is some divergence of techniques with different gases preferred in ICP-CC-MS and ICP-DRC-MS, most notably the difference in gases used for attenuating argon-based interferences, where hydrogen (with or without helium buffer gas) is the primary choice for ICP-CC-MS whereas ammonia is the initially selected gas for ICP-DRC-MS. A wide range of alternative strategies are available to facilitate the determination of some analytes, for example, carbon monoxide, damp helium, hydrogen (with and without helium buffer gas), methane, nitrous oxide and oxygen have all been used to facilitate the

determination of  $^{80}\text{Se}$ , either by attenuating the  $^{40}\text{Ar}_2^+$  interference or by relocating the analyte signal. Table 2.15 summarises the different gases used to determine each element. For appropriate literature citations and more information, consult the appropriate sub-section above.

**Table 2.15** – *Gases used in collision/reaction cell ICP-MS to determine analytes suffering isobaric interference. Analytes listed in italic type are radioisotopes. Not all interference ions may be listed and those given may not relate to each gas/sample matrix used. For more information and citations see Sections 2.3.1–2.3.6. (Table overleaf)*

Table 2.15: (Caption on preceding page)

Analyte	Interference	Ammonia	Ammonia/helium	Carbon monoxide	Chloromethane	Fluoromethane*	Helium (damp)	Helium†	Hydrogen†	Methane	Nitrous oxide	Nitrous oxide/methane	Oxygen	Xenon	Xenon/hydrogen/helium
<sup>28</sup> Si	N <sub>2</sub> <sup>+</sup> , CO <sup>+</sup>	✓							✓						
<sup>31</sup> P	NO <sup>+</sup> , NOH <sup>+</sup> , CH <sub>3</sub> O <sup>+</sup> , N <sub>2</sub> H <sup>+</sup> , CO <sup>+</sup> , COH <sup>+</sup>								✓				✓		
<sup>32</sup> S	O <sub>2</sub> <sup>+</sup> , NO <sup>+</sup> , NOH <sup>+</sup> , NOH <sub>2</sub> <sup>+</sup>												✓		✓
<sup>33</sup> S	NO <sup>+</sup> , NOH <sup>+</sup> , O <sub>2</sub> <sup>+</sup> , O <sub>2</sub> H <sup>+</sup> , SH <sup>+</sup>												✓		✓
<sup>34</sup> S	NOH <sup>+</sup> , O <sub>2</sub> <sup>+</sup> , O <sub>2</sub> H <sup>+</sup> , SH <sup>+</sup>												✓		
<sup>40</sup> Ca	Ar <sup>+</sup>	✓					✓		✓	✓					
<sup>48</sup> Ti	SO <sup>+</sup>	✓	✓												
<sup>51</sup> V	ClO <sup>+</sup>	✓	✓					✓	✓						
<sup>51</sup> Cr	ClO <sup>+</sup>		✓												
<sup>52</sup> Cr	ArC <sup>+</sup>	✓	✓					✓	✓						
<sup>53</sup> Cr	ClO <sup>+</sup>		✓												
<sup>54</sup> Fe	ArN <sup>+</sup>	✓							✓					✓	
<sup>56</sup> Fe	ArO <sup>+</sup> , CaO <sup>+</sup>	✓		✓			✓		✓	✓	✓			✓	
<sup>58</sup> Ni	NaCl <sup>+</sup> , CaO <sup>+</sup>							✓	✓						
<sup>59</sup> Co	MgCl <sup>+</sup>							✓	✓						
<sup>63</sup> Cu	TiO <sup>+</sup> , ArNa <sup>+</sup> , CaNa	✓						✓	✓						
<sup>64</sup> Zn	S <sub>2</sub> <sup>+</sup> , SO <sub>2</sub> <sup>+</sup> , ArMg <sup>+</sup> , ArNaH <sup>+</sup>	✓						✓	✓	✓					
<sup>65</sup> Cu	TiO <sup>+</sup>	✓													
<sup>75</sup> As	ArCl <sup>+</sup>	✓					✓	✓	✓	✓					
<sup>79</sup> Se	KAr <sup>+</sup> , CuO <sup>+</sup> , <sup>158</sup> Gd <sup>++</sup> , <sup>158</sup> Dy <sup>++</sup> , Ar <sub>2</sub> H <sup>+</sup>								✓						
<sup>80</sup> Se	Ar <sub>2</sub> <sup>+</sup>			✓			✓		✓	✓	✓		✓		
<sup>87</sup> Sr	<sup>87</sup> Rb <sup>+</sup>				✓	✓					✓	✓			
<sup>90</sup> Sr	<sup>90</sup> Y <sup>+</sup>												✓		
<sup>90</sup> Zr	ArCr <sup>+</sup>								✓						
<sup>98</sup> Mo	ArNaCl <sup>+</sup>							✓	✓						
<sup>98</sup> Ru	ArNi <sup>+</sup>								✓						
<sup>100</sup> Ru	ArNi <sup>+</sup>								✓						
<sup>103</sup> Rh	ArCu <sup>+</sup>								✓						
<sup>105</sup> Pd	ArCu <sup>+</sup>								✓						
<sup>106</sup> Pd	ZrO <sup>+</sup>												✓		
<sup>107</sup> Ag	ArZn <sup>+</sup> , ZrO <sup>+</sup>								✓				✓		
<sup>108</sup> Pd	ZrO <sup>+</sup>												✓		
<sup>109</sup> Ag	NbO <sup>+</sup>												✓		
<sup>110</sup> Cd	MoO <sup>+</sup> , ZrOH <sup>+</sup>												✓		
<sup>129</sup> I	Xe <sup>+</sup>												✓		
<sup>194</sup> Pt	HfO <sup>+</sup>												✓		
<sup>195</sup> Pt	HfO <sup>+</sup>												✓		
<sup>197</sup> Au	TaO <sup>+</sup>												✓		
<sup>226</sup> Ra	SrBa <sup>+</sup> , SrLa <sup>+</sup> , SrCe <sup>+</sup> , Ar <sub>2</sub> Nd <sup>+</sup> , PbO <sup>+</sup>							✓							

\* with or without neon buffer gas

† polyatomic ion energy discrimination

‡ with or without helium buffer gas

## 2.4 Performance Optimisation Methods

The majority of the work cited above was concerned with the use of collision/reaction cells to determine a specific element or group of elements suffering from isobaric interference, with cell parameters, particularly the nature and flow rates of collision/reaction cell gases, varied to optimise figures of merit for the analytes. Two further concepts can also be used when optimising instrumental performance. Firstly, analyte independent optimisation of collision/reaction cell conditions<sup>35</sup> and, secondly, the effects of ion kinetic energy within and following the collision/reaction cell.<sup>43,59,91,100,108,112,113,140</sup>

### 2.4.1 Multi-element Optimisation Indicators

In collision/reaction cell ICP-MS, optimisation of cell parameters has generally focussed on optimising one elemental signal to background ( $S/B$ ) or signal to noise ( $S/N$ ) ratio with respect to gas flow. This method is unlikely to produce suitable compromise conditions for multi-element analysis. A generic optimisation parameter, similar to Mermet's magnesium ion/atom line ratio<sup>141</sup> to indicate ideal plasma conditions in ICP-atomic emission spectroscopy (ICP-AES) is more desirable.

Ingle *et al.*<sup>35</sup> have identified a generic optimisation parameter for determining the optimum gas flow rate for multi-element analysis by helium/hydrogen ICP-CC-MS. The concept was developed by collecting data for a wide range of  $m/z$  for a 2 % nitric acid blank at a range of helium and/or hydrogen flow rates. At moderate gas flows, far more signals were reduced than increased and the reductions were considerably larger than the increases, up to  $10^5$  times decrease compared with up to  $10^2$  times increase. Correlation analysis was used to group the various ion signals according to their behaviour across the different gas flow rates. Most of the ions studied fell into a small number of groups.

A ratio of two ion signals with opposite responses to changing gas flows was considered to be a good monitor of collision cell effects. The ideal ratio should involve two identifiable background ions, of different chemical origin, at  $m/z$  where no naturally occurring elemental isotopes exist. A number of ions, from different groups, which

varied over the largest range were identified as 'key players'; these are listed in Table 2.16.

**Table 2.16** – The 'key players': ions for which the signals vary most over the helium/hydrogen flow rates studied.<sup>35</sup>

<i>m/z</i>	Ion	Signal intensity/counts s <sup>-1</sup>	
		No gas	He/H <sub>2</sub> *
19	H <sub>3</sub> <sup>16</sup> O <sup>+</sup>	10 <sup>7</sup>	10 <sup>9</sup>
21	H <sub>3</sub> <sup>18</sup> O <sup>+</sup>	10 <sup>4</sup>	10 <sup>6</sup>
31	<sup>14</sup> N <sup>16</sup> OH <sup>+</sup>	10 <sup>4</sup>	10 <sup>6</sup>
43	<sup>40</sup> ArH <sub>3</sub> <sup>+</sup>	10 <sup>3</sup>	10 <sup>5</sup>
14	<sup>14</sup> N <sup>+</sup>	10 <sup>8</sup>	10 <sup>5</sup>
17	<sup>16</sup> OH <sup>+</sup>	10 <sup>8</sup>	10 <sup>7</sup>
36	<sup>36</sup> Ar <sup>+</sup>	10 <sup>7</sup>	10 <sup>3</sup>
38	<sup>38</sup> Ar <sup>+</sup>	10 <sup>6</sup>	10 <sup>3</sup>
80	<sup>40</sup> Ar <sub>2</sub> <sup>+</sup>	10 <sup>6</sup>	10 <sup>4</sup>

\* Data for helium+hydrogen 1.0+1.0 ml min<sup>-1</sup>

The ratios of various ions were considered as possible indicator ratios including <sup>21</sup>(H<sub>3</sub>O)<sup>+</sup>/<sup>36</sup>Ar<sup>+</sup>, <sup>21</sup>(H<sub>3</sub>O)<sup>+</sup>/<sup>80</sup>(Ar<sub>2</sub>)<sup>+</sup>, <sup>21</sup>(H<sub>3</sub>O)<sup>+</sup>/<sup>17</sup>(OH)<sup>+</sup> and <sup>43</sup>(ArH<sub>3</sub>)<sup>+</sup>/<sup>36</sup>Ar<sup>+</sup>. Of these ratios, <sup>21</sup>(H<sub>3</sub>O)<sup>+</sup>/<sup>36</sup>Ar<sup>+</sup> stood out as having a distinct maximum at moderate gas flows. This ratio tracks the behaviour of the H<sub>3</sub>O<sup>+</sup> and Ar<sup>+</sup> species through their minor 21 u and 36 u isotopes and therefore prevents any damage to the detector that could occur with routine examination of the major 19 u and 40 u isotopes.

The presence of chloride in the sample matrix will lower the value of the ratio due to formation of H<sup>35</sup>Cl<sup>+</sup>. This would not necessarily prevent the use of the ratio as the location of the maximum might not change. In any case, the absolute value of the ratio changes from day to day due to variation in instrument stability and plasma and secondary discharge conditions.

Variation of <sup>21</sup>(H<sub>3</sub>O)<sup>+</sup>/<sup>36</sup>Ar<sup>+</sup> with gas flow closely followed *S/N* for a range of elements. The maximum <sup>21</sup>(H<sub>3</sub>O)<sup>+</sup>/<sup>36</sup>Ar<sup>+</sup> value corresponded to optimum or close to optimum *S/N*

for many elements, including those suffering isobaric interference from argon-based ions. In many cases, remaining backgrounds were above noise levels but well below levels present under standard conditions; since the backgrounds were stable and consistent in standards and samples, this was not a problem.

Comparison of theoretical detection limits (DLs) ( $S/N = 3$ ) between no gas and gas conditions for optimal  $^{21}(\text{H}_3\text{O})^+ / ^{36}\text{Ar}^+$  showed considerable reductions for interfered analytes such as  $^{28}\text{Si}$ ,  $^{52}\text{Cr}$ ,  $^{54}\text{Fe}$ ,  $^{56}\text{Fe}$  and  $^{80}\text{Se}$  at the expense of slight increases in DL for low mass uninterfered elements. Thus an analyte independent method for selecting reasonable gas flows for multi-element analysis by ICP-CC-MS by selecting the gas flow rate at which  $\text{H}_3^{18}\text{O}^+ / ^{36}\text{Ar}^+$  maximises was identified. This method was developed using standard solutions in a nitric acid matrix and so should work for samples in simple matrixes. Its efficacy in chloride and other more complex matrixes has not been explored.

Iglesias *et al.*<sup>85</sup> also explored the use of helium/hydrogen ICP-CC-MS to simultaneously determine interfered and uninterfered analytes. Initially, the use of hydrogen, helium/hydrogen, ammonia, helium/ammonia and nitrous oxide to determine  $^{56}\text{Fe}$  and  $^{80}\text{Se}$  was explored (as  $\text{M}^+$  or  $\text{MO}^+$  for nitrous oxide). The lowest DL and highest  $S/B$  for both analytes was observed when helium+hydrogen was used with a flow rate of  $4.0 \pm 2.0 \text{ ml min}^{-1}$ .

The effect of helium/hydrogen on uninterfered analytes across the  $m/z$  range was then explored. To minimise signal suppression by collisional scattering, lower flow rates of helium/hydrogen than those optimal for  $^{56}\text{Fe}$  and  $^{80}\text{Se}$  determination were necessary. Helium+hydrogen  $2.0 \pm 1.0 \text{ ml min}^{-1}$  was found to be a good compromise for determining interfered and uninterfered analytes. Under these conditions, uninterfered isotopes from  $^7\text{Li}$  to  $^{238}\text{U}$  could be determined with DLs 0.5 – 5 times the values with no gas used while  $^{56}\text{Fe}$  and  $^{80}\text{Se}$  could be determined with DLs of  $13 \text{ pg ml}^{-1}$  and  $6 \text{ pg ml}^{-1}$  respectively (compared with  $6 \text{ pg ml}^{-1}$  and  $2 \text{ pg ml}^{-1}$  respectively under optimal conditions of helium+hydrogen  $4.0 \pm 2.0 \text{ ml min}^{-1}$ ).



The use of ICP-CC-MS to simultaneously determine a range of analytes, interfered and uninterfered, is achievable if suitable compromise conditions are selected. These conditions can be selected by the use of generic optimisation indicators such as  $^{21}(\text{H}_3\text{O})^+ / ^{36}\text{Ar}^+$  or by monitoring figures of merit for the desired analytes with changes in conditions.

#### 2.4.2 Ion Energy Techniques

The effect of ion kinetic energy in collision/reaction cell ICP-MS has been considered in a number of papers.<sup>43,59,91,100,108,112,113,140</sup> The majority of these papers have considered the role of a 'retarding potential' between the collision cell and the mass analyser to exclude slower ions, formed within the cell, from the mass analyser/detector.<sup>43,59,108,113,140</sup> This effect has been termed 'kinetic energy discrimination'<sup>81,142</sup> (KED). KED takes advantage of the difference in kinetic energies between plasma-formed and cell-formed ions. Plasma formed ions are highly energetic, with several electronvolts of energy from the high temperature plasma, in contrast, cell-formed ions have much less energy, principally residual energy from the plasma-formed ions involved in the reaction. (During the collision/reaction process, the energy of the reactants, including any energy released by exothermic reactions, is redistributed amongst the products.)

The use of collision cells to discriminate against polyatomic interference ions by relying on these ions, owing to their larger size, losing more energy through collisions than monatomic ions has also been considered.<sup>93-95</sup> This work was discussed in Section 2.3.2.4 above (p52). Energy discrimination of plasma/interface-formed polyatomic ions is not included in the definition of KED adopted herein. The influence of input ion energy on the processes occurring in the collision cell have also been identified.<sup>108,140</sup>

In addition to the dc and rf potentials applied to the rod pairs of a multipole, the entire rod set can also have a potential applied to it, this is termed the 'bias potential'. The bias potentials applied to the collision cell multipole and mass analyser quadrupole are important variables in ion energy techniques.

In one of the earliest reports of ICP-CC-MS, Rowan and Houk<sup>43</sup> showed that a range of polyatomic ions formed in the collision cell from methane gas could be prevented from reaching the detector by use of KED. When the bias potential applied to the quadrupole mass analyser ( $V_{ma}$ ) was negative compared to that on the quadrupole collision cell ( $V_{cell}$ ), polyatomic ions not seen with the cell evacuated were observed. These ions occurred at  $m/z$  of 15 and 29. When  $V_{cell}$  was reduced so  $V_{ma} > V_{cell}$ , the potential barrier between the two quadrupoles prevented the ions formed from reaching the detector. The background ions  $^{16}O^+$  and  $^{16}O_2^+$  were attenuated to similar levels in both cases.

Further explorations of kinetic energy effects were conducted by Jakubowski and co-workers,<sup>59</sup> who explored the role of the collision cell's hexapole bias potential ( $V_H$ ) in analyte ion transmission and cell-generated cluster ion suppression. As  $V_H$  was reduced from 0 to -3 V, analyte sensitivities were reduced. The Y signal was lowered to about 70 % of its initial value, with the lighter elements In and Mn reduced to a much greater extent, about 20 % of the initial value was retained when  $V_H$  was -3 V. Over the same  $V_H$  range, the signals for cell-formed cluster ions (the term used by the authors) at  $m/z$  59, 73 and 97 rapidly fell to less than 1 % of their initial values. Indeed, the vast majority of the decrease had occurred by  $V_H = -1.5$  V where the attenuation of analytes was less pronounced, 30 – 80 % of the signal at  $V_H = 0$  V was retained. Unfortunately, the quadrupole bias potential ( $V_Q$ ) was not quoted in this paper, but KED was apparent in the results as the signals for the cell-formed species decreased much more rapidly than the signals for analyte ions when  $V_H$  was lowered.

Du and Houk<sup>113</sup> showed that  $V_H$  was critical when considering the levels of analyte oxide ions ( $MO^+$ ) produced in the collision cell. The relative levels ( $MO^+/M^+$ ) of oxides of a range of rare earth elements were shown to depend upon  $V_H$ , approximately one order of magnitude suppression was observed on lowering  $V_H$  from +10 to -6 V. ( $V_Q$  was a constant 0 V.) The majority of this change occurred in a steep curve in the region  $+4 \text{ V} > V_H > +1 \text{ V}$ . The discussion provided by the authors describes the results in terms of a KED-type mechanism.

When  $V_H$  is positive with respect to  $V_Q$ , no potential barrier exists between them and ions of low energy are accepted into the quadrupole for mass analysis. As  $V_H$  is lowered,

$V_Q - V_H$  tends towards zero. The energy of slow ions, such as those formed in the cell, is insufficient to propel the ions into the mass analyser. Du and Houk<sup>113</sup> observed the sharp decrease in oxide levels prior to the  $V_Q - V_H = 0$  point. When  $V_Q - V_H$  is positive, slower ions formed in the cell do not reach the mass analyser. As  $V_Q - V_H$  is further increased, the slower analyte ions are also further excluded from the mass analyser. Thus, judicious selection of  $V_Q - V_H$  can be used to prevent the formation of higher backgrounds when a collision cell is employed, yielding only moderate loss of analyte sensitivity.

The KED method of reducing new background ions employed in conventional collision cells contrasts with the bandpass filter method used in Dynamic Reaction Cell.<sup>44,81,82,142</sup>

The initial ion kinetic energy has an important role in the control of reactivity in collision/reaction cells, as would be expected since both the number of collisions occurring in the cell and the reaction rate both depend on ion energy.  $V_H$  can be used to vary ion energy in the cell. The influence of ion kinetic energy on the collision cell has hitherto been little considered in the literature. The concept of the 'ion kinetic energy effect' (IKEE) has been developed by the author and colleagues at Loughborough University.<sup>140</sup> The work that led to the IKEE concept is reported in Section 5.3.1.4 below and in Dexter *et al.*<sup>140</sup> IKEE is the variation of collision cell reactivity by the control of input ion energy.

Becker and co-workers<sup>100,112</sup> explored the effect of  $V_H$  on the attenuation of  $\text{Ar}_2^+$ ,  $\text{ArO}^+$  and other argon-based ions using helium/hydrogen ICP-CC-MS. They found that raising  $V_H$  from 0 to +1.6 V improved the attenuation of the argon-based ions at only modest loss of sensitivity for  $\text{Se}^+$  and  $\text{Fe}^+$  and thus improved  $S/N$  and DLs for the interfered isotopes  $^{80}\text{Se}$  and  $^{56}\text{Fe}$ . No cause of this effect was described in the literature. The argon-based ions were formed in the plasma, not the cell, and therefore the effect cannot be ascribed to KED. Additionally, since the reduction in argon-based ion signals was accompanied by a rise in  $V_H$  it cannot have been due to the energy discrimination of polyatomic ions described in Section 2.3.2.4; increasing  $V_H$  with  $V_Q$  constant would lower  $V_Q - V_H$  and therefore reduce, not enhance, any energy discrimination occurring. The attenuation of argon-based ions can, therefore, only be due to IKEE.

Following the publication<sup>140</sup> of the work reported in Section 5.3.1.4, O'Brien *et al.*<sup>108</sup> explored the influence of  $V_H$  in helium/hydrogen ICP-CC-MS. Regrettably,  $V_Q$  was constant so the effects of KED and IKEE were superimposed and only negative  $V_H$  values were studied so IKEE was not observed as KED dominated. Lowering  $V_H$  from 0 to  $-2$  V (and thereby raising  $V_Q - V_H$  by 2 V) reduced  $\text{CeO}^+/\text{Ce}^+$  to less than 25 % of its initial value, clearly demonstrating KED.

For KED to be most effective, the ion energy distributions of analyte and cell-formed ions cannot overlap. Therefore it is desirable to have the median energies of the distributions sufficiently far apart that overlap does not occur. Narrower energy distributions can be separated more easily than wider ones since less difference in median energies is required. Boulyga and Becker<sup>91</sup>, using a Micromass Platform ICP system, considered the effect of differing flow rates of helium in ICP-CC-MS on the ion energy distribution of  $^{238}\text{U}^+$ . The introduction of helium into the collision cell caused a reduction in median energy and a narrowing of energy distribution. The median energy was lowered from 3.3 eV with no gas used to 1.2 eV with  $5 \text{ ml min}^{-1}$  helium used and further lowered to 0.9 eV when  $10 \text{ ml min}^{-1}$  helium was employed. This shift in median ion energy was due to collisions in the cell redistributing some of the energy of the high-energy ions to the thermal helium atoms. The introduction of helium to the collision cell narrowed the full width at half maximum height (half-width) from *circa* 5.1 eV with no gas used to *ca.* 1.5 eV with  $5 \text{ ml min}^{-1}$  helium in the cell and *ca.* 1.2 eV with  $10 \text{ ml min}^{-1}$  helium used. The narrowing of the energy distribution appeared to be associated with the lowering of median energies, but was not explained.

Work exploring the collision cell ion energy effects, including IKEE and KED, and the effect of collision cell gases on ion energy distribution is reported in Chapter Five below.

## **2.5 Determination of Silicon**

The control of contamination is particularly important in the semiconductor and electronics industry. As the miniaturisation of circuits continues, the need for solvents and other reagents that are free from silicon contamination is greater. In 1999, Denoyer and co-workers<sup>36</sup> reported that for many reagents, Semiconductor Equipment and

Materials International (SEMI) specifications detail maximum levels of contamination in the 10–100 pg ml<sup>-1</sup> range. This is 1–2 orders of magnitude lower than the 1 ng g<sup>-1</sup> maximum level reported by Takaku *et al.* in 1994<sup>143</sup> for water used in the manufacture of dynamic random access memory (DRAM) chips.

Analysis of the level of Si in steels is also important, as the level of Si can have a significant effect on the physical and mechanical properties of the steel.<sup>77</sup> The level of Si in steels is considerably higher than that monitored in semiconductor reagents, in the 80 µg g<sup>-1</sup> range. Sample preparation on the difficult matrix, such as microwave digestion, can introduce a dilution factor of 10 000, giving Si levels around 8 ng ml<sup>-1</sup> in the samples to be determined.<sup>77</sup>

Silicon can readily be determined by inductively coupled plasma atomic emission spectroscopy (ICP-AES) but the best achievable detection limit<sup>144</sup> is only 5 ng ml<sup>-1</sup>, making this technique unsuitable for both semiconductor reagents and steels.

By the use of ICP-MS, detection limits of the pg ml<sup>-1</sup> order can readily be achieved for elements that do not suffer from elemental or polyatomic isobaric interferences. Unfortunately, silicon suffers from isobaric interferences at all three isotopes. These are detailed in Table 2.17. Studies<sup>143</sup> using double focussing ICP-MS instruments in a high resolution mode show that the most significant interference on the major isotope, <sup>28</sup>Si, is <sup>14</sup>N<sub>2</sub><sup>+</sup>.

**Table 2.17 – Isobaric interferences with silicon. (Data from May and Wiedermeyer<sup>11</sup>)**

Isotope	Natural Abundance	Interferences
<sup>28</sup> Si	92.21 %	<sup>14</sup> N <sub>2</sub> <sup>+</sup> , <sup>12</sup> C <sup>16</sup> O <sup>+</sup>
<sup>29</sup> Si	4.7 %	<sup>14</sup> N <sup>15</sup> N <sup>+</sup> , <sup>14</sup> N <sub>2</sub> H <sup>+</sup> , <sup>13</sup> C <sup>16</sup> O <sup>+</sup> , <sup>12</sup> C <sup>17</sup> O <sup>+</sup> , <sup>12</sup> C <sup>16</sup> OH <sup>+</sup>
<sup>30</sup> Si	3.09 %	<sup>15</sup> N <sub>2</sub> <sup>+</sup> , <sup>14</sup> N <sup>15</sup> NH <sup>+</sup> , <sup>14</sup> N <sup>16</sup> O <sup>+</sup> , <sup>12</sup> C <sup>18</sup> O <sup>+</sup> , <sup>13</sup> C <sup>17</sup> O <sup>+</sup> , <sup>13</sup> C <sup>16</sup> OH <sup>+</sup>

A number of different methods have been explored for the determination of Si by ICP-MS: the various isobaric interferences must be resolved, either spectrally (by ICP-SFMS<sup>143</sup>) or chemically (by ICP-DRC-MS<sup>77,133</sup> or ICP-CC-MS<sup>145,146</sup>).

Si can be readily determined by ICP-SFMS,<sup>143</sup> using an intermediate mass resolution ( $m/\Delta m$ ) of 4000, as all of the principal isobaric interferences with Si can be resolved at resolutions of less than 2000. The resolution required for the principal interferences with Si are detailed in Table 2.18.

**Table 2.18 – Resolution ( $m/\Delta m$ ) required for isobaric interferences with Si.<sup>143</sup>**

Isotope	Interference	Resolution required
<sup>28</sup> Si	<sup>12</sup> C <sup>16</sup> O <sup>+</sup>	1560
	<sup>14</sup> N <sub>2</sub> <sup>+</sup>	960
<sup>29</sup> Si	<sup>13</sup> C <sup>16</sup> O <sup>+</sup>	1360
	<sup>12</sup> C <sup>16</sup> H <sup>+</sup>	1110
	<sup>14</sup> N <sub>2</sub> H <sup>+</sup>	780
<sup>30</sup> Si	<sup>14</sup> N <sup>16</sup> O <sup>+</sup>	1240

Takaku *et al.*<sup>143</sup> used ICP-SFMS at a moderate resolution ( $m/\Delta m$ ) of 4000 to determine Si, by <sup>28</sup>Si, in semiconductor grade waters. The levels of Si in the waters were found to be 0.5 – 1.0 ng ml<sup>-1</sup>. An exploration of instrumental contamination was also conducted. Nebulisers, spray chambers and torch injector tubes of a number of different materials were rigorously cleaned. As would be expected, significant levels of Si were detected for a combination of quartz injector and quartz nebuliser and spray chamber, 18.5 ng ml<sup>-1</sup>, which was reduced to 6.5 ng ml<sup>-1</sup> when a platinum injector and Teflon nebuliser/spray chamber were used. Unexpectedly, the use of an alternate silica free system, alumina injector and Teflon nebuliser/spray chamber gave levels of Si contamination two orders of magnitude higher than an all quartz system.

The use of collision/reaction cells to chemically resolve the Si interference has been considered by a number of authors. As was discussed extensively in Chapter Two, the use of highly reactive gases such as ammonia and methane is preferred in Dynamic Reaction Cell systems, whereas lighter, less reactive gases such as hydrogen are preferred in collision cell systems. The methods adopted for the determination of Si reflect this

division, ammonia having been used in ICP-DRC-MS<sup>77,133</sup> and hydrogen (with and without helium buffer gas) being selected for ICP-CC-MS.<sup>145,146</sup>

### 2.5.1 *Determination of Si by Collision Cell ICP-MS*

The use of ICP-CC-MS has been explored within the Atomic Spectroscopy Research Group at Loughborough University. Initial explorations were conducted by the author, whilst an undergraduate student,<sup>146</sup> and by Lawrence.<sup>145</sup>

Si<sup>+</sup> has been shown to react with hydrogen in a collision cell.<sup>30,37</sup> but kinetic considerations show that these reactions proceed more slowly than reactions between hydrogen and the various interference ions. It should, therefore, be possible to use ICP-CC-MS to determine of Si.

Initial work by the author,<sup>146</sup> considered the use of a range of gases to determine Si by ICP-CC-MS. A summary of the results the results is given in Table 2.19

**Table 2.19** – *Effect of different gases on the determination of Si (at m/z 28) by ICP-CC-MS. Sensitivity calculated from 10 ng ml<sup>-1</sup> Si standard and a blank (Data from Hudson<sup>146</sup>)*

Gas	Optimum flow rate /ml min <sup>-1</sup>	Observations at m/z 28	
		Si sensitivity /counts s <sup>-1</sup> ng <sup>-1</sup> ml	Signal for 2 % HNO <sub>3</sub> /counts s <sup>-1</sup>
He	7.0	1 000	490 000
H <sub>2</sub>	3.0	50 000	160 000
Xe	~0.1	50	2 500
He+Xe		A stable signal could not be produced	
Ar		A stable signal could not be produced	
He+H <sub>2</sub>	2.0+1.0	40 000	113 000

It is believed that the instability and poor sensitivity reported for the higher atomic mass gases was due to the low gas-pumping conductance of the collision cell in the VG PQ ExCell instrument. Hydrogen and helium with hydrogen were selected for further study

as they gave acceptable sensitivity for Si and caused some suppression of the background.

Solutions for this initial test were prepared using standard laboratory glassware, so high levels of Si contamination can be assumed. A  $10 \text{ ng ml}^{-1}$  Si in 2 % nitric acid and a 2 % nitric acid blank were prepared and stored using only acid washed polyethylene laboratory-ware were run under the hydrogen and helium with hydrogen conditions detailed above.  $3.0 \text{ ml min}^{-1}$  hydrogen in the cell gave  $10\,000 \text{ counts s}^{-1} \text{ ng}^{-1} \text{ ml}$  sensitivity for  $^{28}\text{Si}$  and  $80\,000 \text{ counts s}^{-1}$  background.  $1.0+2.0 \text{ ml min}^{-1}$  helium+hydrogen produced a sensitivity of less than  $2000 \text{ counts s}^{-1} \text{ ng}^{-1} \text{ ml}$ , so was not further considered.

To confirm that determination of Si at  $^{28}\text{Si}$  was possible by ICP-CC-MS using hydrogen, a quantitative experiment using 0, 10, 20 and  $30 \text{ ng ml}^{-1}$  Si standards in 2 % nitric acid was performed. Excluding the blank, a linear calibration was produced; suggesting that determination of Si is possible under the conditions described. The blank produced a similar signal to the  $20 \text{ ng ml}^{-1}$  standard, which was believed to be due to contamination.

Work on this theme was continued by Lawrence.<sup>145</sup> The use of different types of ICP conditions and nebulisers under different a range of flow rates of helium, hydrogen and mixtures of helium and hydrogen was explored. Two different nebulisers were explored, a standard concentric nebuliser and a microconcentric nebuliser with desolvation. These were both explored under standard plasma conditions. The standard nebuliser was also used with the plasma screen and full power plasma. Data were collected for all Si isotopes, at  $m/z$  28, 29 and 30 for a nitric acid blank.

For all  $m/z$ , except as otherwise noted, the various nebulisers and plasma conditions had little effect on the signal observed. At  $m/z$  28, the greatest reduction in background compared to standard mode was observed when hydrogen alone, or in mixtures with  $1.0 \text{ ml min}^{-1}$  helium, so further work concentrated on these gas conditions. At  $m/z$  29, low flow rates of hydrogen caused a slight increase in background, possibly due to formation of  $^{14}\text{N}_2\text{H}^+$  and/or  $^{12}\text{C}^{16}\text{OH}^+$ . At moderate flow rates, background attenuation was considerably less than at  $m/z$  28. At  $m/z$  30, attenuation was negligible, although the



background was 100 times lower with the desolvation system employed, removing the oxygen required to form  $^{14}\text{N}^{16}\text{O}^+$ . Since  $^{28}\text{Si}$  is the major isotope and the background attenuation at  $m/z$  28 was so much more there than at the other isotopes, further investigation concentrated on that  $m/z$ . Due to instrumental difficulties and a shortage of time, further investigations were restricted to standard nebulisation without the use of the plasma screen.

The optimum flow rate was determined by measuring the signal at  $m/z$  28 for 0, 10 and 100 ng ml<sup>-1</sup> Si in water standards with a range of different hydrogen flow rates. Signal to background ratios ( $S/B$ ) were calculated and found to optimise at the low flow rate of 1.0 ml min<sup>-1</sup>. This was presented as the optimal flow rate for the determination of Si by ICP-MS. Ingle and co-workers<sup>35</sup> discussed the use of  $S/N$  and  $S/B$  in ICP-MS. They considered that, owing to the stability of background signals in ICP-MS,  $S/N$  was more informative than  $S/B$ ; a small signal coincident with a high background can still be determined provided the noise in the background is sufficiently low. The 1.0 ml min<sup>-1</sup> flow rate of hydrogen cannot, therefore, be considered the optimal condition for the determining Si without first considering the variation of  $S/N$  with flow rate.

The optimum conditions for determining Si appeared to feature the use of hydrogen or hydrogen with 1.0 ml min<sup>-1</sup> helium. Backgrounds were similar with the use of standard solution nebulisation or the use of desolvation. Desolvation involves the use of additional equipment and so it complicates the method and presents additional opportunity for contamination. The use of conventional solution sample introduction is therefore preferable. Further investigations into the use of ICP-CC-MS with hydrogen are reported in Chapter Three below.

### 2.5.2 Determination of Si by Dynamic Reaction Cell ICP-MS

Gregoire and others<sup>133</sup> used ammonia in a Dynamic Reaction Cell to improve the determination of Si. Ammonia was found to be unsuitable for determination of  $^{30}\text{Si}$  due to the formation of high levels of  $^{14}\text{N}^{16}\text{O}^+$  in the collision cell masking the analytical signal. Ammonia was, however, more successful for the more abundant isotopes  $^{28}\text{Si}$  and  $^{29}\text{Si}$ . The optimal ammonia flow rate for Si selected was that with maximum  $S/B$  for Si at

both isotopes. At the selected flow rate,  $1.1 \text{ ml min}^{-1}$ , the signal for interferences at  $m/z$  28 was approximately five orders of magnitude lower than when no gas was introduced whereas the signal for  $^{28}\text{Si}$  was only suppressed by three orders of magnitude. At  $m/z$  29 the interference signal was reduced by around four orders of magnitude and the  $^{29}\text{Si}$  signal was reduced by around three orders. Backgrounds of some 500 and 200 counts  $\text{s}^{-1}$  remained at  $m/z$  28 and 29 respectively. Despite the remaining interferences, Si could be determined, *via* either isotope, with detection limits 15 times lower than those calculated for standard mode.

Liu and Jiang<sup>77</sup> investigated the use of ICP-DRC-MS for the determination of Si. The suitability of ammonia, hydrogen, methane and oxygen as reaction cell gases to ameliorate the determination of Si at  $m/z$  28 was explored. Of the four gases considered, only ammonia was considered suitable. Hydrogen caused little suppression of the background, less than two orders of magnitude, when gas was first introduced to the cell with minimal further reduction as the gas flow was increased. The analyte signal was distinguishable above this background, suffering only one order of magnitude suppression over the range studied. Oxygen and, to a lesser degree, methane caused moderate suppression of the background but also suppressed the signal for the Si solution so it was virtually indistinguishable from the background. Over the range studied, ammonia caused the largest suppression of background, five orders of magnitude, and the signal for the  $10 \text{ ng ml}^{-1}$  Si solution was readily distinguishable. A flow rate of  $0.6 \text{ ml min}^{-1}$  was selected as the best estimated detection limit was calculated there.

The method was used to determine Si in steels. The samples underwent a microwave digestion procedure, and were introduced to the instrument as solutions in 1 % nitric acid, with a dilution factor of 10 000. Determination of Si in steel certified reference materials was used to validate the method, the concentrations measured were very close to the certified level, and well within the uncertainty range quoted. The detection limit was approximately  $0.2 \text{ ng ml}^{-1}$ ; corresponding to  $2 \text{ } \mu\text{g g}^{-1}$  in the solid samples, around 35 times lower than the certified values. This detection limit is just above the maximum levels desirable for semiconductor reagent analysis. Further work using appropriate

sample matrices could well enable determination of Si at the low levels required for semiconductor reagents by ICP-DRC-MS

## **Chapter Three**

### **Determination of Silicon**

### **3.0 Determination of Silicon**

The determination of Si at low levels, *ca.* 10 pg ml<sup>-1</sup>, in a range of different reagents is necessary in the semiconductor industry. As discussed in Section 2.5 above, one promising method for such determination is ICP-CC-MS with helium/hydrogen. Further work is necessary to develop and test an appropriate method for Si determination using helium/hydrogen ICP-CC-MS. This chapter reports work to develop an appropriate method for the determination of Si using ICP-CC-MS. The work discussed in Section 3.1 above was used as a starting point and therefore helium/hydrogen cell gas was used together with standard pneumatic sample introduction.

#### **3.1 *Instrumentation and General Experimental***

A VG PQ ExCell ICP-MS instrument (Thermo Electron, Winsford, Cheshire) equipped with Collision Cell Technology was used throughout this work. Standard nickel sample (1.0 mm diameter orifice) and skimmer (0.7 mm diameter orifice) cones were used throughout. Collision cell gases were supplied to the calibrated mass flow controllers through 0.125 inch o.d. stainless steel lines.

The instrument location and sample introduction system were varied at several points in this work, but for the majority of the work (except where otherwise stated), were as described below:

The instrument was located in a general-purpose laboratory without air filtration or conditioning equipment. A Meinhard® (Meinhard Glass Products, Golden, CO, USA) or Conikal (Glass Expansion, Hawthorn, Victoria, Australia) concentric quartz nebuliser, silica impact bead spray chamber, cooled to 5 °C by a Peltier cooler, and standard torch (both from Thermo Electron) were used. Hydrogen was supplied to the collision cell by a hydrogen generator (99.9995 % hydrogen) (Parker Balston H2-90, Parker Hannifan plc, Maidstone, Kent) or by cylinder (99.999 % hydrogen) (BOC Special Gases, Guildford, Surrey). Helium (99.999 %) and oxygen (99.999 %) were supplied to the collision cell by cylinder (BOC special gases). For safety reasons, hydrogen and oxygen were never simultaneously connected to the instrument, nor were the hydrogen and oxygen cylinders

located in the laboratory at the same time. (Oxygen was not used during the period the hydrogen generator was available for use.) Different regulators, gas lines and mass flow controllers were used for hydrogen and oxygen.

With the instrument in standard mode (the collision cell was not pressurised), ion optics and torch position and nebuliser gas flow were tuned daily to optimise the signal at  $m/z$  115 (In) for a  $1.0 \text{ ng ml}^{-1}$  tune solution. Sensitivity, stability and oxide levels were monitored daily. Sensitivity for  $^{115}\text{In}$  was typically  $60\,000 - 120\,000 \text{ counts s}^{-1} \text{ ng}^{-1} \text{ ml}$  with a relative standard deviation of less than 1.5 %. The  $^{140}\text{Ce}^{16}\text{O}^+ / ^{140}\text{Ce}^+$  ratio did not exceed 0.02. When the instrument was taken into collision cell mode (*i.e.* the cell pressurised), a minimum of 30 min was allowed for the gas lines to flush out before experimental work continued. The tune solution was prepared in 2 % nitric acid from  $10 \text{ } \mu\text{g ml}^{-1}$  Ba, Be, Ce, Co, In, Li, Mg, Pb, Rh, Tl, U and Y multi-element standard solution (CLMS-Tune-1, SPEX CertiPrep, Metuchen, NJ, USA), 'Aristar'-grade 70 % nitric acid (Fisher Scientific, Loughborough, Leicestershire) and  $18 \text{ M}\Omega \text{ cm}^{-1}$  de-ionised water (Barnstead, Dubuque, IA, USA).

## 3.2 Experimental

### 3.2.1 Preliminary Work – Si in a Water Matrix

In order to minimise possible contamination, a VG PQ ExCell instrument located in a class 10 000 clean room at Thermo Electron, Winsford Cheshire was used. The instrument was equipped with a polyamide nebuliser, plastic spray chamber, plastic elbow (linking the spray chamber to the torch) and a standard silica torch.

Standard solutions were prepared in acid washed polyethylene bottles using appropriate autopipettes with acid washed tips and a top pan balance located in a positive pressure cabinet within the clean room. The matrix used was  $18 \text{ M}\Omega \text{ cm}^{-1}$  deionised water (Barnstead). No acid was added to the system to minimise possible sources of contamination and to avoid adding N to the system.  $1.0, 2.0$  and  $5.0 \text{ ng g}^{-1}$  Si standards were prepared in water from  $10\,000 \text{ } \mu\text{g ml}^{-1}$  Si in water (SPEX CertiPrep, Metuchen, NJ, USA).  $0.5, 1.0, 2.0, 5.0$  and  $10.0 \text{ ng g}^{-1}$  B, Ge, Mo, Nb, P, Re, S, Si, Ta, Ti, W and Zr were prepared in water from a  $10 \text{ } \mu\text{g ml}^{-1}$  standard (CLMS-4, SPEX CertiPrep)

In standard mode, the torch position and lenses were tuned to optimise the  $^{24}\text{Mg}$  signal. Hydrogen (from a hydrogen generator) and helium were then introduced. The lens parameters were changed as listed in Table 3.1. No further retuning was conducted, either on introduction of gas or changing of flow rates.

In order to identify the optimum collision cell gas flow rates, a deionised water blank and the  $1.0 \text{ ng g}^{-1}$  Si in water standard were run at a range of helium+hydrogen flow rates from  $1.0+2.0$  to  $1.0+4.0$  and from  $3.0+1.0$  to  $9.0+1.0 \text{ ml min}^{-1}$ . Details of the data acquisition parameters are given in Table 3.1.

The single and multi-element standards were then run at the optimum flow rate identified. To investigate the stability of the Si standards, a trace (100  $\mu\text{l}$  of approx. 10 % acid) of hydrofluoric acid was added to the standards (*circa* 0.01 % HF) and the determination repeated. Acquisition parameters for these experiments are detailed in Table 3.1.

**Table 3.1 – Instrumental parameters used for Si experiments**

Peltier temperature/ $^{\circ}\text{C}$	3	
RF power/W	1350	
<i>Ion optics: -</i>	Varied to maximise $^{24}\text{Mg}$ signal (in standard mode)	
	<b>Standard mode</b>	<b>Collision cell mode</b>
Focus lens/V	<i>ca.</i> +20	+16
Quadrupole bias setting/V	<i>ca.</i> +1	-9
Hexapole bias setting/V	<i>ca.</i> -2	<i>ca.</i> +4
<i>Acquisition parameters: -</i>		
	<b>Gas flow optimisation</b>	<b>Standards</b>
No. of scans	50	100
Channels per mass	3	1
Dwell time/ms	10	30
No. of repeats	3	5 (standards), 10 (blanks)
<i>m/z</i> measured	28–34, 36	28–34, 36

### 3.2.2 *Si in an Aqueous Fluoroboric-boric Acids Matrix*

Experiments were conducted on a VG PQ ExCell located in a general-purpose laboratory. The instrument was equipped with a Teflon Burgener nebuliser, plastic spray chamber and elbow (linking the spray chamber and torch injector) and a standard torch with silica injector.

0, 0.5, 1.0, 2.0 and 5.0 ng g<sup>-1</sup> Si standards were prepared in a fluoroboric-boric acids matrix (28 mg dm<sup>-3</sup> H<sub>3</sub>BO<sub>3</sub> and 17 mg dm<sup>-3</sup> HF) using 10 000 µg ml<sup>-1</sup> Si (Aldrich, Gillingham, Dorset), 48 % hydrofluoric acid, boric acid (both CertiFied grade, Fisher Scientific) and 18 MΩ cm<sup>-1</sup> deionised water (Barnstead). 0, 0.5, 1.0 and 2.0 ng g<sup>-1</sup> multi-element standards were also prepared in the same matrix (using the CLMS-4 standard described in Section 3.2.1 above. The standards were prepared and stored in nitric acid washed polypropylene bottles (Nalgene, Rochester, NY, USA). No glass was used in the preparation of the standards.

The VG PQ ExCell instrument was prepared as described in Section 3.1. Helium and hydrogen were used at flow rates of 1.0 and 2.0 ml min<sup>-1</sup> respectively. The quadrupole, hexapole and focus settings and 'standards' acquisition parameters listed in Table 3.1 were employed, except that *m/z* were as detailed below. 2 min uptake time was allowed per sample and 1 min for washout with deionised water between samples.

The Si and multi-element standards were run under these conditions over a period of three consecutive days. (The multi-element standards were only considered on days one and two.) On day one, the day the samples were prepared, data was collected at *m/z* 28, 92 and 94. Data was collected at *m/z* 28 only on days two and three.

In a separate experiment, the torch box was flushed with argon (99.998 %, BOC), which was supplied independently of the ICP system *via* a suitable multistage regulator and 0.125 inch o.d. polyethylene tubing. The end of the tubing was initially located parallel to and approximately 4 cm below the torch, with the ends of the torch and tube in line with each other. The torch was lit and torch position and lenses optimised, as in Section 3.1, prior to introduction of the flush gas. Helium+hydrogen 2.0+1.0 ml min<sup>-1</sup>



was used in the collision cell throughout. The effect of the gas flow on the signal for deionised water at  $m/z$  28 was considered. Gas was introduced at regulator pressures of 1 and 2 bar. The tube was withdrawn to a position approximately 10 cm behind the front of the torch whilst Ar continued to be introduced at a pressure of 1 bar.

A 100  $\mu\text{m}$  filter was connected to the front of the gas line, held in place in a ground glass butt joint in a length of 10 mm i.d. glass tubing. The outlet of the gas line was located below the end of the torch with the same orientation as described above. Argon was introduced at pressures of 0.5, 1.0, 1.5 and 2.0 bar and the signal for deionised water at  $m/z$  28 monitored

Further work was conducted on a VG PQ ExCell instrument located in the class 10 000 clean room at Thermo Electron. The instrument was equipped with a polyamide concentric nebuliser, plastic spray chamber and elbow and a demountable torch with a sapphire injector. Si and multi-element solutions in a fluoroboric-boric acids matrix were prepared as above in a class 100 clean area and made up to mass on a top pan balance in a positive pressure cabinet in the clean room. The instrument was tuned as in Table 3.1, with 1.0  $\text{ml min}^{-1}$  helium and 2.0  $\text{ml min}^{-1}$  hydrogen in the cell. Data was collected for  $m/z$  28 and 182 for deionised water and the prepared standards with the 'standards' acquisition parameters shown in Table 3.1. This determination was repeated with data collected at  $m/z$  24 in addition to  $m/z$  28 and 182.

### 3.3 Results and Discussion

#### 3.3.1 Preliminary Work – Si in a Water Matrix

To determine the optimum gas flows from the Si standard and blank data collected, background equivalent concentrations (BECs) and theoretical detection limits (DLs) were calculated. DLs were calculated using the method described by Ingle *et al.*<sup>35</sup> The detection limit was defined as the point at which  $S/N = 3$ . DLs were calculated using Equations 3.1 and 3.2.

The analyte signal ( $N_S$ ) at the detection limit was calculated using Equation 3.1, using the measured background signal ( $N_B$ ),  $S/N$  of 3 (by definition) and the flicker factor values

calculated by Ingle *et al.*<sup>35</sup> i.e.  $f = 0.014$  and  $p = 0.024$ . The DL was then calculated using Equation 3.2 using the calculated analyte signal at the detection limit ( $N_S$ ),  $N_B$  and the concentration ( $c$ ) for a measured standard (total signal  $N_T$ )

$$S/N = N_S \frac{1}{\sqrt{N_S + f^2 N_S^2 + 2N_B + 2p^2 N_B^2}}$$

**Equation 3.1**

$$DL = \frac{cN_S}{N_T - N_B}$$

**Equation 3.2**

The calculated DLs and BECs for each gas flow are, together with the background count and analyte sensitivity, shown in Table 3.2.

**Table 3.2 – Background signal, analyte sensitivity, theoretical detection limits (DLs) and background equivalent concentrations (BECs) for Si at m/z 28 with varying helium and hydrogen flows.**

Helium flow /ml min <sup>-1</sup>	Hydrogen flow /ml min <sup>-1</sup>	Background /10 <sup>3</sup> counts s <sup>-1</sup>	Si sensitivity /10 <sup>3</sup> counts s <sup>-1</sup> ng <sup>-1</sup> g	DL /ng g <sup>-1</sup>	BEC /ng g <sup>-1</sup>
1.0	1.5	325	51	0.46	6.32
1.0	1.7	334	52	0.46	4.34
1.0	2.0	72	16	0.32	4.34
1.0	2.5	36	3	1.04	14.11
1.0	3.0	57	7	0.59	8.05
1.0	4.0	31	0.4	6.04	81.54
1.5	1.0	73	5	1.14	15.67
3.0	1.0	35	4	0.71	9.53
4.5	1.0	18	1	1.15	15.19
6.0	1.0	11	0.03	23.56	301.57
7.5	1.0	7	*	*	*
9.0	1.0	4	*	*	*

\* – signal for blank higher than for the standard

The DLs shown in Table 3.2 show a clear minimum at helium+hydrogen gas flows of  $1.0+2.0 \text{ ml min}^{-1}$ , the BEC is also at a minimum at these gas flows. This is consistent with the optimum identified by Lawrence.<sup>145</sup> It is important to note that the optimum BEC does not coincide with the lowest background, as the Si sensitivity falls faster than the background at high gas flows.

In order to check for contamination in the fashion described in Section 2.2.1 above, the background signal at  $m/z$  28 as helium flow increases was plotted on a semi-logarithmic scale against the helium flow. This graph is shown in Figure 3.1.

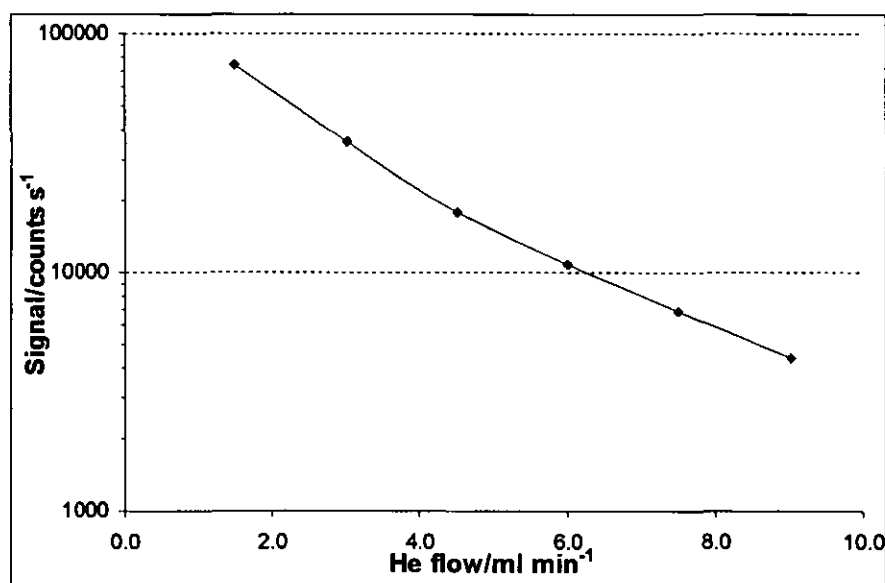


**Figure 3.1** – Semilogarithmic graph of counts at  $m/z$  28 for deionised water against helium flow. (Hydrogen flow  $1.0 \text{ ml min}^{-1}$ )

The pattern shown in Figure 3.1 is difficult to interpret. Unlike the extreme examples shown in Figure 2.4 (p35) and discussed in Section 2.2.1, the points fall along a very gentle curve. A straight line would indicate the absence of contamination at this mass, two distinct regions, as shown in Figure 2.4(ii), would indicate the presence of contamination. The gentle curve suggests that Si contamination is present, but at a very low level. Due to the ubiquity of Si in nature and the use of a standard ICP torch with a silica injector, the presence of Si contamination was expected, despite the experiment being undertaken in a clean room. If the range of gas flows considered was extended to

higher levels, a plateau may be reached in the curve, confirming the presence of Si contamination. This theory cannot be tested as the mass flow controllers employed in the instrument to deliver collision cell gases at flow rates in the range 0.1 – 10.0 ml min<sup>-1</sup>.

The data collected for the range of Si standards in water with helium+hydrogen 1.0+2.0 ml min<sup>-1</sup> in the cell is shown in Figure 3.2. Data for repeat readings for a sample of semiconductor grade water are also presented.

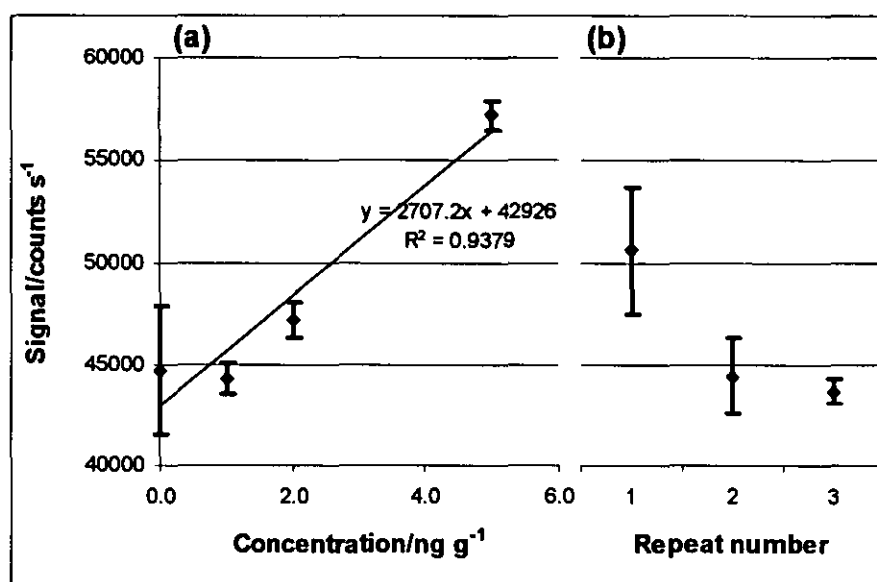


**Figure 3.2 – Determination of Si in water at m/z 28: (a) calibration curve and (b) repeat readings of a sample of semiconductor grade water. (1s error bars shown)**

The calibration curve for Si in water (Figure 3.2(a)) shows that the determination of <sup>28</sup>Si with helium+hydrogen 1.0+2.0 ml min<sup>-1</sup> in the collision cell is possible. There is a moderate degree of linearity,  $R^2 = 0.94$ , and a reasonable sensitivity of 2700 counts s<sup>-1</sup> ng<sup>-1</sup> ml. This is less than one sixth of the value shown in Table 3.2. This variation is somewhat in excess of the variations expected due to day-to-day variations in instrumental sensitivity and may be an indication of sample instability. The poor precision in the blank was a cause for some concern. This and the sample instability are discussed below.

The range of multi-element standards were also run at this time, although regrettably the data collected was subsequently erroneously deleted. No linearity could be observed for

$^{28}\text{Si}$  in the standards. Although they were run in order of increasing concentration to minimise the influence of any memory effects, the  $0.5 \text{ ng g}^{-1}$  standard gave the highest signal with each subsequent standard giving a lower signal. This suggests that Si was sorbing to some part of the sample introduction system leading to a greatly increased washout time (usually described as 'memory' effects).

Repeat readings at  $m/z$  28 for a deionised water blank (Figure 3.2(b)) suggest that the effects discussed above were due to an exceptionally long washout time of several minutes in length. The three results shown were collected at four-minute intervals, commencing 4 min after the  $10 \text{ ng g}^{-1}$  multi-element standard. The high standard deviation of the signals and the elevated count rate of the initial runs suggest that the level of Si detected was gradually falling. Similarity between the second of these readings and the water blank used with the Si-only standards (Figure 3.2(a)) suggests that a similar problem was experienced there. The lower standard deviation of the third reading suggests that a stable background position had been reached. This would suggest a washout time of 10–12 minutes.

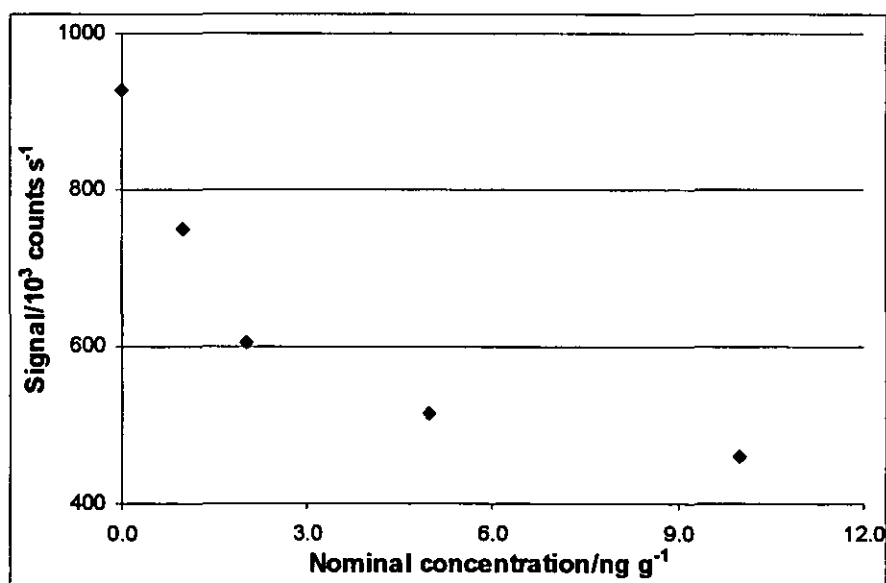


**Figure 3.3** – Signal recorded at  $m/z$  28 for a range of Si standards in water with a trace of hydrofluoric acid. The samples were run in order of increasing concentration.

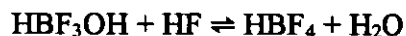
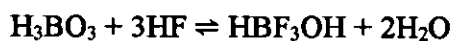
Results at  $m/z$  28 for the Si-only standards with trace HF added are shown in Figure 3.3. HF was added to the solutions to try to stabilise Si in the solutions as  $\text{SiF}_4(\text{aq})$  and

thereby prevent Si depositing within the sample introduction system and causing the long washout times observed above. The count levels observed for the standards in trace HF were considerably higher than for deionised water, due to hydrofluoric acid stripping Si from the sample introduction system and torch. As the range of standards was run, the signal rapidly decreased, suggesting that the Si deposited in the sample introduction system from the earlier standards was being washed out. The 430 000 counts s<sup>-1</sup> plateau reached is ten times higher than the backgrounds recorded earlier in the day, suggesting that the hydrofluoric acid was also stripping Si from the injector of the ICP torch.

These results suggest that the determination of Si at <sup>28</sup>Si by ICP-CC-MS using a mixture of helium and hydrogen is possible at concentrations as low as 0.32 ng g<sup>-1</sup>. Considerable difficulty was experienced due to the instability of the Si standards, so the identification of a suitable sample chemistry to stabilise the samples is necessary. The use of a silica free sample introduction system is necessary when hydrofluoric acid is present in the samples.

As demonstrated by the results discussed above, it is difficult to prepare stable Si standards in aqueous media. In aqueous media, Si leaves solution and sorbs to the container. The conventional solvent for Si solutions is dilute or trace hydrofluoric acid as this forms stable silicon fluoride complexes. Unfortunately, hydrofluoric acid has such an affinity for Si that it strips Si from silica, even in the short period spent in the sample introduction system. This necessitates the use of a sample introduction system where the sample does not have contact with silica, with plastic nebulisers and spray chambers and a torch with a platinum or alumina injector. The hazardous nature of hydrofluoric acid also discourages its use.

One possible means of producing stable Si solutions is to use fluoroboric acid to produce stable Si complexes.<sup>147,148</sup> This matrix has two advantages over hydrofluoric acid, firstly it does not strip Si from silica and the need for a total absence of silica from the sample introduction system is reduced, and secondly, the matrix does not have significant health hazards associated with it. Fluoroboric acid is produced by equilibrium reactions between boric acid and hydrofluoric acid.<sup>147</sup>



### Equation 3.3

Unfortunately, in a stoichiometric solution, the position of these equilibria lies to the left, requiring a considerable excess of boric acid in order to neutralise the fluoride ions and prevent the hydrolysis of fluoroboric acid.<sup>147</sup> The matrix is thus correctly described as fluoroboric-boric acids.

Bernas<sup>147</sup> showed that a 119 % excess of free boric acid is adequate to ensure the stability of Si standards. The matrix, used for silicon standards in the range 100–200 µg ml<sup>-1</sup> Si for determination by flame atomic absorption spectrometry, comprised 2.80 % (*m/v*) boric acid and 1.44 % hydrofluoric acid. That is, 0.207 mol dm<sup>-3</sup> fluoroboric acid with 0.246 mol dm<sup>-3</sup> free boric acid. As this represents ~ 5 mg ml<sup>-1</sup> boron, it is unsuitable for use in ICP-MS as memory effects have been observed for boron. High levels of dissolved solids can cause rapid deterioration of sample cones and can also cause nebulisers to become blocked.

The level of Si determined by ICP-MS in this study was much lower than that reported by Bernas<sup>147</sup> with atomic absorption spectroscopy; 0.5–5 ng g<sup>-1</sup> in this study compared with 100–200 µg ml<sup>-1</sup> in Bernas' study – a reduction of around 60 000 fold. The level of the fluoroboric-boric acids matrix could therefore also be reduced. To ensure an ample excess of fluoroboric-boric acids to stabilise Si, only a 1000 fold reduction in the level of the matrix was selected (*i.e.* produced from 28 mg dm<sup>-3</sup> boric acid and 17 mg dm<sup>-3</sup> hydrofluoric acid). This level of matrix represents approximately 5 µg ml<sup>-1</sup> boron, sufficiently low to prevent the problems associated with high levels of solid from occurring. The use of this matrix is explored in below.

### 3.3.2 *Si in an Aqueous Fluoroboric-boric Acids Matrix*

Results collected for the range of Si only and multi-element standards in the fluoroboric-boric acids matrix over three consecutive days are shown in Figures 3.4, 3.5 and 3.6

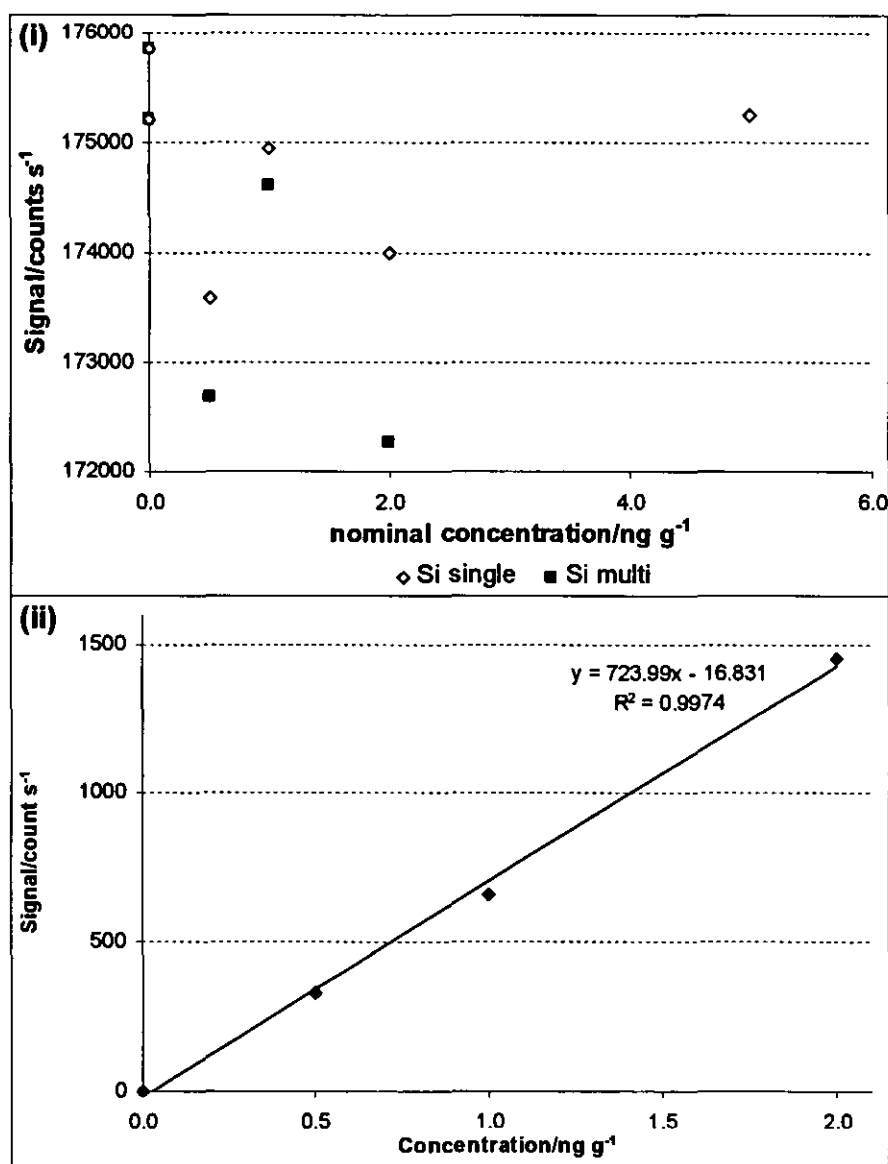
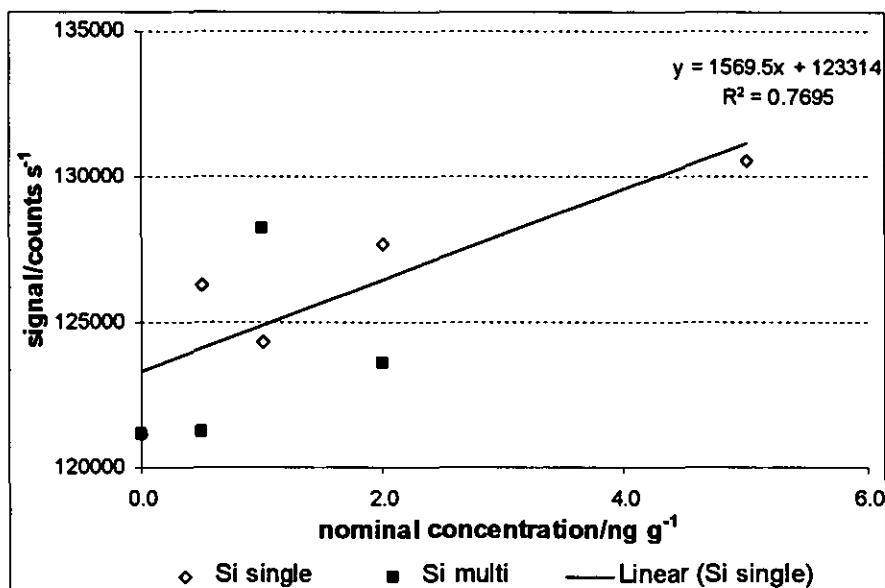
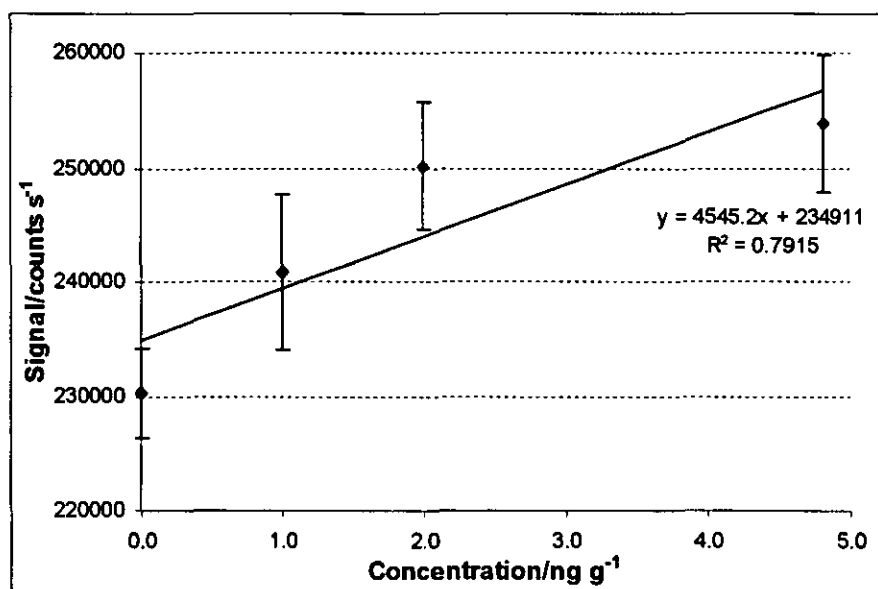


Figure 3.4 – Day one: calibration curves for (i) Si at m/z 28 and (ii) Zr at m/z 92





*Figure 3.5 – Day two: calibration curve for Si at m/z 28*



*Figure 3.6 – Day three: calibration curve for Si at m/z 28 (1s error bars shown)*

On initial examination, the results for Si using the fluoroboric-boric acids are not promising. Figure 3.4(i) shows no correlation for Si, overall or within either range of standards and the correlations shown in Figures 3.5 and 3.6 are poor.

Figure 3.4(ii) shows a good, linear correlation for the Zr in the multi-element standards, with  $R^2 > 0.99$ . This confirms that the multi-element standards were correctly prepared

from the CLMS-4 standard solution and that good calibrations could be achieved at  $m/z$  where no interference was present and the collision cell was pressurised.

The level of background at  $m/z$  28 on day one (Figure 3.4(i)) was at least 170 000 counts  $s^{-1}$ , many times higher than that observed under the same helium+hydrogen conditions for deionised water (for example 45 000 counts  $s^{-1}$  in Figure 3.2). Two possible sources of the high background levels were Si contamination in the reagents and elevated levels of entrained nitrogen at the plasma-sample cone interface. The high background observed at  $m/z$  28 may have been responsible for the lack of correlation between the Si concentration and signal at  $m/z$  28. The noise in the elevated background signal may have masked the analyte signals.

When the analysis was repeated on day two (Figure 3.5), the background at  $m/z$  28 had decreased to around 122 000 counts  $s^{-1}$  and some correlation was observed between the signal at  $m/z$  28 and the Si concentration. The correlation observed for Si was still poor;  $R^2 = 0.77$  for the Si only standards and poorer for the multi-element standards. The improvement in the analysis may well have been the result of the reduced background levels. The reduced noise of the lower background signal allowed the analytical signal to be observed. The reduction in background levels is difficult to explain, the samples were the same as those prepared and studied on day one, the cones, torch and sample introduction system had not been cleaned or replaced and the instrument had not been used for other work during the intervening period. A sample of the deionised water used in the preparation of the fluoroboric-boric acids matrix was also run on day two. This gave a signal of 112 000 counts  $s^{-1}$  at  $m/z$  28, just 10 000 counts  $s^{-1}$  lower than the signal observed for the fluoroboric-boric acids blank, so the high background cannot be attributed to contamination of the hydrofluoric acid or boric acid reagents used.

On day three, Figure 3.6 shows that both the correlation and sensitivity observed for the Si standards had increased, despite the background having increased to 230 000 counts  $s^{-1}$ . If the 5 ng  $g^{-1}$  standard was treated as an outlier and excluded from the calibration curve,  $R^2$  increased from 0.792 to 0.999 and sensitivity doubled from 4500 counts  $s^{-1}$  ng $^{-1}$  g to 10 000 counts  $s^{-1}$  ng $^{-1}$  g. Thus, provided stability of the background could be achieved or the background attenuated, the determination of Si at

ng g<sup>-1</sup> levels is possible at  $m/z$  28 by ICP-CC-MS. The linearity achieved for the standards two days after they were prepared shows that Si is adequately stable in the fluoroboric-boric acids matrix.

A further method of reducing the interference at  $m/z$  28 was explored. The major interference at that  $m/z$  is  $^{14}\text{N}_2^+$ . Air entrained with the plasma can be expected to contribute a significant part of the nitrogen that is ionised to form  $\text{N}_2^+$ . A range of experiments was conducted to try to flush the torch box with argon and thereby remove air from the torch environs. The results of these experiments are shown in Table 3.3.

**Table 3.3 – Summarised results of torch box argon flushing experiments. Counts recorded are for deionised water at  $m/z$  28.**

Location of tube outlet	Filter in tube?	argon pressure/bar	Signal /counts s <sup>-1</sup>	Comments
Below end of torch	No	1.0	460 000	
Below end of torch	No	2.0	290 000	Plasma unstable
10 cm behind torch	No	2.0	400 000	
Below end of torch	Yes	0.0	250 000	
Below end of torch	Yes	0.5	250 000	
Below end of torch	Yes	1.0	250 000	
Below end of torch	Yes	1.5	250 000	
Below end of torch	Yes	2.0	250 000	Plasma unstable

Initially, argon was introduced *via* the unobstructed tube located beneath the end of the ICP torch. When the pressure of argon introduced to the torch box increased from 1.0 to 2.0 bar, the signal at  $m/z$  28 for de-ionised water decreased to three-quarters of its initial level. Thus, a considerable proportion of the  $^{14}\text{N}_2^+$  interference observed originated in the air entrained by the plasma. With the gas introduced at 2.0 bar, the steady flow of air to one side of the plasma destabilised it, causing the plasma to flicker and the central channel to drift around the sample cone.

The large size of the torch box (approximately 200 dm<sup>3</sup>) and the extraction system and supplementary fans used to remove the heat generated by the plasma prevent the displacement of sufficient air from the area surrounding the plasma for an argon line located away from the plasma to have any effect on the signal at  $m/z$  28. Similarly, when a filter was introduced to the gas line to disperse the gas jet and minimise disturbance to the plasma, no noticeable effect was observed on the  $m/z$  28 signal even when the flow was high enough to destabilise the plasma.

It is clear that, although the use of a flush gas will reduce the background, modifications are necessary to the region surrounding the ICP torch to evenly distribute the gas around the torch, preventing the plasma from disturbing the gas before the technique can be analytically useful. Such modifications could take the form of a torch bonnet with axial symmetry, to which gas is introduced tangentially to provide a laminar flow enveloping the plasma with an evenly distributed flow of gas. An illustration of one possible torch bonnet system conforming to these ideas is given in Figure 3.7. This design could not be tested as the necessary engineering support was not available to produce the system or to modify the torch box to provide suitable space for the bonnet.

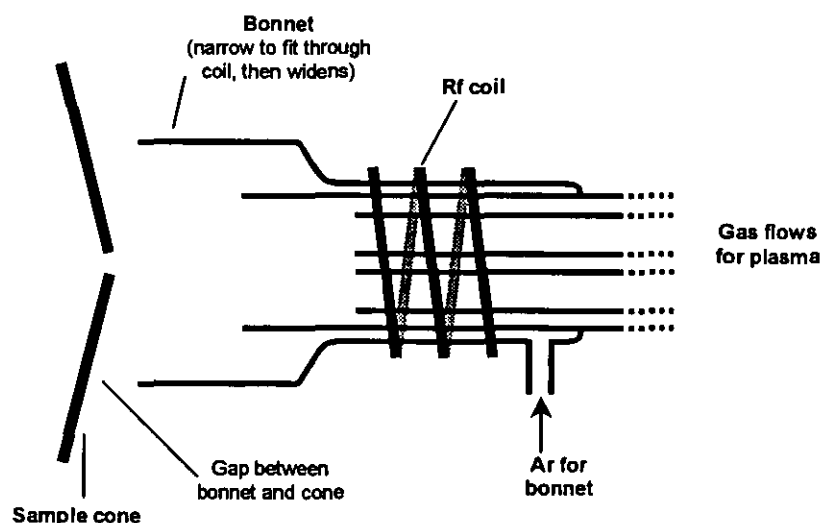


**Figure 3.7** – *Illustration of a design for a torch bonnet system to envelop the plasma in an argon atmosphere (axial projection)*

The high backgrounds observed at  $m/z$  28 may have been caused by contamination. To investigate this, a range of Si standards were prepared in a class 10 000 clean room and

data collected on an instrument in the same clean room. The results of this determination are shown in Figure 3.8.

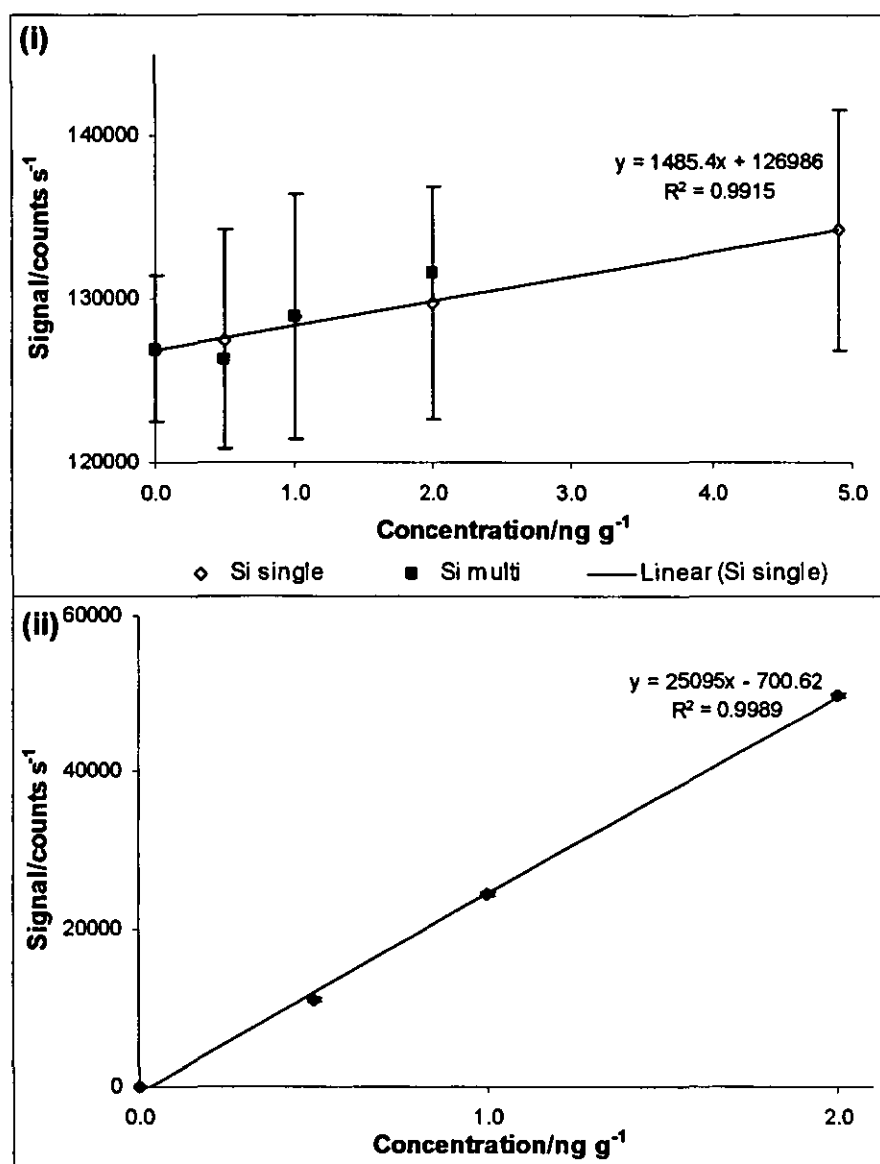


**Figure 3.8** – Calibration curves for (i) Si at m/z 28 and (ii) W at m/z 182. Data was collected at m/z 28 and 182 only. (1s error bars shown)

High backgrounds similar to those observed on the instrument in the general-purpose laboratory were observed at  $m/z$  28 on the instrument located in the clean room. The results shown in Figure 3.8(i) show that the background was over 125 000 counts s<sup>-1</sup>. The correlation of the standards was very good,  $R^2 > 0.99$ , with the signals for the multi-element standards at the same concentrations falling close to the curve, well within the

error. The noise in the signal was, however very high, due to the high backgrounds. By contrast, the calibration curve for W in the multi-element samples, where very good linearity was achieved ( $R^2 = 0.999$ ) together with much higher precision. (1s error bars for W fall within the area of the data point at the scale used for Figure 3.8(ii).

On each peak-jumping sweep, the first (lowest)  $m/z$  studied can have poorer precision due to poor alignment of the quadrupole potentials after their return from the values used at higher  $m/z$ . As 28 was the lowest  $m/z$  studied for the data above, some of the noise in that data may be due to poor quadrupole settle. To remove the influence of quadrupole settling, the experiment was modified to include data collection at  $m/z$  24, so that any error due to quadrupole settling would occur there and not at  $m/z$  28. The results of this analysis are shown in Figure 3.9. Inclusion of this additional  $m/z$  noticeably reduces the noise at  $m/z$  28, although it is still much higher than the noise observed for uninterfered  $m/z$ .

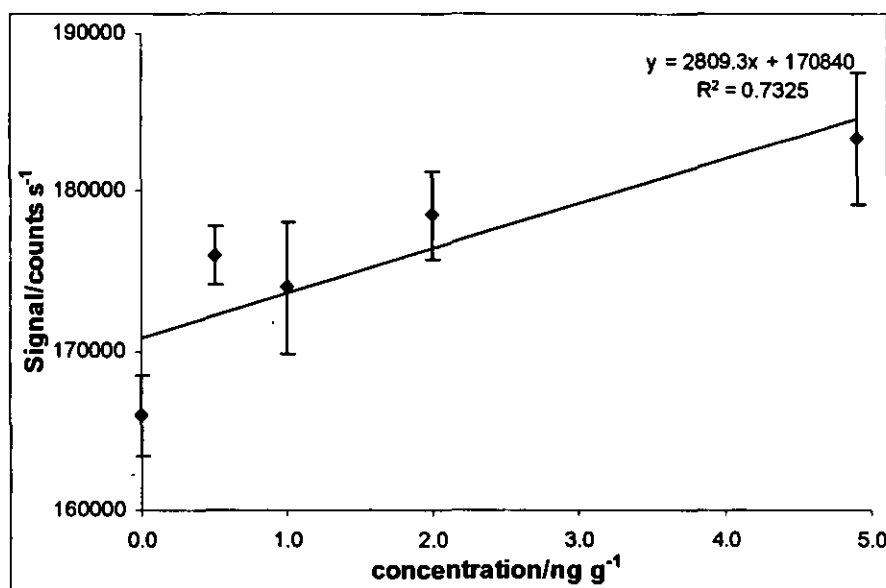


**Figure 3.9** – Calibration curve for Si at  $m/z$  28. Data was collected at  $m/z$  24, 28 and 182. (1s error bars shown)

### 3.4 Summary

A method for the determination of Si by ICP-CC-MS has been identified. A mixture of 1 part helium and 2 parts hydrogen (1.0 and 2.0 ml min<sup>-1</sup> respectively in the VG PQ ExCell) was identified as the optimum collision cell gas to determine Si at its major

isotope,  $^{28}\text{Si}$ . A fluoroboric-boric acids sample matrix was identified to stabilise the Si standards.

For reasons as yet unexplained, the background at  $m/z$  28 became greatly elevated, on two different instruments, compared to the levels observed during earlier work. Further work is necessary to identify the cause of these elevated backgrounds and restore backgrounds to the levels initially observed. Engineering input is necessary to solve these difficulties.

It was shown that the background at  $m/z$  28 could be reduced by use of an argon atmosphere around the plasma torch to minimise air entrainment as a source of  $^{14}\text{N}_2^+$ . A possible means of introducing this gas and maintaining a stable plasma was presented, although some remodelling of the torch box is necessary before this design can be tested.

## **Chapter Four**

# **The Role of Water in the Collision Cell Gas**



#### ***4.0 The Role of Water in the Collision Cell Gas***

The use of 'damp' helium to attenuate argon-based interferences such as  $\text{ArO}^+$  and  $\text{Ar}_2^+$  to facilitate the determination of analytes with which these polyatomic ions interfered was discussed in Section 2.3.2.1. It was clear from this work that the presence of water in the collision cell had a significant effect on the chemistry occurring in a helium filled collision cell. Previous studies have not considered the contribution of water in the collision cell to the formation of polyatomic ions or the contribution of differing levels of water in the collision cell to variations in background levels and analyte sensitivity. This chapter reports the results of experiments to investigate the origin of protons in proton-containing interference ions and the effect of water on background ion levels and analyte sensitivity when a reactive helium/hydrogen collision cell gas was employed.

#### ***4.1 Thermodynamics***

To investigate the likelihood of reactions with water and with helium to remove argon-based ions, the database of ion-molecule reactions (with thermal reaction enthalpies and rate constants where available) discussed in Section 2.2.2 was interrogated for reactions between  $\text{Ar}_2^+$ ,  $\text{ArO}^+$  or  $\text{Ar}^+$  with water or helium and a reaction enthalpy of +1 eV or less. The extract of the database produced is shown in Table 4.1.

**Table 4.1 – Reactions between selected argon-based ions and helium or water with  $\Delta H_r \leq +1$  eV**

Reaction	$\Delta H_r^\dagger$ /eV	$k^\ddagger$ /mol <sup>-1</sup> cm <sup>3</sup> s <sup>-1</sup>	Product distribution
$\text{Ar}_2^+ + \text{He} \rightarrow \text{no reactions listed}$	-	-	-
$\text{Ar}_2^+ + \text{H}_2\text{O} \rightarrow \text{H}_2\text{O}^+ + \text{Ar}_2$	-2.0	-	-
$\text{Ar}_2^+ + \text{H}_2\text{O} \rightarrow \text{H}_2\text{O}^+ + 2\text{Ar}$	-2.0	-	-
$\text{Ar}_2^+ + \text{H}_2\text{O} \rightarrow \text{H}_2\text{O} + \text{Ar}^+ + \text{Ar}$	-1.9	-	-
$\text{Ar}_2^+ + \text{H}_2\text{O} \rightarrow \text{ArH}^+ + \text{Ar} + \text{OH}$	+0.4	-	-
$\text{ArO}^+ + \text{He} \rightarrow \text{He} + \text{Ar} + \text{O}^+$	+0.7	-	-
$\text{ArO}^+ + \text{He} \rightarrow \text{HeAr} + \text{O}^+$	+0.7	-	-
$\text{ArO}^+ + \text{H}_2\text{O} \rightarrow \text{H}_2\text{O}^+ + \text{O} + \text{Ar}$	-0.3	-	-
$\text{ArO}^+ + \text{H}_2\text{O} \rightarrow \text{H}_2\text{O} + \text{O}^+ + \text{Ar}$	+0.7	-	-
$\text{ArO}^+ + \text{H}_2\text{O} \rightarrow \text{OH}^+ + \text{OH} + \text{Ar}$	+0.8	-	-
$\text{Ar}^+ + \text{He} \rightarrow \text{ArHe}^+$	0.0	-	-
$\text{Ar}^+ + \text{H}_2\text{O} \rightarrow \text{H}_2\text{O}^+ + \text{Ar}$	-3.2	$1.62 \times 10^{-9}$	0.80
$\text{Ar}^+ + \text{H}_2\text{O} \rightarrow \text{OH} + \text{ArH}^+$	-0.8	$1.62 \times 10^{-9}$	0.20

<sup>†</sup> Calculated from data in Lias *et al.*<sup>49</sup>

<sup>‡</sup> Data from Anicich<sup>52</sup>

A maximum enthalpy of +1 eV was selected as data in Baranov and Tanner<sup>44</sup> and other experimental work (for example, that reported in Chapter Five) suggested that reactions with enthalpies over +1 eV were unlikely to be observed. Consideration of the reaction enthalpies listed in Table 4.1 reveals that of the four reactions with helium, none are exothermic although one is thermoneutral whereas six of the nine reactions with water are exothermic. Water thus appears considerably more reactive than helium and it can be assumed that any reactive attenuation of these argon-based ions when helium was used alone in the cell was due to reaction with adventitious water and not with helium.

## 4.2 Experimental

The VG PQ ExCell instrument was configured, routinely optimised and used as described in Section 3.1 (from p92). The only nebuliser used was a Meinhard® and hydrogen was supplied by the hydrogen generator. A capped T-piece was inserted into the stainless steel gas line used to supply helium to the instrument to permit the gas to be wetted. The

gas line was coiled (three turns, approximately 12 cm in diameter) between the T-piece and the instrument to ensure the gas was well mixed and thus evenly wetted. Plasma, ion optic and acquisition parameters used are listed in Table 4.2.

*Table 4.2 – Plasma, ion optic and acquisition parameters used.*

Parameter	Value(s)	
<i>ICP torch: -</i>		
RF power/W	1350	
Reflected power/W	< 2	
Gas flows/l min <sup>-1</sup> : Cool	12.6	
Auxiliary	0.85	
Nebuliser	0.95 – 1.00	
<i>Ion optics: -</i>		
	<i>Standard mode</i>	<i>Collision cell mode</i>
Focus/V	ca. +20	+16
Quadrupole bias/V	ca. +1	-6
Hexapole bias/V	-1.96	+3.86
<i>Acquisition parameters: -</i>		
No. of scans	50	
Channels per mass	3	
Dwell time/ms	10	
No. of repeats	3	

To identify the source of proton containing polyatomic interference ions in the collision cell, de-ionised water (18 M $\Omega$  cm<sup>-1</sup>, Barnstead, Dubuque, IA, USA) and deuterium oxide (99.9 at. % D minimum, Goss Scientific Instruments Ltd., Great Baddow, Essex) were introduced to the helium gas line *via* the T-piece, on different days. H<sub>2</sub>O and D<sub>2</sub>O were introduced by soaking folded 3.3 × 3.8 cm pieces of 4-ply tissue paper in either de-ionised water or deuterium oxide and placing these in the side arm of the T-piece. Helium was then introduced to the collision cell at a flow rate of 2.5 ml min<sup>-1</sup>. Data were collected for *m/z* 1–88 and 130–160 inclusive for samples of de-ionised water and deuterium oxide under each of the two gas conditions. These experiments were conducted twice, to ensure reproducibility of results.

To investigate the effect of water in the collision cell gas when a reactive helium/hydrogen mixture was employed, data were collected for 2 % nitric acid and a multi-element standard solution with helium/hydrogen in the collision cell and under the same conditions with the collision cell gas wetted. The standard solution consisted of 20 ng ml<sup>-1</sup> Ag, Al, As, Ba, Be, Bi, Cd, Co, Cr, Cu and Fe and 50 ng ml<sup>-1</sup> B, Ge, Nb, P, Re, S, Si, Ta, Ti, W and Zr in 2 % nitric acid, prepared from multi-element standards (Claritas PPT, SPEX CertiPrep, Metuchen, NJ, USA), 'Aristar'-grade nitric acid (Fisher Scientific, Loughborough, Leicestershire) and de-ionised water. To introduce low levels of water, the helium gas was wetted by the introduction of approximately 1 ml of de-ionised water to the T-piece separated from the gas flow by a 0.275 mm thick PTFE membrane (Goodfellow, Cambridge, Cambridgeshire). Collision cell gas flows of helium+hydrogen 1.0+1.7 ml min<sup>-1</sup> were used. Data were collected at *m/z* 5, 8, 9–11, 13–15, 17–39, 42–121, 123, 127, 130, 132, 134–138, 180–188, 203–209, 220 and 245.

To confirm that this method suitably wetted the helium gas, spectra were collected for de-ionised water with 2.5 ml min<sup>-1</sup> helium and 2.5 ml min<sup>-1</sup> wetted helium. When these spectra were compared, a number of peaks characteristic of the presence of water in the collision cell were apparent for the wetted helium. These peaks included large increases in signal for the species H<sub>2</sub><sup>16</sup>O<sup>+</sup>, H<sub>3</sub><sup>16</sup>O<sup>+</sup> and <sup>40</sup>ArH<sup>+</sup> at *m/z* 18, 19 and 41 respectively. Thus, the helium was confirmed to be wetted.

### 4.3 Results and Discussion

The results of experiments to determine the source of proton containing interference ions are shown in the form of difference plots of (signal for D<sub>2</sub>O case) – (signal for H<sub>2</sub>O case) *versus m/z*. 'Cell' plots show the difference between D<sub>2</sub>O and H<sub>2</sub>O wetted helium with a different series shown for each of the two samples. 'Sample' plots show the difference between D<sub>2</sub>O and H<sub>2</sub>O samples with separate series for each gas condition. These data were for blanks only and so the formation of analyte-based polyatomic ions is not considered.

Data from these experiments were difficult to interpret due to the complex nature of the plots produced. The results expected of an ideal experiment are therefore shown in

Figure 4.1 to aid interpretation of the data. Given the overall quality of the data and the poor experimental control of some variables, most notably the degree of wetting of the cell gas, interpretation of the levels of different ion intensities is not possible. The discussion is therefore limited to the patterns of peaks observed and the presence or absence of new peaks in the spectrum.

Where two peaks take the form  $m/z\ N$  below the axis and  $m/z\ (N + 1)$  above the axis then the polyatomic species  $^N(\text{XH})^+$  or  $^{(N+1)}(\text{XD})^+$  was contributed to by  $\text{H}_2\text{O}$  or  $\text{D}_2\text{O}$  of sample origin in 'sample' plots and cell origin in 'cell' plots. Thus if the proton in a species was of cell origin only, the pattern shown in Figure 4.1(a) can be observed, if it was of sample origin only the pattern shown in Figure 4.1(b) can be observed and if it was of sample or cell origin (*i.e.* both sources contributed to the total signal) the pattern shown in Figure 4.1(c) can be observed.

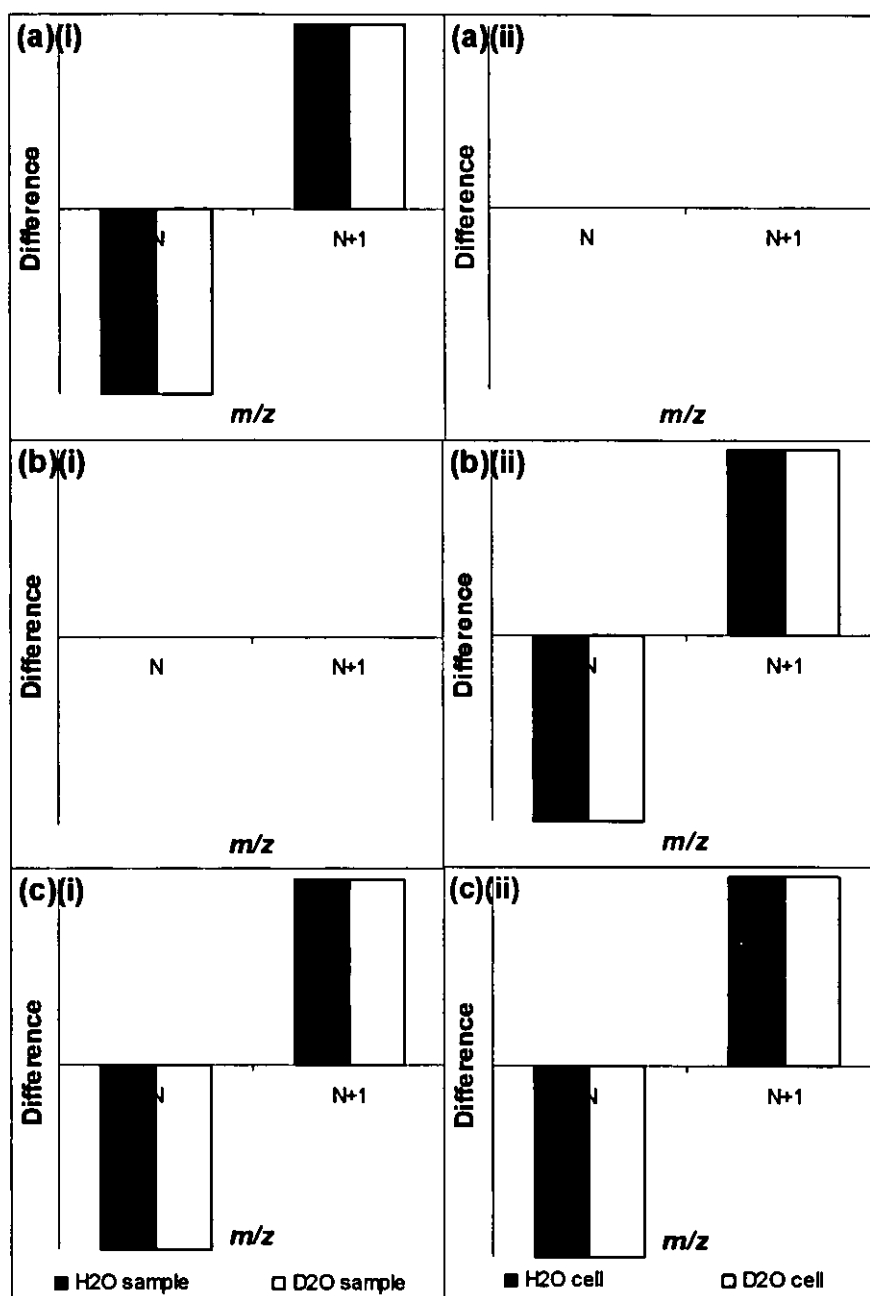


**Figure 4.1** – Expected patterns of peaks for  $XH^+$  on  $D_2O - H_2O$  plots where (a) the proton is from the 'cell' only, (b) the proton is from the 'sample' only and (c) the proton is from the 'cell' or the 'sample'. (i) 'Cell' (for the sample indicated, the difference between the spectra with gas wet with  $D_2O$  and with  $H_2O$ ) and (ii) 'sample' (for the cell gas condition indicated, the difference between the spectrum for a  $D_2O$  sample and for an  $H_2O$  sample).

When a species contained more than one proton, the pattern observed is more complex. For a species  $^N(XH_2)^+$  contributed to by  $H_2O$  or  $D_2O$  for the sample, the expected sequence of peaks on the 'sample' plot would be  $m/z$   $N$  below the axis (due to reduced

$\text{XH}_2^+$  in the  $\text{D}_2\text{O}$  case),  $m/z (N + 1)$  above the axis (due to  $\text{XHD}^+$ ) and  $m/z (N + 2)$  above the axis (due to  $\text{XD}_2^+$ ) i.e. the pattern shown in Figure 4.2.

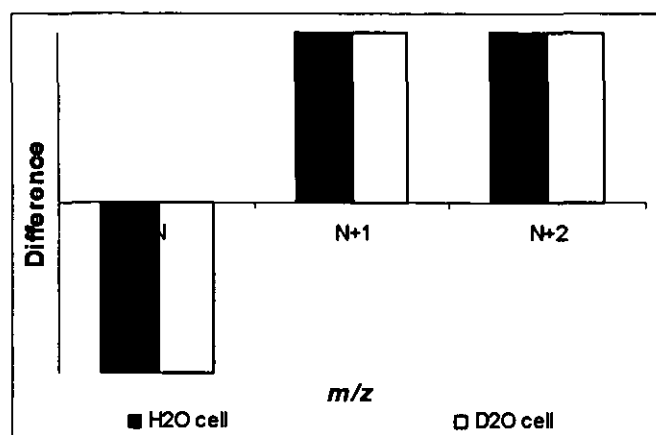


**Figure 4.2** – Expected pattern of peaks for  $\text{XH}_2^+$  on  $\text{D}_2\text{O} - \text{H}_2\text{O}$  'sample' plots where the protons in  $\text{XH}_2^+$  are contributed to by the sample. (Definitions are as in Figure 4.1 caption.)

The two 'cell' conditions were run on two different days and therefore the data from the two days were normalised against the signal due to  $1 \text{ ng ml}^{-1}$  In recorded in the routine daily tuning experiments (described in Section 3.1). As normalisation was relative to variations in analyte signal, variations in the sensitivity due to the detector and lenses were compensated for but differences in the condition of the cones and therefore in air entrainment and secondary discharge were not. As the results are presented as difference plots, these effects will be cancelled out on 'sample' plots as the data used for each of the series were collected on one day. The effects are, however, apparent on the 'cell' plots as each series is based on data from both days and so includes day-to-day variation.

The difference in magnitude of the absolute signals at each  $m/z$  across the mass range was considerable, only the pattern of peaks is important – not their magnitude. The peaks apparent at  $m/z$  16, 32 and 40 in Figure 4.3 were due to small variations ( $< 5\%$ ) in the very large signals recorded for  $\text{O}^+$ ,  $\text{O}_2^+$  and  $\text{Ar}^+$  ions respectively and so are of no importance in this work.

For clarity, results are not shown for all  $m/z$ , only those  $m/z$  where pairs or other patterns of peaks were observed are shown. The results shown are for the second set of

experiments only, except where otherwise noted, these were consistent with earlier results.

Figures 4.3 and 4.4 show, in the manner described above, the results of exchanging  $\text{H}_2\text{O}$  and  $\text{D}_2\text{O}$  for  $m/z$  14–45 and  $m/z$  81–84 respectively.

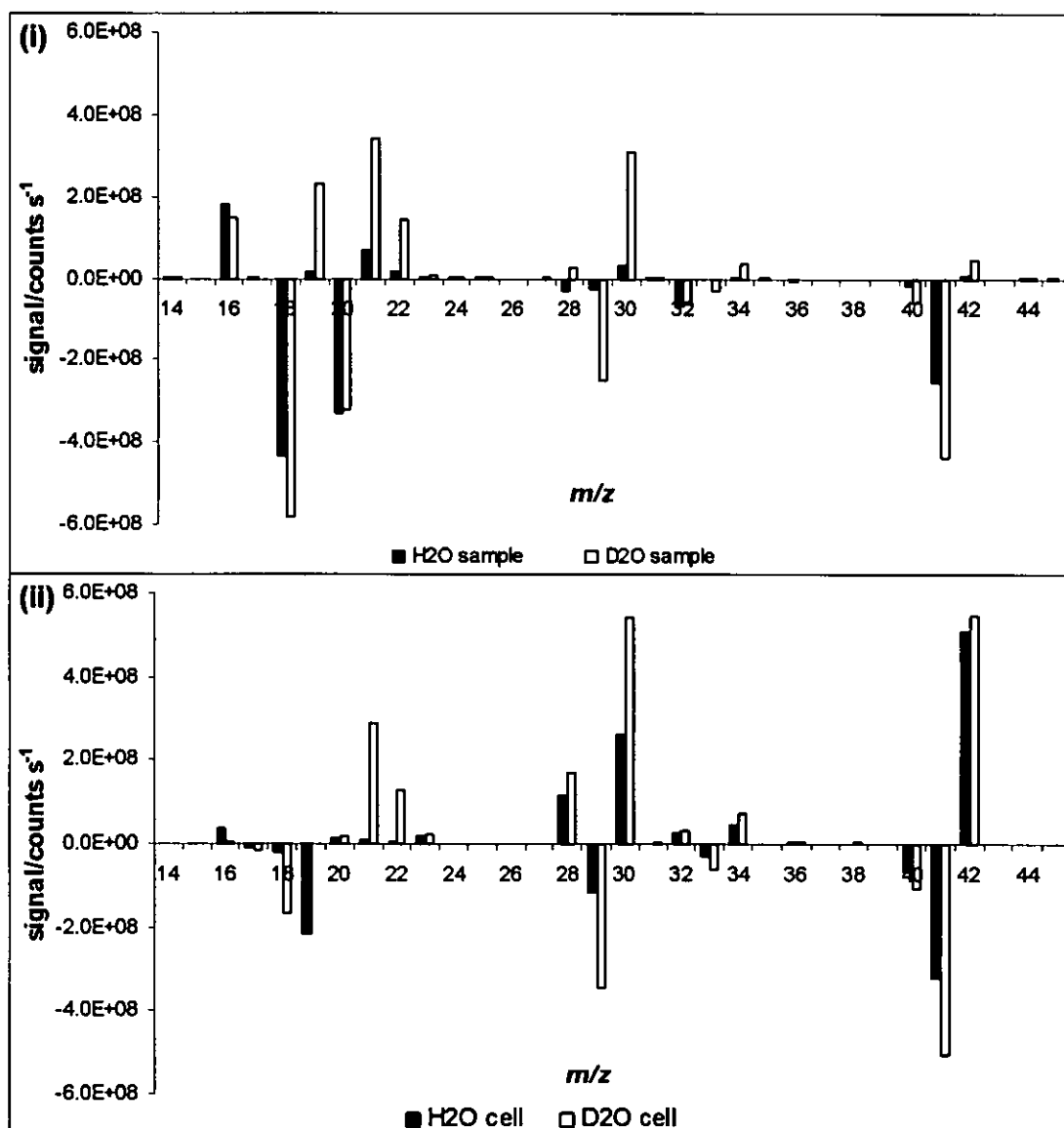


**Figure 4.3** –  $\text{D}_2\text{O}$  –  $\text{H}_2\text{O}$  plots for the  $m/z$  region 14–45. (i) ‘cell’ and (ii) ‘sample’ (definitions as in Figure 4.1 caption).

Examination of Figure 4.3(i) reveals ‘peak pairs’ at  $m/z$  29–30 and 41–42 indicating that monohydride species of  $m/z$  29 and 41 included protons originating from the cell gas. Similarly, Figure 4.3(ii) shows peak pairs at  $m/z$  29–30, 33–34 and 41–42 indicating that



the monohydride species at  $m/z$  33 included protons originating in the sample and that the monohydride species at  $m/z$  29 and 41 were contributed to by 'sample' water as well as 'cell' water. Thus, the species  $^{29}(\text{N}_2\text{H})^+$  and  $^{41}(\text{ArH})^+$  are contributed to by water of both 'sample' and 'cell' water whereas  $^{33}(\text{O}_2\text{H})^+$  is due principally to 'sample' water.

**Table 4.3 – Hydroxy and deuterioxy species in the region  $m/z$  17–22**

$m/z$	Hydroxy species	Deuterioxy species
17	<u><math>\text{OH}^+</math></u>	–
18	<u><math>\text{H}_2\text{O}^+</math></u>	<u><math>\text{OD}^+</math></u>
19	<u><math>\text{H}_3\text{O}^+</math></u>	<u><math>\text{HDO}^+</math></u>
20	–	<u><math>\text{D}_2\text{O}^+</math></u> , <u><math>\text{H}_2\text{DO}^+</math></u> ( $\text{Ar}^{++}$ also)
21	–	<u><math>\text{HD}_2\text{O}^+</math></u>
22	–	<u><math>\text{D}_3\text{O}^+</math></u>

In Figure 4.3, the  $m/z$  17–22 region is complex on both plots. The complexity of this region is due to the isobaric overlap of various hydroxy and deuterioxy species, these are listed in Table 4.3. The peak at  $m/z$  17, due to  $^{17}(\text{OH})^+$ , is below the line on the 'sample' plot (Figure 4.3(i)) and is very small with one line above and one below the axis on the 'cell' plot (Figure 4.3(ii)). The presence of a much larger change in  $^{18}(\text{H}_2\text{O})^+$  levels masks any signals due to the appearance of  $^{18}(\text{OD})^+$ , but given the signal at  $m/z$  17, it can be assumed to be above the line in the 'sample' plot and below the line in the 'cell' plot. Thus,  $^{17}(\text{OH})^+$  contained protons that were predominantly of 'sample' origin.

Two species are listed at  $m/z$  18 in Table 4.3,  $\text{H}_2\text{O}^+$  and  $\text{OD}^+$ , but as discussed above the magnitude of the  $\text{H}_2\text{O}^+$  signal and changes in that signal are sufficiently large that they conceal any signal or change in signal due to  $\text{OD}^+$ . The signal due to  $^{18}(\text{H}_2\text{O})^+$  is below the line on both the 'sample' and 'cell' plots (Figure 4.3). Due to the presence of  $\text{H}_3\text{O}^+$  at  $m/z$  19 and of two deuterated species at  $m/z$  20 it is not possible to conclusively identify peaks above the line due to  $\text{HDO}^+$  or  $\text{D}_2\text{O}^+$ . The peak below the line at  $m/z$  18 is, however, present on both the 'cell' and 'sample' plots (Figure 4.3) so it can be inferred that the  $\text{H}_2\text{O}^+$  ion contains protons of both 'sample' and 'cell' origin.

The peak patterns at  $m/z$  19–22 are due to  $\text{H}_3\text{O}^+$  with overlap of deuterated  $\text{H}_2\text{O}^+$  peaks at  $m/z$  19 and 20. The intensity of the  $\text{H}_2\text{O}^+$  and  $\text{H}_3\text{O}^+$  were similar in the raw data, less than an order of magnitude apart. The result of the overlap at  $m/z$  19 is therefore difficult to interpret. The signals for both series in the ‘cell’ plot (Figure 4.3(i)) are above the axis and in the ‘sample’ plot (Figure 4.3(ii)) they are below the axis. This is consistent with the similarity in signal magnitude noted above, with the  $\text{HDO}^+$  signal dominating over the similar  $\text{H}_3\text{O}^+$  signal in the ‘cell’ plot and the  $\text{H}_3\text{O}^+$  signal dominating over the  $\text{HDO}^+$  signal in the ‘sample’ plot. With the exception of  $m/z$  20 in the ‘cell’ plot, which is discussed below, the signals at  $m/z$  20–22 are above the axis on both ‘sample’ and ‘cell’ plots (Figure 4.3) so it can be concluded that  $\text{H}_3\text{O}^+$  contains protons of both sample matrix and collision cell gas origin.

The decrease in  $m/z$  20 on the ‘cell’ plot (Figure 4.3(i)) is due to day-to-day variation in the level of an unidentified ion. As mentioned above, the series on the ‘cell’ plots include day-to-day variations. Such variation is not on ‘sample’ plots as each series was prepared from within-day data only. Appelblad and others<sup>88</sup> showed that a peak at  $m/z$  20 was a dominant spectral feature for a nitric acid blank when a large potential barrier of *ca.* 180 V was introduced before the collision cell to ‘cut off’ the ion beam. One possible identity of the ion causing this signal is a high energy ion such as  $\text{Ar}^{++}$ .

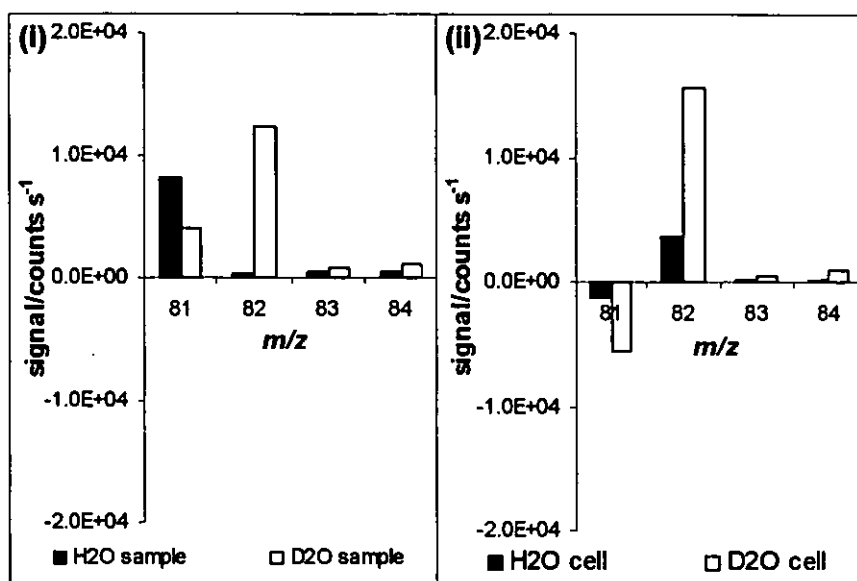


**Figure 4.4** – D<sub>2</sub>O – H<sub>2</sub>O plots for the  $m/z$  region 81–84. (i) 'Cell' and (ii) 'sample' (definitions as in Figure 4.1 caption)

The pattern of peaks at  $m/z$  81–82 in Figure 4.4(ii) shows that a monohydride species at  $m/z$  81 contained protons of 'sample' origin. Figure 4.4(i) does not show this pattern of peaks and so no contribution to this species by protons of 'cell' origin was evident. The species  $^{81}(\text{Ar}_2\text{H})^+$  thus contains only protons from the sample matrix. Similar pairs of peaks were also observed at  $m/z$  1–2 and 5–6 on both 'sample' and 'cell' plots, indicating that monohydride species at  $m/z$  1 and 5,  $\text{H}^+$  and  $\text{HeH}^+$ , consist of protons of both 'sample' and 'cell' origin.

During the initial series of experiments, a small peak below the axis at  $m/z$  59 with similar peaks above the axis at  $m/z$  60, 61 and 62 were observed on the 'cell' plots, suggesting the presence of a species  $\text{XH}_3^+$  contributed to by protons from the cell. These peaks were not observed on the equivalent 'sample' plot so this species, believed to be  $\text{ArH}_3\text{O}^+$ , was of 'cell' origin only. In the latter series of experiments this pattern of peaks was not observed. Owing to the small size of the peaks and the lack of corroborating evidence the source of protons for this species cannot be confidently identified.

A summary of the conclusions drawn is given in Table 4.4.

**Table 4.4** – *Source of protons in various polyatomic species*

<i>m/z</i>	Ion	Source of protons
1	H <sup>+</sup>	Cell and sample
5	HeH <sup>+</sup>	Cell and sample
18	H <sub>2</sub> O <sup>+</sup>	Cell and sample
19	H <sub>3</sub> O <sup>+</sup>	Cell and sample
29	N <sub>2</sub> H <sup>+</sup>	Cell and sample
41	ArH <sup>+</sup>	Cell and sample
17	OH <sup>+</sup>	Sample only
33	O <sub>2</sub> H <sup>+</sup>	Sample only
81	Ar <sub>2</sub> H <sup>+</sup>	Sample only
59	ArH <sub>3</sub> O <sup>+</sup>	Unidentified

The results of the investigation into the effect of wetting a reactive helium/hydrogen mixture are shown in Figure 4.5. The results are shown as the ratio of signals 'wet'/'dry'. Thus, for example, a ratio of 1 indicates that the two signals were the same and a ratio of 0.5 indicates that the signal intensity with the 'wet' gas was half the level observed with the 'dry' gas. For clarity, the results are shown up to *m/z* 120 only.

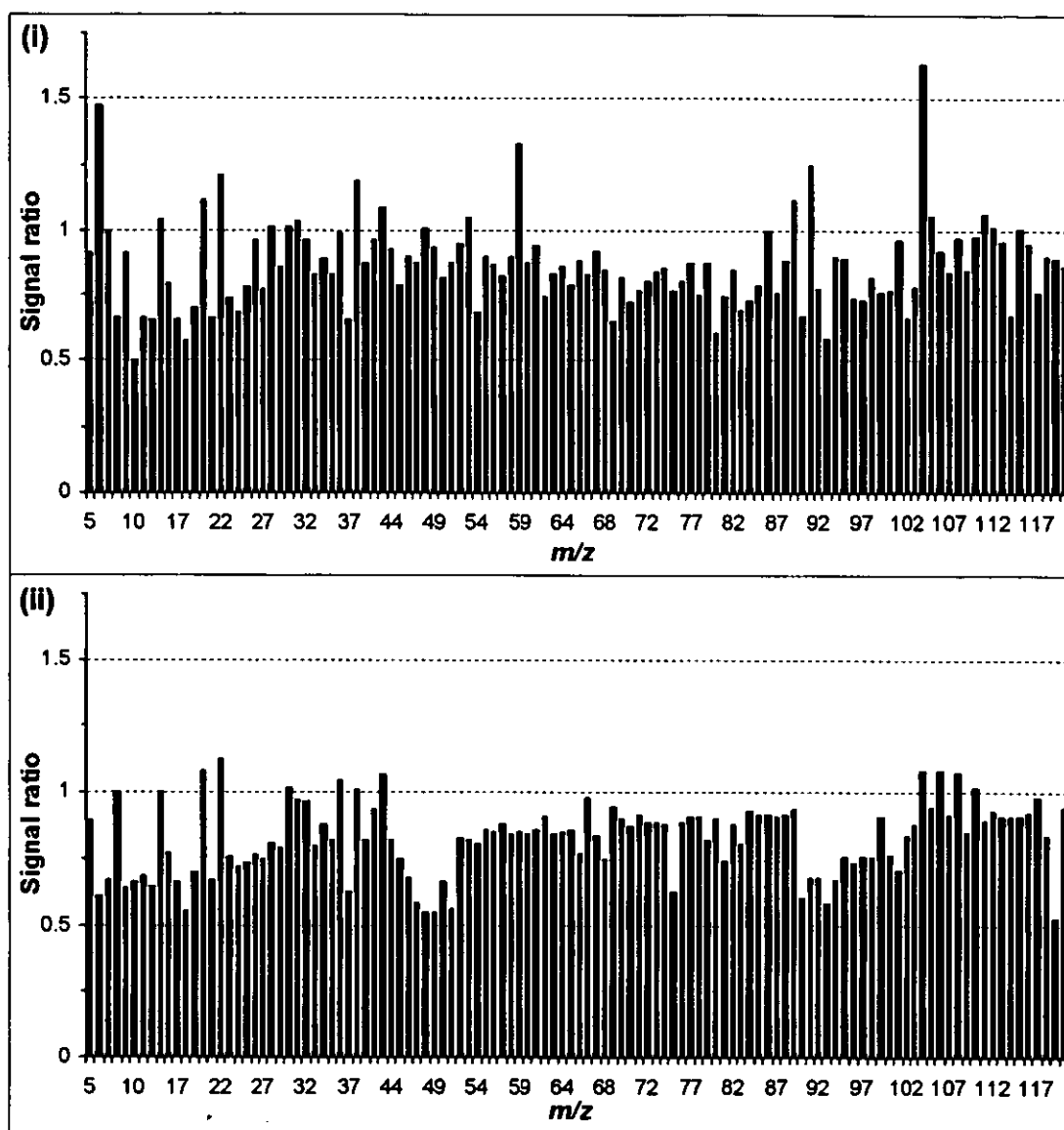


**Figure 4.5** – Ratio of signals 'wet'/'dry' with helium+hydrogen  $1.0+1.7 \text{ ml min}^{-1}$  in the cell for (i) a multi-element standard and (ii) a 2 % nitric acid blank.

Figure 4.5 shows that the signals for both the blank and the standard with the gas wet were, in general, 90–110 % of the signal with the gas dry. Almost all of the ratios of wet and dry gas mixtures were in the range 50–110 % for the blank and 50–150 % for the standard. The reduction in the apparent effect of water in this reactive system was due to competition with hydrogen. The partial pressure of hydrogen in the cell was much greater than that of water, so reactions with hydrogen were much more likely than those with water.

Some of the signals are considerably different with wet gas in the cell, for example the  $m/z$  7, 59 and 104 increased for the standard and  $m/z$  49 and 119 decreased for the blank. When these are compared with the effect of wetted helium alone on the mass spectrum<sup>88</sup> they are much less significant. This result indicates that the elevation of water levels in an already reactive helium/hydrogen mixture does not result in large changes in the chemistry of the cell. Some of the changes are sufficiently large to warrant measures to ensure that water levels in the cell gas do not vary during the course of the day, as this would cause large changes in background or sensitivity levels. Delivery of the gas through stainless steel (as in this work) or other impermeable material and allowing time for gas lines to flush after the gas has been introduced would ensure that this criterion was met.

Following the publication<sup>88</sup> of the work described above, a number of papers<sup>95,106</sup> have further explored the role of water and other contaminants in ICP-CC-MS. Mason and Kraan<sup>106</sup> considered the attenuation of a range of interference ions using helium or hydrogen in the cell with laser ablation sample introduction. Two different plasma conditions were compared: 'dry' with laser ablation and 'wet' with laser ablation and the addition of 2 % nitric acid aspirated by conventional nebulisation. Helium, 'dry' or 'wet', caused little variation in the level of  $^{40}\text{Ar}^{16}\text{O}^+$  and  $^{40}\text{Ar}_2^+$  although at higher flow rates 'wet' plasma did cause a little suppression of the level (less than one order of magnitude). 'Dry' plasma caused a slight increase in the  $^{12}\text{C}^{16}\text{O}_2^+$  signal due to collisional focussing while 'wet' plasma caused some reactive attenuation.  $^{14}\text{N}^{16}\text{O}^+$ , which was not believed to react with helium or hydrogen, was not attenuated with 'dry' plasma but its signal was reactively reduced when 'wet' plasma was used. The effect of using helium alone in a collision cell is thus strongly dependent on plasma conditions as water from the sample matrix can cause reactive effects in the cell. When hydrogen was used in the cell, varying levels of attenuation of  $\text{CO}_2^+$ ,  $\text{ArO}^+$  and  $\text{Ar}_2^+$  were observed. When 'wet' plasma was used instead of 'dry' the degree of attenuation was distinctly less, possibly due to reactions with water generating ions at those masses in the cell.

Yamada *et al.*<sup>95</sup> investigated the effect of different grades of hydrogen in the collision cell. With the use of a small potential barrier (+1 V), variation in the level of water in

hydrogen (< 1 – 100 ppm) had little effect on the attenuation of  $^{40}\text{Ar}^+$ ,  $^{40}\text{Ar}^{16}\text{O}^+$  and  $^{40}\text{Ar}_2^+$  or on  $^{40}\text{Ca}$ ,  $^{56}\text{Fe}$  and  $^{80}\text{Se}$  sensitivity. The differing grades of hydrogen did however affect general spectral backgrounds. Without the use of a potential barrier, backgrounds between  $m/z$  30 and 100 were generally between  $10^3$  and  $10^4$  counts  $\text{s}^{-1}$  with < 1 ppm water impurity in the hydrogen with up to an additional order of magnitude interference when lower purity hydrogen with < 100 ppm water was used, due to the formation of polyatomic and cluster ions in the cell. The use of kinetic energy discrimination (see Section 2.4.2) lowered these backgrounds to less than  $10^2$  counts  $\text{s}^{-1}$  with no discernable difference in signals observed with the different grades of hydrogen used. This would appear to confirm that small variations in the level of water in reactive hydrogen collision cell gas do not significantly affect the reactive attenuation of polyatomic ions in the cell.

#### **4.4 Summary**

The presence of adventitious water in the collision cell significantly alters the cell chemistry when the unreactive gas helium is used alone. In this event, controlling the level of such water is necessary in order to obtain reproducible results. Adventitious water contributes to the levels of proton containing polyatomic ions detected, but does not appear to introduce any new proton containing polyatomic ions when a blank is aspirated. The presence of adventitious water does not greatly alter the chemistry of a reactive helium/hydrogen mixture. Hydrogen is present at much higher partial pressure than water and so collides with and therefore reacts with polyatomic and other ions much more frequently than water, masking the effect of reactions with water.

## **Chapter Five**

### **Ion Energy Effects**



## 5.0 ***Ion Energy Effects***

The role of ion energy effects in ICP-CC-MS was considered in Section 2.4.2 above. The concept of 'kinetic energy discrimination' (KED) has been described in the literature and the concept of the 'ion kinetic energy effect' (IKEE) has been developed by the author and evidence of IKEE identified in the literature. This chapter explores the roles of IKEE and KED in collision cell ICP-MS by studying the effects of  $V_H - V_P$  where  $V_P$  is the offset potential of the plasma, and  $V_Q - V_H$  on a range of species. The indicators considered were the levels of the argon-based ions  $\text{ArO}^+$  and  $\text{Ar}_2^+$ , the relative levels of a range of analyte oxide ions, unreactive analyte sensitivity and the  $^{21}(\text{H}_3\text{O})^+ / ^{36}\text{Ar}^+$  ratio. The  $^{21}(\text{H}_3\text{O})^+ / ^{36}\text{Ar}^+$  ratio has been identified<sup>35</sup> as an indicator of cell reactivity and maximises under conditions (cell gas flow) suitable for multi-element analysis.

The effect of collision cell gases and the plasma screen on the ion energy distribution is considered, as are the effects of various modifications to the plasma screen grounding arrangements and biasing the plasma screen with a dc potential. The effect of different sample and skimmer cones on the ion energy distribution is also briefly considered.

## 5.1 ***Experimental***

### 5.1.1 ***Instrumentation and Optimisation***

The VG PQ ExCell instrument was configured and used as described in Section 3.1 (starts p92). The only nebulisers used in this work were of the Conikal type and hydrogen was supplied only by cylinder. When in standard mode,  $V_H$  and  $V_Q$  values of  $-1.96\text{ V}$  and  $+1.0\text{ V}$  were used. The plasma parameters used are listed in Table 5.1.

***Table 5.1 – Plasma parameters used***

<b>Parameter</b>		<b>Setting</b>
Rf power/W		1350
Reflected power/W		< 2
Gas flows/l min <sup>-1</sup> :	Cool	12.6
	Auxiliary	0.80
	Nebuliser	1.03

The VG PQ ExCell was fitted with a retractable nickel plasma screen around the torch. The plasma screen consisted of a thin nickel cylinder with a 3 – 4 mm wide gap along its length. When inserted, the plasma screen fitted closely around the exterior of the torch between the torch and the rf coil. The plasma screen was supported and insulated from the coil by a cylindrical silica collar located between the screen and the coil. When used, the plasma screen was inserted ungrounded, with the plasma rf power lowered to 650 – 700 W. The plasma screen was then grounded to the interface plate of the instrument *via* a relay. The rf power was then raised to 1350 W before experimental work continued.

For the ‘active’ plasma screen experiments, the factory fitted grounding circuit for the plasma screen was modified to enable a dc potential to be applied to the plasma screen (see Figure 5.1). The existing ground wire was detached from the interface plate and connected to the negative terminal of a custom-built battery assembly. The positive terminal of the assembly was connected to ground by attaching it to the interface plate of the instrument at the point where the ground wire was previously attached. The battery assembly consisted of a die-cast aluminium box, grounded to the interface plate as described, inside of which eight individual AA cell holders were affixed. The appropriate number of cell holders to supply the desired potential in each experiment were linked together in series by short lengths of multi-core copper wire, soldered to the tabs on the terminals of the cell holders. The negative terminal of the series of cell holders was connected by a length of multi-core wire to the plasma screen wire. The positive terminal of the series of cell holders was connected to a bolt through the die-cast box that was acting as a grounding point. (The box ground to the interface plate was also connected there.) To protect the cells from any potential rf current on the plasma screen, the terminals of the battery were bridged with a 10 000 pF capacitor. The ‘active’ plasma screen assembly is depicted in Figure 5.1.

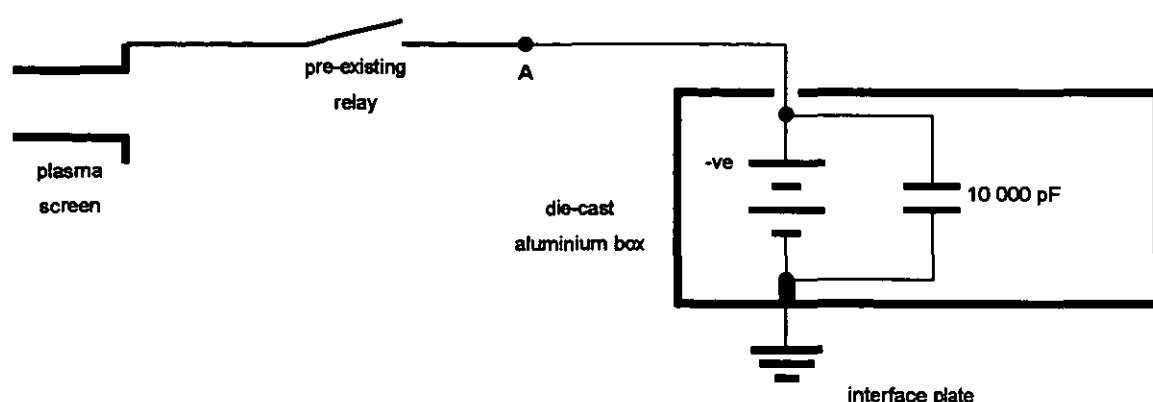


**Figure 5.1** – Diagrammatic representation of the ‘active’ plasma screen apparatus. (The point labelled ‘A’ is the connection between factory-fitted (heavy lines) and new wiring (thin lines))

On each occasion that the ‘active’ plasma screen was used, the die-cast box was opened and AA cells inserted into the connected holders (one cell for  $-1.5$  V nominal, two for  $-3$  V nominal). The lid was then firmly screwed down. The assembly was then continuity tested between the connection with the existing plasma screen and the interface plate and between the die-cast box, its lid and the interface plate. The potential difference between the connection to the pre-existing circuit and ground was monitored before the plasma was ignited. All wire used was  $0.5 \text{ mm}^2$  PTFE sleeved multi-core copper wire.

For the plasma screen grounding experiments, a separate ‘rf’ ground was attached to the plasma screen. The rf ground consisted of a length of copper braid (from a piece of television aerial co-axial cable) which was linked to the plasma screen by a crimped connector. A  $330 \text{ pF}$  ATC ceramic capacitor was soldered into the braid. The braid was earthed to the grounded side of the rf coil, via the mounting plate depicted in Figure 5.2(i). This mounting plate was located around the plumbing fitting connecting the rf coil to the bulkhead and cooling water supply, sandwiched between the wide portion of the fitting on the coil side of the bulkhead and a plastic insulator grommet electrically isolating the rf coil and circuitry from the bulkhead. The mounting disc and fitting were secured in place by a nut around the fitting on the non-coil side of the bulkhead tightened against the insulator grommet. The mounting disc is shown *in situ* in Figure 5.2(ii). Dc electrical continuity between the mounting disc and the plumbing fitting was checked. The circuit diagram for the rf grounding arrangement is shown in

Figure 5.3(i). When the rf ground was used alone, the wire ground was physically disconnected from the interface plate (the point marked 'G' in Figure 5.3(ii)).

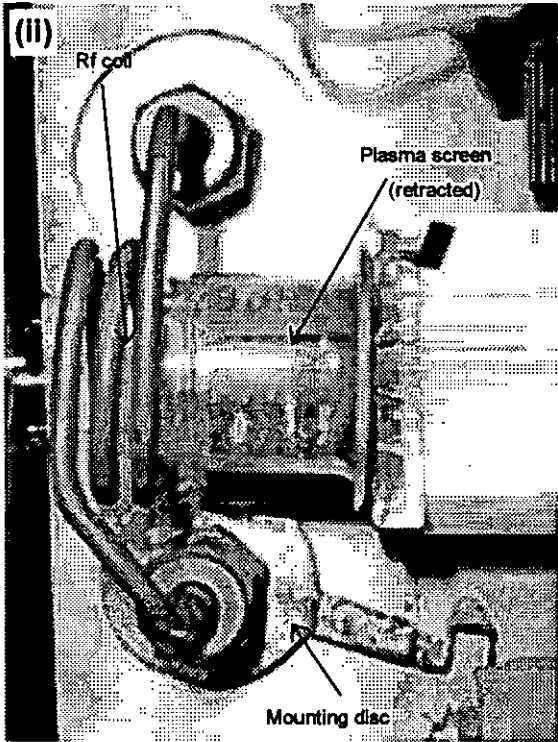
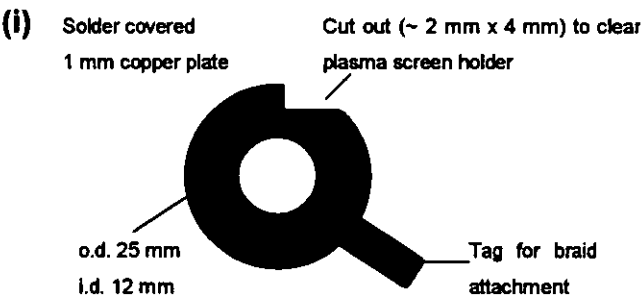


**Figure 5.2 – (i) Diagram of the mounting disc used to connect the braid to the grounded side of the rf coil and (ii) the disc in situ**

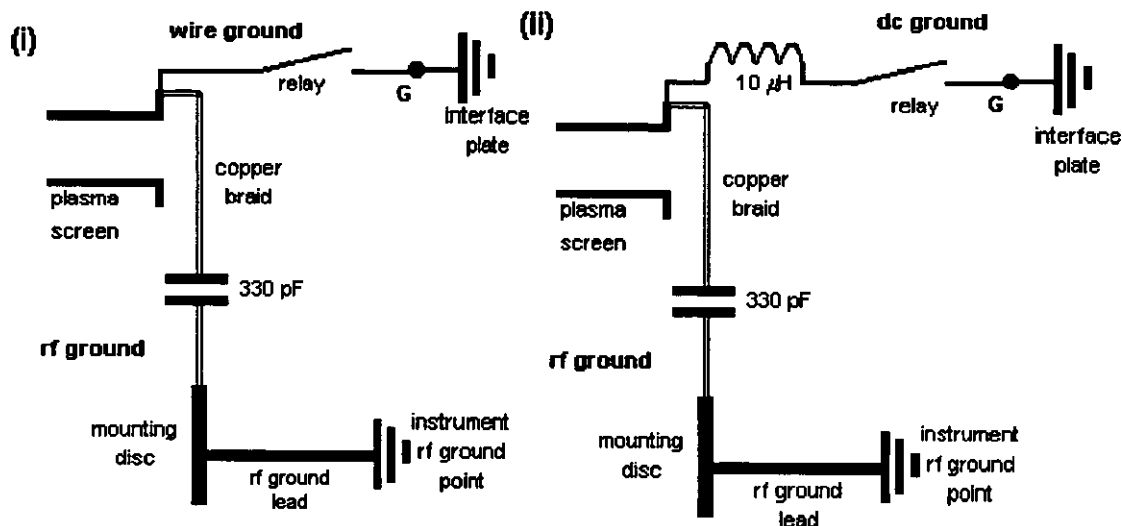


**Figure 5.3 – Diagrammatical representation of (i) wire ground and rf ground plasma screen and (ii) dc ground and rf ground plasma screen. (The wire or dc ground was disconnected at the point labelled ‘G’ when the rf ground alone was required.)**

For further plasma screen grounding experiments, the standard ‘wire’ grounding of the plasma screen was modified to include an inductor, as shown in Figure 5.3. Low microhenry inductors suitable for use with 2 kV potentials are not available, so a wire coil inductor was prepared and inserted into the ground wire. The coil was secured with its axis perpendicular to that of the plasma coil to prevent induction interactions between the two coils.

The coil consisted of a single layer of eleven turns of 24 AWG PTFE coated multi-core copper wire around a polypropylene bottle 35 mm in diameter. The inductance of the coil was calculated using Equation 5.1.<sup>149</sup> In Equation 5.1,  $L$  is the inductance in  $\mu\text{H}$ ,  $n$  is the number of turns,  $r$  is the coil radius in mm and  $l$  is the coil length in mm. (The wire had a diameter of approximately 2 mm, as it was tightly wound, this gave  $l = 2n$ ) The inductance of the coil was calculated to be approximately 10  $\mu\text{H}$ .

$$L = \frac{r^2 n^2}{25.4(9r + 10l)}$$

**Equation 5.1**

### **5.1.2 Materials and Reagents**

All test solutions run were prepared in acid-washed LDPE bottles from single- or multi-element standard solutions, 'Aristar'-grade 70 % nitric acid (Fisher Scientific, Loughborough, Leicestershire) and 18 M $\Omega$  cm<sup>-1</sup> deionised water (Barnstead, Dubuque, IA, USA). Several different multi-element solutions were used in these ion energy effect studies. These are detailed below.

*Multi-element solution 1:* 50 ng ml<sup>-1</sup> As, Ba, Cr, Cs, In, Ir, Pb, Pd, Pt, Rb, Se, Te, V and Yb in 2 % nitric acid.

*Multi-element solution 2:* 20 ng ml<sup>-1</sup> Ba, Be, Ce, Cr, Co, In, Li, Mg, Pb, Rh, Te, Tl, U, V and Y in 2 % nitric acid.

*Multi-element solution 3:* 20 ng ml<sup>-1</sup> Cd, Ce, Cr, In, Te and V in 2 % nitric acid.

*Multi-element solution 4:* 20 ng ml<sup>-1</sup> Ba, Cd, Ce, In and U in 2 % nitric acid.

Multi-element solution 1 was prepared from single-element standard solutions (principally SPEX Certiprep (Metuchen, NJ, USA), also Fisher Scientific and Aldrich (Gillingham, Dorset)). Multi-element solution 2 was prepared from Cr, Te and V single-element solutions (Fisher Scientific and SPEX CertiPrep) and a Ba, Be, Ce, Co, In, Li, Mg, Pb, Rh, Tl, U and Y multi-element standard (CLMS-Tune-1 (SPEX CertiPrep)). Multi-element solutions 3 and 4 were prepared from single-element standard solutions (Aldrich, Fisher Scientific, and SPEX CertiPrep). A 20 ng ml<sup>-1</sup> In and U in 2 % nitric acid solution in was prepared from single-element standard solutions (SPEX Certiprep and Aldrich respectively).

### **5.1.3 Methodology**

#### **5.1.3.1 Collision Cell Effects**

Data were collected for a wide range of  $V_H$  and  $V_Q$  settings with various gases and flow rates employed: oxygen at 1.0 ml min<sup>-1</sup>; helium at 2.0 ml min<sup>-1</sup> and helium+hydrogen at 1.0+1.0, 1.0+1.7 and 1.0+2.5 ml min<sup>-1</sup>. The sequence of  $V_H$  values was randomised in

order to minimise any drift as were  $V_Q$  values at each  $V_H$  setting. Data were collected using the acquisition parameters listed in Table 5.2 at the  $m/z$  values specified in the appropriate row of Table 5.3.

**Table 5.2 – Acquisition parameters used**

Parameter	Value
Number of scans	100
Channels per mass	1
Dwell time/ms	10
Number of repeats	3

Three different sets of  $m/z$  values were employed as the experimental methodology developed. The initial experiments used  $m/z$  set A which comprised the  $m/z$  of the major isotope(s) of the analytes in multi-element solution 1 (see Section 5.1.2 for details) and the major isotopes of their monoxide, dioxide or hydroxide ions, as listed in Table 5.7.

For later experiments, a revised set of  $m/z$ , set B, was studied. The differences between  $m/z$  sets A and B reflect the findings of the earlier work (Section 5.3.1.1).  $m/z$  set B contained  $m/z$  for the major isotopes of the analytes in multi-element solution 2 (see Section 5.1.2 for details), the monoxide ions listed in Table 5.8, a range of argon-based ions,  $^{21}(\text{H}_3\text{O})^+$  and  $^{36}\text{Ar}^+$ . These changes reflect the shift in emphasis from characterising the energy available in the cell for reactions to studying the effects of  $V_Q$  and  $V_H$  on reactivity.

Where data was acquired at a particularly wide range of  $V_Q$  and  $V_H$  settings,  $m/z$  set C was used. This  $m/z$  set was an abridged version of  $m/z$  set B in which the  $m/z$  of elements present in solution 2 and, with the exception of In, not featured in Table 5.8 were omitted. This arrangement shortened the analysis time per point, enabling more  $V_H$  and  $V_Q$  points to be studied in each instrumental run.

**Table 5.3 – m/z monitored in each m/z set**

<b>m/z set</b>	<b>m/z monitored</b>
A	32, 51, 52, 67, 68, 75, 82, 84, 85, 86, 101, 102, 108, 115, 124, 125, 129, 133, 138, 141, 149, 150, 154, 155, 172, 188, 193, 195, 208, 209, 211, 224 and 227
B	7, 9, 21, 25, 26, 36, 51, 52, 53, 54, 56, 59, 67, 68, 68.5, 69, 76, 80, 89, 103, 115, 126, 128, 130, 137, 138, 140, 142, 143, 144, 145, 146, 147, 156, 158, 203, 205, 206, 207 and 208
C	21, 36, 51, 52, 53, 54, 56, 59, 67, 68, 69, 76, 80, 115, 126, 127, 128, 129, 130, 140, 142, 144, 146, 156 and 158
D	21, 36, 51, 52, 53, 54, 56, 67, 68, 69, 76, 80, 112, 114, 115, 126, 128, 129, 130, 132, 140, 142, 144, 146 and 156
E	54, 69, 76, 114, 115, 138, 140, 156 and 238

In earlier experiments, the lens settings (with the exception of the  $V_Q$  and  $V_H$  settings being studied) were not varied from those established in the initial tuning in standard mode. In later experiments, the software ‘autotune’ feature was used to maximise the In sensitivity at each step. Where ‘autotune’ was used, this is noted in the results.

$V_H$  was monitored against ground *via* pin 5 of connector PL20 on the rearmost circuit board in the electronics compartment and was varied using the ‘PB (pressurised)’ control on the ‘multipole electronics’ control box.  $V_Q$  was monitored and varied using the software ‘pole bias’ control.

Data were also collected for a range of  $V_Q$  values with no gas in the cell in order to infer the ion energy distribution and plasma offset potential. Some experiments were conducted, with and without collision cell gases employed, in which a grounded plasma shield was used.

### *5.1.3.2 Ion Energy Effects*

#### *Effect of Collision/Reaction Cell Use*

Data were collected at a range of  $V_Q$  values between  $-16$  V and  $+12$  V.  $V_H$  was  $+4$  V throughout. The order of the  $V_Q$  values was, as in all work reported, randomised to minimise the effect of any drift that occurred. Collision cell gases of helium+hydrogen



1.0+1.7 ml min<sup>-1</sup> were used. Data were collected using 1350 W plasma, multi-element solution 3 (details in Section 5.1.2), the acquisition parameters listed in Table 5.2 and *m/z* set D (details in Table 5.3). The experiment was conducted twice, once with and once without the use of plasma screen.

Data were collected at a range of *V<sub>Q</sub>* values with or without helium in the collision cell. 1350 W plasma was used throughout. Data were collected at *m/z* 115 and 238 only, using the acquisition parameters listed in Table 5.2 and a 20 ng ml<sup>-1</sup> In and U in 2 % nitric acid solution. In an initial experiment, data were collected with and without the use of plasma screen and with and without the use of 3.0 ml min<sup>-1</sup> helium in the collision cell at *V<sub>H</sub>* values of +4.00 V and -1.96 V; combinations used are listed in part (i) of Table 5.4. In a subsequent experiment, data were collected with and without plasma screen and with and without the use of 6.0 ml min<sup>-1</sup> helium in the collision cell; the combinations and *V<sub>H</sub>* values used are listed in part (ii) of Table 5.4.

**Table 5.4 – Combinations of collision cell gas flow rates, *V<sub>H</sub>* settings and plasma screen use used. (Parts (i) and (ii) relate to different experiments.)**

	Helium flow rate/ml min <sup>-1</sup>	Plasma screen used?	<i>V<sub>H</sub></i> /V
<b>Part (i):</b>			
	0.0	No	-1.96
	0.0	Yes	-1.96
	3.0	No	-1.96
	3.0	Yes	-1.96
	3.0	No	+4.00
<b>Part (ii):</b>			
	0.0	No	-1.96
	0.0	Yes	-1.96
	6.0	No	+4.00
	6.0	Yes	+4.00

### Effect of 'Active' Plasma Screen Use

Data were collected at a range of  $V_H$  values, with  $V_Q - V_H = 10$  V and helium+hydrogen  $1.0+1.7$  ml min<sup>-1</sup> in the collision cell. The sequence of  $V_H$  values was randomised in order to minimise the effect of any drift that occurred. Data were collected using multi-element solution 3 and  $m/z$  set D (listed in Table 5.3, above) using the acquisition parameters listed in Table 5.2. A full power plasma (1350 W) was used throughout. Data were collected with a standard plasma (no plasma screen in use), the plasma screen with standard grounded plasma screen in use and with a  $-1.5$  V 'active' plasma screen use. The use of a  $-3$  V 'active' plasma screen was also explored.

### Effect of Plasma Screen Grounding

Data were collected at a range of  $V_Q$  values, with  $V_H = -1.96$  V and no collision cell gas in use. A 1350 W plasma was used. The acquisition parameters were as in Table 5.2, with multi-element solution 4 and  $m/z$  set E used throughout (see Section 5.1.2 and Table 5.3, respectively, for details).

In an initial experiment, data were collected for four different plasma screen conditions over two days. On one day, data were collected for the standard plasma conditions (no plasma screen used) and with the plasma screen and 330 pF rf grounding described in Section 5.1.1 used. On the other day, data were again collected for the standard plasma conditions and also for two different plasma screen conditions – plasma screen with the conventional factory fitted ground wire used and plasma screen with both the factory fitted ground wire and the 330 pF rf ground connected.

In a subsequent experiment, data were collected for standard plasma conditions and a range of different plasma screen grounding arrangements: standard, factory-fitted, wire grounded plasma screen; dc grounded plasma screen (*circa* 10  $\mu$ H inductor, as described in Section 5.1.1); 330 pF rf grounded plasma screen and divided ground plasma screen (both 10  $\mu$ H dc ground and 330 pF rf ground connected).

### Use of Different Cones and Tuning for Plasma Screen Use

Data were collected at a range of  $V_Q$  values, with  $V_H$   $-1.96$  V and no collision cell gas used. A 1350 W plasma was used throughout, as were the acquisition parameters in Table 5.2, multi-element solution 4 and  $m/z$  set E. Details of multi-element solution 4 and  $m/z$  set E are given in Section 5.1.2 and Table 5.3 respectively.

The experiment was conducted for the standard plasma and with the standard wire ground plasma screen in use. Initially, no re-optimisation of plasma and lens settings was conducted when the plasma screen was introduced. The experiment was repeated with the plasma retuned for plasma screen use. With  $V_Q = -3$  V, the torch gas flows were adjusted to reduce  $CeO^+/Ce^+$  levels and maintain or improve In sensitivity. The only change made was a reduction in the nebuliser gas flow rate from  $1.10\text{ l min}^{-1}$  to  $1.05\text{ l min}^{-1}$ .

An experiment was conducted using a range of different cones (standard cones were used in all other work reported herein). The plasma screen was not used. Data were collected for a range of different  $V_Q$  values. In each case, the ion optics were tuned to optimise the  $^{115}\text{In}$  signal with  $V_Q = +1$  V. Two different extraction lens potentials were used:  $-566$  V ('hard' extraction) and  $-200$  V ('soft' extraction). The various combinations of cones and extraction potentials used are listed in Table 5.5.

**Table 5.5 – Cone and extraction potential combinations used.**

Sample cone	Skimmer cone	Extraction lens potential/V
Standard	Standard	$-566$
Standard	Standard	$-200$
$X_i$	$X_i$	$-566$
$X_i$	$X_i$	$-200$
Standard	Trial	$-566$

The 'standard' cones are those supplied by the instrument manufacturer (Thermo Electron). ' $X_i$ ' cones are supplied by the instrument manufacturer for use with

environmental samples. The 'trial' skimmer cone is a cone of experimental design, known as 'PS6R', also provided by the instrument manufacturer.

## ***5.2 Reactions and Thermodynamics***

In order to study IKEE and KED, a range of reactions of known enthalpy were required. These reactions had to cover a wide range of different reaction enthalpies to enable the energy availability of the collision/reaction cell to be understood and also have easily studied reactant and product ions. That is, ions that do not suffer from significant isobaric interference, either from other elements in the test solution or from argon- or atmospheric gas-based ions. This requirement was to enable the extent of reaction to be better characterised than if the reactant or product ion were not so readily measured. Ideally, the reaction sequence needed to be studied by use of a single test solution and a single collision/reaction cell gas so as to minimise the time required to run the experiments and thereby permit a wider range of pole bias values to be studied. This requirement also simplified analysis of results as if only one gas and gas flow is involved, ion energy effects caused by non-reactive collisions with the gas are invariant.

To minimise the influence of day-to-day variations on the results, each data set should be collected in a single run.

One possible reaction scheme was proposed by Baranov and Tanner.<sup>44</sup> A range of reactions of known enthalpy which could be studied to ascertain the available energy in the cell. This reaction scheme for the thermodynamic evaluation of collision/reaction cells is reproduced in Table 5.6 below.

**Table 5.6** – Proposed reactions for thermodynamic evaluation of a collision/reaction cell for ICP-MS. Reproduced from Baranov and Tanner.<sup>44</sup>

Ion	Reaction		Products	$\Delta H_r$ /eV
	gas			
Ce <sup>+</sup>	+ O <sub>2</sub>	→	CeO <sup>+</sup> + O	-3.1
Xe <sup>+</sup>	+ O <sub>2</sub>	→	O <sub>2</sub> <sup>+</sup> + Xe	+0.058
Se <sup>+</sup>	+ NH <sub>3</sub>	→	NH <sub>3</sub> <sup>+</sup> + Se	+0.4
Zn <sup>+</sup>	+ NH <sub>3</sub>	→	NH <sub>3</sub> <sup>+</sup> + Zn	+0.78
I <sup>+</sup>	+ O <sub>2</sub>	→	O <sub>2</sub> <sup>+</sup> + I	+1.6
Se <sup>+</sup>	+ N <sub>2</sub>	→	N <sub>2</sub> <sup>+</sup> + Se	+5.8
CeO <sup>+</sup>	+ H <sub>2</sub>	→	Ce <sup>+</sup> + H <sub>2</sub> O	+8.2

The use of this reaction scheme is problematic. The scheme includes reactions using four different gases, so data could not be collected in a single run. The majority of the reactions presented are charge transfer reactions. The use of a charge transfer reaction can obscure the results as it is necessary to study the loss of a signal, rather than its appearance. (The majority of the product ions are either ubiquitously present in mass spectra at high levels, *e.g.* O<sub>2</sub><sup>+</sup> or N<sub>2</sub><sup>+</sup>, or are present from the test solution, *e.g.* Ce<sup>+</sup>.) Reactions to form polyatomic ions based on the reactant ion are preferable, as the appearance of a new signal is easily characterised whereas small variations in large signals are often difficult to identify due to noise in the signal.

In order to establish a reaction scheme for use in this study, reaction enthalpies were calculated for a wide range of reactions with monoatomic ions and a variety of gases, using the formation enthalpy data compiled by Lias *et al.*<sup>49</sup> and Equation 2.2 (p32), in the same manner as that adopted in Section 2.2.2. The focus was on reactions to form monoxide ions (MO<sup>+</sup>), as these are simpler to study than reactions to form hydride ions and they have previously been shown to occur in collision cell systems.<sup>35</sup> Reactions to form hydride ions can be difficult to study as many elements consist of a range of isotopes at adjacent nominal masses; M<sup>+</sup> and MH<sup>+</sup> signals can therefore frequently be superimposed.

Data were compiled on the formation of  $\text{MO}^+$  by reaction between  $\text{M}^+$  and oxygen or water. These reactants were selected as both are believed to be present in collision/reaction cells from the plasma/sample matrix and due to contamination of the collision/reaction cell gases.<sup>38,82,88</sup> Oxygen can also be employed as a collision/reaction cell gas.

A subset of the reactions was selected for use as a monitor of reactivity within the cell. Two criteria were applied to select the reactions: firstly, that the reaction set covered a wide range of reaction enthalpies and, secondly, that the species involved had isotopes free from isobaric interference. The second criterion was the more difficult to apply as it required each analyte to have an isotope which did not suffer from isobaric interference, either at its  $m/z$  ( $N$ ) or at  $N + 16$ . Potential isobaric interferences fell into two groups, those interferences commonly experienced in ICP-MS, from argon-based and atmospheric gas-based ions and interference from other analytes in the test solution ( $\text{M}^+$  and  $\text{MO}^+$ ). The set of reactions selected is shown in Table 5.7.

**Table 5.7 – Reactions between metal cations and oxygen or water forming  $MO^+$  selected for use in the study of collision/reaction cell reactivity**

Reactions with oxygen	$\Delta H_r/\text{eV}$	Reactions with water	$\Delta H_r/\text{eV}$
$U^+ + O_2 \rightarrow UO_2^+$	-11.12		
$U^+ + O_2 \rightarrow UO^+ + O$	-3.20	$U^+ + H_2O \rightarrow UO^+ + H_2$	-3.28
$Pt^+ + O_2 \rightarrow PtO_2^+$	-1.48		
$Cr^+ + O_2 \rightarrow CrO_2^+$	-1.19		
$V^+ + O_2 \rightarrow VO^+ + O$	-0.67	$V^+ + H_2O \rightarrow VO^+ + H_2$	-0.75
		$Ba^+ + H_2O \rightarrow BaOH^+ + H$	-0.35
$Xe^+ + O_2 \rightarrow O_2^+ + Xe$	+0.058		
$Te^+ + O_2 \rightarrow TeO^+ + O$	+0.97	$Te^+ + H_2O \rightarrow TeO^+ + H_2$	+0.89
$Ba^+ + O_2 \rightarrow BaO^+ + O$	+1.13	$Ba^+ + H_2O \rightarrow BaO^+ + H_2$	+1.05
$Yb^+ + O_2 \rightarrow YbO^+ + O$	+1.13	$Yb^+ + H_2O \rightarrow YbO^+ + H_2$	+1.06
$Cr^+ + O_2 \rightarrow CrO^+ + O$	+1.81	$Cr^+ + H_2O \rightarrow CrO^+ + H_2$	+1.74
$Sr^+ + O_2 \rightarrow SrO^+ + O$	+2.06	$Sr^+ + H_2O \rightarrow SrO^+ + H_2$	+1.99
$Ir^+ + O_2 \rightarrow IrO^+ + O$	+2.58	$Ir^+ + H_2O \rightarrow IrO^+ + H_2$	+2.51
$Pt^+ + O_2 \rightarrow PtO^+ + O$	+2.59	$Pt^+ + H_2O \rightarrow PtO^+ + H_2$	+2.52
$Pb^+ + O_2 \rightarrow PbO^+ + O$	+2.88	$Pb^+ + H_2O \rightarrow PbO^+ + H_2$	+2.80
$Pd^+ + O_2 \rightarrow PdO^+ + O$	+3.01	$Pd^+ + H_2O \rightarrow PdO^+ + H_2$	+2.93
$Zn^+ + O_2 \rightarrow ZnO^+ + O$	+3.77	$Zn^+ + H_2O \rightarrow ZnO^+ + H_2$	+3.69
$Cs^+ + O_2 \rightarrow CsO^+ + O$	+4.56	$Cs^+ + H_2O \rightarrow CsO^+ + H_2$	+4.49
		$Cs^+ + H_2O \rightarrow CsOH^+ + H$	+4.70
$Rb^+ + O_2 \rightarrow RbO^+ + O$	+4.88	$Rb^+ + H_2O \rightarrow RbO^+ + H_2$	+4.80

A comparison of the reactions with oxygen and their equivalents with water shows that the reaction enthalpies for any given ion are very similar for reactions with both molecules. The two reaction enthalpies are no more than 0.1 eV apart. Thus, in collision cell systems where neither oxygen nor water is deliberately added, the reaction enthalpy for the reaction to produce a given  $MO^+$  ion can be approximated without knowledge of the precise reaction. For this reason, in work reported below in which neither gas has been deliberately introduced to the system, which of the two distinct reaction pathways was followed is not identified and reaction enthalpies are quoted so as to include both values given above. Work considering the role of reaction cell collision cell ICP-MS

(Chapter Four above and Dexter *et al.*<sup>88</sup>), leads the author to believe that water is the most likely reactant in these cases, although this cannot be definitively stated.

Studying the reactant and product ions of the reactions listed in Table 5.7 should make it possible to estimate the energy available for reactions in the collision cell. Reactions with enthalpies below that point would proceed, higher levels of product ions would be observed, whilst reactions with enthalpies over that value would not be observed, the relative levels of products observed would be minimal.

The full matrix of reactions listed in Table 5.7 was used for the initial studies reported in Section 7.3.1.1 below. For the more detailed work reported in Sections 5.3.1.3 to 5.3.1.5 a smaller series of  $\text{MO}^+$  forming reactions was considered. This subset of reactions is listed in Table 5.8 together with reactions with hydrogen that remove  $\text{Ar}^+$  and reactions forming  $\text{H}_3\text{O}^+$ .

Where available, rate constants are included in Table 5.8. The rate constants are for reactions under thermal conditions and therefore cannot be applied to the reactions occurring in the collision cell at higher energies. However, they can be used as a guide to which reactions are likely to proceed in the cell (see Sections 2.2 to 2.2.2).



**Table 5.8 – Possible reactions for the formation of  $MO^+$  ( $M = Ce, Cr, Ti, V$ ) and  $H_3O^+$  and for the removal of  $Ar^+$  and  $Ar_2^+$**

Reaction		$\Delta H_r/\text{eV}^a$	$k/\text{cm}^3 \text{ molecule}^{-1} \text{ s}^{-1}$	Ref. for $k$
$Ce^+$	$+ H_2O \rightarrow CeO^+ + H_2$	-3.9	n/a	
$Ce^+$	$+ O_2 \rightarrow CeO^+ + O$	-3.8	$5.1 \times 10^{-10}$	150
$Cr^+$	$+ H_2O \rightarrow CrO^+ + H_2$	+1.7	n/a	
$Cr^+$	$+ O_2 \rightarrow CrO^+ + O$	+1.8	n/a	
$Te^+$	$+ H_2O \rightarrow TeO^+ + H_2$	+0.9	n/a	
$Te^+$	$+ O_2 \rightarrow TeO^+ + O$	+1.0	No reaction	151
$V^+$	$+ H_2O \rightarrow VO^+ + H_2$	-0.8	n/a	
$V^+$	$+ O_2 \rightarrow VO^+ + O$	-0.7	$2.8 \times 10^{-10}$	56
$H_2O^+$	$+ H_2 \rightarrow H_3O^+ + H$	-1.7	$7.6 \times 10^{-10}$	52
$H_2O^+$	$+ H_2O \rightarrow H_3O^+ + OH$	-1.1	n/a	
$Ar^+$	$+ H_2 \rightarrow Ar + H_2^+$	-0.3	$8.9 \times 10^{-10}$	52
$Ar^+$	$+ H_2 \rightarrow {}^bArH^+ + H$	-1.5	n/a	
$Ar_2^+$	$+ H_2 \rightarrow {}^bArH^+ + Ar + H$	-0.2	$5 \times 10^{-10}$	52
${}^b[ArH^+ + H_2 \rightarrow H_3^+ + Ar]$		$[-0.5]$	$[6.3 \times 10^{-10}]$	52

<sup>a</sup> Calculated from data in ref. 49.

<sup>b</sup>  $ArH^+$  is removed by further reaction.

### 5.3 Results and Discussion

#### 5.3.1 Ion Energy Effects in Collision/reaction Cells

##### 5.3.1.1 Use of Oxygen as a Cell Gas

Initial experiments were conducted using oxygen in the collision cell. Two criteria were used to select the optimum flow rate:

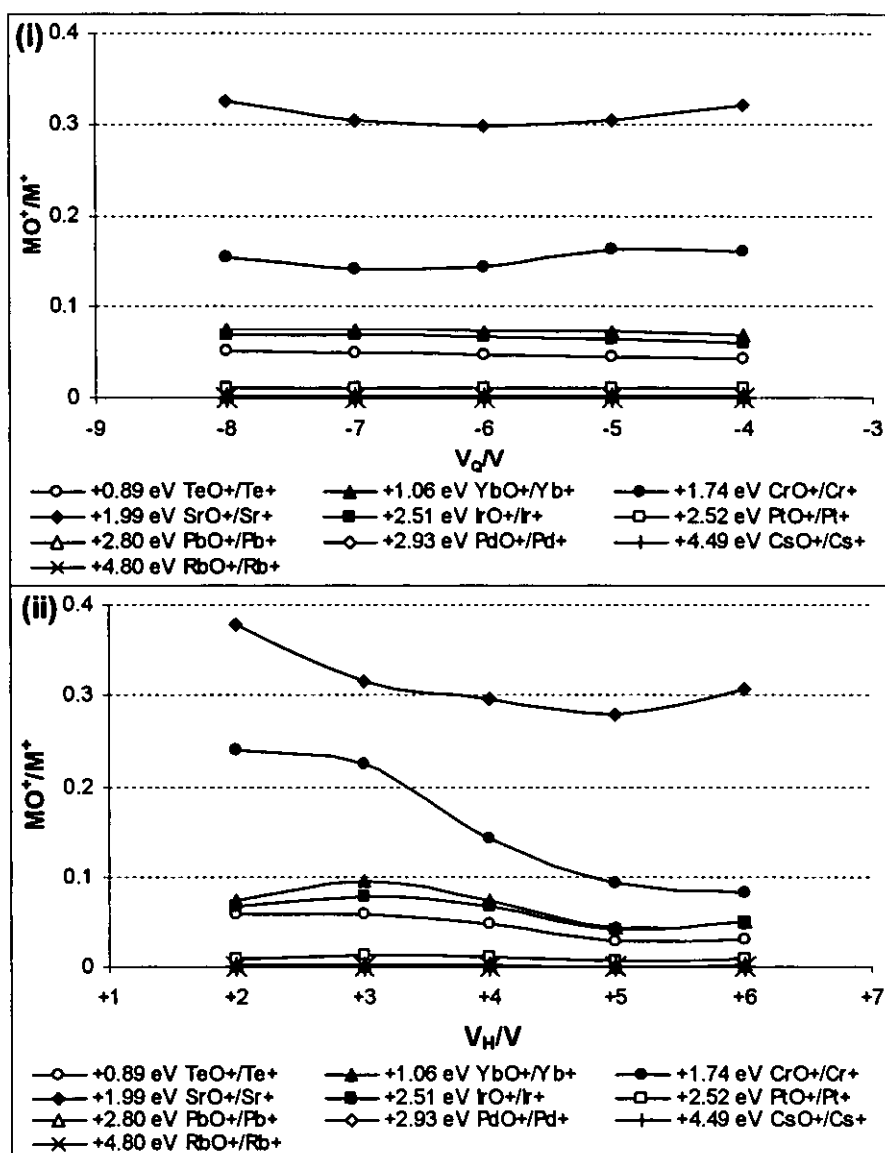
1. The sensitivity for In should be greater than 25 % of the signal for In at the same concentration with no gas in the cell.
2. The signal for  ${}^{36}Ar^{40}Ar^+$  should be reduced to less than 1 % of the level observed with no gas in the cell.

These criteria were selected as heavy gases such as oxygen can suppress analyte sensitivity.  $Ar_2^+$  (monitored *via* a minor isotope) was selected as a representative of

argon-based ion interferences.  $\text{Ar}_2^+$  is known to react with oxygen (see Section 2.3.5 and Equation 2.21 in particular).

For  $1.0 \text{ ml min}^{-1}$  oxygen (with  $V_H +3.86 \text{ V}$  and  $V_Q -6 \text{ V}$ ),  $^{36}\text{Ar}^{40}\text{Ar}^+$  was  $300 \text{ counts s}^{-1}$  compared with  $30\,000 \text{ counts s}^{-1}$  with no gas in the cell. Under the same conditions, the signal for  $1 \text{ ng ml}^{-1} \text{ In}$  was  $6\,000 \text{ counts s}^{-1}$  compared to  $47\,000 \text{ counts s}^{-1}$  with no gas in the cell. Thus, with  $1.0 \text{ ml min}^{-1}$  oxygen in the cell, the  $^{36}\text{Ar}^{40}\text{Ar}^+$  signal was 1 % of the signal with no gas in the cell and the In signal was 13 % of that with no gas in the cell – only the second of the two criteria was met. At lower flow rates, the signal at  $m/z$  rapidly increased, failing the second criterion.  $1.0 \text{ ml min}^{-1}$  oxygen was used for further experimentation as it met the  $\text{Ar}_2^+$  criterion, despite having only half the sensitivity required to meet the first criterion.

Data were collected at a range of different  $V_H$  and  $V_Q$  values, using  $m/z$  set A (see Table 5.3) and multi-element solution 1 (see Section 5.1.2). Selected results from this experiment are presented in Figure 5.4.



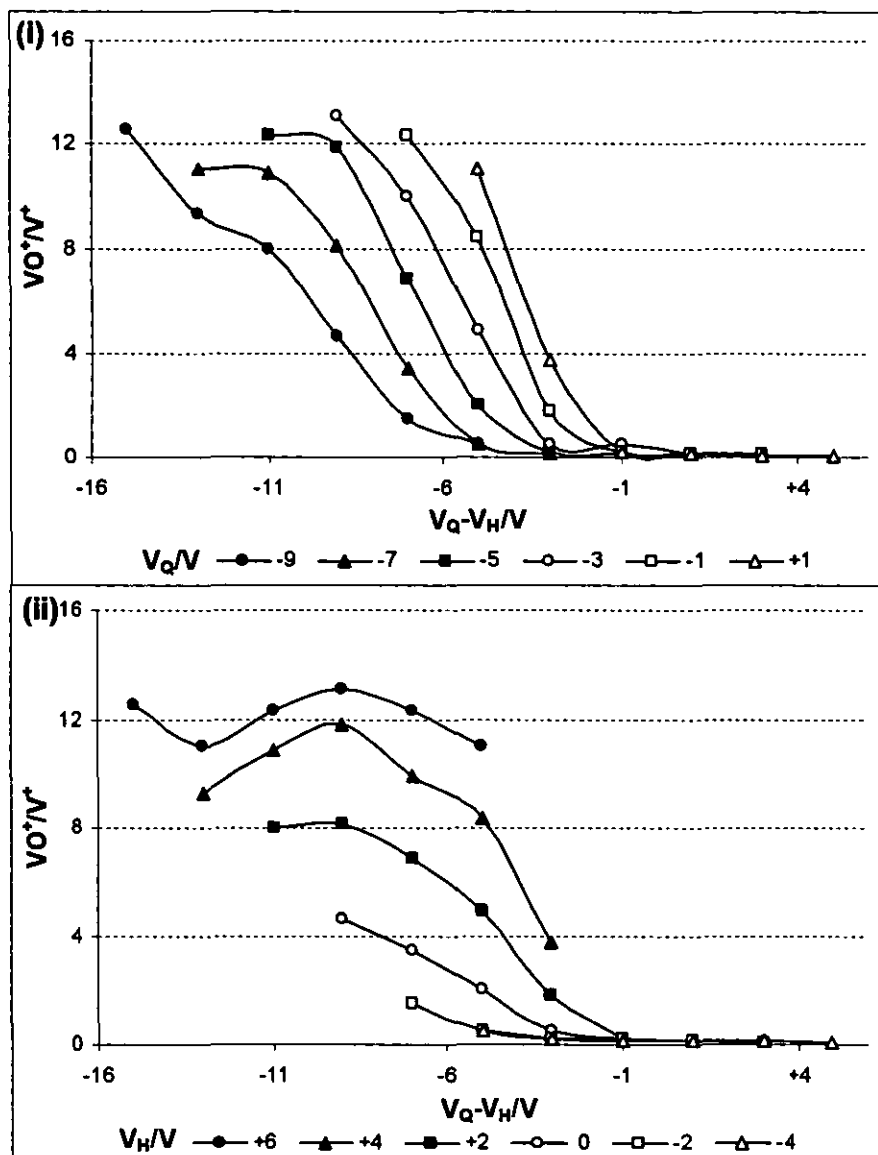
**Figure 5.4** – Variation in selected analyte oxide signals with (i)  $V_Q$  (at  $V_H = +4 V$ ) and (ii)  $V_H$  ( $V_Q = -6 V$ ). Collision cell gas  $1.0 \text{ ml min}^{-1}$  oxygen.  $\Delta H_r$  values for the appropriate reactions are quoted.

Figure 5.4 shows that the range of values used for  $V_Q$  and  $V_H$  in the experiment were too narrow. Little variation was observed in the relative levels of analyte oxide ions with changing  $V_Q$ . Only modest variation was observed in the relative levels of analyte oxide ions with  $V_H$ ; increasing  $V_H$  from +2 to +6 V generally resulted in relative  $\text{MO}^+$  levels remaining at over 50 % of the initial value. The large range of reactions studied to ascertain the maximum energy available in the collision cell for reactions provided some ambiguous data. The dioxide and hydroxide ion products of reactions listed in Table 5.7 were not observed at levels greater than the background noise. It was expected that the

relative levels of the different oxides would allow the amount of energy available for reactions in the collision cell to be estimated, however this was not possible. The relative levels of products observed did not correlate with reaction enthalpies. Some products of highly endothermic reactions were observed at high levels, for example those forming  $\text{SrO}^+$  ( $\Delta H_r = +1.99$  eV) and  $\text{IrO}^+$  ( $\Delta H_r = +2.51$  eV), but a number of less endothermic reactions, such as  $\text{TeO}^+$  ( $\Delta H_r = +0.89$  eV), were observed at much lower levels. It is possible that these observations were due to kinetics, that the reactions not observed had much lower rate constants. This theory cannot be tested, as the rate constant data for many of the reactions involved was not available.

The dc potentials applied to the ion lenses varied the absolute potential of the ion beam, but it was not clear if these potentials would influence IKEE or KED. In order to observe the influence of the ion lenses on the reactivity of the collision cell or the transmission of cell-formed ions to the mass analyser, the ion lenses were individually systematically varied. Multi-element solution 1 (see Section 5.1.2) was used for this work, and  $1.0 \text{ ml min}^{-1}$  oxygen was in the collision cell. The  $^{115}\text{In}^+$  signal was monitored, as were the  $^{144}(\text{TeO})^+ / ^{128}\text{Te}^+$ ,  $^{216}(\text{PtO})^+ / ^{195}\text{Pt}^+$ ,  $^{224}(\text{PbO})^+ / ^{208}\text{Pb}^+$  and  $^{121}(\text{PdO})^+ / ^{105}\text{Pd}^+$  ratios. For all of the lenses studied, only minimal variation in the levels of oxides studied was apparent across the range of values for the lens giving an  $m/z$  115 signal of one half or greater the signal observed under optimum tuning conditions.

A further experiment was conducted with  $1.0 \text{ ml min}^{-1}$  oxygen in the cell. Data were collected using  $m/z$  set A and multi-element solution 1 (see Table 5.3 and Section 5.1.2, respectively, for details) at a range of  $V_H$  and  $V_Q$  values. Representative results from this experiment are shown in Figures 5.5 and 5.6. These results are presented in the form of graphs of response or ratio against  $V_Q - V_H$  (to show KED effects) for a range of different  $V_Q$  or  $V_H$  values (to show IKEE effects).  $V_H$  is used in place of  $V_H - V_P$  as  $V_P$  is unknown, but is expected to be stable and reproducible for a given set of ICP conditions.



**Figure 5.5 – Variation in the  $VO^+/V^+$  ratio with  $V_Q - V_H$  for a range of (i)  $V_Q$  values and (ii)  $V_H$  values. Collision cell gas  $1.0 \text{ ml min}^{-1}$  oxygen.**

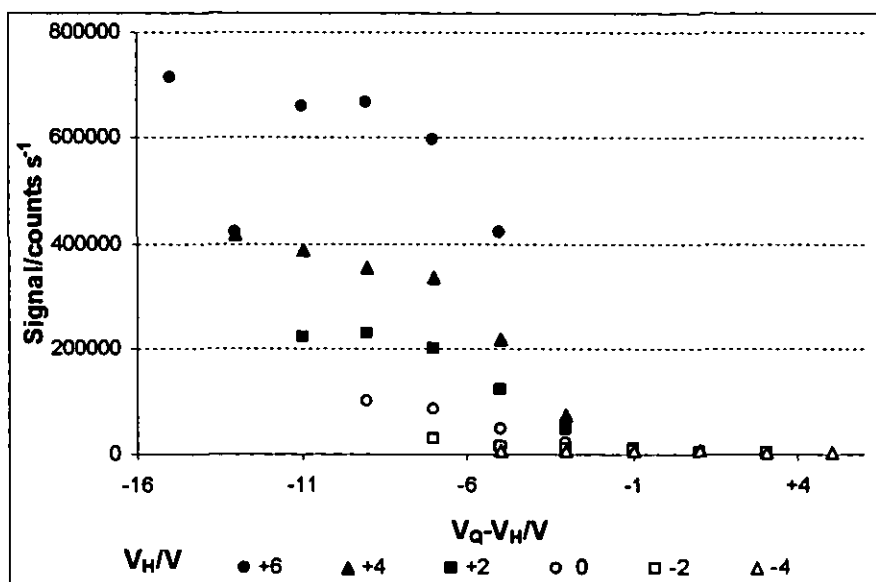


**Figure 5.6** – Variation in  $\text{In}^+$  signal with  $V_Q - V_H$ . Collision cell gas  $1.0 \text{ ml min}^{-1}$  oxygen.

The increased range  $V_H$  and  $V_Q$  values studied in this experiment provided evidence to support the existence of KED. Figure 5.5 shows that as a positive ‘potential barrier’ was introduced between the quadrupole and hexapole ( $V_Q - V_H > 0 \text{ V}$ ), the relative levels of  $\text{MO}^+$  ions detected fell away. ( $\text{VO}^+$  was formed by exothermic reactions,  $\Delta H_r = -0.7 \text{ eV}$ .) The  $\text{MO}^+$  ions, which were formed in the cell, had much lower kinetic energy than the  $\text{M}^+$  ions formed in the plasma. Thus,  $\text{MO}^+$  ions had insufficient energy to overcome low positive  $V_Q - V_H$  barriers that the more energetic  $\text{M}^+$  ions could still overcome.

Figure 5.6 shows the effect of  $V_Q - V_H$  on the transmission of  $\text{In}^+$  through the system. As  $V_Q - V_H$  was raised, the  $\text{In}^+$  signal decreased to a much lesser extent than  $\text{VO}^+/\text{V}^+$ . Raising  $V_Q - V_H$  significantly reduced the level of  $\text{MO}^+$ , due to KED, whilst the reduction in  $\text{M}^+$  was generally less than a sixth of that for  $\text{MO}^+$ . When  $V_Q - V_H > -1 \text{ V}$ , the levels of  $\text{In}$  detected had fallen from  $\sim 70\,000 \text{ counts s}^{-1}$  to negligible levels. It is also apparent from Figure 5.6 that the signal detected depends significantly on  $V_H$  as well as  $V_Q - V_H$ .

Figure 5.5(i) shows that as  $V_Q$  increased, the decrease in  $\text{VO}^+/\text{V}^+$  levels began at higher  $V_Q - V_H$  levels. Variation in ion beam focussing efficiency, discussed below is the most likely explanation of this effect. Figure 5.5(ii) shows that as  $V_H$  increased, the level of

$VO^+/V^+$  also increased. There are two possible explanations for this: that higher  $V_H$  produced elevated levels of  $VO^+$ , due to various effects occurring in the collision cell, which are discussed in detail in subsequent sections, or variation in the efficiency of the efficiency of ion beam focussing, discussed below.

The wide spread of signals in both Figures 5.5(ii) and 5.6 may have been caused by the other ion lenses. In the work reported above, the lenses were tuned initially and the same potentials applied to them for the duration of the experiment. However, as  $V_H$  was altered, the mean kinetic energy of the ion beam leaving the collision cell was varied. The energy spread may also have varied. The role of the ion lenses is to focus the ions into a narrow beam. As the kinetic energy of the ions was varied, the potentials required on the ion lenses to focus the ion beam would also have varied. Thus, the results reported above do not show purely quadrupole and hexapole bias effects, as the other ion lenses were not always optimally focussing the ion beam. This ion beam focussing problem was addressed in further work, reported in Sections 5.3.1.3 to 5.3.1.5 below, by the use of the Plasmalab software's inbuilt 'autotune' facility. This used an algorithm to vary the ion lens potentials to maximise a selected signal, in this case the  $^{115}\text{In}$  signal was used.

#### 5.3.1.2 Use of Helium/hydrogen as a Cell Gas

Mixtures of helium and hydrogen were employed in further work instead of oxygen. Oxygen was originally employed to maximise the levels of oxides produced for the cell energy characterisation work. The results of this work were inconclusive, so the emphasis of the study was redirected towards consideration of the roles of IKEE and KED. The  $1.0 \text{ ml min}^{-1}$  flow rate of oxygen employed lowered analyte sensitivity excessively, restricting the range of  $V_Q - V_H$  values that could be studied to those below 0 V as higher values gave negligible signals, thus making the study of KED very difficult. In contrast, when helium/hydrogen mixtures were employed, as discussed in Section 5.3.1.4 below, significant analyte signals were observed at positive values of  $V_Q - V_H$ .

Further experiments utilised the helium/hydrogen mixture established by Ingle *et al.*<sup>35</sup> as compromise conditions for multi-element analysis using ICP-CC-MS. This gas

combination was employed as elevated levels of  $\text{MO}^+$  ions were reported under those conditions ( $V_H = +3.86$  V,  $V_Q = -6$  V). For example, the presence of  $\text{TiO}^+$  in the spectra prevented the accurate determination of several Ni and Zn isotopes, causing the isotopic abundances recorded for the various Ni and Zn isotopes to be considerably different from the accepted values. To confirm that  $\text{TiO}^+$  was the cause of this effect, single-element solutions of  $50 \text{ ng ml}^{-1}$  Ti,  $20 \text{ ng ml}^{-1}$  Ni and  $20 \text{ ng ml}^{-1}$  Zn in 2 % nitric acid were prepared. Data were collected for these solutions using the helium+hydrogen  $1.0+1.7 \text{ ml min}^{-1}$  gas flows and the standard  $V_H$  and  $V_Q$  settings of  $+3.86$  V and  $-6$  V respectively.

Isotopic abundances for Zn and Ni, calculated from the single-element solution data are shown in Table 5.9. The results for the Ti solution showed the presence of a range of peaks in the  $m/z$  62–66 region corresponding to the various isotopes of  $\text{TiO}^+$ . The isotopic abundances calculated for Ni and Zn are close to the agreed<sup>9</sup> values, so the presence of  $\text{TiO}^+$  is confirmed to be the cause of the deviations observed in the earlier multi-element work.<sup>35</sup>

**Table 5.9** – Isotopic abundances of Ni and Zn calculated for  $20 \text{ ng ml}^{-1}$  single-element solutions. Data were acquired with helium+hydrogen  $1.0+1.7 \text{ ml min}^{-1}$  in the collision cell and  $V_H$  and  $V_Q$  values of  $+3.86$  V and  $-6$  V respectively.

Element	Isotope	Natural abundance <sup>9</sup> (%)	Calculated Abundance † (%)	Signal for Ti solution ( $\text{TiO}^+$ ) as a proportion of the signal for a blank (%)
Ni	58	68.30	65.8	96
	60	26.10	27.8	100
	61	1.13	1.3	100
	62	3.59	4.4	1800
	64	0.91	0.7	3700
Zn	64	48.60	44.7	3700
	66	27.90	28.6	620
	67	4.10	4.5	68 *
	68	18.80	21.4	54 *
	70	0.60	0.8	80 *

\* The level of Zn contamination was lower in the Ti standard than in the blank.

† No Ti was included in this solution.



In order to simplify multi-element analysis under these preferred conditions, it is necessary to minimise  $\text{MO}^+$  interferences. Experiments reported in the following sections explore the roles of IKEE and KED for this gas mixture. One of the applications of IKEE and KED is to minimise the detection of  $\text{MO}^+$ , by minimising its formation in the collision cell using IKEE and/or minimising its detection using KED.

#### *5.3.1.3 Energy Distribution in the Ion Beam*

To characterise the energy distribution of the ion beam, data were collected to produce 'stopping curves'.  $V_Q$  was varied with  $V_H$  and the ion lens voltages held constant to provide the stopping curve data.  $V_H$  was kept negative,  $-1.96\text{ V}$ , to prevent losses of ions due to energy discrimination occurring there. No collision cell gases used. The experiment was conducted twice, once with a conventional ICP and again with a grounded plasma screen employed, so as to determine the influence of the plasma screen on  $V_P$  and on the energy distribution. Hot (1350 W) plasma conditions were employed throughout. Differentiation of the 'stopping curve' data provides an approximation of the energy distribution of the ion beam. The raw stopping curve data were smoothed with a two point moving window, prior to differentiation, to produce consistency in change of slope. The 'stopping curves' and ion energy distributions are shown in Figure 5.7.

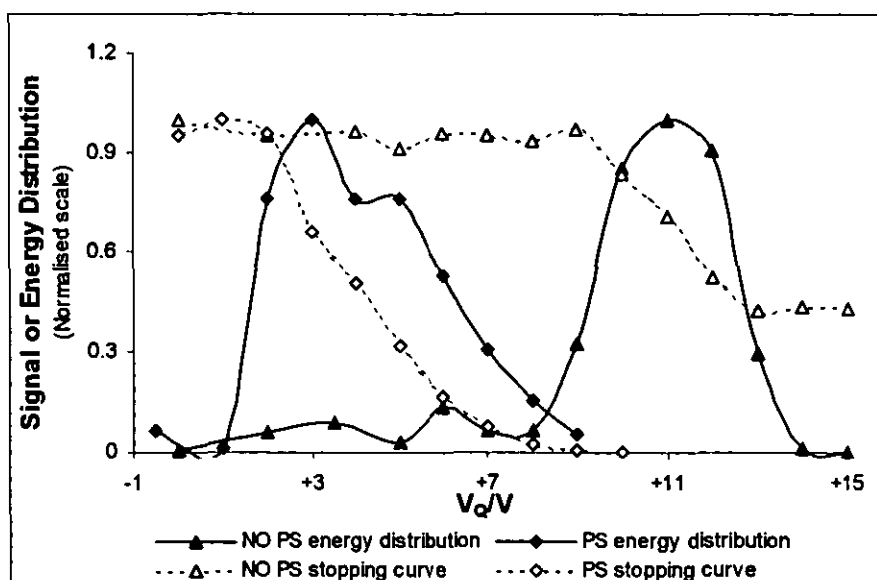


**Figure 5.7** – ‘Stopping curves’ and ion beam energy distributions for  $^{115}\text{In}^+$  with and without the use of a plasma screen. No collision cell gases were employed. (PS = plasma screen)

With no plasma screen employed, the energy distribution of the ion beam was Gaussian, peaking at  $V_Q \approx +11$  V with a width at half-height (half-width) of approximately 4.5 V. Thus the energy distribution of the ion beam was well defined, and occupied a relatively narrow range of values. When the grounded plasma screen was used, the energy distribution was no longer Gaussian. The ion distribution was asymmetric, with a peak at  $V_Q \approx +3$  V and a half-width of approximately 5.5 V. The asymmetry of the peak is evident when the two sides of the peak, either side of the maximum, are considered separately. The left side has a half-width of *ca.* 1.5 V and the right side is more than twice as wide, with a half-width of  $\sim 4$  V.

The median energy of the ion beam when the plasma screen was employed was some 8 V lower than when the plasma screen was not used. This was due to the influence of  $V_P$ . When the plasma screen was not employed, the plasma developed a positive offset potential, principally due to capacitive coupling with the rf coil. The ion beam was then accelerated by the potential difference itself and the grounded cones of the interface region. When the grounded plasma screen is introduced, this prevents capacitive coupling to the plasma. Instead the rf coils capacitatively couple with the grounded screen. The plasma still develops a slight positive potential that accelerates it through the interface region, but this is much smaller than the potential deriving from capacitive

coupling. The residual positive charge on the plasma is caused by the high mobility of electrons compared with cations, thus 'floating' plasmas are negative on the outside and positive in the centre. Where the plasma is close to the grounded sample cone, electrons migrate across the boundary layer leaving the plasma positive with respect to ground.

The asymmetry of the ion energy distribution when the plasma screen is employed may have been due to a variety of reasons. The most likely reason is that the introduction of the grounded screen established a potential gradient across the plasma, with a higher potential region remaining at the centre, producing the bias towards higher energy ions. Other possibilities are that the plasma screen did not entirely stop capacitive coupling to the plasma, so some rf leakage into the plasma caused the formation of higher potential regions which resulted in the bias towards faster ions.

The energy spread of the ion beam was relatively wide, regardless of the use of the plasma screen. The anticipated reduction in energy spread with plasma screen use did not occur. A small energy spread is important as it improves the efficacy of IKEE and KED as both effects utilise the control of ion energy. KED relies on ions produced in the plasma being faster than ions produced by reactions in the collision cell. A small energy spread minimises any overlap of the kinetic energy spreads of ions produced in the cell and ions produced in the plasma, making removal of cell-formed ions possible without significant loss of plasma-formed ions by the 'potential barrier' used for KED.

A number of other plasma screen-based strategies were employed to further explore the influence of plasma conditions on  $V_p$  and ion energy distribution. These are discussed in Section 5.3.2, following further discussions on ion energy, IKEE and KED and the influence of the plasma screen thereon.

#### 5.3.1.4 Ion Energy, Reactivity and Species Selectivity

In this section, the ion kinetic energy effect and kinetic energy discrimination are discussed. The following definitions apply to the two terms, as used here.

‘Ion kinetic energy effect’ (IKEE) – variation of the collision cell reactivity by control of input ion energy.

‘Kinetic energy discrimination’ (KED) – exclusion of slow, cell-formed, ions from the mass analyser.

The term IKEE was defined by the author.<sup>140</sup> The definition of KED adopted here is based on definitions given, or implied, in the literature.<sup>81,140,142</sup> Other effects of varying  $V_H - V_P$  or  $V_Q - V_H$ , e.g. multipole transmission effects, are not IKEE or KED under these definitions. Thus, for example, the work in which helium was used to slow ions, with polyatomic ions slowed more than atomic ions due to their larger size and those slower ions excluded from the cell by a ‘potential barrier’, as discussed in Section 2.3.2.4 above did not feature KED by this definition.

Results are presented as graphs of response or ratio against  $V_Q - V_H$  for a range of different  $V_H$  values. (As before,  $V_H$  values are given in place of  $V_H - V_P$  as  $V_P$  is unknown, but expected to be stable for a given set of operating conditions.) The results presented focus on the reactive removal of argon dimer ions ( $\text{Ar}_2^+$ ) by hydrogen and the formation of the metal oxide ions  $\text{CeO}^+$ ,  $\text{CrO}^+$ ,  $\text{TeO}^+$  and  $\text{VO}^+$ . These oxides were selected because of their thermodynamics (see Section 5.2 generally). Possible pathways for the reactions, together with reaction enthalpies and, where available, rate constants are given in Table 5.8 (p143).

All of the work reported in this section employed multi-element solution 2 (details in Section 5.1.2) and ‘autotune’ was used to optimise the  $^{115}\text{In}$  signal at each step. The majority of this work used  $m/z$  set B (Table 5.3), with the exceptions of work using helium only (Figures 5.10(ii) and 5.13(ii)) and various flow rates of helium and hydrogen (Figure 5.14) where  $m/z$  set C (Table 5.3) was used to reduce the data acquisition time and therefore maximise the range of  $V_Q$  and  $V_H$  values studied in a single run.

An initial investigation was conducted to identify an analytically useful range of  $V_H$  values for further study. Helium+hydrogen 1.0+1.7 ml min<sup>-1</sup> cell gas was used.  $V_Q - V_H = -10$  V was used to ensure that KED was not significant.

The effect of  $V_H$  on the  $^{115}\text{In}$  signal and  $^{156}(\text{CeO})^+ / ^{140}\text{Ce}^+$  ratio are shown in Figure 5.8. As  $V_H$  increased, the  $\text{In}^+$  signal gradually increased to reach a maximum when  $V_H \approx +8$  V and then decreased successively as more ions were excluded from reaching the analysing quadrupole. The reasons for this are discussed below, with respect to Figure 5.9.

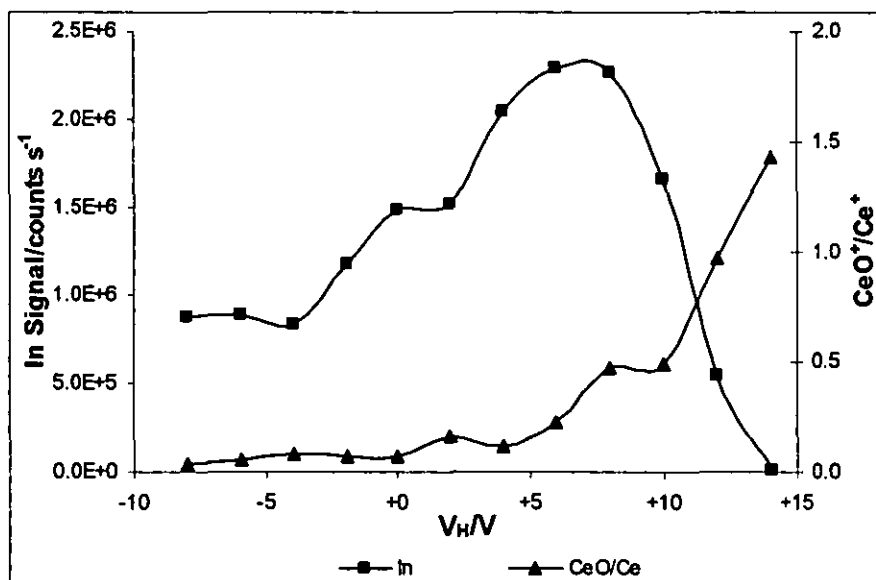


**Figure 5.8** – Variation in  $^{115}\text{In}^+$  signal and  $^{156}(\text{CeO})^+ / ^{140}\text{Ce}^+$  with  $V_H$ .  $V_Q - V_H = -10$  V throughout. Helium+hydrogen 1.0+1.7 ml min<sup>-1</sup> cell gas.

The  $\text{CeO}^+ / \text{Ce}^+$  ratio increased with increasing  $V_H$ . The  $V_H$  region  $-4$  V to  $+4$  V was chosen for further study as the  $\text{In}$  sensitivity was analytically useful in this region and  $\text{CeO}^+$  levels were moderate.

### Analyte Sensitivity

Variation in analyte sensitivity ( $^{115}\text{In}$  signal) with  $V_H$  and  $V_Q - V_H$  is shown in Figure 5.9. As the data points were collected in a single run, points are linked together into  $V_H$  series for illustrative purposes only. The accelerating potential between the quadrupole and hexapole ensured that the majority of the transmitted ions were mass analysed.

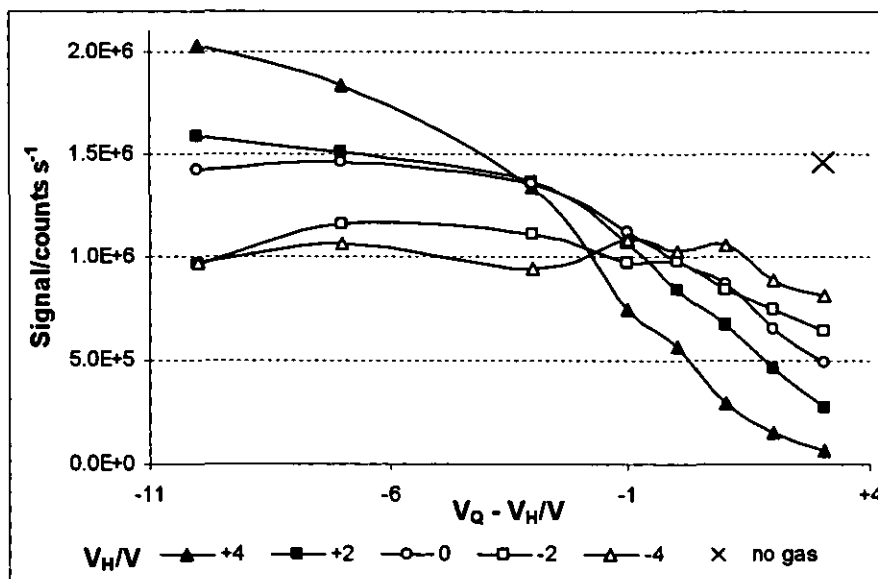


Figure 5.9 – Variation in  $^{115}\text{In}^+$  signal with  $V_Q - V_H$  at a range of  $V_H$  values. Helium+hydrogen  $1.0+1.7 \text{ ml min}^{-1}$  cell gas.

The highest signals were observed when  $V_H$  was high positive and  $V_Q - V_H$  was negative. Increasing  $V_H$ , as shown in here (Figure 5.9) and in Figure 5.8, slows ions entering the hexapole which appeared to improve its transmission, although the reasons for this are not entirely clear. One likely explanation is that slower ions will experience more rf cycles on their transit through the cell and will thus be better focussed towards the axis of the hexapole.

As  $V_Q - V_H$  was increased, analyte sensitivity decreased. This was due to exclusion from the quadrupole of low energy ions from the plasma. On raising  $V_H$ , the energy of the ion beam is lowered leaving successively less of the ions with sufficient energy to overcome the  $V_Q - V_H$  potential difference. This effect was dominant at positive  $V_Q - V_H$  so the order of the  $V_H$  series was reversed. When the data was considered in terms of  $V_Q$ , rather than  $V_Q - V_H$ , the role of  $V_H$  in controlling ion energy was more evident. For a given  $V_H$  value, the fall in analyte sensitivity began at a  $V_Q$  value 1–2 V lower than  $V_H$ . The ion energy is thus closely related to  $V_H$ .

Collisional focussing<sup>152</sup> is the enhancement of analyte signals when collision cell gases are employed. Ions are better contained along the axis of the collision cell multipole

when they have less energy. In collisional focussing, ions lose energy by collision with gases in the cell. Collisional focussing effects are thus influenced by the nature (how much energy is lost in the collision) and pressure (or flow rate) (number of collisions) of the gas employed. Collisional focussing arguments cannot be applied in this case as the gas flows were constant throughout so variations in the level of collisional focussing did not occur. Furthermore, workers at Loughborough University<sup>140</sup> found that collisional focussing was only evident in this collision cell at much higher gas flows ( $> 7 \text{ ml min}^{-1}$  helium) and only for heavier elements, *e.g.* Pb.

### Argon-based Ions

Figure 5.10 shows the results obtained for  $\text{Ar}_2^+$ . Results are shown for the reactive gas mixture helium+hydrogen  $1.0+1.7 \text{ ml min}^{-1}$  and for  $2.0 \text{ ml min}^{-1}$  helium only.

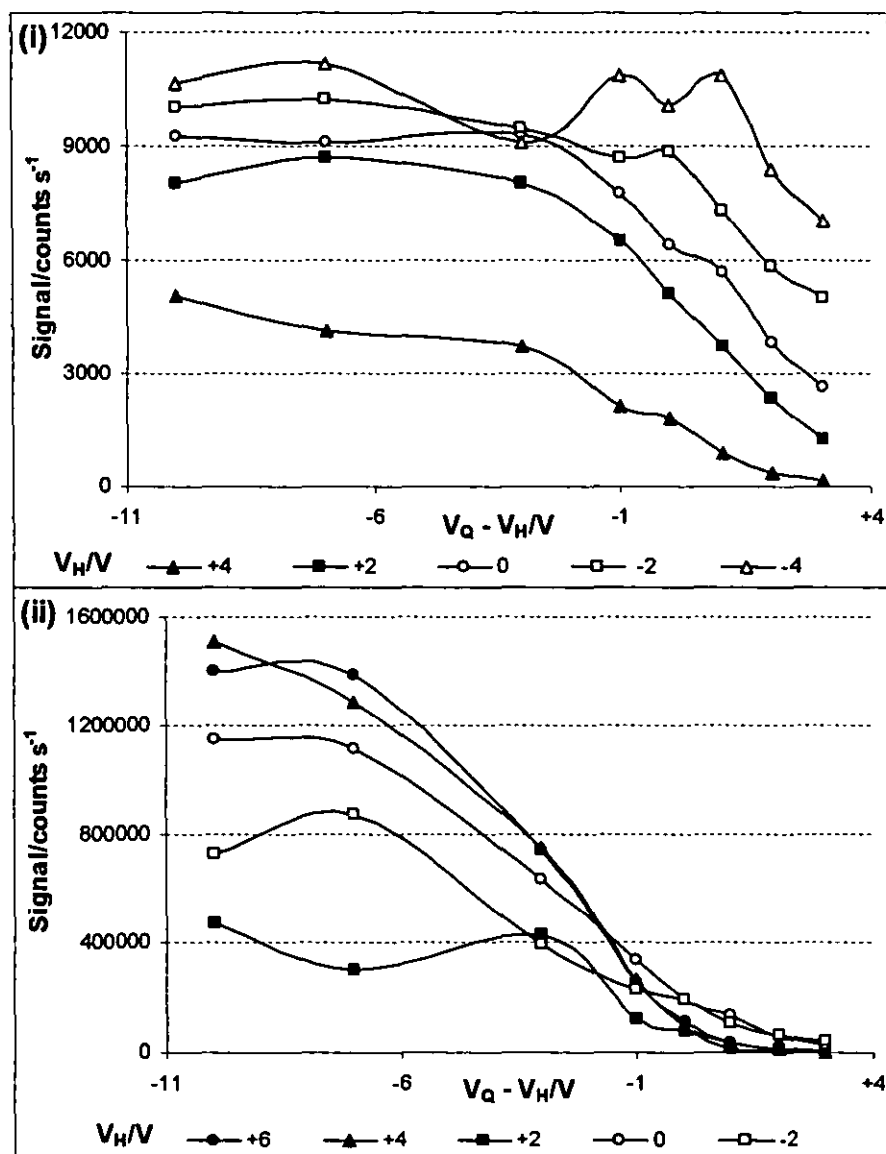


**Figure 5.10** – Variation in  $^{80}(\text{Ar}_2)^+$  signal with  $V_Q - V_H$  at a range of  $V_H$  values. Collision cell gases (i) helium+hydrogen  $1.0+1.7 \text{ ml min}^{-1}$  and (ii) helium  $2.0 \text{ ml min}^{-1}$

The results obtained for  $\text{Ar}_2^+$  with the helium/hydrogen mixture are shown in Figure 5.10(i) and are discussed first. The  $V_H$  series fell in the opposite order to that observed for  $\text{In}^+$  (Figure 5.9) at negative  $V_Q - V_H$ . The lowest  $\text{Ar}_2^+$  signal corresponded with the most positive  $V_H$  value studied. With  $V_Q - V_H$  held constant at  $-10 \text{ V}$ , raising  $V_H$



from  $-4$  to  $+4$  V reduced the  $\text{Ar}_2^+$  signal to less than half its original value, indicating a significant change in cell reactivity between the two conditions. The results clearly show that reactivity in the cell depends on the initial ion kinetic energy, as varied by  $V_H - V_P$ . The fall in  $\text{Ar}_2^+$  with increasing  $V_H$  was achieved against an underlying increase in hexapole transmission efficiency.

Slowing the ions produced a higher degree of reactive attenuation of the argon dimer. This is to be expected for two reasons; firstly, reaction cross-sections tend to increase as ion energy is reduced<sup>47</sup> and, secondly, lowering the energy increases the number of collisions that an ion experiences during its transit through the cell. Observed reactivity is the product of these two effects, although they are difficult to resolve in this situation. Hydrogen is not a highly reactive gas and therefore reactions do not generally proceed at the collision rate thereby allowing scope for IKEE to be modified by thermalising collisions before reaction takes place. For highly reactive gases, such as ammonia, the reaction may well proceed at the collision rate and therefore IKEE should operate because the first collision counts and this occurs at the initial ion energy. Reactions in collision cells do not proceed to equilibrium in the normal sense because concentration ratios virtually exclude the reverse reaction. In the original reaction, the level of the reactant gas is high, whereas the concentration of neutral products, especially those only present as the result of reactions such as O and H, are much lower, greatly reducing the probability of the appropriate reactants colliding – the first step necessary for the reverse reaction to occur. Considerations such as this indicate that normal concepts of thermal equilibrium are not necessarily helpful in describing these devices. The issue is further complicated because the kinetic and thermodynamic data quoted to support arguments have almost invariably been obtained under conditions of thermal equilibrium.

$\text{Ar}_2^+$  is predominantly a plasma- (or interface-) formed ion, with little or none formed in the collision cell, so no KED was expected or observed. The signals at constant  $V_H$  were approximately constant for  $V_Q - V_H < 0$ . When  $V_Q - V_H > 0$ , the fall in signal observed was, as with  $\text{In}^+$ , due to exclusion of low energy ions formed in the plasma. Conveniently, for  $V_Q - V_H < -3$  V (the normal operating region), the lowest level of  $\text{Ar}_2^+$ , *i.e.* the maximum reactivity in the cell, occurred at the same  $V_H$  as maximum  $\text{In}^+$  transmission,  $+4$  V. Lower levels of  $\text{Ar}_2^+$  were obtained at positive  $V_Q - V_H$ , but here the

analyte signals were grossly attenuated too. When  $V_H = +4$  V, the analyte signal was reduced to less than 25 % of its maximum level when  $V_Q - V_H$  was increased to positive values.

Figure 5.10(ii) shows results for  $Ar_2^+$  with  $2.0 \text{ ml min}^{-1}$  helium (only) in the cell. In the absence of the reactive gas, the series order reverted to that observed for  $In^+$ . The absence of reactivity in the cell means that IKEE associated with the  $Ar_2^+/H_2$  reaction was not observed. The hexapole transmission and mass analyser exclusion effects were dominant.

#### Oxide Ion Products of Exothermic Reactions

Variation in  $CeO^+/Ce^+$  and  $VO^+/V^+$  with  $V_H$  and  $V_Q - V_H$  is shown in Figure 5.11.  $CeO^+$  and  $VO^+$  were formed by exothermic reaction with oxygen and/or water in the cell; the reactions are detailed in Table 5.8 (p143).

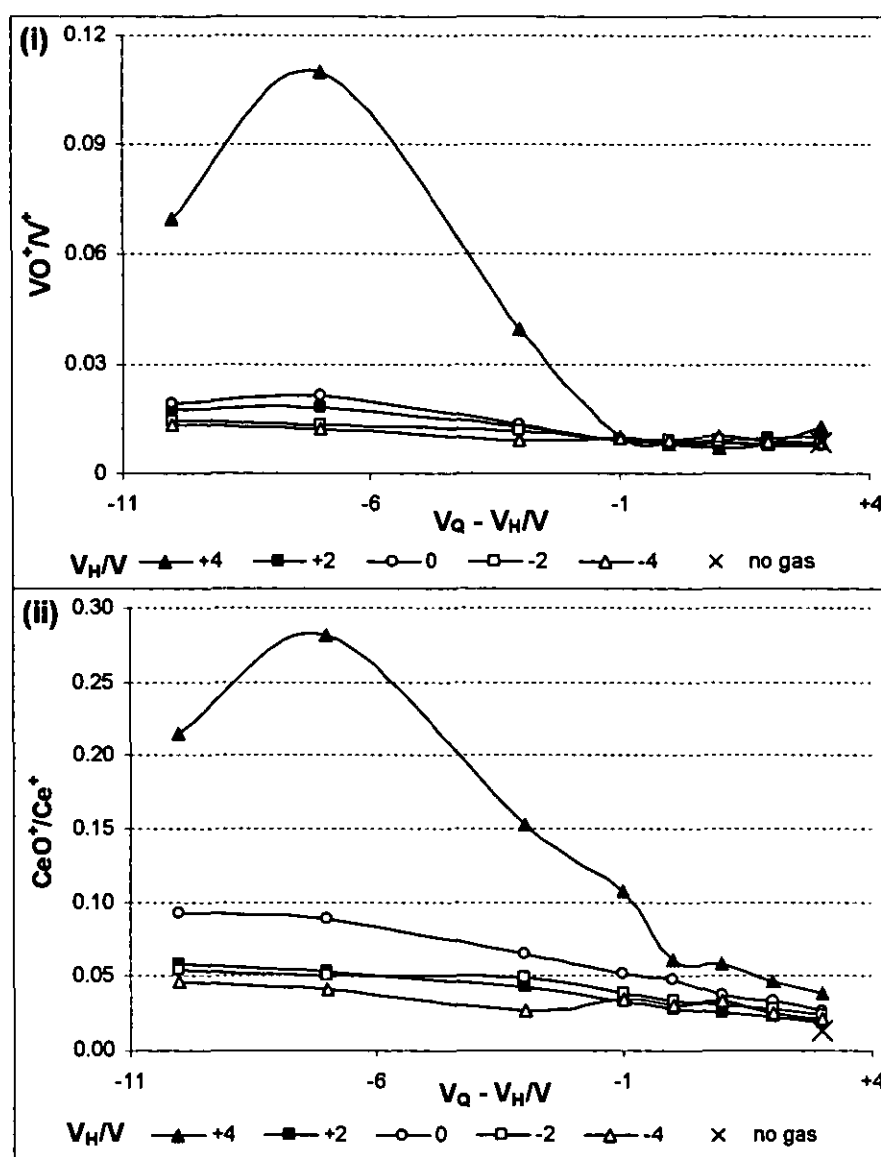


**Figure 5.11** – Variation in (i)  $^{67}(VO)^+/^{51}V^+$  and (ii)  $^{156}(CeO)^+/^{140}Ce^+$  with  $V_Q - V_H$  at a range of  $V_H$  values. Collision cell gases helium+hydrogen  $1.0+1.7 \text{ ml min}^{-1}$

The results clearly show that the  $MO^+/M^+$  ratio for oxides produced by exothermic reactions in the cell depend strongly on both  $V_H$  and  $V_Q - V_H$ . When  $V_Q - V_H$  was negative, as in Figure 5.8, the  $MO^+/M^+$  ratio varied considerably with  $V_H$ , due to increased reactivity at high  $V_H$ . IKEE thus had a significant influence on the level of oxide ions in the cell. On increasing  $V_Q - V_H$  from -10 to -1 V the level of  $MO^+/M^+$  rapidly decreased due to the onset of KED. However as  $CeO^+$  was formed in both the plasma and the cell and KED only discriminates against ions formed in the cell, the attenuation was less (a factor of five for  $V_Q - V_H$  changing from -7 to -1 V) than for  $VO^+$

which is predominantly formed in the cell (a factor of ten over the same range). The rapid increase in  $MO^+/M^+$  when  $V_H$  was raised from +2 to +4 V was unexpected, but appears to be a further indication that reaction rates can be very sensitive to ion energy. This sensitivity is illustrated in the data even though the input ion energy distribution has a width of a few volts. Ervin and Armentrout<sup>47</sup> showed that reaction rate cross-sections generally increased at lower ion energies, but not at a steady rate and could show significant variation over small energy ranges (their data was obtained under quasi-thermal conditions, they did not employ an ICP source).

#### Oxide Ion Products of Endothermic Reactions

Variation in  $CrO^+/Cr^+$  and  $TeO^+/Te^+$  with  $V_H$  and  $V_Q - V_H$  is shown in Figure 5.12.  $CrO^+$  and  $TeO^+$  were formed by endothermic reaction with oxygen and/or water in the cell; the reactions are detailed in Table 5.8 (p143). The  $^{52}Cr^+$  signal was not corrected for  $ArC^+$  as predictions of the  $^{52}Cr^+$  signal from  $^{53}Cr^+$  showed that the contribution of  $ArC^+$  was minimal.

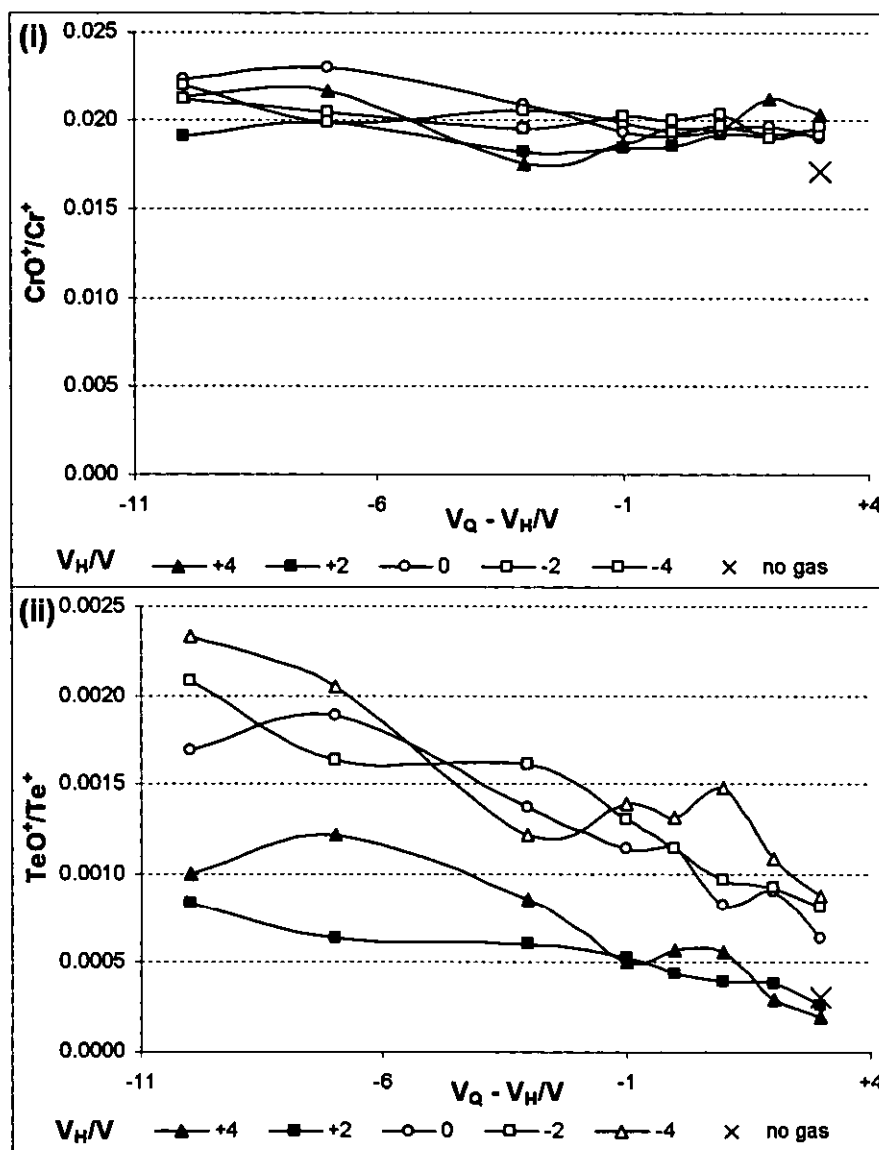


**Figure 5.12** – Variation in (i)  $^{68}\text{CrO}^+ / ^{52}\text{Cr}^+$  and (ii)  $^{144}\text{TeO}^+ / ^{128}\text{Te}^+$  with  $V_Q - V_H$  at a range of  $V_H$  values. Collision cell gases helium+hydrogen  $1.0+1.7 \text{ ml min}^{-1}$ .

The relative levels of  $\text{CrO}^+$  and  $\text{TeO}^+$  were significantly lower than those for the oxides formed by exothermic reactions.  $\text{TeO}^+/\text{Te}^+$  was lower than the equivalent  $\text{CrO}^+/\text{Cr}^+$  value despite  $\text{TeO}^+$  being formed by a less endothermic reaction than that producing  $\text{CrO}^+$ ; this is believed to be due to the effect of the reaction kinetics.

$\text{TeO}^+$  does not appear to have been formed in the plasma to any significant extent (note the data with no gas in the cell) and with an enthalpy of +1 eV was not significantly produced in the cell (maximum  $\text{TeO}^+/\text{Te}^+$  level 0.25 %). Nevertheless, the trend of the  $V_H$  series was, as expected, the opposite of that observed for  $\text{CeO}^+$  and  $\text{VO}^+$ , with the

highest oxide levels corresponding to the most negative  $V_H$ . This effect was due to the energy requirements of the endothermic reactions, which proceed faster as ion energy increases. The lack of  $\text{TeO}^+$  formation in the cell indicates that less than 1 eV was available in the centre-of-mass frame in the cell, from rf or other sources, to promote endothermic reactions.

The data presented here shows that IKEE significantly affects reactivity in the cell for both exo- and endothermic reactions.

#### $\text{H}_3\text{O}^+/\text{Ar}^+$ Reactivity Monitor

Figure 5.13 shows results for  $^{21}(\text{H}_3\text{O})^+ / ^{36}\text{Ar}^+$  with helium+hydrogen 1.0+1.7 ml min<sup>-1</sup> and with 2.0 ml min<sup>-1</sup> helium in the cell. The  $^{21}(\text{H}_3\text{O})^+ / ^{36}\text{Ar}^+$  ratio has previously been identified<sup>35</sup> as maximising under helium/hydrogen collision cell gas conditions optimal for multi-element analysis. The ratio was considered in this work in order to investigate its relevance as a cell reactivity monitor when ion energies were varied.

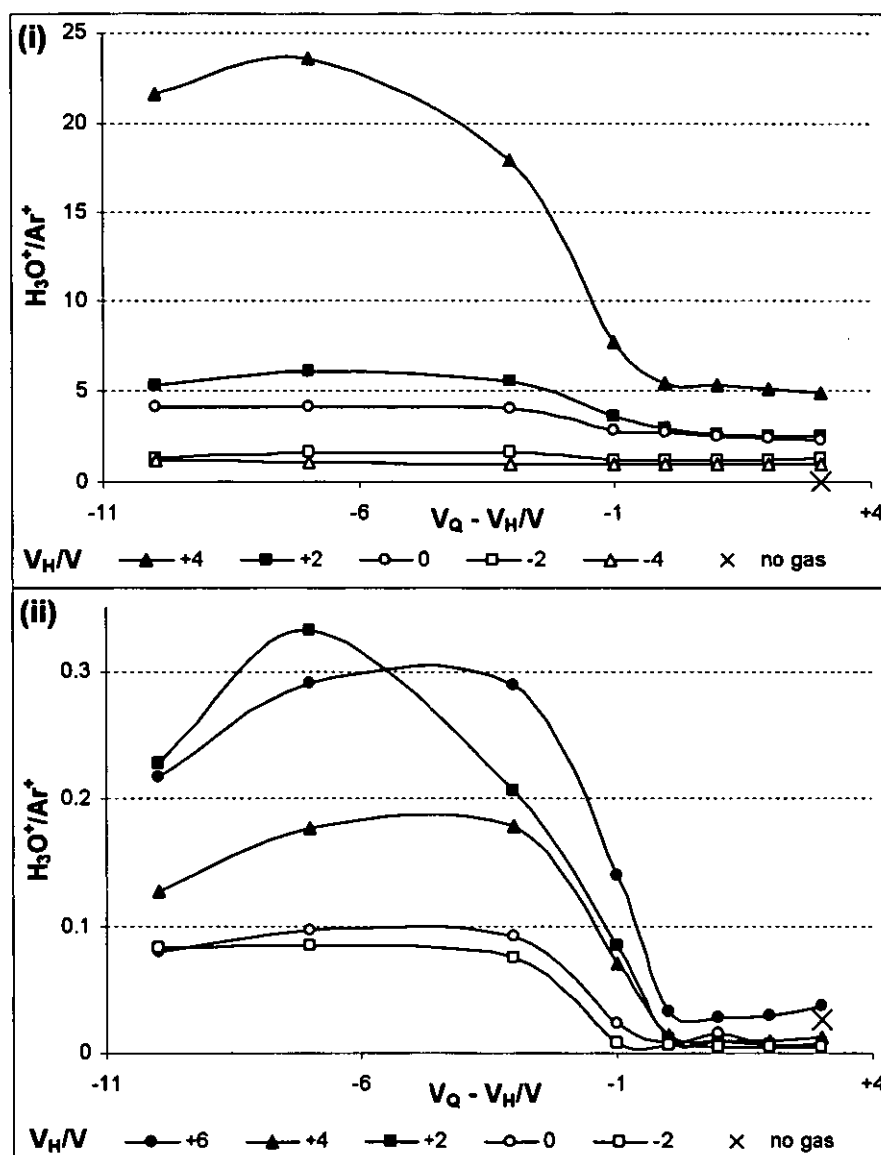


**Figure 5.13** – Variation in  $^{21}\text{H}_3\text{O}^+ / ^{36}\text{Ar}^+$  with  $V_Q - V_H$  at a range of  $V_H$  values. Collision cell gases (i) helium+hydrogen 1.0+1.7 ml min<sup>-1</sup> and (ii) helium 2.0 ml min<sup>-1</sup>

The maximum value of the  $^{21}\text{H}_3\text{O}^+ / ^{36}\text{Ar}^+$  ratio with helium/hydrogen was almost two orders of magnitude higher than that observed when helium alone was in the cell. The results show that  $^{21}\text{H}_3\text{O}^+ / ^{36}\text{Ar}^+$  can be used to monitor both IKEE and KED effects as the variation in the ratio closely mirrored the formation of oxides by exothermic reactions.

The two ions represented by their minor isotopes in the ratio are affected in different ways by  $V_H$  and  $V_Q - V_H$ . The  $\text{H}_3\text{O}^+$  ion is formed, and the  $\text{Ar}^+$  ion removed, by exothermic reactions in the cell (possible reactions are given in Table 5.8, p143). Thus,

at optimal conditions for exothermic reactions the numerator of the ratio increased and the denominator decreased – both effects increasing the value of the ratio. The highest value of the ratio corresponded with the highest  $V_H$  values studied, when incoming ions were slowed (IKEE). In addition, as  $H_3O^+$  was formed in the cell, these ions were of low energy compared to those formed in the plasma. These low energy ions were unable to overcome a positive  $V_Q - V_H$  'potential barrier' and so were excluded from the mass analyser (KED). The order of the series was not affected by KED, so maximising  $^{21}(H_3O)^+/^{36}Ar^+$  when KED is occurring will still optimise sensitivity/exothermic reactivity. The maximum occurred under conditions of optimum sensitivity/exothermic reactivity and when KED was not occurring. The  $^{21}(H_3O)^+/^{36}Ar^+$  reactivity indicator ratio can therefore be used to optimise sensitivity and exothermic reactivity in the cell using IKEE, whether or not KED is employed.

The  $^{21}(H_3O)^+/^{36}Ar^+$  ratio was much lower when helium alone (Figure 5.13(ii)) was used in the cell, although the small amount of  $H_3O^+$  formed and  $Ar^+$  removed still showed similar IKEE and KED effects to those observed with the reactive helium/hydrogen cell gas mixture.

#### Variation of Gas Flow Rate

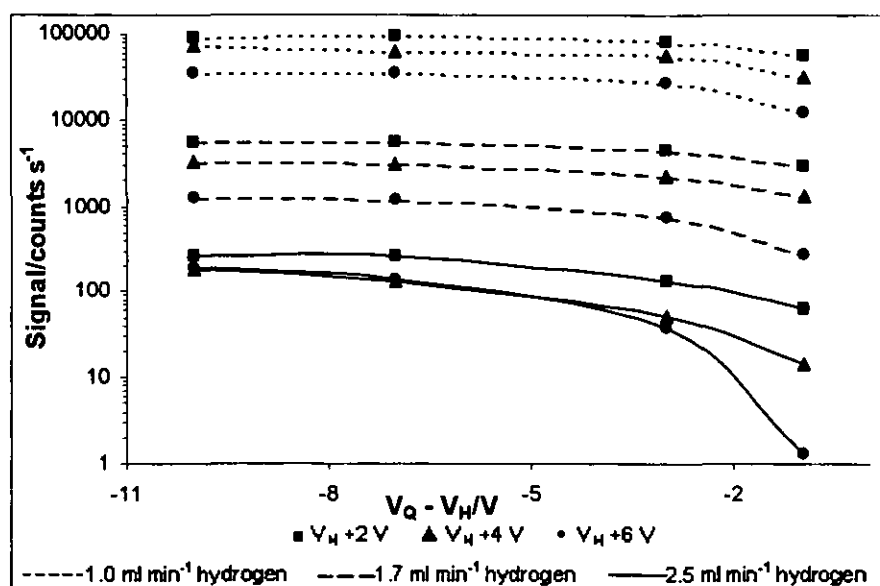


**Figure 5.14** – Variation in  $^{80}(Ar_2)^+$  signal with  $V_Q - V_H$  at  $V_H$  values of +2, +4 and +6 V for helium+hydrogen collision cell gas flows of 1.0+1.0, 1.0+1.7 and 1.0+2.5 ml min<sup>-1</sup>



Figure 5.14 shows the variation on  $\text{Ar}_2^+$  with  $V_H$  and  $V_Q - V_H$  at a range of gas flows. Two effects were observed in these results. Firstly, the  $V_H$  trends discussed for argon dimer above are still apparent at each gas flow and the level of argon dimer observed decreased with increasing hydrogen flow rate as was expected. Secondly, thermalisation of the ions, which results in loss of axial velocity, was indicated by the increasingly steep fall off in signal (with increasing  $V_Q - V_H$ ) as the hydrogen flow rate increased.

#### *5.3.1.5 Influence of the Plasma Screen on IKEE*

As was shown in Section 5.3.1.3 above, the use of a grounded plasma screen significantly reduced plasma offset potential. Such a reduction in  $V_P$  would vary the  $V_H - V_P$  potential difference, and therefore affect IKEE. Experiments were conducted using multi-element solution 2; data were collected using  $m/z$  set C (details in Section 5.1.2 and Table 5.3 respectively). Collision cell gas of helium+hydrogen  $1.0+1.7 \text{ ml min}^{-1}$  was used throughout. Data were collected at a range of  $V_H$  and  $V_Q$  potentials with and without the grounded plasma screen employed. 'Autotune' was used at each step to optimise the  $^{115}\text{In}$  signal. The data presented were collected during a single run to minimise any non-plasma screen related variation in operating conditions occurring.

#### Analyte Transmission

The effects on In sensitivity of varying  $V_H$  and  $V_Q - V_H$  with and without the use of the plasma screen are shown in Figure 5.15. When the plasma screen was not used, the results show the same trend as was previously observed (Section 5.3.1.4). At negative  $V_Q - V_H$ , the best transmission occurred at the most positive  $V_H$  value, *i.e.* the slowest ions were the best transmitted. At positive  $V_Q - V_H$ , the fastest ions (most negative  $V_H$ ) were best able to overcome the 'potential barrier' and so were the best transmitted.

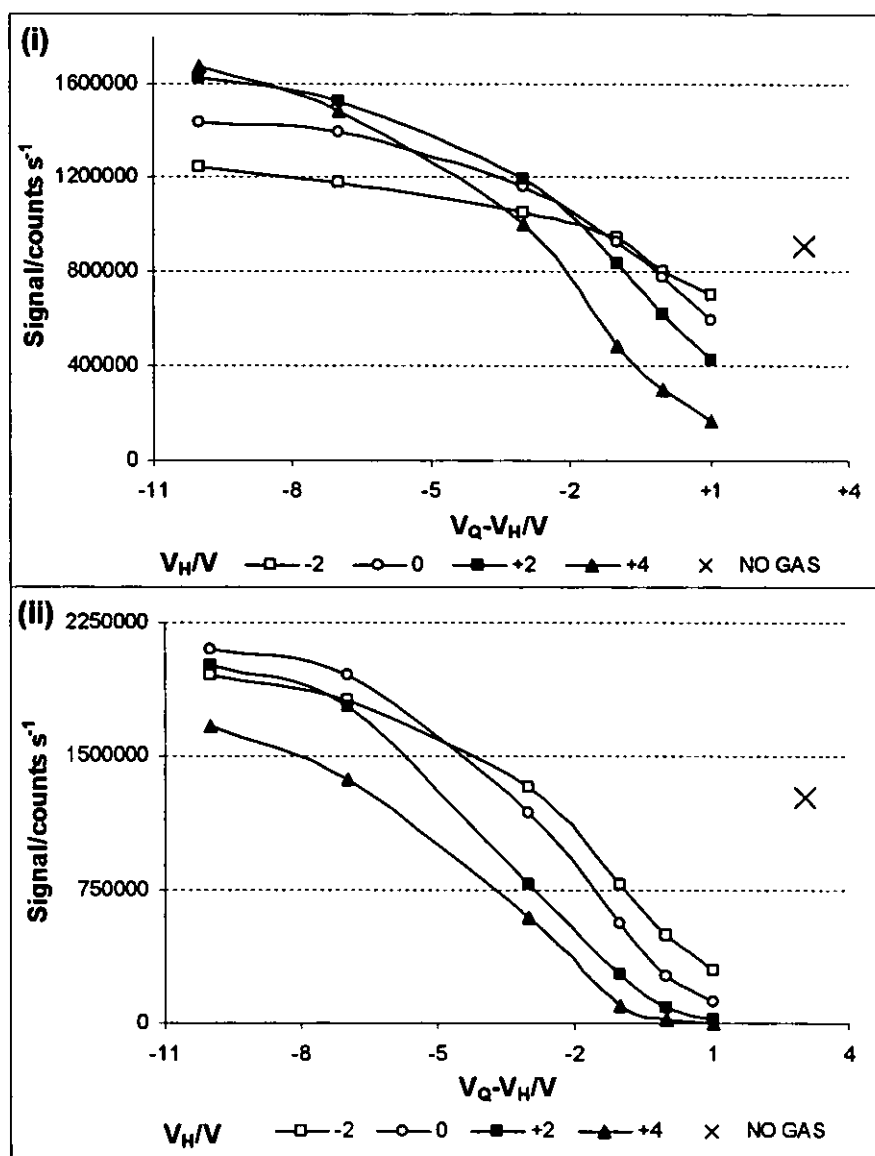


**Figure 5.15** – Variation in  $^{115}\text{In}^+$  signal with  $V_Q - V_H$  at various  $V_H$  values; (i) without and (ii) with plasma screen. Collision cell gases helium+hydrogen  $1.0+1.7 \text{ ml min}^{-1}$ .

When the plasma screen was introduced (Figure 5.15(ii)), the results were quite different. The general suppression of signals as  $V_Q - V_H$  increased remained, with the fastest ions giving the best signals. When  $V_Q - V_H$  was negative, and thus rejection of ions by the quadrupole was minimised, the order of the  $V_H$  values was quite different to when no plasma screen was employed. With the plasma screen employed, the slowest ions,  $V_H = +4$  V, gave the lowest signal and the next slowest,  $V_H = +2$  V, gave the second lowest signal. The remaining two series, 0 V and -2 V, followed the pattern observed with no screen; the slower ions were better transmitted at the most negative  $V_Q - V_H$  and the faster ions were the better transmitted at more positive  $V_Q - V_H$ . The changeover

point was some 6 V more negative than when the plasma screen was not used. These observations show the effects of the lower plasma offset potential ( $V_P$ ) when the plasma shield was employed. When the plasma screen was used,  $V_P$  was some 8 V lower (see Section 5.3.1.3), so the  $V_H - V_P$  barrier was, for a given  $V_H$  value, raised by the same amount. At the more positive  $V_H$  values studied, the  $V_H - V_P$  potential difference rejected ions before they reached the collision cell or left the ions with insufficient energy to traverse the cell. Thus, two effects are noticeable when  $V_H$  is varied, IKEE from varying collision cell reactivity and a loss of signal at high  $V_H$  due to the 'potential barrier' between the hexapole and the plasma, similar to that between the quadrupole and hexapole used in KED.

#### Argon-based Ions

Figure 5.16 shows the effect on  $\text{Ar}_2^+$  levels of varying  $V_Q - V_H$  with and without plasma screen use. The effect of the plasma screen on  $\text{Ar}_2^+$  levels was less dramatic than its effect on analyte sensitivity. The order of the series was not affected by the use of the plasma screen, the slowest ions (most positive  $V_H$ ) still gave the lowest levels of  $\text{Ar}_2^+$ . (Slower ions promote the exothermic reaction that removes  $\text{Ar}_2^+$ .)

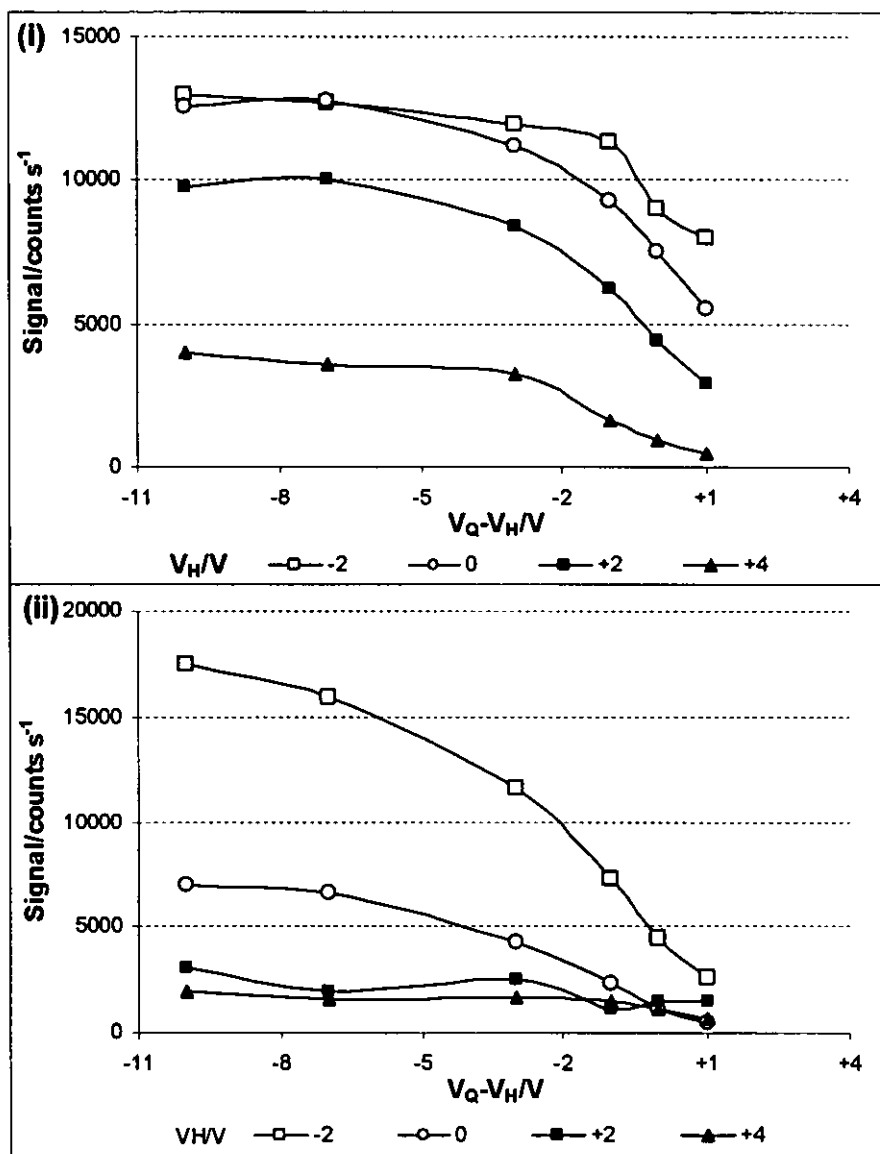


**Figure 5.16** – Variation in  $^{80}\text{Ar}_2^+$  signal with  $V_Q - V_H$  at a range of  $V_H$  values; (i) without and (ii) with plasma screen. Collision cell gas helium+hydrogen  $1.0+1.7 \text{ ml min}^{-1}$ .

The only significant difference when the plasma screen was introduced was the more rapid loss of  $\text{Ar}_2^+$  as  $V_H$  increased, representing the shift in  $V_H - V_P$  values. Without the plasma shield, the  $V_H -2, 0$  and  $+2 \text{ V}$  series were close in value, with the  $V_H +4 \text{ V}$  series less than half the value of the  $+2 \text{ V}$  series. By contrast, with the grounded plasma screen in use, the  $-2 \text{ V}$  series is more than twice as high as the remaining series, which are all close in value. This suggests that reactivity changes very rapidly over a small change in energy, represented by the  $+4$  and  $-2 \text{ V}$  series in Figure 5.16(i) and (ii) respectively.

The 6 V difference in  $V_H$  approximately cancelling out the  $V_P$  change when the plasma screen was used; the two series having similar  $V_H - V_P$  values.

#### *Oxide Ion Products of Exothermic Reactions*

Results for  $CeO^+$ , which was formed by exothermic reaction in the cell, are presented in Figure 5.17.  $VO^+$ , which was also formed by exothermic reaction, is not shown, as the results for both exothermic oxides were very similar to each other and not especially informative.

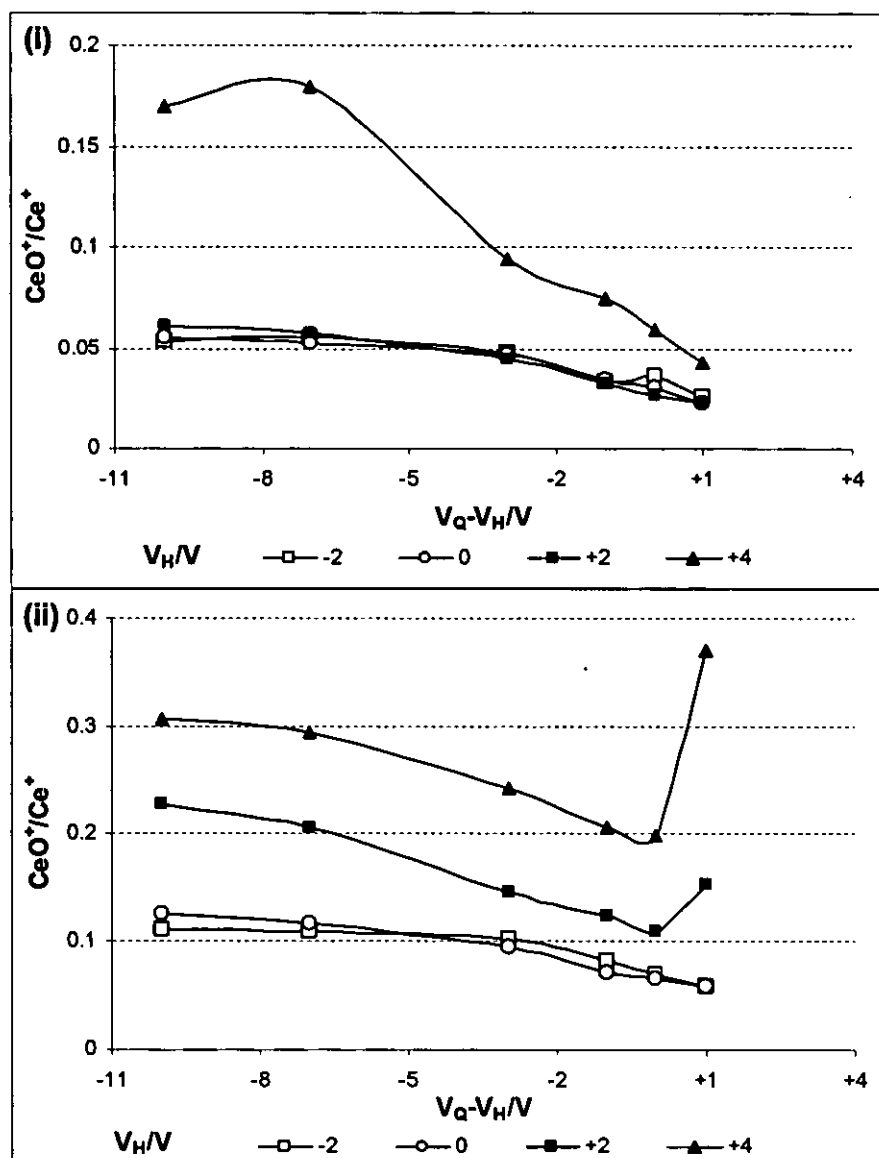


**Figure 5.17 – Variation in  $^{156}(\text{CeO})^+ / ^{140}\text{Ce}^+$  with  $V_Q - V_H$  at a range of  $V_H$  values; (i) without and (ii) with plasma screen. Collision cell gas helium+hydrogen  $1.0+1.7 \text{ ml min}^{-1}$ .**

When the plasma screen was employed, no change in the order of the  $V_H$  series was observed, the slowest ions (highest  $V_H$ ) gave the highest levels of  $\text{MO}^+$ . The dramatic change in relative levels of  $\text{MO}^+$  observed between  $V_H +4$  and  $V_H +2$  V when the plasma screen was not employed was not observed when the plasma shield was introduced, due to the shift in  $V_H - V_P$  values discussed above. The upward ‘kick’ at positive  $V_Q - V_H$  for the slowest ions ( $V_H +2$  and  $+4$  V) was caused by the dramatic decrease in analyte sensitivity there, rather than any sudden increase in oxide levels, and was therefore of no

significance. The reduced  $V_H - V_P$  value appears to leave the plasma formed ions with insufficient energy to traverse the cell.

Oxide Ion Products of Endothermic Reactions

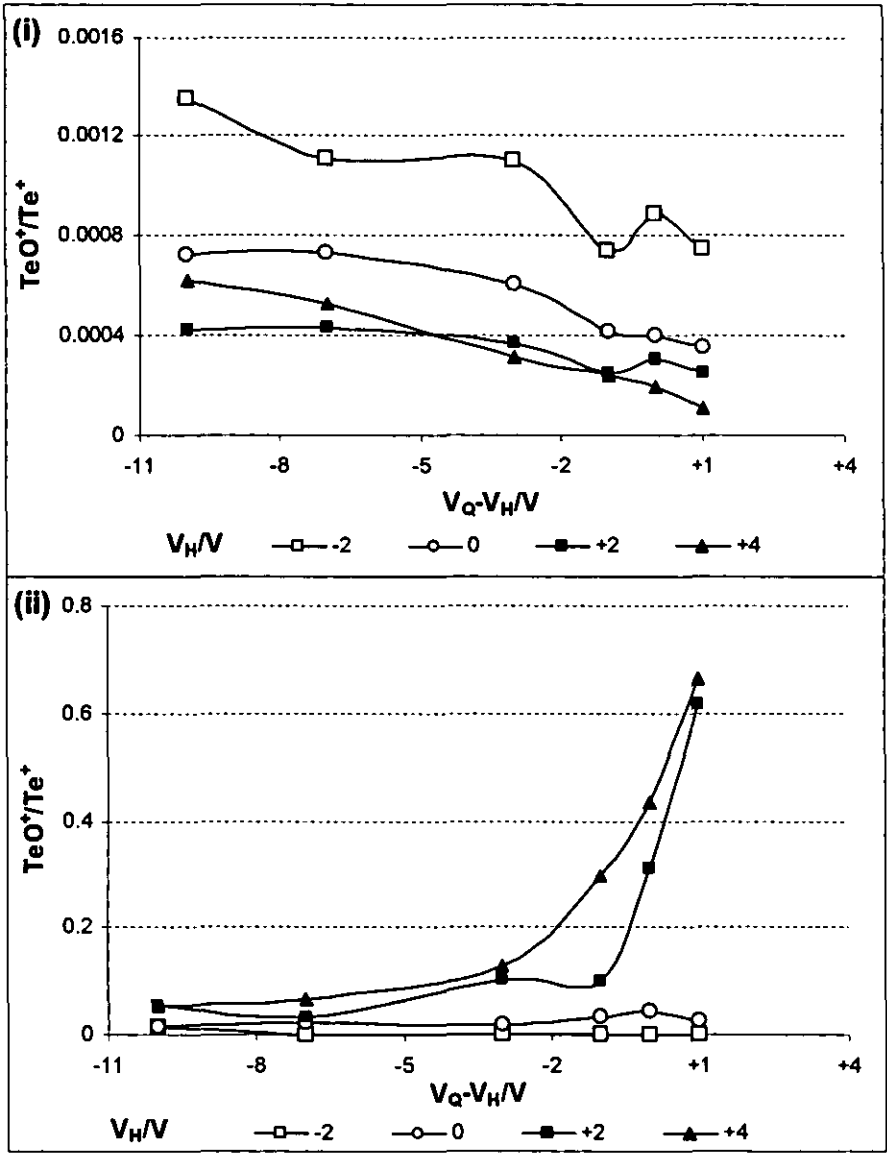


**Figure 5.18 – Variation in  $^{144}\text{TeO}^+ / ^{128}\text{Te}^+$  with  $V_Q - V_H$  at a range of  $V_H$  values; (i) without and (ii) with plasma screen. Collision cell gas helium+hydrogen 1.0+1.7 ml min<sup>-1</sup>**

Variation in relative  $\text{TeO}^+$  levels with  $V_Q - V_H$  at various  $V_H$  values with and without the use of a plasma screen is shown in Figure 5.18. The results with the plasma screen employed differed considerably from those where it was not used. This was due to two effects, one IKEE based and one plasma based. Without the use of a plasma screen, the

fastest ions (most negative  $V_H$ ) gave the highest relative levels of  $\text{TeO}^+$ , as the extra energy was required for the endothermic reaction producing  $\text{TeO}^+$  to proceed. With the plasma screen employed, the highest relative levels of  $\text{TeO}^+$  were observed for the slowest ions, due to transmission effects discussed before. The production of  $\text{TeO}^+$  in the cell was not observed due to the much higher levels of  $\text{TeO}^+$  from the plasma. The elevated levels of  $\text{TeO}^+$  from the plasma were consistent with the observation of Nonose *et al.*<sup>12</sup> that elevated levels of  $\text{MO}^+$  were present when a 'hot' plasma screen was used. (Recall that, for consistency, the plasma parameters were not re-optimised when the plasma screen was used. Retuning the plasma gas flows can increase sensitivity and lower oxide levels – see Section 5.3.2.4 below.)

The apparently large increases in  $\text{TeO}^+/\text{Te}^+$  at  $V_Q - V_H \geq -1$  V for  $V_H$  of +2 and +4 V were not significant.  $\text{TeO}^+$  signals were negligible for all these data points, with levels of  $\text{Te}^+$  continuing to fall away as  $V_Q - V_H$  increased, resulting in the elevated  $\text{TeO}^+/\text{Te}^+$  levels observed.



### $H_3O^+/Ar^+$ Reactivity Monitor

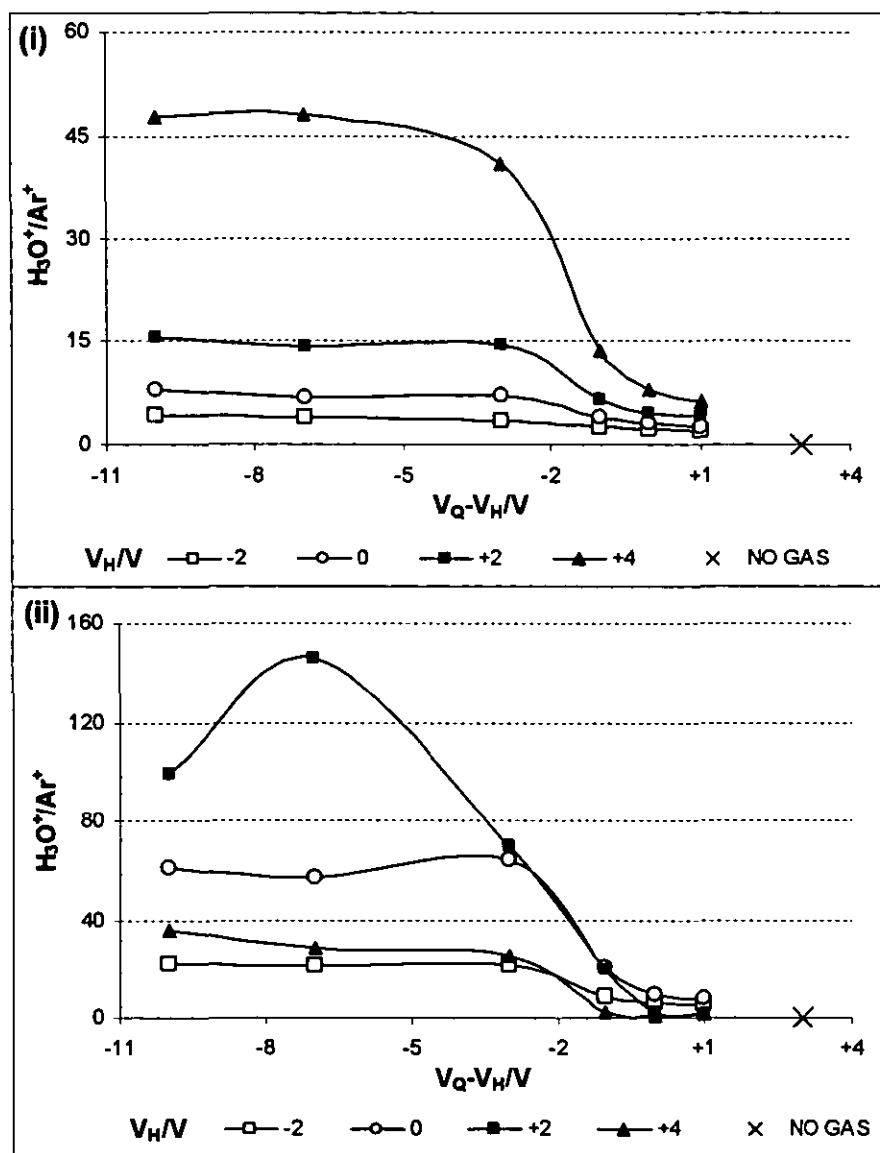


**Figure 5.19** – Variation in  $^{21}(H_3O)^+/^{36}Ar^+$  with  $V_Q - V_H$  at a range of  $V_H$  values; (i) without and (ii) with plasma screen. Collision cell gases helium+hydrogen  $1.0+1.7 \text{ ml min}^{-1}$ .

The influence of the plasma screen on the  $^{21}(H_3O)^+/^{36}Ar^+$  monitor ratio is shown in Figure 5.19. cursory examination of the results showed that the ratio did not appear to be as effective a monitor when the plasma screen was employed. When the plasma screen was not used (see Section 5.3.1.4),  $H_3O^+/Ar^+$  maximised at conditions for optimum sensitivity and high collision cell reactivity (for exothermic reactions). Figure 5.19 shows that when the plasma screen was employed, the absolute levels of  $H_3O^+/Ar^+$  also rose, consistent with the increased reactivity of the cell. However, the relative levels of

$\text{H}_3\text{O}^+/\text{Ar}^+$  between the various  $V_{\text{H}}$  series, which are of more utility than the absolute levels as the ratio is intended as a tool for use in the optimisation of collision cell settings,<sup>35</sup> did not follow the reactivity and sensitivity trends observed for the system elsewhere in this section. The  $\text{H}_3\text{O}^+/\text{Ar}^+$  ratio was at its maximum when  $V_{\text{H}} = +2$  V with progressively lower values for 0 V and  $-2$  V.  $+4$  V gave similar values to  $-2$  V. However, In sensitivity maximised when  $V_{\text{H}} = 0$  V and exothermic reactivity maximised when  $V_{\text{H}} = +4$  V. It is possible that the  $\text{H}_3\text{O}^+/\text{Ar}^+$  maximum corresponded to reasonable compromise conditions between sensitivity and reactivity.

### 5.3.2 Ion Energy Distribution

In order for kinetic energy discrimination (KED) to work most efficiently, it is important that the energy distributions of the ions of analytical interest and the ions to be excluded from the mass analyser do not overlap. If there is some overlap of the two distributions, depending on the  $V_{\text{Q}} - V_{\text{H}}$  potential adopted, some of the interfering ions will reach the detector and/or some of the ions of interest will be excluded from the mass analyser. This concept is illustrated in Figure 5.20. In Figure 5.20(i) the energy distributions of the analyte and interference are separated, so if a potential between  $V_1$  and  $V_2$  is applied the interference will be excluded from the mass analyser and the analyte will be transmitted. In Figure 5.20(ii) the energy distributions of the analyte and interference overlap; if  $V_3$  was applied, all of the analyte signal would be transmitted together with the horizontally ruled portion of the interference signal; if  $V_4$  was applied, all the interference signal would be excluded, together with the vertically ruled portion of the of the analyte signal. Similarly, application of potentials between  $V_3$  and  $V_4$  would result in transmission of some interference signal and exclusion of some analyte signal.

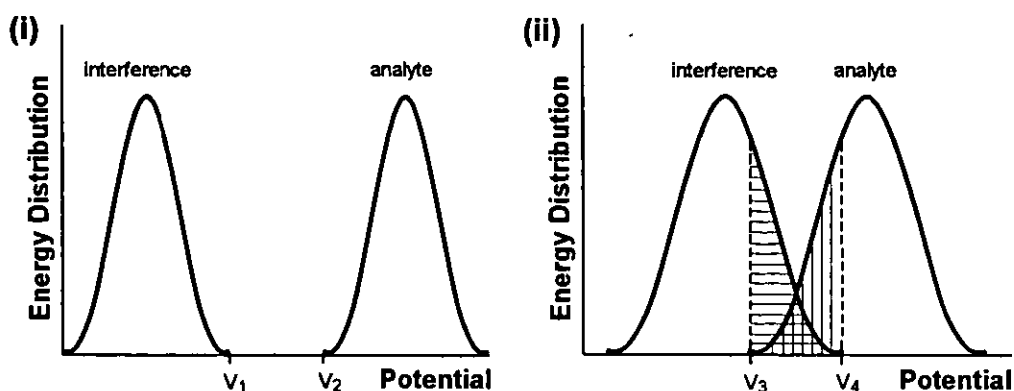


**Figure 5.20 – Illustrative ion energy distributions (i) analyte ion and interference ion energy distributions separated and (ii) analyte ion and interference ion energy distributions overlap**

To aid discussion of IKEE and KED in Section 5.3.1 above, the energy distribution of ions from the plasma, with and without the use of conventional plasma screen, was considered in Section 5.3.1.2 above (from p152). Ion energy distribution is also important for transmission through the ion optic system. Since the transmission of ions depends on their energy,<sup>96</sup> Minimising the width of the distribution will enhance transmission of ions through the system, assuming that the ion optics are tuned to best transmit ions with the median energy.

The plasma offset potential ( $V_P$ ) is important for IKEE, which, as discussed in Section 5.3.1 above, depends on the  $V_H - V_P$  potential difference. The median energy of the plasma distribution after the collision cell is also of interest for KED as wide energy distributions can still be separated from each other if a suitably large difference in median energies is present.

The remainder of this chapter explores the influence of various factors on ion energy distribution. The effect of various gases and gas flows in a collision cell and the use of a modified plasma screen are considered. The effect of two different types of plasma screen modification has been investigated, the application of a potential to the screen, which is herein termed ‘active’ plasma screen, and different grounding arrangements from the factory-fitted relay-controlled multi-core wire grounding to the interface plate.

### 5.3.2.1 Effect of the Collision/reaction Cell

#### Modelling

A simple model has been developed to predict the energy distribution of the ion beam and the effect of the collision cell thereon. The system was modelled as three distinct but connected components: the plasma, the interface region and the collision cell. These are presented and discussed in turn below.

The energy and speed distribution of ions in the plasma was assumed to be Maxwellian and, therefore, could be modelled<sup>61,153</sup> by Equations 5.2 and 5.3. Equations 5.2 and 5.3 are the Maxwell distributions of speeds and energies respectively.  $E$  is energy,  $s$  is speed,  $R$  the gas constant,  $T$  temperature and  $M$  the molar mass of the ion (all in SI units).

$$f(s) = 4\pi \left( \frac{M}{2\pi RT} \right)^{3/2} s^2 \exp\left( \frac{-Ms^2}{2RT} \right)$$

**Equation 5.2**

$$f(E) = \frac{2\pi}{(\pi RT)^{3/2}} E^{1/2} \exp\left( \frac{-E}{RT} \right)$$

**Equation 5.3**

The nominal temperature of the plasma,  $T_p$ , was assumed to be 7500 K as this value was given by Douglas<sup>5</sup> and is within the range quoted by Montaser *et al.*<sup>3</sup> The speed distributions of ions of mass 59 u (Co), 115 u (In) and 238 u (U) and the energy distribution, which is independent of mass, are shown in Figure 5.21.

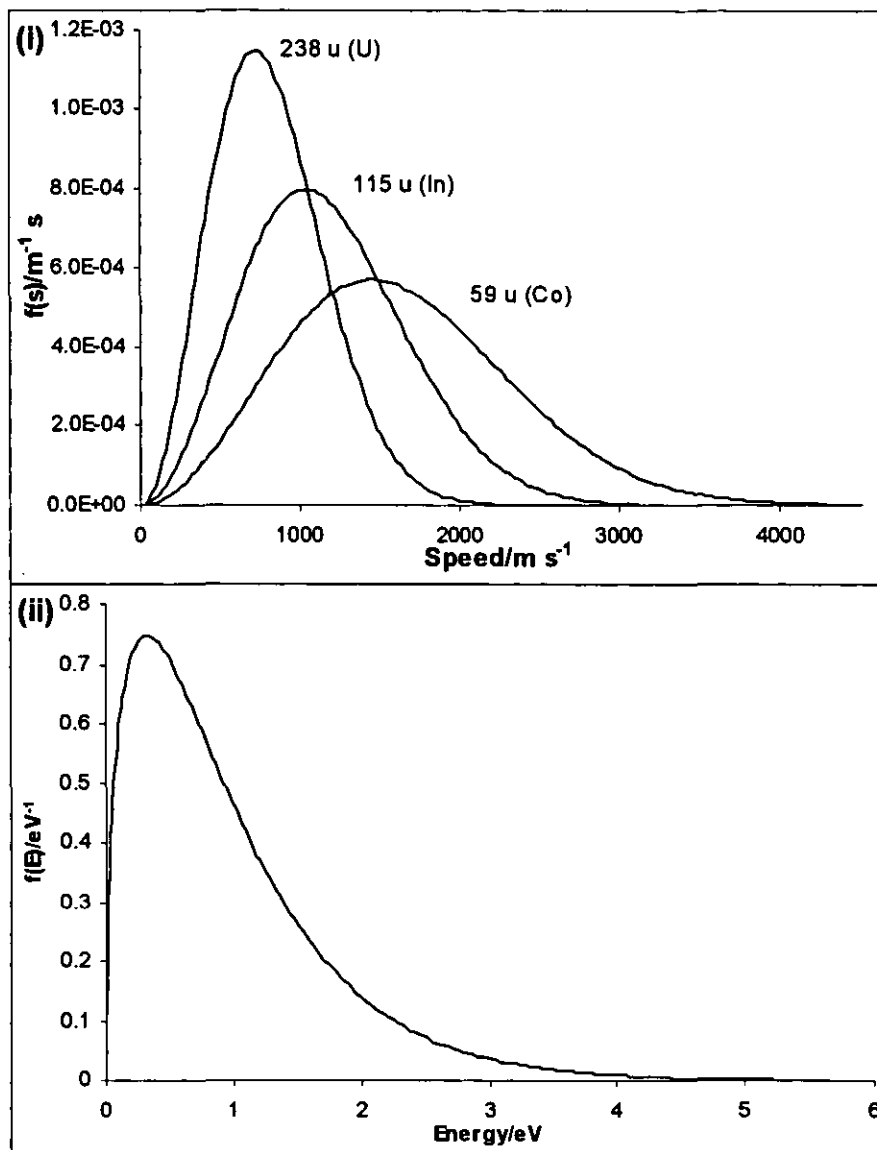


**Figure 5.21 – Maxwell distributions of (i) speeds and (ii) energies in the plasma.**

Figure 5.21(i) shows an inverse relationship between speed and mass for Maxwell distributions, as expected. Figure 5.21(ii) shows that, in this model, the ion energy distribution has a full width at half maximum height (half-width) of approximately 1 eV with a median energy of 0.30 eV. The energy distribution is independent of mass.

Between the sample cone and the skimmer cone, the ion beam undergoes adiabatic supersonic expansion.<sup>5,23</sup> The adiabatic supersonic expansion of a monatomic gas through an orifice of diameter  $D_0$  has a Mach number  $M_x$  a distance  $x$  from the orifice, where  $M_x$  is given by Equation 5.4.<sup>5</sup>

$$M_x = 3.26 \left( \frac{x}{D_0} \right)^{2/3} - 0.61 \left( \frac{x}{D_0} \right)^{-2/3}$$

**Equation 5.4**

If  $D_0 = 1$  mm (as in the sample cone used experimentally herein) and the distance between the sample and skimmer cone orifices,  $x$ , is estimated to be 6 mm, the Mach number of the gas when sampled by the skimmer cone is 10.58.  $M_x$  can be used in Equations 5.5 and 5.6 to give the temperature<sup>154</sup> ( $T_s$ ) and speed<sup>5</sup> ( $u_s$ ) of the gas at the skimmer cone. ( $\gamma_{Ar}$  is the ratio of the specific heats ( $C_p/C_v$ ) (4/3 for argon),  $a_0$  is the source speed of sound given<sup>5</sup> by Equation 5.7 and other terms are as previously defined.)

$$T_s = T_p \left( 1 + \frac{\gamma_{Ar} - 1}{2} M_x^2 \right)^{-1}$$

**Equation 5.5**

$$u_s = 2a_0 \left( \frac{2}{M^2} + \gamma_{Ar} - 1 \right)^{-1/2}$$

**Equation 5.6**

$$a_0 = \left( \frac{\gamma_{Ar} RT_p}{M} \right)^{1/2}$$

**Equation 5.7**

For the system, as defined above, Equations 5.5 and 5.6 gave  $T_s = 183$  K and  $u_s = 2662$  m s<sup>-1</sup>.

The energy and speed distribution at the skimmer sampling point was calculated. Due to the low pressure of the system at the interface, only small numbers of collisions will occur, so the ion beam will not be thermalised. To produce a distribution at which  $u_s$  was the median speed, a Maxwell distribution of speeds using  $T_s$  was adopted with  $[u_s - (2RT/M)^{1/2}]$  added to  $s$  as plotted to move the distribution so  $u_s$  and the median speed coincided. (The median speed is given by  $(2RT/M)^{1/2}$ .)<sup>153</sup> Similarly, the Maxwell distribution of energies was generated using  $T_s$  with  $[Mu_s^2/2 - RT/2]$  added to  $E$  as

plotted to relocate the distribution so the most probable energy  $(RT/2)^{153}$  coincided with the kinetic energy of ions of speed  $u_s$ . The speed and energy distributions of ions of mass 59 u (Co), 115 u (In) and 238 u (U) are shown in Figure 5.22.

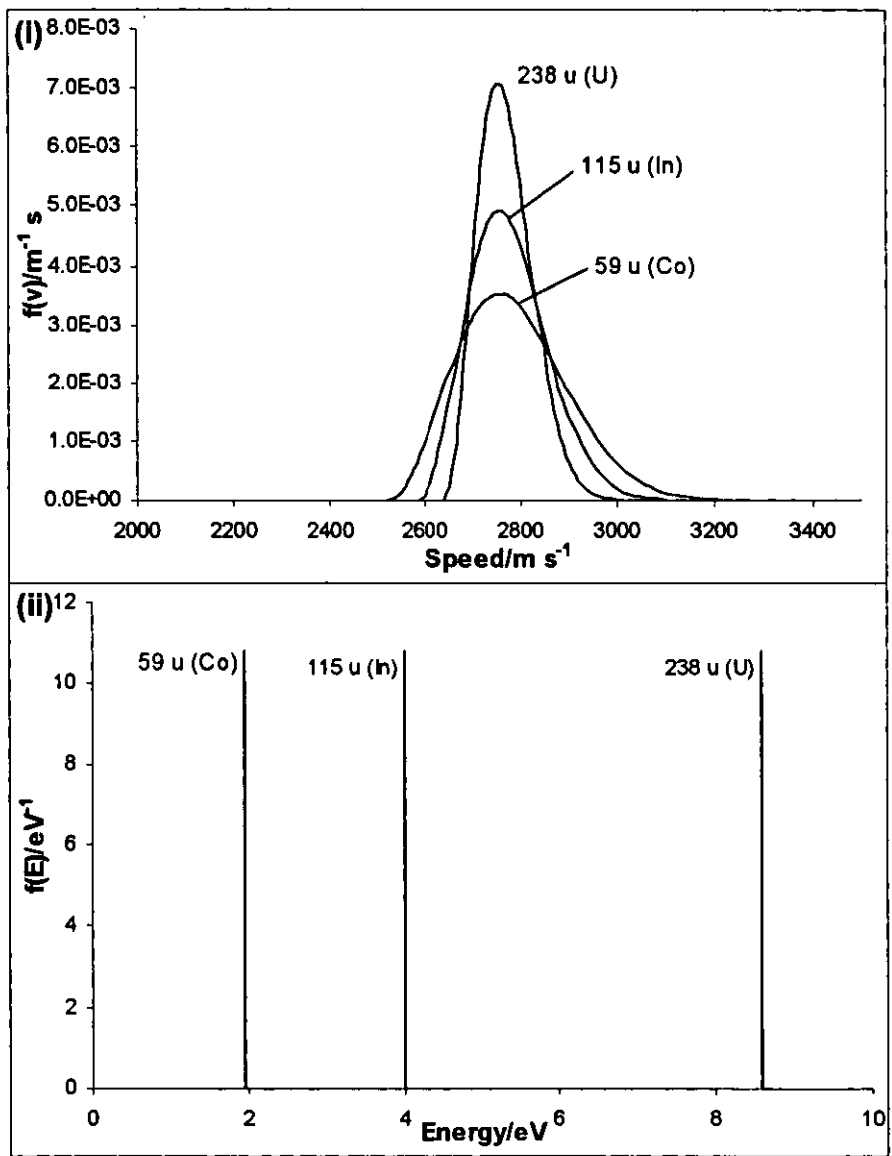


**Figure 5.22 – Distributions of (i) speeds and (ii) energies at the skimmer orifice.**

The strong mass dependence of ion energy that appears in this model (Figure 5.22(ii)) is due to the assumption of constant speed extraction. The very narrow energy distributions are due to the low calculated temperature of the system. It is most likely that the distributions are in fact wider than this as energy the kinetic energy of the system will not be totally uniform. Figure 5.22(i) shows that the mass dependence of the width of the

speed distribution was reversed between the plasma and the interface, with higher mass ions having wider distributions than lower mass ions following the supersonic expansion. As the ions will be rapidly decelerated after sampling by the skimmer cone, for which no simple model was available, it is assumed that all of the energy held by the ions was redistributed to kinetic/thermal energy.

The proportion of this energy lost by the ions through collisions within the collision cell was calculated for the collision cell of a PQ ExCell instrument containing 6 ml min<sup>-1</sup> helium, which equates to a partial pressure of 6.0 Pa in the cell.<sup>155</sup> The mean free path length of gas particles,  $\lambda$ , can be calculated<sup>61</sup> using Equation 5.8, where  $k$  is the Boltzmann constant,  $T$  the temperature and  $p$  the pressure of the gas and  $\sigma$  the collision cross section of the gas (0.21 nm<sup>2</sup> for helium).<sup>61</sup>

$$\lambda = \frac{kT}{\sqrt{2}\sigma p}$$

**Equation 5.8**

The large speed differential between the ion beam entering the cell and the thermal helium atoms within the cell means that the gas can be assumed to be static and  $\lambda$  increased by a factor of  $\sqrt{2}$  for the ions. Assuming that the collision cell gas is at room temperature, 300 K,  $\lambda = 3.29$  mm. The collision cell of a PQ ExCell instrument is 130 mm.<sup>155</sup> The minimum number of collisions experienced by an ion on its transit through the cell,  $n$ , will therefore be  $130/3.29 = 39.5$ .

Assuming that collisions occurring in the cell are inelastic and that the gas in the cell is stagnant, the proportion of an ion's initial energy remaining after a collision with helium in the cell,  $\alpha$ , is given by Equation 5.9, where  $M$  is the mass of the ion and  $M_{\text{He}}$  the mass of the helium atom.<sup>41,142</sup>

$$\alpha = \frac{M^2 + M_{\text{He}}^2}{(M + M_{\text{He}})^2}$$

**Equation 5.9**



The proportion of the initial energy remaining after each collision is therefore  $\alpha$  so the proportion of the energy of an ion entering the cell remaining when the ion leaves the cell is  $\alpha^n$ . For example, for an ion of mass 115 u (In),  $\alpha = 0.93$  and  $\alpha^n = 0.067$  and are greater for higher mass ions. If the energy of ions entering the cell is taken to be  $Mu_i^2/2$ , *i.e.* their energy at the skimmer cone, then the energy of ions after the cell is  $\alpha^n Mu_i^2/2$ . Assuming this energy to be thermal, the nominal temperature of the ions,  $T_i$ , can be calculated<sup>61</sup> by Equation 5.10.

$$E = \frac{3}{2} RT_i$$

**Equation 5.10**

These temperatures can then be used to produce Maxwell distributions of speeds and energies of ions leaving the collision cell using Equations 5.2 and 5.3. The speed and energy distributions of ions of mass 59 u (Co), 115 u (In) and 238 u (U) leaving the collision cell are shown in Figure 5.23.

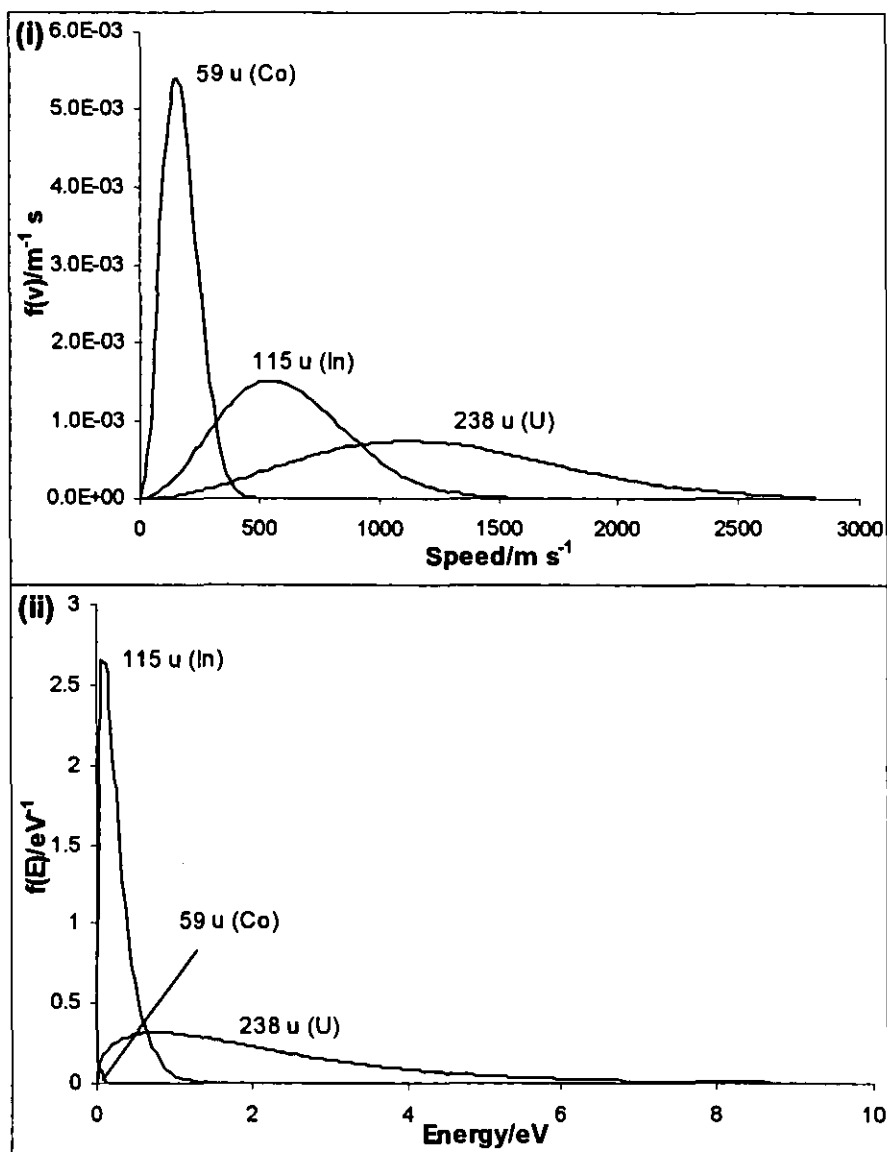


**Figure 5.23 – Distributions of (i) speeds and (ii) energies of ions exiting the collision cell.**

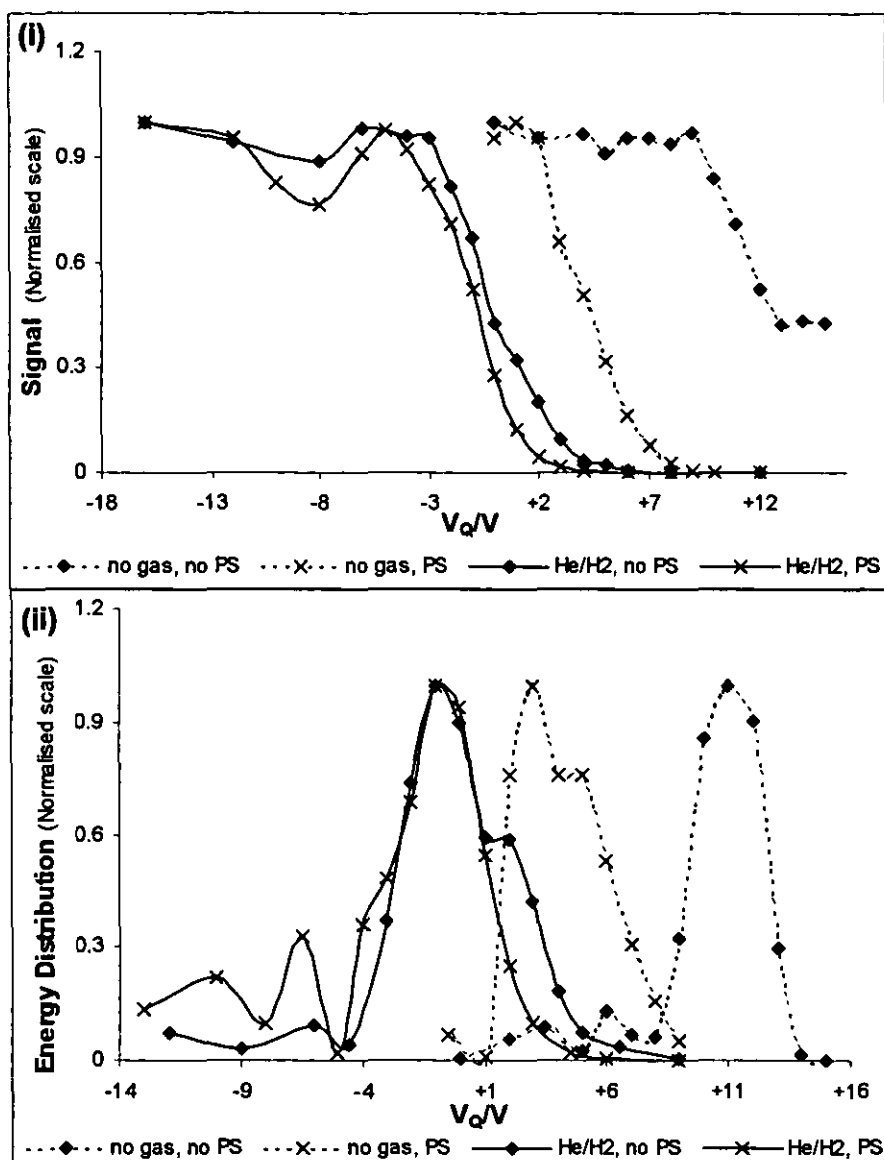
Figure 5.23(i) shows that both the median speed and the width of the distribution depend on mass. Higher mass ions having higher median speeds and wider distributions. These effects are the opposite of those observed for the plasma (Figure 5.21(i)), the reversal caused by the equal velocity expansion in the extraction region and by mass dependent energy loss in the collision cell. The width of the distribution of speeds for U was increased and those for In and Co significantly decreased compared to the distributions in the plasma (Figure 5.21(i)).

The energy distribution for Co after the collision cell was too narrow to be shown correctly at the scale used in Figure 5.23(ii). The energy distribution after the collision cell was considerably different to that in the plasma. In the plasma (Figure 5.21(ii)), the energy distribution was mass independent, with a median value of 0.33 eV. Following the collision cell, due to the effects of expansion in the interface and collisional energy loss in the cell, the energy distribution is mass dependent. The median energy for U (0.77 eV) was more than twice that for ions in the plasma (0.33 eV), whilst those for In and Co were much lower, 0.09 and 0.004 eV respectively. The median energy for Co, and indeed the entire energy distribution, fell well below thermal energy levels of 0.04 eV so it is unlikely that they would be observed as they had insufficient energy to exit the cell. The gas flow in the collision cell had a significant effect on the median energy and width of the distribution. With 6 ml min<sup>-1</sup> helium in the cell, U had a median energy of 0.77 eV and a half-width of 2.5 – 3.0 V. When the helium flow rate was raised to 10 ml min<sup>-1</sup>, U had a median energy of 0.32 eV and half-width of less than 1 eV.

Due to the crude nature of certain aspects of this model, especially the distributions of energies and speeds after the interface, data from it are unlikely to be directly comparable with experimental data. The trends observed, for example the mass dependence of energy distributions and the effect of altering collision cell gas flows can be compared.

#### Effect of Collision/reaction Cell Gases

Normalised  $V_Q$  stopping curves and two point moving window smoothed energy distributions for In<sup>+</sup> are shown in Figure 5.24 with and without the use of plasma screen with helium+hydrogen 1.0+1.7 ml min<sup>-1</sup>. (Data with no collision cell gas used; as shown in Figure 5.7 (p153); is included for comparison.  $V_H$  was -1.96 V with no collision cell gas use and +4.00 V with gas use.)



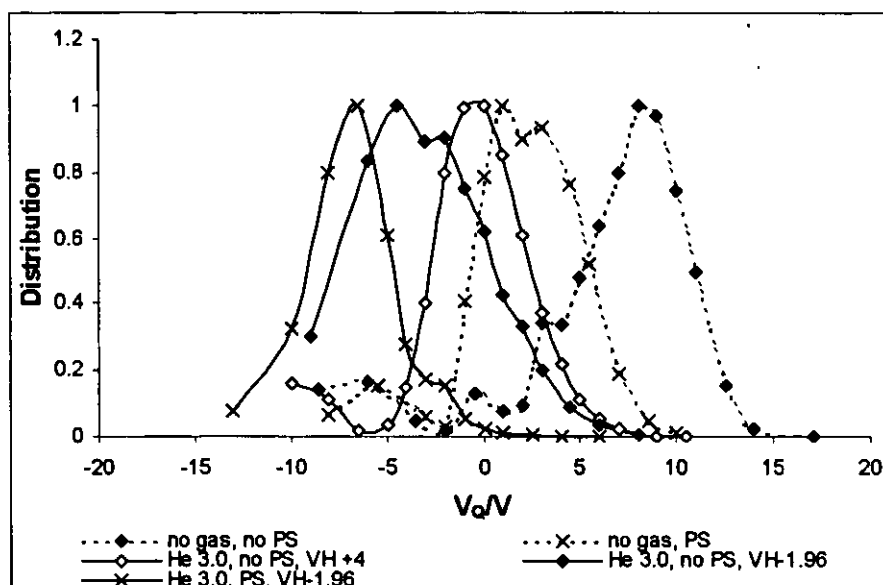
**Figure 5.24** – Normalised  $V_Q$  (i) stopping curves and (ii) energy distributions for  $\text{In}^+$  with  $V_H + 4.00$  V and helium+hydrogen  $1.0+1.7 \text{ ml min}^{-1}$  (He/H2) with and without plasma screen (PS) use. (Reference data from Figure 5.7 for  $V_H - 1.96$  V and no collision cell gas use with and without plasma screen use is included.)

Figure 5.24(i) shows that the stopping curves when helium/hydrogen was used were somewhat noisy at high negative  $V_Q$ ; they therefore produce energy distributions with very noisy low  $V_Q$  tails. Fortunately, this noise did not prevent identification of the widths of the distributions in the form of full-widths at half maximum height (half-widths). The large downward shift in the median potential when the plasma screen was used was not observed when the collision cell was also employed. The use of the collision cell greatly reduced the potential of the ion beam. The median potential without

collision cell use was approximately +11 V when the plasma screen was not used and approximately +3 V when it was. The use of the collision cell lowered the median potential to -1 V, with no perceivable difference between use and non-use of plasma screen. This was in marked contrast to the ~ 8 V difference in median potential between use and non-use of the plasma screen when collision cell gas was not used. That the potential of the ion beam could fall below 0 V shows that the potential cannot be directly equated with ion energy, which cannot be negative.

The use of helium/hydrogen collision cell gas caused no large changes in the widths of the ion energy distributions, as shown in Figure 5.24(ii). With no plasma screen use helium/hydrogen caused a slight increase in half-width, from *circa* 4.5 to 5.0 V, whereas with plasma screen use helium/hydrogen caused a slight decrease in half-width, from *ca.* 5.5 to 4.0 V. The noise in the system means that no significance can be attached to these changes in half-width. If the use of a collision cell can effect a reduction in the width of the ion energy distribution, this may well occur at higher gas flow rates or with the use of heavier gases such as neon, where the ions are taken closer to thermal energy levels.

Figure 5.25 shows normalised  $\text{In}^+$  ion energy distributions with  $3.0 \text{ ml min}^{-1}$  helium in the collision cell, with and without plasma screen use at two different  $V_H$  settings: -1.96 V and +4.00 V. The stopping curves from which the energy distributions were calculated, by two point moving window smoothing followed by differentiation, are not shown as the smooth stopping curves did not provide any additional information that the well defined energy distributions they produced.



**Figure 5.25 – Normalised  $\text{In}^+$  energy distributions with and without plasma screen (PS) use with  $3.0 \text{ ml min}^{-1}$  helium (He 3.0) or no gas at  $V_H$  (VH)  $-1.96 \text{ V}$  or  $+4.00 \text{ V}$ .**

Figure 5.25 shows that  $3.0 \text{ ml min}^{-1}$  helium has a somewhat confusing effect on the width of the energy distribution.  $3.0 \text{ ml min}^{-1}$  helium narrowed the energy distribution by almost  $2 \text{ V}$ , from  $6.4 \text{ V}$  to  $4.6 \text{ V}$ , when the plasma screen was employed. This narrowing was not however replicated for the higher mass  $^{238}\text{U}^+$  where, under the same conditions, the half-width widened by more than half a volt, from  $8.2 \text{ V}$  to  $8.9 \text{ V}$ , on helium use. Consideration of the data when the plasma screen was not used further complicates the apparent effect of  $3.0 \text{ ml min}^{-1}$  helium use. The half-width for  $\text{In}$  without plasma screen or helium use is  $5.7 \text{ V}$  in Figure 5.25; with  $3.0 \text{ ml min}^{-1}$  helium use, this was marginally reduced to  $5.4 \text{ V}$  with  $V_H +4 \text{ V}$  but significantly increased to  $8.6 \text{ V}$  with  $V_H -1.96 \text{ V}$ . For  $\text{U}^+$ , with no plasma screen use, helium resulted in a marginal increase in half-width from  $9.3 \text{ V}$  to  $9.6 \text{ V}$  ( $V_H -1.96 \text{ V}$ ). (At  $V_H +4.00 \text{ V}$ , the  $\text{U}$  data were too noisy to identify the half-width.) The data are overall difficult to interpret, with use of  $3.0 \text{ ml min}^{-1}$  helium causing narrowing and widening of the half-width under different  $V_H$  and plasma screen conditions with little repetition of effects between  $\text{In}^+$  and  $\text{U}^+$ . One trend identifiable for both  $\text{In}^+$  and  $\text{U}^+$  was an increase in half-width on helium use with  $V_H -1.96 \text{ V}$  and no plasma screen use, although the reason for this is unclear.

The effect of  $3.0 \text{ ml min}^{-1}$  helium on median potentials was similar to that observed with helium/hydrogen use, reducing the potential to below  $0 \text{ V}$ . The change in  $V_H$  from

+4.00 V to -1.96 V with no plasma screen use and 3.0 ml min<sup>-1</sup> helium further reduced the plasma potential by approximately 5 V. As +4.00 V approximated the factory setting of  $V_H$  and  $V_H$  -1.96 V had consistently increased half-width,  $V_H$  +4.00 V alone was used in further experiments. Plasma screen use, with  $V_H$  -1.96 V and 3.0 ml min<sup>-1</sup> helium, had an observable effect on the median potential that was not observed with helium/hydrogen use; introducing the plasma screen lowered the median potential by a further 2 V. When  $V_H$  was +4.00 V and the plasma screen was not employed, the median potential was approximately 0 V, similar to the level observed when helium/hydrogen was used. Since the use of 3.0 ml min<sup>-1</sup> helium did not produce consistent narrowing of the width of the ion energy distribution, the experiment was repeated with the helium flow doubled. When helium was used,  $V_H$  +4.00 V alone was used for the reasons given above.

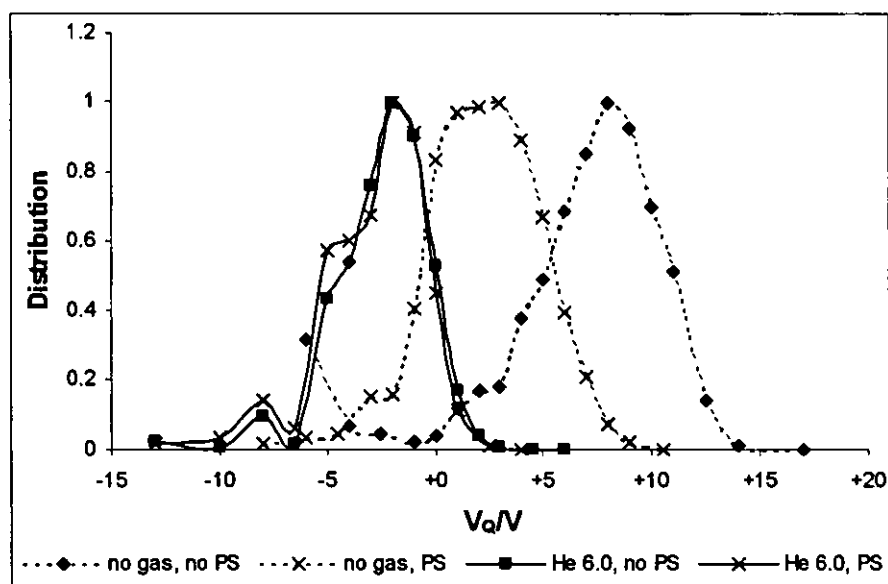


**Figure 5.26** – Normalised  $In^+$  energy distributions with and without plasma screen (PS) use with 6.0 ml min<sup>-1</sup> helium (He 6.0) or no gas in the collision cell. ( $V_H$  +4.00 when helium used, -1.96 V when helium not used)

Figure 5.26 shows normalised energy distributions for 6.0 ml min<sup>-1</sup> helium or no gas, with and without plasma screen use. These data are much more consistent with the earlier helium/hydrogen data than the data for 3.0 ml min<sup>-1</sup> helium was. When 6.0 ml min<sup>-1</sup> helium was used, the median potential was *ca.* -2 V whether plasma screen was used or not. Without collision cell use, the median potential was approximately +8 V with no plasma screen, reducing to +2 V with plasma screen use. This suggests that

the relative energy losses by collision in the cell were greater when the screen was not used than they were when it was, so that the residual energy was the same in both cases. The use of  $6.0 \text{ ml min}^{-1}$  helium resulted in a slight reduction in half-width from 6 V to 5 V, regardless of plasma screen use.

The use of helium+hydrogen  $1.0+1.7 \text{ ml min}^{-1}$  in a collision cell has little effect on the width of the energy distribution, with the half-widths for the various In distributions all falling within  $\pm 0.5 \text{ V}$  of 5 V. Helium/hydrogen use also reduced the median potential of the distribution from +11 V (with plasma screen) or +3 V (without) to -1 V, obscuring the variation in plasma potential affected by the plasma screen. With  $3.0 \text{ ml min}^{-1}$  helium in the cell, a reduction in half-width of between 0.3 and 1.8 V was observed for In compared with no gas use, whereas an increase in half-width of 0.3–0.7 V was observed for U. Consistent with the model, the distributions for U was distinctly wider than that for In.

Increasing the helium flow to  $6.0 \text{ ml min}^{-1}$  did not result in a significant reduction in the energy distribution for In compared with  $3.0 \text{ ml min}^{-1}$  helium. With  $6.0 \text{ ml min}^{-1}$  helium in the cell, the half widths were approximately 5.0 V, compared with half-widths of 4.6 and 5.4 V at  $3.0 \text{ ml min}^{-1}$ . This is inconsistent with the model, which showed a significant reduction in half-width on increasing the gas flow. The half-width of the In energy distribution was 5 V with  $6.0 \text{ ml min}^{-1}$  helium in the cell, much wider than the equivalent distribution in the model. It is therefore apparent that the energy distributions resulting from the model do not conform to experimental data and so further development of the model is required. The most likely area for further development is the modelling of supersonic expansion in the interface region and the distributions of speed and energy associated with this.

The use of high flows of helium in the collision cell resulted in a slight narrowing of the energy distribution of In, from 6 V with no gas in the cell to 5 V with  $6.0 \text{ ml min}^{-1}$  helium in use. The use of collision cell gases also caused a reduction in the median potential of the distribution to a level lower than that observed for the plasma screen alone, whether or not the plasma screen was used.



#### 5.3.2.2 Effect of 'Active' Plasma Screen Use

The effect of applying a negative dc potential to the plasma screen has been investigated with two goals in mind. Firstly to further extend the range of achievable  $V_H - V_P$  potentials by further reducing the applied  $V_P$  below the level observed when the grounded plasma screen was employed. Secondly, to reduce the width of the ion energy distribution to enhance transmission and enhance KED, as described in Section 5.3.2 above. The term “‘active’ plasma screen” is used in this section to refer to a plasma screen to which a non-zero potential has been applied.

The ‘active’ plasma screen was used with a single cell ( $-1.5$  V nominal on the screen). The potential on the screen was  $-1.484$  V before the experiment and  $-1.329$  V afterwards. To study the effect of the plasma potential on IKEE and simultaneously collect the input ion stopping curve, data were collected with helium+hydrogen  $1.0+1.7$  ml min $^{-1}$  in the cell and  $V_H$  rather than  $V_Q$  was used to apply the stopping potential. On a separate day, data were collected under the same conditions for standard plasma and grounded plasma screen. The data discussed below have been normalised to correct for variation in standard mode (no collision cell gas or plasma screen use) sensitivity levels.

Stopping curves and two-point moving window smoothed differentials of those stopping curves, *i.e.* ion energy distributions of the ions entering the collision cell, are shown in Figure 5.27 for standard plasma (no plasma screen use) and standard power plasma with grounded plasma screen and separately  $-1.5$  V ‘active’ plasma screen.

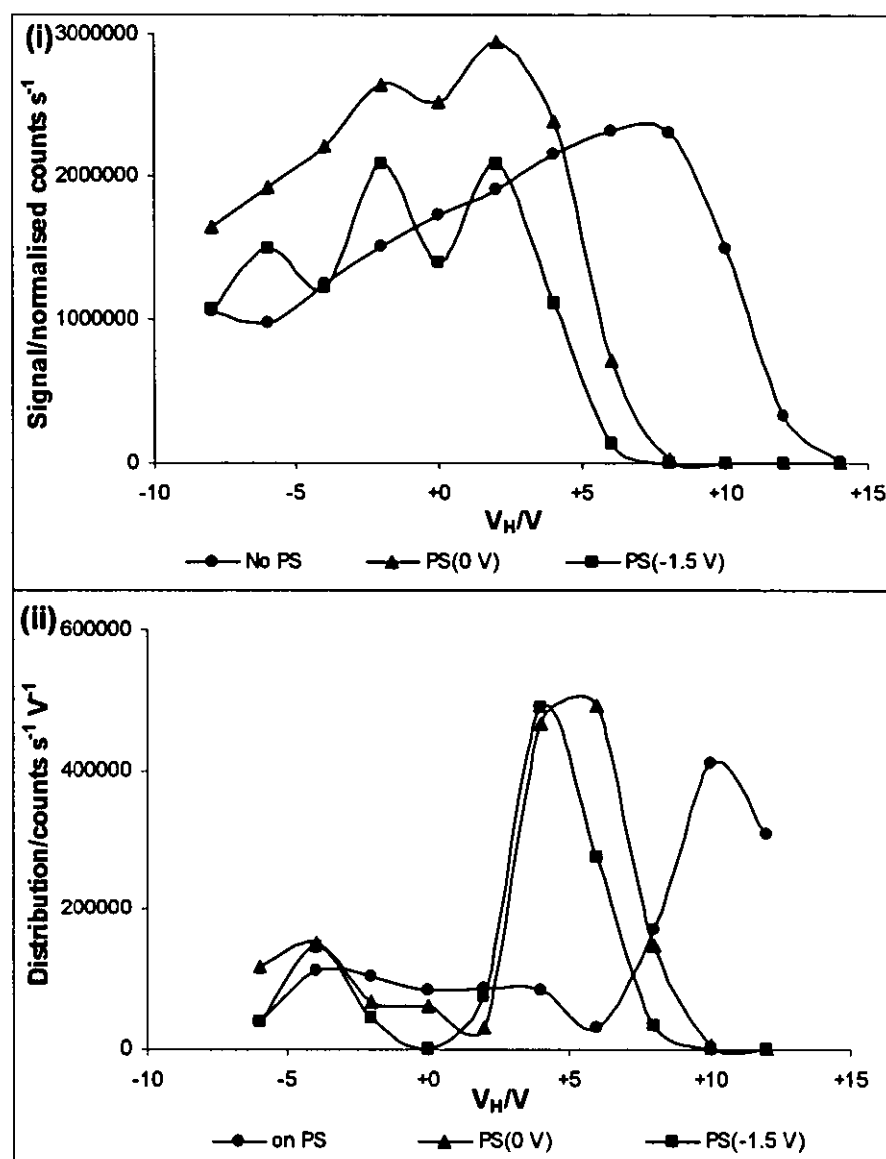


**Figure 5.27** – Normalised (i)  $V_H$  stopping curves and (ii) ion energy distributions for  $In^+$  with standard plasma (no PS), grounded plasma screen (PS(0 V)) and  $-1.5$  V ‘active’ plasma screen (PS( $-1.5$  V)).  $V_Q - V_H = -10$  V, helium+hydrogen  $1.0+1.7$  ml  $min^{-1}$

Figure 5.27(ii) shows that the  $-1.5$  V ‘active’ plasma screen took  $V_P$  to a lower value than the grounded plasma screen did. The median potential for the standard plasma was lowered to *circa* 5 V by the use of a grounded plasma screen. Use of the ‘active’ plasma screen further lowered the median potential by approximately 1 V to approximately 4 V as was predicted. It is not possible to comment on the half-widths of the ion energy distribution as the relatively low number of data points remaining following smoothing result in peaks drawn from four or five points – too few points to plot the energy distribution with sufficient accuracy for meaningful observations to be made.

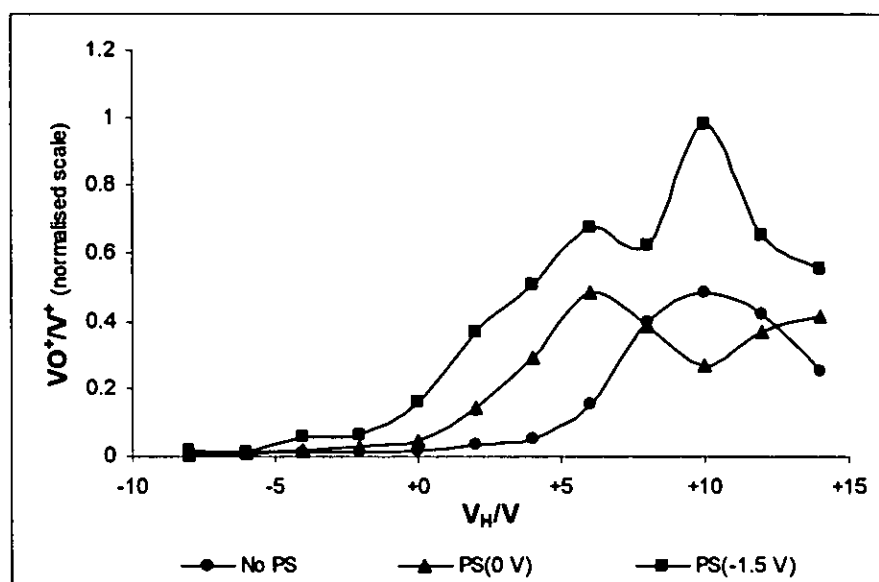


**Figure 5.28** – Variation in normalised  $^{67}(VO)^+/^{51}V^+$  level with  $V_H$  for standard plasma (no PS), grounded plasma screen (PS(0 V)) and  $-1.5$  V active plasma screen (PS( $-1.5$  V)).  $V_Q - V_H = -10$  V, helium+hydrogen  $1.0+1.7$  ml min $^{-1}$ .

$VO^+$  was formed in the cell by exothermic reaction with adventitious oxygen or water ( $\Delta H_r = -0.8$  eV) as well as in the plasma. The level is affected by IKEE – slower ions promote exothermic reactions – and the slower, cell-formed,  $VO^+$  ions can be excluded from the mass analyser by KED. ( $V_Q - V_H$  was  $-10$  V here so KED did not occur.) Figure 5.28 shows the effect of standard plasma, grounded plasma screen and  $-1.5$  V ‘active’ plasma screen on the  $VO^+/V^+$  level. The  $V_H - V_P$  dependence of IKEE is clearly apparent in Figure 5.28. The relative level of  $VO^+$  began to rise at higher  $V_H$  values as the plasma potential increased, *i.e.* the level of  $VO^+/V^+$  started to become elevated for ‘active’ plasma screen at a lower  $V_H$  than for grounded plasma screen which, in turn, started to become elevated at a lower potential than standard plasma. Due to the noise in each data set, it was not possible to differentiate the data or to identify the potential equivalent to the most probable energy for  $In^+$ . It is however clear that IKEE relates to  $V_H - V_P$  and not to  $V_H$  alone.

When a potential of  $-3$  V was applied to the ‘active’ plasma screen it was not possible to collect any data due to plasma instability; for 2–3 s every 20–30 s the plasma reduced in size as the rf matching circuits unsuccessfully attempted to tune the plasma. Increasing the cool gas flow, stepwise up to  $18$  l min $^{-1}$ , or the auxiliary gas flow, to  $1.0$  or  $1.5$  l min $^{-1}$ , did not result in a stable plasma, neither did reducing the rf power to  $1200$  or

1100 W. It was therefore not possible to explore the use of more negative 'active' plasma screen potentials than  $-1.5$  V.

The way in which 'active' plasma screen influenced the ICP, and the plasma potential, is somewhat intriguing. On the most basic level, application of a dc potential to the plasma screen should have no effect on the plasma. If the newly formed plasma is treated as bulk neutral, with electron and cation densities equal throughout, the dc field on the plasma screen will have no influence on the plasma as the fields from the cations and electrons will be equal and opposite and therefore cancel out. However, if the plasma is considered as a charge within the dc field of the 'active' plasma screen, the two will interact, and therefore the 'active' plasma screen could feasibly alter the plasma potential.

The most obvious way of altering the model to allow the plasma to be considered as having a net charge is to consider the cation and electron densities as not equal. (The mean densities will be equal as each cation in the plasma will have an associated electron, they need not, however, be evenly distributed throughout the plasma, a spatial charge separation may occur.) The small size of electrons relative to cations means that they are much more mobile. Electrons will therefore diffuse more rapidly than cations away from the high charge density in the centre of the plasma. This will result in the plasma having higher cation density in the centre and higher electron density at the edge. (Such cation distribution has been discussed in the context of mass bias.)<sup>156</sup> This electron density will be repelled by the negative potential on the plasma screen, changing the electron density gradient within the plasma.

Another possibility is that the observed effects of the 'active' plasma screen were due to the influence of the bypass capacitor around the battery, causing the assembly to act in a similar manner to the 'rf ground' plasma screen in Section 5.3.2.3 below. The plasma rf tuning instability when  $-3$  V were applied suggests that the cells did interact with the plasma, thus the latter explanation is less likely than the former.

5.3.2.3 Effect of Plasma Screen Grounding

Electronic Modelling

A basic electronic model of a plasma in an ICP-MS system was prepared using Electronics Workbench modelling software (version 4.0d, Electronics Workbench U.K., London, W1). The specified parameters for the model are listed in Table 5.10.

**Table 5.10 – Specified parameters for a simple electronic model of an ICP-MS system.**

Parameter	Value	Source
rf generator: voltage	2 kV	Generator in VG PQ ExCell
frequency	27 MHz	Generator in VG PQ ExCell
ICP power	Circa 1350 W	Setting used throughout this work
Plasma potential	+10 – +11 V	Section 5.3.1.3

The circuit derived from this specification is shown in Figure 5.29. The oscilloscope, ammeters and voltmeters would not be present in ICP-MS systems; thin lines are used to represent additional wires associated with these components. All voltages and currents are ac and thus are reported below as root-mean-squared (rms) values.

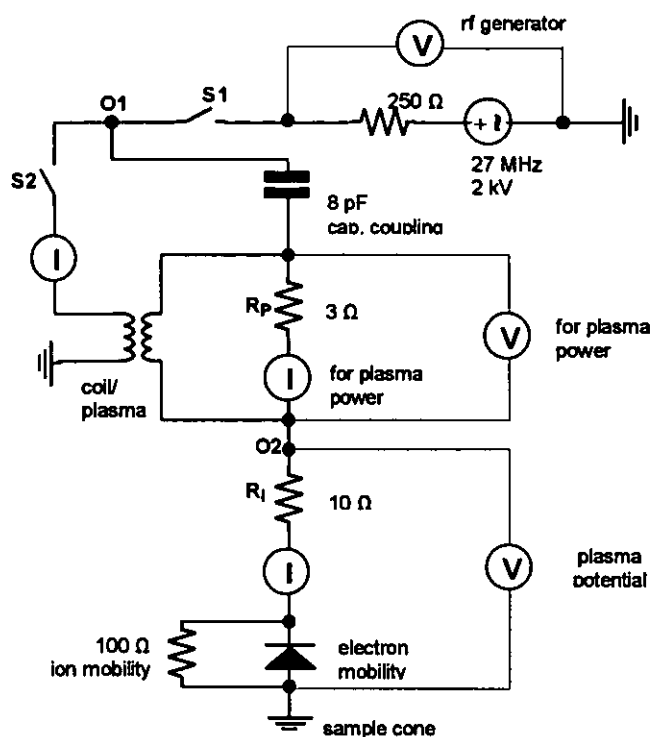


**Figure 5.29 – Simple electronic model of an ICP-MS system**

The rf generator was modelled as a 2 kV, 27 MHz ac power supply with an internal resistance of 250  $\Omega$ . The plasma/coil interaction was modelled as a 3:1 turn transformer with three turns on the coil side. (Transformer settings: leakage inductance,  $L_e = 1 \times 10^{-12}$  H, magnetising inductance,  $L_m = 4.22 \times 10^{-7}$  H.) The plasma-side terminals of the transformer were bridged by a 3  $\Omega$  resistor to represent the internal resistance of the plasma. The capacitive coupling of the rf generator to the plasma was modelled by an 8 pF capacitor linking the power supply to the plasma. Switches S1 and S2 were included to enable the power supply to be isolated. Except where otherwise noted, they were in the left in the 'on' position.

Modelling of the plasma-sample cone interaction was more complex than modelling of the coil-plasma interaction. The sample cone was represented by a ground point and a 10  $\Omega$  resistor was used to model the resistance of the plasma-cone interface. The higher mobility of electrons compared with cations was represented by a diode with minimal junction potential to reflect high electron mobility with a 100  $\Omega$  leakage path resistor to reflect the lower mobility of cations.

The resistances of the power supply and plasma (labelled  $R_G$  and  $R_P$  respectively on Figure 5.29) were adjusted until the plasma power ( $V_{rms} \cdot I_{rms}$ ) was approximately 1300 W. The leakage path resistor around the diode was adjusted so that the waveform at this point represented good electron mobility during the negative rf phase and poor, but non-zero, cation mobility during the positive rf phase. Figure 5.30 shows the waveforms of the applied rf and plasma potential, measured against ground at the points labelled 'O1' and 'O2' respectively in Figure 5.29. The value of the capacitive coupling was selected to give a plasma potential of +10 – +11 V.

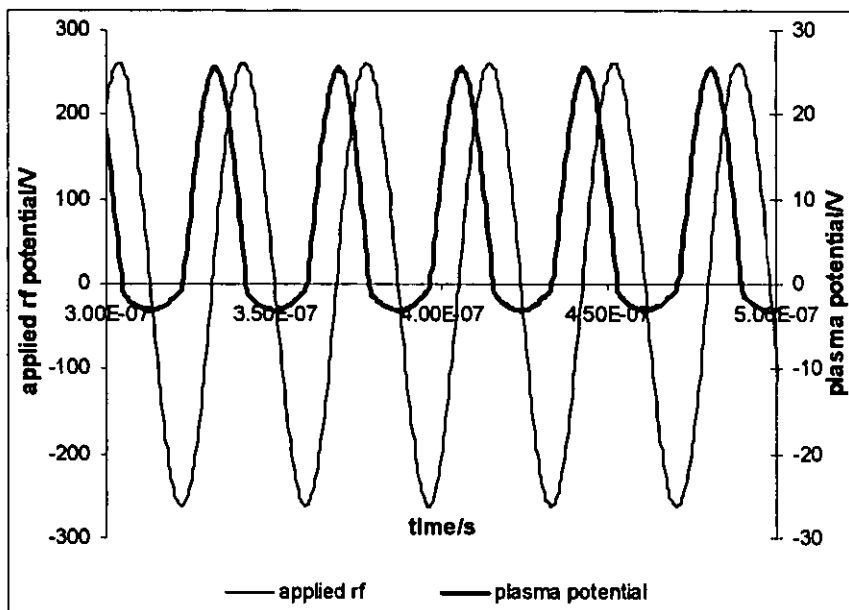


**Figure 5.30 – Waveforms of the applied rf (measured at 'O1') and plasma potential (measured at 'O2') in the electronic model shown in Figure 5.29, switches S1 and S2 both on.**

When switch S1 was off, the power supply was isolated and its potential rose to 2 kV. When switch S1 was on and switch S2 off, capacitive coupling dissipated approximately 20 W from the secondary circuit components and the supply voltage dropped to 1.8 kV. When both switches were on, the supplied voltage dropped to 185 V and the supplied current rose to 7.5 A. When the capacitive coupling link was removed, the plasma potential dropped to zero.

Two important observations concerning the plasma potential in this model have been made:

1. The plasma potential is a partially-rectified rf potential, not a dc potential.
2. The presence of capacitive coupling cause a non-zero plasma potential to be observed.

The crude nature of the model means that these observations are best considered as hypotheses for the nature of the plasma potential in ICP-MS that remain to be tested.

If the two hypotheses were valid, then the role of the plasma screen can be considered very important. The plasma screen interrupts capacitive coupling by introducing a grounded metal plate into what is, in essence, an air capacitor, splitting the capacitor into two parts. Since the reciprocals of capacitances are additive for capacitors in series, dividing the capacitor in this manner reduces the level of capacitive coupling, and the ground-wire attached to the screen will provide an alternative path to ground for the rf current and so will reduce capacitive coupling to the plasma. Also, an ungrounded, or 'floating', plasma screen should reduce the capacitive coupling and therefore reduce the plasma potential. As rf is carried to ground at the plasma screen, the nature of the rf ground should be important as the form and geometry of conductors is significant in the conduction of rf currents.

To explore the role of the plasma screen, the model was adapted to include the plasma screen. This model is shown in Figure 5.31.



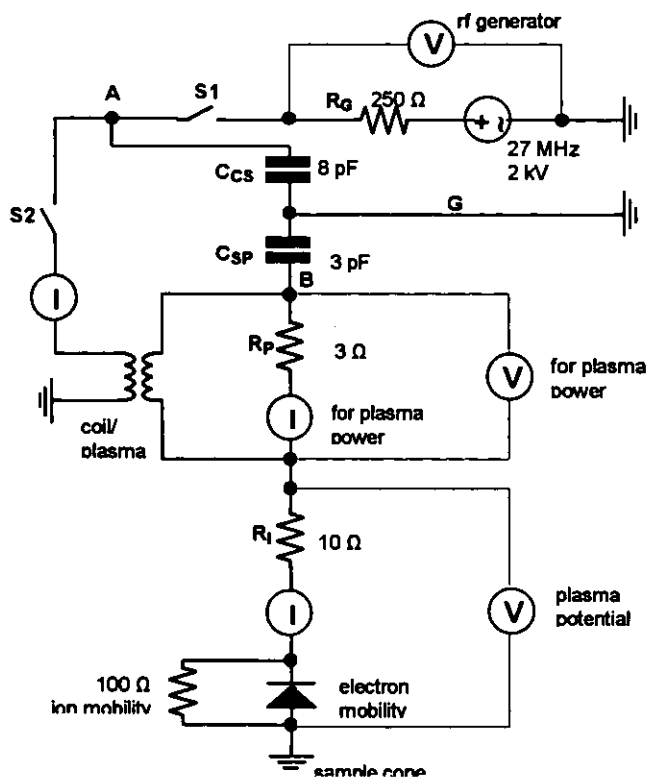


**Figure 5.31** – A simple electronic model of an ICP-MS system including a plasma screen.

The only modifications to the model shown in Figure 5.29 to include the plasma screen were the replacement of the 8 pF capacitive coupling link with two capacitors in series, grounded between the two. The grounding represents the plasma screen ground, capacitor  $C_{CS}$  represents capacitive coupling between the coil and the plasma screen and capacitor  $C_{SP}$  represents the capacitive coupling between the plasma screen and the plasma. The values of  $C_{CS}$  and  $C_{SP}$  were selected as they resulted in a plasma potential close to the +3 V previously experimentally determined (Section 5.3.1.3). The plasma potential in the model was +2.3 V. A low current of less than 300 mA was directed to ground *via* the plasma screen.

That the model could be adapted to include the plasma screen and give a suitable plasma potential with only the capacitive coupling part of the circuit being altered provides further evidence to support the validity of the model.

The model was further modified to predict the effect of use of a ‘floating’ plasma screen; that is a plasma screen with no ground wire attached to it. The only alteration made to the circuit to effect this change was the deletion of the plasma screen ground wire –

marked 'G' in Figure 5.31. In this 'floating' plasma screen configuration, the plasma potential was +3 V, slightly higher than the +2.3 V observed with the plasma screen grounded and somewhat lower than the +10.8 V observed for the standard plasma screen model (Figure 5.29).

The plasma screen ICP-MS electronic model was altered to predict the effects of the various plasma screen investigated experimentally below and shown in Figure 5.3 above (p132). The plasma screen grounding modifications consisted of the substitution of the circuit between the points marked 'A' and 'B' in Figure 5.31 with that shown in Figure 5.32.

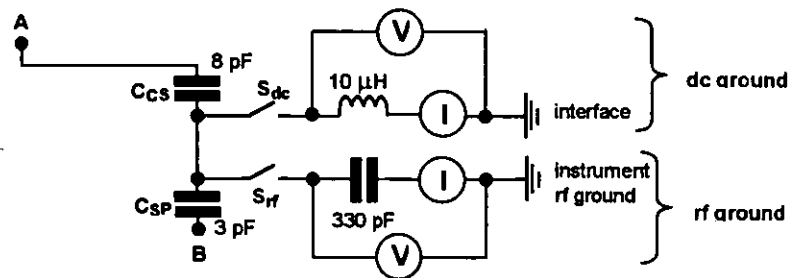


**Figure 5.32 – Modified plasma screen circuit (replaces the circuit between points 'A' and 'B' in Figure 5.31)**

The potentials on the plasma screen and currents on each of the grounds are listed, together with the plasma potential, in Table 5.11 for each of the various plasma screen grounding patterns of the circuit in Figure 5.31 as modified by Figure 5.32.

**Table 5.11 – Potentials and currents on the plasma screen grounds and the plasma potential for the various plasma screen grounding patterns of the circuit in Figure 5.31 as modified by Figure 5.32.**

Ground switches		Plasma	Dc ground		Ac ground	
S <sub>dc</sub>	S <sub>ac</sub>	potential/V	I/mA	V/V	I/mA	V/V
On	Off	+5 – +6	120–140	200–240	-	-
On	On	+2.0 – +2.2	6–35	3–10	270–290	3–10
Off	On	+2.13	-	-	275	4.92

The data in Table 5.11 show that the dc ground did not produce a stable plasma potential – when switch ‘S<sub>dc</sub>’ was on, the electronics modelling software was unable to run the circuit at a steady state. The dc ground, used alone, reduced the plasma potential to +5 – +6 V with a small current of less than 140 mA taken to ground *via* the plasma screen and a large potential on the plasma screen. The rf ground, with or without the dc ground, gave a plasma potential of approximately +2.1 V. The current on the rf ground was approximately 280 mA in both cases. The plasma screen with rf ground used alone had a potential of +5 V upon it. When the dc and rf grounds were used together the potential on the plasma screen fluctuated between +3 and +10 V.

The work reported below explores experimentally the effect of the plasma screen grounding.

#### Plasma Screen Grounding Modifications

All data were collected using *m/z* set E and multi-element solution 4 (see Table 5.3 and Section 5.1.2 respectively). These analytes and *m/z* were selected to monitor the effect of the plasma screen on a number of different parameters: analyte sensitivity at mid and high mass (<sup>115</sup>In, <sup>238</sup>U), high ionisation potential analytes (<sup>114</sup>Cd, IP 9 eV), argon-based polyatomic ions (<sup>40</sup>Ar<sup>14</sup>N<sup>+</sup>, <sup>40</sup>Ar<sup>36</sup>Ar<sup>+</sup>), metal oxide ions (<sup>140</sup>Ce<sup>16</sup>O<sup>+</sup> and <sup>140</sup>Ce<sup>+</sup>) and divalent ions (<sup>138</sup>Ba<sup>+</sup> and <sup>138</sup>Ba<sup>++</sup>).

Stopping curves were collected with standard plasma, wire grounded plasma screen, 330 pF rf grounded plasma screen and combined wire and 330 pF rf grounded plasma screen used. The different plasma screen grounding arrangements used are shown in Figure 5.3(i) above (p132). The wire ground was used alone prior to connection of the rf ground. The rf ground was used alone by disconnecting the wire ground at the point labelled ‘G’. The wire ground plasma screen and combined ground plasma screen data were collected on a different day from the rf grounded plasma screen data. Data for standard plasma were collected on both days for reference purposes. Figure 5.33 shows the stopping curves collected for In<sup>+</sup>, together with the energy distributions (2 point moving window smoothed, differentiated stopping curves). For simplicity, only the standard plasma data collected on the same day as the rf grounded plasma screen data is shown.

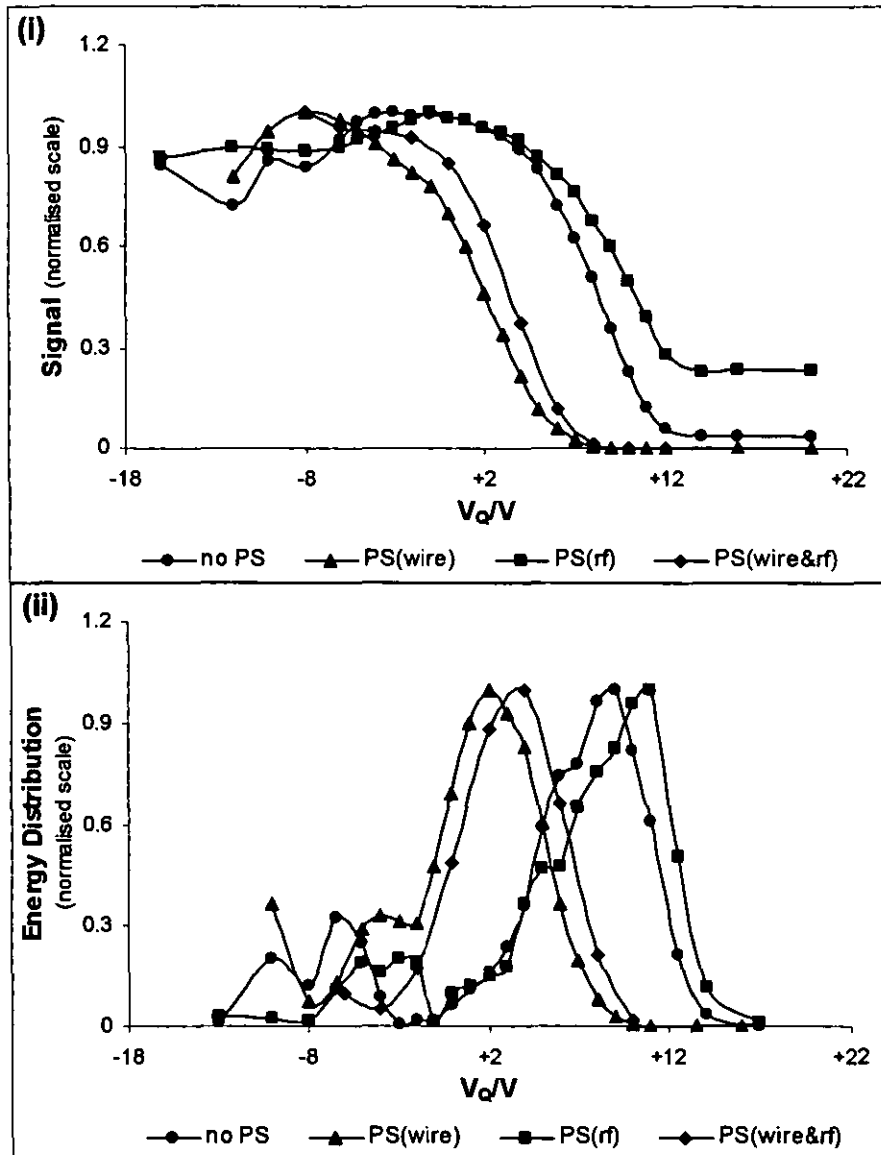


**Figure 5.33** – Normalised  $\text{In}^+$  (i) stopping curves and (ii) energy distributions for standard plasma (no PS), wire grounded plasma screen (PS(wire)), rf grounded plasma screen (PS(rf)) and combined wire and rf grounded plasma screen (PS(wire&rf)).

Figure 5.33 shows that the plasma screen, with the various grounding methods used, had a significant effect on the ion energy distribution. The wire ground reduced the median potential by 6 V compared with standard plasma. The rf ground raised the median potential by 3 V compared with standard plasma – this change is principally due to the increased asymmetry of the peak when the rf grounded plasma screen was used, as the tails of both peaks were located at the same potential. When the rf ground was used in addition to the wire ground, this raised the median potential to around 1 V above the level observed with wire ground plasma screen alone. The effect of the rf grounded plasma screen (alone or with the wire ground) is somewhat puzzling, electronic modelling of the

plasma, described above, suggested that the plasma potential was caused by partially rectified rf, rather than dc and yet the wire ground, which transmits dc but should not readily transmit rf, causes the plasma potential to lower whilst the copper braid and ground with 330 pF capacitor should readily transmit rf, thereby reducing the plasma potential, as it was observed in the model, whilst not transmitting dc. This issue is further explored below, along with the effects of further modifications to the plasma screen grounding arrangements.

The various plasma screen grounding methods had a significant effect on In sensitivity at high negative  $V_Q$ . The wire ground plasma screen and the rf grounded plasma screen both resulted in a reduction of sensitivity to approximately half the level observed when the plasma screen was not employed. The combined rf and wire grounded plasma screen more than tripled the sensitivity compared to standard plasma. If the ICP-MS were retuned for each plasma screen condition these variations in sensitivity may well disappear.

None of the plasma screen conditions used caused any narrowing of the ion energy distributions. For In, all of the ion energy distributions had a full width at half-height (half-width) of approximately 6.5 V. For the higher mass ion  $^{238}\text{U}^+$ , the median potentials occurred at the same potentials as those for  $\text{In}^+$  and the half-widths were approximately 1 V wider than those for In. The higher ionisation potential of Cd did not cause any significant variation in its ion energy distribution, including the location of the median potential when compared with In. After correcting for abundance, the drop in sensitivity between In and Cd was only minimal.

The median potentials of the two argon-based ions,  $\text{Ar}_2^+$  and  $\text{ArN}^+$ , were the same as for  $\text{In}^+$ . The half-widths for  $\text{Ar}_2^+$  were *circa* 6 V, very similar to In, whereas the half-widths for  $\text{ArN}^+$  were slightly narrower, *ca.* 5 V. This narrowing and the broadening at U suggest that mass affected the width of the ion energy distribution.

Relative levels of  $\text{CeO}^+$  and  $\text{Ba}^{++}$ , normalised to the level in standard plasma, are shown in Table 5.12 for  $-6\text{ V } V_Q$ . The  $\text{CeO}^+/\text{Ce}^+$  level is distinctly affected by plasma screen grounding. The use of wire grounded plasma screen resulted in a considerable rise in

CeO<sup>+</sup>/Ce<sup>+</sup> levels' they were more than ten times higher than for standard plasma. The use of rf grounded plasma screen did not cause any significant elevation in CeO<sup>+</sup> levels. The use of the rf ground in conjunction with the wire ground reduces the level of CeO<sup>+</sup>/Ce<sup>+</sup> to one third of the level with the wire ground alone in use. This level is still several times that observed when the rf ground alone was used:

**Table 5.12** – Normalised CeO<sup>+</sup>/Ce<sup>+</sup> and Ba<sup>++</sup>/Ba<sup>+</sup> levels at V<sub>0</sub> – 6 V for standard plasma, wire ground plasma screen, rf ground plasma screen and combined rf and wire ground plasma screen.

Type of plasma screen	<sup>140</sup> Ce <sup>16</sup> O <sup>+</sup> / <sup>140</sup> Ce <sup>+</sup>	<sup>138</sup> Ba <sup>++</sup> / <sup>138</sup> Ba <sup>+</sup>
	(*)	(*)
None	1.0	1.0
Rf ground	1.1	2.4
Wire ground	12	0.5
Wire + rf ground	4.1	0.6

\* normalised to no plasma screen data.

Relative levels of Ba<sup>++</sup> were less dramatically affected by the plasma screen with the various grounding modes. The level of Ba<sup>++</sup> was approximately halved by wire ground plasma screen or combined wire and rf ground plasma screen compared with standard plasma. The level of Ba<sup>++</sup> more than doubled with rf ground plasma screen use.

During the plasma screen introduction procedure, the plasma was run at the lower power of 600 W with the plasma screen in place. The lower plasma power enabled the presence or absence of secondary discharge to be observed. The presence of secondary discharge was observed for standard plasma and rf ground plasma screen. No secondary discharge was observed when the wire ground plasma screen was used. No observation of the presence or absence of secondary discharge was made when the combined wire and rf ground plasma screen was used but, given the low plasma potential with this grounding arrangement, a visible secondary discharge was unlikely. Considerable chemistry occurs in the secondary discharge,<sup>12</sup> so the influence of the plasma screen grounding on plasma potential and thereby on secondary discharge will have a noticeable effect on polyatomic and divalent ions formed or removed by this discharge. The high oxide levels observed for the wire ground plasma screen (Table 5.12) may be related to the absence of a

secondary discharge. It is possible that oxide ions formed in the plasma are atomised in the secondary discharge.

The plasma screen and its grounding arrangements will also influence polyatomic and divalent ions formed in the plasma by varying the plasma temperature. The plasma screen alters the electrical environment surrounding the plasma. The diameter of the plasma is affected by the electrical field, repelling the plasma and thus reducing its diameter and causing the plasma temperature to elevate. Alternatively, the field will attract the plasma, causing its diameter to increase and so reduce the plasma temperature. Increasing the plasma temperature would increase the  $\text{Ba}^{++}$  level, as more energy is available for the second ionisation. The effect of small variations in plasma temperature on  $\text{CeO}^+$  levels is less clear as both ionisation of CeO and reduction of  $\text{CeO}^+$  to  $\text{Ce}^+$  (or CeO to Ce) will be promoted by elevation in plasma temperature.

Either, or both, of the two possible reasons for the reported variations in  $\text{CeO}^+$  and  $\text{Ba}^{++}$  may have occurred, particularly as they involve different parts of the plasma and interface system and are influenced by different changes in plasma properties caused by plasma screen use.

The isolation of rf and dc related plasma screen effects was complicated in the experiment above as the wire ground transmitted both rf and dc current. The experiment was repeated with the wire ground adapted to form a dc only ground by the addition of an inductor (approximately 10  $\mu\text{H}$ ) into the wire between the plasma screen and the relay. Data were collected for five different plasma screen configurations: no plasma screen (standard plasma), (standard) wire ground plasma screen, 10  $\mu\text{H}$  dc ground plasma screen, 330 pF rf ground plasma screen and divided ground plasma screen (both 10  $\mu\text{H}$  dc and 330 pF rf grounds connected). The different plasma screen grounding configurations are shown in Figure 5.3(ii) above (p132). The rf ground was isolated by removing the capacitor when the dc ground was used alone. The dc ground was disconnected at the point marked 'G' when the rf ground was used alone. The different plasma screen grounding configurations were also modelled electronically, as shown in Figures 5.31 and 5.32.

Table 5.13 shows the normalised relative levels of  $\text{CeO}^+$  and  $\text{Ba}^{++}$  for each of the conditions with  $V_Q$  high negative,  $-6\text{ V}$ . (The data are normalised to level observed in standard plasma.) As was observed previously (Table 5.12), the use of the standard wire ground plasma screen caused the  $\text{CeO}^+/\text{Ce}^+$  level to become highly elevated however, unlike previously, the use of rf ground also caused the  $\text{CeO}^+/\text{Ce}^+$  level to become elevated. This inconsistency between the two sets of data is difficult to explain, it may be due to possible failure of the capacitor or indicate the importance of plasma tuning on oxide levels, since in each case the plasma gas flows and sample uptake were optimised for stability and maximum In signal without plasma screen use. Neither of these possibilities is particularly probable, as the various stopping curves for the three plasma screen conditions that were also in the previous data set – no plasma screen, wire ground plasma screen and rf ground plasma screen – were very similar in each data set. In addition, other experiments showed that the injector gas flow rate and the sample uptake rate were the variables that could be used to cause significant alteration in oxide levels with plasma screen use and these two variables had the same values in both experiments.

Dc ground plasma screen caused a significant elevation in the  $\text{CeO}^+/\text{Ce}^+$  level, approximately one third of the level observed with wired ground plasma screen use. The divided ground plasma screen generated similar levels of  $\text{CeO}^+/\text{Ce}^+$  levels to the rf ground plasma screen. Relative levels of  $\text{Ba}^{++}$  were generally higher than those observed previously, due to variation in plasma conditions with time. The  $\text{Ba}^{++}$  level was, as before, much less dramatically affected by the plasma screen than  $\text{CeO}^+$  was, and the results for no plasma screen use, wire ground plasma screen and rf ground plasma screen followed the same pattern as before, with the wire ground causing some reduction in  $\text{Ba}^{++}/\text{Ba}^+$  and rf ground causing an elevation of that level when compared with the levels with no plasma screen use. The dc ground plasma screen and divided ground plasma screen both resulted in elevation of the plasma screen level.



**Table 5.13** – Normalised  $CeO^+/Ce^+$  and  $Ba^{++}/Ba^+$  levels at  $V_Q = -6$  V for standard plasma, (standard) wire ground plasma screen, dc ground plasma screen, rf ground plasma screen and divided ground plasma screen (dc and rf grounds).

Type of plasma	$^{140}Ce^{16}O^+/^{140}Ce^+$	$^{138}Ba^{++}/^{138}Ba^+$
Screen	(*)	(*)
None <sup>a</sup>	1.0	1.0
(standard) wire ground	94	0.5
Dc ground	31	3.8
Rf ground	76	1.7
Divided ground	75	2.2

\* normalised to no plasma screen data.

Figure 5.34 shows the  $In$  stopping curves for the five different plasma screen configurations. Stopping curves are not presented as the noise in the dc ground plasma screen and divided ground plasma screen curves minimised the information that could be determined by differentiation. Table 5.14 shows the median potentials and half-widths for  $Ar_2^+$ ,  $In^+$  and  $U^+$ .

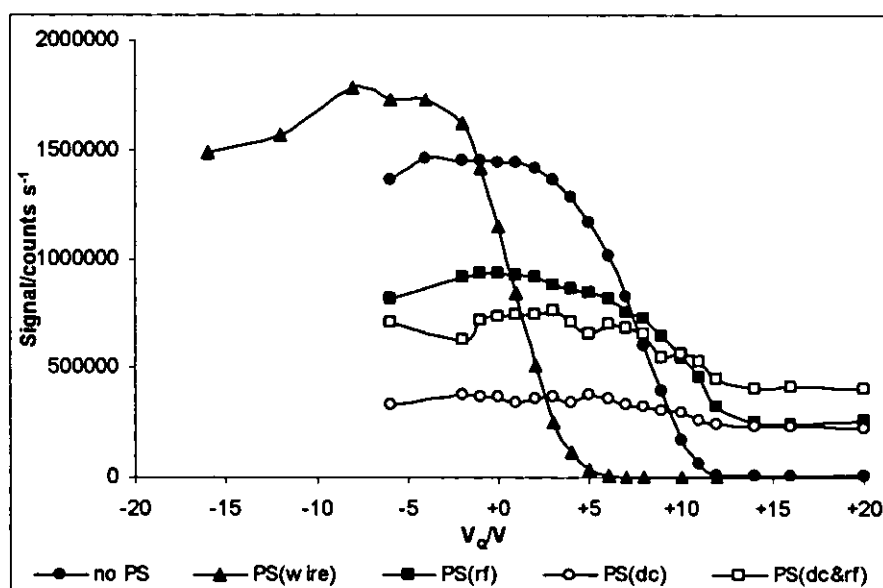


**Figure 5.34** –  $In^+$  stopping curves for standard plasma (no PS), wire grounded plasma screen (PS(wire)), rf grounded plasma screen (PS(rf)), dc grounded plasma screen (PS(dc)) and divided ground plasma screen (PS(dc&rf)).

**Table 5.14 – Energy distribution median potentials ( $V_{mdn}$ ) and half-widths ( $V_{1/2}$ ) for standard plasma, wire grounded plasma screen, rf grounded plasma screen, dc grounded plasma screen and divided ground plasma screen.**

Type of plasma	$^{40}\text{Ar}^{36}\text{Ar}^+$		$^{115}\text{In}^+$		$^{238}\text{U}^+$	
Screen	$V_{mdn}/V$	$V_{1/2}/V$	$V_{mdn}/V$	$V_{1/2}/V$	$V_{mdn}/V$	$V_{1/2}/V$
None <sup>a</sup>	+8	6	+9	7	+9	9
(standard) wire ground	+1	5	+1	5	+3	6
Dc ground	+9	*	*	*	*	*
Rf ground	+11	6	+11	5	+11	*
Divided ground	+10	6	*	*	*	*

\* could not be identified due to noise

The data shown in Figure 5.34 and Table 5.14 are very similar to the results of the earlier experiment, shown in Figure 5.33. The dc ground plasma screen did not have the same effect as the wire ground plasma screen, either alone or in conjunction with the rf ground. The standard wire plasma screen reduced the median potential of the ion beam by approximately 7 V and the rf ground increased it by approximately 2 V compared with the ion beam when the plasma screen was not used. The dc ground plasma screen produced a slight elevation in the median potential compared with no plasma screen, suggesting that dc grounding of the plasma screen was not responsible for the reduction in median potential observed when no the wire ground plasma screen was employed.

During the plasma screen introduction procedure, the plasma was run at 600 W with the plasma screen in place. The presence or absence of secondary discharge was noted at this stage. Secondary discharge was observed for standard plasma, dc ground plasma screen, rf ground plasma screen and combined dc and rf ground plasma screen. Secondary discharge could not be observed when the wire ground plasma screen was employed. This is consistent with the potential difference between the plasma and interface being the cause of secondary discharge, since the discharge was observed when the plasma potential was high, but was not observed when the median potential was reduced by the wire ground plasma screen.

The median potentials for the various plasma screen grounding arrangements were significantly different from the plasma potentials found in the electrical modelling above. The two sets of data are summarised in Table 5.15.

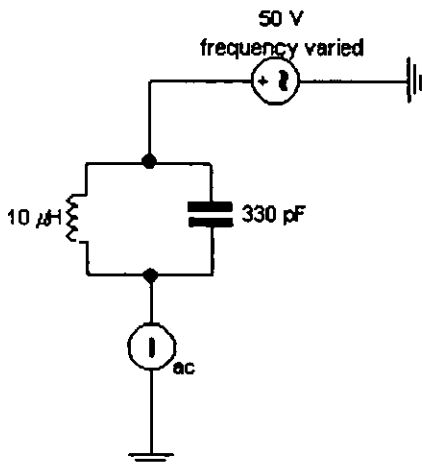
**Table 5.15 – Experimentally determined median potentials and plasma potentials from electronic modelling for standard plasma, wire grounded plasma screen, dc grounded plasma screen, rf grounded plasma screen and divided ground (dc and rf grounded) plasma screen**

Type of plasma screen	Median potential/V (experimental data)	Plasma potential/V (electronic model)
None	+9	+11
(Standard) wire ground	+1	+2
Dc ground	+9	+6
Rf ground	+11	+2
Divided ground	+10	+2

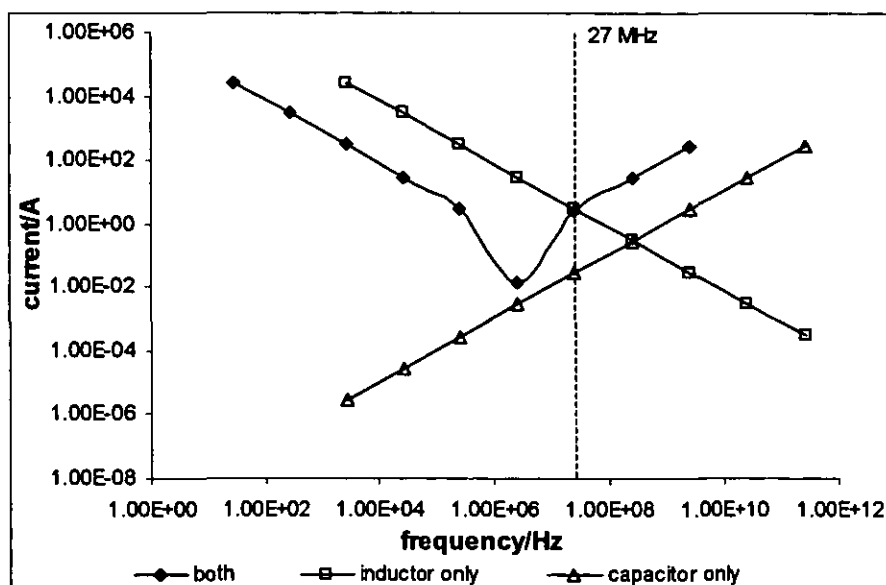
Since the electronic model was produced to give the plasma potentials for plasma and wire ground plasma screen which had been experimentally observed, strong similarity between the experimental and modelling data for these conditions occurred as was expected. The data for the rf ground, dc ground and divided ground plasma screen do not show the same consistency between experimental work and the electronic model. The use of the rf ground (with or without the dc ground) lowered the plasma potential to the same level as the wire ground plasma screen in the electronic model however in the experimental data the rf ground raised the median potential beyond the level observed with no plasma screen use. When the dc ground was used alone experimentally no significant change in the median potential from the value for standard plasma was noted whereas in the electronic model the plasma potential for the dc ground plasma screen was approximately half-way between those for standard plasma and wire ground plasma screen. These observations suggest that the electronic model did not approximate the true ICP system sufficiently well when the rf or dc ground was used although results for the standard plasma and wire ground plasma screen were in accord with experimental levels. The electronic modelling of the dc and rf ground plasma screen would therefore appear to require further development to correctly represent the real system.

The experimental data in Table 5.14 show that the mass dependence of the width of the ion beam energy distribution was again evident; there was also some evidence suggesting that plasma screen use resulted in some slight narrowing of the energy distribution. The half-widths narrowed with decreasing mass, from around 9 V at 238 u through 7 V at 115 u to approximately 6 V at 76 u with no plasma screen use. At higher masses, there is some evidence to suggest that the use of the wire grounded or rf grounded plasma screen narrowed the energy distribution, although the degree of noise in the system prevents this from being quantified with any certainty.

The different effects of the wire ground and dc ground suggest that the grounding required to reduce the median potential of the ion energy distribution fell into a frequency region that was not transmitted through the 10  $\mu$ H inductor of the dc ground (or over the 330 pF capacitor of the rf ground). The maximum current transmitted by the inductor/capacitor pairing depends on frequency. The circuit shown in Figure 5.35 was used in the ‘Electronics Workbench’ modelling software to simulate the divided ground plasma screen. Variation in rms current with frequency for this circuit and for similar circuits omitting the inductor or capacitor path are shown in Figure 5.36.



**Figure 5.35** – Circuit used to ascertain the frequency dependence of the divided ground plasma screen.



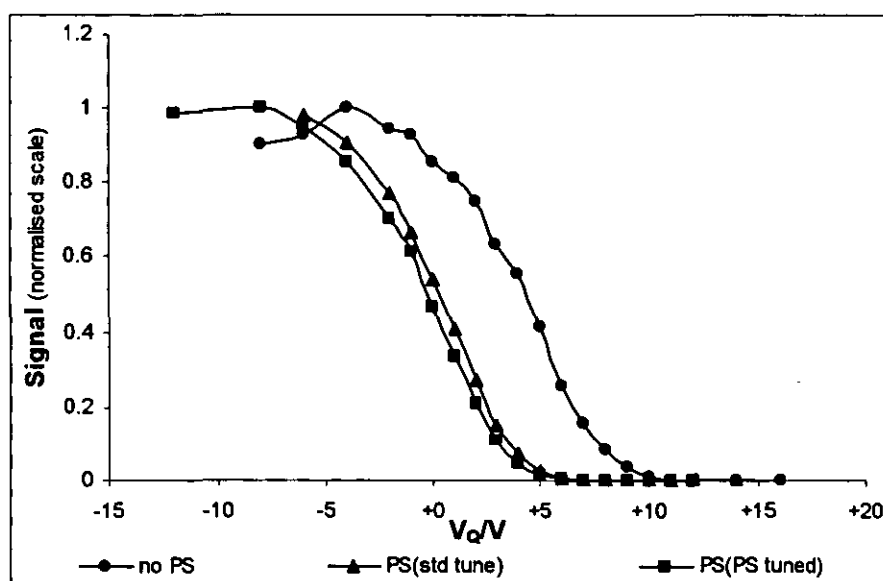
**Figure 5.36 – Frequency dependence of current in the circuit shown in Figure 5.35.** (The ‘inductor only’ and ‘capacitor only’ series are offset horizontally by two orders of magnitude.)

Figure 5.36 shows that the divided ground plasma screen does not conduct well at frequencies just below the load frequency (27 MHz), it has a maximum current of less than an amp at frequencies of  $10^6 - 10^7$  Hz. The capacity in this range is lower for the divided ground than for the dc-only (inductor) or rf-only (capacitor) grounds. If a higher capacitance were used, better grounding over the  $10^6 - 10^7$  Hz range would be provided. The use of a higher capacitance may lower the plasma potential and prevent the occurrence of secondary discharge as the standard wire ground does.

#### 5.3.2.4 Use of Different Cones and Tuning for Plasma Screen Use

In the work reported in Sections 5.3.1.5 and 5.3.2.1 – 5.3.2.3, the plasma screen was used (with, variously, collision cell gas use and plasma screen modifications) with no retuning of ion optics or plasma conditions. As previously stated, this lack of retuning was to provide consistency of plasma settings throughout the work, but did result in elevated oxide levels.  $V_Q$  stopping curves were collected for standard plasma, plasma screen with no retuning and plasma screen with the argon gas flows re-optimised to minimise  $CeO^+/Ce^+$  levels and maintain In sensitivity. (The three conditions are hereafter referred to as standard plasma, standard tune plasma screen and retuned plasma screen respectively.)

The gas flow retuning resulted in a reduction in nebuliser gas flow from  $1.10 \text{ l min}^{-1}$  to  $1.05 \text{ l min}^{-1}$ . Use of plasma screen resulted in a doubling of sensitivity compared to standard plasma. No significant difference in sensitivity was observed between the two plasma screen tuning conditions. The most obvious change on retuning the plasma screen was a reduction in  $^{140}\text{Ce}^{16}\text{O}^+ / ^{140}\text{Ce}^+$  from 36 % to 3.0 % with  $V_Q -4 \text{ V}$ . (Standard plasma had a  $\text{CeO}^+/\text{Ce}^+$  level of 1.5 % at  $V_Q -4 \text{ V}$ .) Normalised  $\text{In}^+$  stopping curves are presented in Figure 5.37.



**Figure 5.37** – Normalised  $\text{In}^+$  stopping curves for standard plasma (no PS), standard tuned plasma screen (PS(std tune)) and retuned plasma screen (PS(PS tuned)). (Terms are explained in text.)

The stopping curve for standard plasma shown in Figure 5.37 has a median potential of +6 V, several volts lower than the value of this potential in earlier experiments – indicating a degree of day-to-day variation in the plasma potential, for whatever cause. The median potential for the plasma screen, with either tuning option, was approximately +1 V. The median potential for retuned plasma screen was less than 0.5 V lower than that for standard tuned plasma screen. The half-widths for the  $\text{In}^+$  ion energy distributions were approximately 7 V in all cases. Thus, whilst plasma screen tuning had a significant effect on oxide levels, it had no significant effect on ion energy distribution.

All of the experimental work reported above used the standard cones supplied by the instrument manufacturer with 'hard' extraction of  $-550$  to  $-600$  V on the extraction lens. A brief investigation was conducted to explore the effect of different cones and extraction conditions on the ion energy distribution.  $V_Q$  stopping curves were collected for three different cone sets: standard,  $X_i$  and a standard sample cone with a trial skimmer cone. (Details of the cones are given in Section 5.1.3.2 above.) For the standard and  $X_i$  cones, data were collected for both hard ( $-566$  V) and soft ( $-200$  V) extraction conditions. For the standard/trial combination, data were only collected for hard extraction conditions.

The normalised  $I_n$  stopping curves and energy distributions for the different cones and extraction conditions are shown in Figure 5.38. The various cone and extraction combinations tested, with the exception of standard cones with soft extraction, cause no large variations in the energy distribution of the ion beam. Four combinations: standard cones with hard extraction;  $X_i$  cones with hard extraction,  $X_i$  cones with soft extraction and standard sample cone /trial skimmer cone with hard extraction; all had a median potential of *circa*  $+5$  V ( $+4.5$  V  $\leq V_{\text{median}} < +5.5$  V). The combination of standard cones and soft extraction had a median potential of  $+2$  V. The extraction potential had no noticeable effect on the half-width of the energy distribution although cone design did have a slight effect; standard cones with hard or soft extraction and standard sample cone/trial skimmer cone with hard extraction all had a half-width of approximately  $7$  V while  $X_i$  cones, with both hard and soft extraction, had a half-width of approximately  $8$  V. These results showed that cone design and extraction potential were important to the ion energy distribution, although variations caused for the cones tested were small.

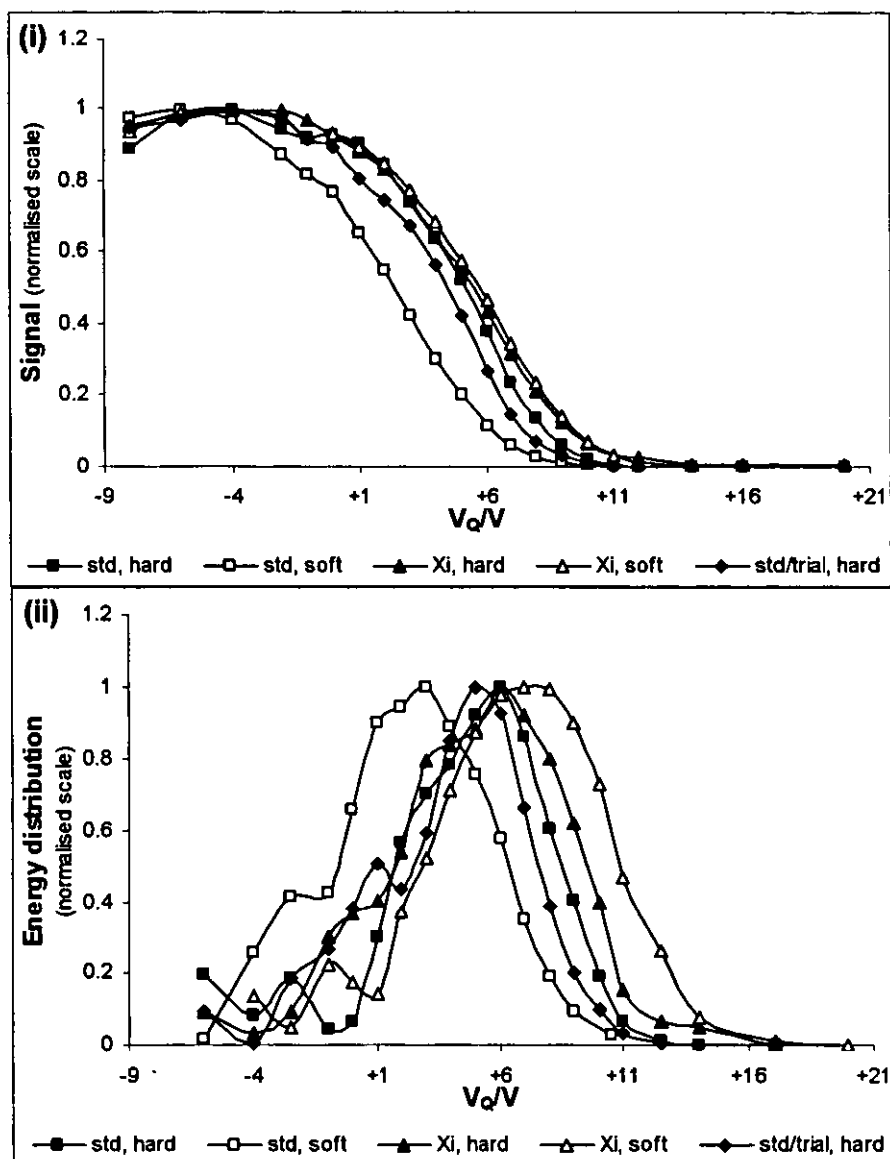


**Figure 5.38** – Normalised  $\text{In}^+$  (i) stopping curves and (ii) energy distributions for standard cones (std),  $X_i$  cones ( $X_i$ ) and standard sample cone with trial skimmer cone (std/trial) under  $-566\text{ V}$  (hard) and  $-200\text{ V}$  (soft) extraction conditions.

The widening of the distribution on changing from standard cones to  $X_i$  cones was less than the variations in the plasma potential reported for standard cones with no collision cell or plasma screen use elsewhere in this chapter. The variation was however important as it indicated the importance of cone design on ion energy distribution. Further study and modelling of the interface region is necessary to identify the phenomenon affected by the cone design that alters the ion energy distribution.



The reduction in median potential on changing from hard to soft extraction for standard cones but not for  $X_i$  cones showed that the interaction of cone design and extraction potential was important in determining the median potential of the ion beam. Thus, the expansion of the ion beam behind the skimmer cone due to space charge and the effect of the cone design and extraction potential on this have an important effect on the potential of the ion beam. Alternatively, the use of soft extraction when standard cones are used may have been insufficient to focus the faster ions into the ion optics with their loss resulting in the perceived reduction in plasma potential. Modelling of the interface and extraction system is necessary to determine which of these two possibilities is correct.

#### 5.3.2.5 Summary

The use of collision cell gases reduced the median potential of the ion beam observed. The median potential was lower than that observed when the plasma screen was used without collision cell gases and was not influenced by the use of plasma screen. The energy distribution was wider for higher mass ions than for mid-mass ones, although it was several volts wide in all cases. The use of collision cell gases (hydrogen and/or helium) had no significant effect on the width of the energy distribution. This reduction may be affected by the use of heavier gases.

The application of a dc potential to the plasma screen, *i.e.* the use of 'active' plasma screen, modified the ion energy distribution by altering the median potential of the distribution by approximately the value of the potential applied. 'Active' plasma screen did not cause narrowing of the energy distribution. Thus, 'active' plasma screen could be used to widen the range of  $V_H - V_P$  potentials available for variation of collision cell reactivity using IKEE.

Various modifications to the plasma screen grounding had no distinct effect on the width of the energy distribution. The modifications intended at restricting the plasma screen grounding, dc- or rf-only ground or the use of a potential divider ground path, all resulted in a slight increase in the median potential of the distribution whereas the standard wire ground caused a reduction in the median potential.

The use of different cones did not significantly affect the plasma potential when the cones were used under optimal extraction potential, however using soft extraction ( $-200$  V) with standard cones did result in a reduction in plasma potential. The use of 'X<sub>i</sub>' cones produced a slight increase in the width of the energy distribution compared with standard cones.

A simple model of energy distribution in ICP-CC-MS and a basic electronic model of the plasma were prepared. Comparison of the experimental data with these models showed mixed results. Some effects were well modelled; others were poorly shown, if at all, in the models. It is therefore clear that further work is necessary to develop the models so they correctly model the system.

## **Conclusion**

Collision/reaction cell inductively coupled plasma mass spectrometry is a recently developed technique for elemental analysis. The collision/reaction cell permits the chemical resolution of spectral interferences occurring in the system with the gas used in the cell providing a degree of specificity to the reactions occurring.

To aid the selection of appropriate gases to remove an interference ion, a database of ion-molecule reactions has been prepared. The database includes reactions between a range of interference ions commonly encountered in ICP-MS and helium, neon, argon, krypton, hydrogen and water collision/reaction cell gases with thermodynamic and kinetic data given where available.

Further development of the database could increase its utility. The addition of reactions between elemental ions and the various gases would allow easy selection of gases that react with the interference but do not react with the analyte ion. Extension of the range of gases included in the database (especially the inclusion of ammonia) would enhance the utility of the database to collision/reaction cell ICP-MS users.

The determination of Si at low levels in a variety of sample types is of particular interest to the semiconductor industry. The determination is hindered by isobaric interference from atmospheric gas-based polyatomic ions at all of its isotopes.  $^{14}\text{N}_2^+$  is the largest interference to the major isotope,  $^{28}\text{Si}$ . A method for the determination of Si *via* its major isotope by collision cell ICP-MS has been developed. A helium/hydrogen mixture was found to be effective at attenuating the various interferences at  $m/z$  28 with theoretical detection limits (based on the signal-to-noise ratios) minimising at  $0.32 \text{ ng g}^{-1}$  with helium+hydrogen  $1.0+2.0 \text{ ml min}^{-1}$ .

Instability of the Si in water solution hindered quantitative analysis. A fluoroboric-boric acids matrix was identified to stabilise the solutions without the silica incompatibility and health hazards of hydrofluoric acid.

Unexpected elevation of  $m/z$  28 backgrounds was encountered which hindered quantitative analysis. This change in interference levels was possibly related to the condition of the spectrometer interface. The background could be reduced by flushing the area surrounding the plasma with argon. The required flow of argon destabilised the plasma and so could not be used. Further work is required to produce a method of introducing sufficient flush gas to the plasma environs whilst retaining a stable plasma.

The presence of adventitious water in the collision cell has a significant effect on the chemistry occurring in the cell when unreactive helium is used. Control of the level of adventitious water is therefore important to ensure reproducibility of results when helium is used alone. Studies using deuterium oxide and water to identify the origin of proton-containing polyatomic ions revealed that very few such ions occur with water-only samples. Addition of water to the helium collision cell gas did not result in the formation of new species of proton containing polyatomic ions, it did however contribute to the levels of ions detected. Nine proton-containing polyatomic ions were observed. Six of the ions;  $H^+$ ,  $HeH^+$ ,  $H_2O^+$ ,  $H_3O^+$ ,  $N_2H^+$  and  $ArH^+$ ; were contributed to by adventitious water in the collision cell gas as well as water from the sample matrix. The other three ions;  $OH^+$ ,  $O_2H^+$  and  $Ar_2H^+$ ; were not contributed to by protons from water in the cell gas. Further investigation is required to determine the role of adventitious water in the formation of polyatomic ions contributed to by non-water matrix constituents or analyte ions.

The presence of adventitious water did not greatly affect the chemistry of a reactive helium/hydrogen mixture. The much higher partial pressure of hydrogen resulted in many more reactive collisions and therefore masked the effect of reactions with water. In general, signals across the mass range for the gas mixture with added water were within  $\pm 10\%$  of the signals for the helium/hydrogen mixture without the addition of water.

Ion energy effects can be used to influence the chemistry occurring in the collision cell and the range of ions detected. Two specific effects have been identified, the ion kinetic energy effect (IKEE) and kinetic energy discrimination (KED). IKEE is the variation of collision cell reactivity by altering input ion energy using the collision cell hexapole bias potential – plasma potential ( $V_H - V_P$ ) potential difference. KED is the exclusion of slow,

cell-formed ions from the mass analyser by the use of a suitable potential difference between the quadrupole and hexapole pole bias potentials ( $V_Q - V_H$ ).

IKEE significantly affected reactivity in the cell. Slowing ions by elevating  $V_H$  increased the rate of exothermic reactions such as those removing  $Ar_2^+$  and forming  $CeO^+$  and decreased the rate of endothermic reactions such as those forming  $CrO^+$ . Use of the plasma screen lowered the plasma potential and extended the range of  $V_H - V_P$  values attainable as well as confirming that  $V_H - V_P$  (and not  $V_H$  alone) was the controlling factor of IKEE.

KED was used to exclude cell formed ions from the cell. Raising  $V_Q - V_H$  from *circa* -10 V towards 0 V dramatically decreased the level of ions formed in the cell, such as metal-oxide ions, and so could be used to exclude ions formed under reactive IKEE conditions where elevated oxide ion levels occur.

Both IKEE and KED have been used by a number of authors to solve particular analytical problems. KED has been used explicitly to prevent the detection of unwanted side products generated in the cell whereas the use of IKEE has been implicit, with the variation in analyte and interference signals with  $V_H$  considered without regard to the causative relationship between  $V_H$  and the effects observed. There is therefore considerable scope to deliberately employ IKEE in developing solutions to analytical problems.

Energy discrimination of polyatomic ions in collision cells based on their larger collision cross-sections depends on ion energy. The input ion energy, as influenced by IKEE should influence the level of this energy discrimination possible. Further investigation is required to ascertain its role.

To optimise the effectiveness of IKEE and KED, narrow ion energy distributions are required. The use of helium or helium/hydrogen in the cell reduced the median potential of the ion beam but had little or no discernable effect on the width of the distribution. The use of heavier cell gases, which was not investigated, may possibly reveal that such gases reduce the width of the distribution.

Application of a negative dc potential to the plasma screen altered the median potential of the distribution by the approximate value of the potential applied to the screen but did not narrow the energy distribution. Adjusting the ICP to allow the use of larger potentials may result in narrowing of the ion energy distribution.

Various modifications to the plasma screen grounding had no particular effect on the width of the distribution although they did increase or decrease the median potential. The use of different designs of cone (under optimal extraction potentials) had little effect on the median potential or the width of the distribution although the use of 'X<sub>i</sub>' cones did result in a slight (1 V) increase in the width of the distribution. Further modifications of the plasma screen grounding to more effectively ground the plasma screen may achieve the desired reduction in the width of the distribution.

It is apparent that the ion energy distribution is a major unresolved issue in ICP-MS. With hindsight, ion energy distribution in collision/reaction cell ICP-MS is one of the most important considerations. Input ion energy influences all aspects of the collision and reaction processes occurring in the cell and the width of the distribution is a key factor in KED. It is possible that differences in ion energy distribution between the various manufacturers' instruments are a key hindrance to ready transfer of techniques between the different collision/reaction cell instrument models. A thorough exploration of the cause and effects of the ion energy distribution will reveal the nature of this relationship and should result in improved analytical performance of the technique.

## References

1. J. J. Thomson, *Rays of Positive Electricity and Their Application to Chemical Analysis*, Longmans Green, London, 1913, cited in E. de Hoffmann, J. Charette, and V. Strooband, *Mass Spectrometry: Principles and Applications*, John Wiley & Sons Ltd., Chichester, 1996.
2. R. S. Houk, V. A. Fassel, G. D. Flesch, H. J. Svec, A. L. Gray and C. E. Taylor, *Anal. Chem.*, 1980, **52**, 2283.
3. A. Montaser, J. A. McLean, H. Liu and J.-M. Mermet in *Inductively Coupled Plasma Mass Spectrometry*, ed. A. Montaser, Wiley-VCH, New York, 1998, pp1-31 (Chapter 1).
4. R. Thomas, *Spectroscopy*, 2001, **16**, 22.
5. D. J. Douglas in *Inductively Coupled Plasmas in Analytical Atomic Spectrometry*, 2nd edn., eds. A. Montaser and D. W. Golightly, VCH, New York, 1992, pp613-650 (Chapter 13).
6. G. Horlick and A. Montaser in *Inductively Coupled Plasma Mass Spectrometry*, ed. A. Montaser, Wiley-VCH, New York, 1998, pp503-588 (Chapter 7).
7. P. J. Turner, D. J. Mills, E. Schröder, G. Lapitajs, G. Jung, L. A. Iacone, D. A. Haydar and A. Montaser in *Inductively Coupled Plasma Mass Spectrometry*, ed. A. Montaser, Wiley-VCH, New York, NY, USA, 1998, pp421-501 (Chapter 6).
8. E. de Hoffmann, J. Charette and V. Stroobant, *Mass Spectrometry: Principles and Applications*, John Wiley & Sons Ltd., Chichester, 1996.
9. K. J. R. Rosman and P. D. P. Taylor, *Pure Appl. Chem.*, 1998, **70**, 217.
10. H. Ying, M. Antler, J. W. Tromp and E. D. Salin, *Spectrochim. Acta, Part B*, 2002, **57**, 277.
11. T. W. May and R. H. Wiedermeyer, *At. Spectrosc.*, 1998, **19**, 150.
12. N. Nonose, N. Matsuda, N. Fudagawa and M. Kubota, *Spectrochim. Acta, Part B*, 1994, **49**, 955.
13. W. Tittes, N. Jakubowski, D. Stüwer and G. Tölg, *J. Anal. At. Spectrom.*, 1994, **9**, 1015.
14. A. Montaser, M. G. Minnich, H. Liu, A. G. T. Gustavsson and R. F. Browner in *Inductively Coupled Plasma Mass Spectrometry*, ed. A. Montaser, Wiley-VCH, New York, 1998, pp335-420 (Chapter 5).

15. N. Jakubowski, I. Feldmann and D. Stüwer, *Spectrochim. Acta, Part B*, 1992, **47**, 107.
16. A. Montaser, J. A. McLean, H. Liu and J.-M. Mermet in *Inductively Coupled Plasma Mass Spectrometry*, ed. A. Montaser, Wiley-VCH, New York, 1998, pp83-264 (Chapter 3).
17. L. C. Alves, D. R. Weiderin and R. S. Houk, *Anal. Chem.*, 1992, **64**, 1164.
18. L. C. Alves, L. A. Allen and R. S. Houk, *Anal. Chem.*, 1993, **65**, 2468.
19. S.-J. Jiang, R. S. Houk and M. A. Stevens, *Anal. Chem.*, 1988, **60**, 1217.
20. H. Niu and R. S. Houk, *Spectrochim. Acta, Part B*, 1996, **51**, 779.
21. K. Y. Patterson, C. Veillon, A. D. Hill, P. B. Moser-Veillon and T. C. O'Haver, *J. Anal. At. Spectrom.*, 1999, **14**, 1673.
22. S. D. Tanner, *J. Anal. At. Spectrom.*, 1995, **10**, 905.
23. D. J. Douglas and S. D. Tanner in *Inductively Coupled Plasma Mass Spectrometry*, ed. A. Montaser, Wiley-VCH, New York, 1998, pp615-679.
24. K. Sakata and K. Kawabata, *Spectrochim. Acta, Part B*, 1994, **49**, 1027.
25. I. L. Turner and A. Montaser in *Inductively Coupled Plasma Mass Spectrometry*, ed. A. Montaser, Wiley-VCH, New York, 1998, pp265-334 (Chapter 4).
26. C. J. Park and J. K. Suh, *J. Anal. At. Spectrom.*, 1997, **12**, 573.
27. N. Nonose and M. Kubota, *J. Anal. At. Spectrom.*, 2001, **16**, 560.
28. J. Riondato, F. Vankaecke, L. Moens and R. Dams, *J. Anal. At. Spectrom.*, 1997, **12**, 933.
29. H. Wildner, *J. Anal. At. Spectrom.*, 1998, **13**, 573.
30. G. C. Eiden, C. J. Barinaga and D. W. Koppenaal, *Rapid Commun. Mass Spectrom.*, 1997, **11**, 37.
31. A. Montaser and H. Zhang in *Inductively Coupled Plasma Mass Spectrometry*, ed. A. Montaser, Wiley-VCH, New York, 1998, pp809-890 (Chapter 10).
32. J. Wang, E. H. Evans and J. A. Caruso, *J. Anal. At. Spectrom.*, 1992, **7**, 929.
33. N. N. Sesi, A. MacKenzie, K. E. Shanks, P. Yang and G. M. Hieftje, *Spectrochim. Acta, Part B*, 1994, **49**, 1259.
34. R. Thomas, *Spectroscopy*, 2002, **17**, 42.
35. C. P. Ingle, P. K. Appelblad, M. A. Dexter, H. J. Reid and B. L. Sharp, *J. Anal. At. Spectrom.*, 2001, **16**, 1076.
36. E. R. Denoyer, S. D. Tanner and U. Völlkopf, *Spectroscopy*, 1999, **14**, 43.



37. G. C. Eiden, C. J. Barinaga and D. W. Koppenaal, *J. Anal. At. Spectrom.*, 1996, **11**, 317.
38. S. D. Tanner and V. I. Baranov in *Plasma Source Mass Spectrometry: New Developments and Applications*, eds. G. Holland and S. D. Tanner, Royal Society of Chemistry, Cambridge, UK, 1999, pp46-62.
39. D. R. Bandura, S. D. Tanner, V. I. Baranov, G. K. Koyanagi, V. V. Lavrov and D. K. Bohme in *Plasma Source Mass Spectrometry: the New Millennium*, eds. G. Holland and S. D. Tanner, Royal Society of Chemistry, Cambridge, 2001, pp130-147.
40. L. Moens, F. F. Vanhaecke, D. R. Bandura, V. I. Baranov and S. D. Tanner, *J. Anal. At. Spectrom.*, 2001, **16**, 991.
41. S. D. Tanner, V. I. Baranov and D. R. Bandura, *Spectrochim. Acta, Part B*, 2002, **57**, 1361.
42. D. J. Douglas, *Can. J. Spectrosc.*, 1989, **34**, 38.
43. J. T. Rowan and R. S. Houk, *Appl. Spectrosc.*, 1989, **43**, 976.
44. V. I. Baranov and S. D. Tanner, *J. Anal. At. Spectrom.*, 1999, **14**, 1133.
45. D. R. Bandura, V. I. Baranov and S. D. Tanner, *J. Am. Soc. Mass Spectrom.*, 2002, **13**, 1176.
46. S. D. Tanner and V. I. Baranov, Winter Conference on Plasma Spectrochemistry, Fort Lauderdale, Florida, USA, 10-15 January 2000 (workshop).
47. K. M. Ervin and P. B. Armentrout, *J. Chem. Phys.*, 1985, **83**, 166.
48. S. D. Tanner and V. I. Baranov, *At. Spectrosc.*, 1999, **20**, 45.
49. S. G. Lias, J. E. Bartmess, J. F. Liebman, J. L. Holmes, R. D. Levin and W. G. Mallard, *J. Phys. Chem. Ref. Data*, 1988, **17**, suppl. 1, 1.
50. V. G. Anicich and W. T. Huntress, Jr., *Astrophys. J. Suppl. Ser.*, 1986, **62**, 553.
51. V. G. Anicich, *Astrophys. J. Suppl. Ser.*, 1993, **84**, 215.
52. V. G. Anicich, *J. Phys. Chem. Ref. Data*, 1993, **22**, 1469.
53. G. K. Koyanagi, V. V. Lavrov, V. I. Baranov, D. R. Bandura, S. D. Tanner, J. W. McLaren and D. K. Bohme, *Int. J. Mass Spectrom.*, 2000, **194**, L1.
54. G. K. Koyanagi, V. I. Baranov, S. D. Tanner and D. K. Bohme, *J. Anal. At. Spectrom.*, 2000, **15**, 1207.

55. G. K. Koyanagi and D. K. Bohme in *Plasma Source Mass Spectrometry: the new Millennium*, eds. G. Holland and S. D. Tanner, Royal Society of Chemistry, Cambridge, UK, 2001, pp117-129.
56. G. K. Koyanagi, D. K. Bohme, I. Kretzschmar, D. Schröder and H. Schwarz, *J. Phys. Chem. A*, 2001, **105**, 4259.
57. G. K. Koyanagi, D. Caraiman, V. Blagojevic and D. K. Bohme, *J. Phys. Chem. A*, 2002, **106**, 4581.
58. P. R. D. Mason, K. Kaspers and M. J. van Bergen, *J. Anal. At. Spectrom.*, 1999, **14**, 1067.
59. I. Feldmann, N. Jakubowski and D. Stüwer, *Fresenius' J. Anal. Chem.*, 1999, **365**, 415.
60. D. J. Douglas, *J. Phys. Chem.*, 1982, **86**, 185.
61. P. W. Atkins, *Physical Chemistry*, 5th edn., Oxford University Press, Oxford, 1994.
62. D. D. Wagman, W. H. Evans, V. B. Parker, R. H. Schumm, I. Halow, S. M. Bailey, K. L. Churney and R. L. Nuttall, *J. Phys. Chem. Ref. Data*, 1982, **11**, suppl. 2, 2.
63. D. R. Bandura, V. I. Baranov and S. D. Tanner, *J. Anal. At. Spectrom.*, 2000, **15**, 921.
64. V. I. Baranov and S. D. Tanner in *Plasma Source Mass Spectrometry: New Developments and Applications*, eds. G. Holland and S. D. Tanner, Royal Society of Chemistry, Cambridge, 1999, pp34-45.
65. D. S. Bollinger and A. J. Schleisman in *Plasma Source Mass Spectrometry: new Developments and Applications*, eds. G. Holland and S. D. Tanner, Royal Society of Chemistry, Cambridge, 1999, pp80-92.
66. Y.-Y. Chan and S. C.-L. Lo, *J. Anal. At. Spectrom.*, 2003, **18**, 146.
67. Y.-L. Chang and S.-J. Jiang, *J. Anal. At. Spectrom.*, 2001, **16**, 1434.
68. A.-P. Deng, H.-T. Liu, S.-J. Jiang, H.-J. Huang and C.-W. Ong, *Anal. Chim. Acta*, 2002, **472**, 55.
69. B. Hattendorf and D. Günther, *J. Anal. At. Spectrom.*, 2000, **15**, 1125.
70. C.-Y. Ho and S.-J. Jiang, *J. Anal. At. Spectrom.*, 2002, **17**, 688.
71. C.-Y. Ho and S.-J. Jiang, *Spectrochim. Acta, Part B*, 2003, **58**, 63.
72. K. Kawabata, Y. Kishi and R. Thomas, *Spectroscopy*, 2003, **18**, 16.
73. J. Latino, K. R. Neubauer, R. E. Wolf, G. Wallace and M. Thomsen, *At. Spectrosc.*, 2001, **22**, 306.

74. Y. Li, N. K. Pradhan, R. Foley and G. K. C. Low, *Talanta*, 2002, **57**, 1143.
75. H. Liu and S.-J. Jiang, *J. Anal. At. Spectrom.*, 2002, **17**, 556.
76. H.-T. Liu and S.-J. Jiang, *Anal. Bioanal. Chem.*, 2003, **375**, 306.
77. H.-T. Liu and S.-J. Jiang, *Spectrochim. Acta, Part B*, 2003, **58**, 153.
78. H. Louie, M. Wu, P. Di, P. Snitch and G. Chapple, *J. Anal. At. Spectrom.*, 2002, **17**, 587.
79. D. E. Nixon, K. R. Neubauer, S. J. Eckdahl, J. A. Butz and M. F. Burritt, *Spectrochim. Acta, Part B*, 2002, **57**, 951.
80. J. W. Olesik, C. Hensman, S. Rabb and D. Rago in *Plasma Source Mass Spectrometry: the New Millennium*, eds. G. Holland and S. D. Tanner, Royal Society of Cambridge, Cambridge, UK, 2001, pp3-16.
81. S. D. Tanner and V. I. Baranov, *J. Am. Soc. Mass Spectrom.*, 1999, **10**, 1083.
82. S. D. Tanner, V. I. Baranov and U. Völlkopf, *J. Anal. At. Spectrom.*, 2000, **15**, 1261.
83. F. F. Vanhaecke, L. Balcaen, G. de Wannemacker and L. Moens, *J. Anal. At. Spectrom.*, 2002, **17**, 933.
84. U. Völlkopf, V. I. Baranov and S. D. Tanner in *Plasma Source Mass Spectrometry: New Developments and Applications*, eds. G. Holland and S. D. Tanner, Royal Society of Chemistry, Cambridge, UK, 1999, pp63-80.
85. M. Iglesias, N. Gilon, E. Poussel and J.-M. Mermet, *J. Anal. At. Spectrom.*, 2002, **17**, 1240.
86. B. Spence, S. Nelms and J. Aggarwal, 11th Biennial National Atomic Spectroscopy Symposium, Loughborough, 08-10 July 2002 (paper C11).
87. P. Turner, T. Merren, J. Speakman and C. Haines in *Plasma Source Mass Spectrometry: Developments and Applications*, eds. G. Holland and S. D. Tanner, Royal Society of Chemistry, Cambridge, UK, 1997, pp28-34.
88. M. A. Dexter, P. K. Appelblad, C. P. Ingle, J. H. Batey, H. J. Reid and B. L. Sharp, *J. Anal. At. Spectrom.*, 2002, **17**, 183.
89. J. S. Becker, *J. Anal. At. Spectrom.*, 2002, **17**, 1172.
90. S. F. Boulyga, J. S. Becker, J. L. Matusevitch and H.-J. Dietze, *Int. J. Mass Spectrom.*, 2000, **203**, 143.
91. S. F. Boulyga and J. S. Becker, *J. Anal. At. Spectrom.*, 2002, **17**, 1202.

92. S. F. Boulyga, I. Segal, T. I. Platzner, L. Halicz and J. S. Becker, *Int. J. Mass Spectrom.*, 2002, **218**, 245.
93. P. Leonhard, R. Pepelnik, A. Prange, N. Yamada and T. Yamada, *J. Anal. At. Spectrom.*, 2002, **17**, 189.
94. T. Nakazato, H. Tao, T. Taniguchi and K. Isshiki, *Talanta*, 2002, **58**, 121.
95. N. Yamada, T. Takahashi and K. Sakata, *J. Anal. At. Spectrom.*, 2002, **17**, 1213.
96. Q. Xie and R. Kerrich, *J. Anal. At. Spectrom.*, 2002, **17**, 69.
97. S. F. Boulyga and J. S. Becker, *J. Anal. At. Spectrom.*, 2002, **17**, 965.
98. Q. Xie and R. Kerrich, *J. Anal. At. Spectrom.*, 2002, **17**, 967.
99. F. Abou-Shakra in *Plasma Source Mass Spectrometry: New Developments and Applications*, eds. G. Holland and S. D. Tanner, Royal Society of Chemistry, Cambridge, 1999, pp120-131.
100. S. F. Boulyga and J. S. Becker, *Fresenius' J. Anal. Chem.*, 2001, **370**, 618.
101. S. F. Boulyga, H.-J. Dietze and J. S. Becker, *J. Anal. At. Spectrom.*, 2001, **16**, 598.
102. D. Larivière, V. N. Epov, R. D. Evans and R. J. Cornett, *J. Anal. At. Spectrom.*, 2003, **18**, 338.
103. T. Lindemann and H. Hintelmann, *Anal. Chem.*, 2002, **74**, 4602.
104. J. M. Marchante-Gayón, C. Thomas, I. Feldmann and N. Jakubowski, *J. Anal. At. Spectrom.*, 2000, **15**, 1093.
105. J. M. Marchante-Gayón, I. Feldmann, C. Thomas and N. Jakubowski, *J. Anal. At. Spectrom.*, 2001, **16**, 457.
106. P. R. D. Mason and W. J. Kraan, *J. Anal. At. Spectrom.*, 2002, **17**, 858.
107. S. Mazan, N. Gilon, G. Crétier, J. L. Rocca and J.-M. Mermet, *J. Anal. At. Spectrom.*, 2002, **17**, 366.
108. S. E. O'Brien, B. W. Acon, S. F. Boulyga, H.-J. Dietze and A. Montaser, *J. Anal. At. Spectrom.*, 2003, **18**, 230.
109. Q. Xie, R. Kerrich, E. Irving, K. Liber and F. Abou-Shakra, *J. Anal. At. Spectrom.*, 2002, **17**, 1037.
110. J. S. Becker, *Can. J. Anal. Sci. Spectrosc.*, 2002, **47**, 98.
111. J. S. Becker, *Spectrochim. Acta, Part B*, 2002, **57**, 1805.
112. S. F. Boulyga, H.-J. Dietze and J. S. Becker, *Mikrochim. Acta*, 2001, **137**, 93.
113. Z. Du and R. S. Houk, *J. Anal. At. Spectrom.*, 2000, **15**, 383.

114. I. Feldmann, N. Jakubowski, C. Thomas and D. Stüwer, *Fresenius' J. Anal. Chem.*, 1999, **365**, 422.
115. L. Hinojosa Reyes, J. M. Marchante-Gayón, J. I. García Alonso and A. Sanz-Medal, *J. Anal. At. Spectrom.*, 2003, **18**, 11.
116. A. M. Leach and G. M. Hieftje, *Int. J. Mass Spectrom.*, 2001, **212**, 49.
117. M. Wind, M. Edler, N. Jakubowski, M. Linscheid, H. Wesch and W. D. Lehman, *Anal. Chem.*, 2001, **73**, 29.
118. D. Günther, D. Bleiner, M. Guillong, B. Hattendorf and I. Horn, *Chimica*, 2001, **55**, 778.
119. D. Günther, B. Hattendorf and A. Audétat, *J. Anal. At. Spectrom.*, 2001, **16**, 1085.
120. B. Hattendorf, D. Günther, M. Schönbachler and A. Halliday, *Anal. Chem.*, 2001, **73**, 5494.
121. B. Hattendorf and D. Günther, *Spectrochim. Acta, Part B*, 2003, **58**, 1.
122. K. S. K. Danadurai, Y.-L. Hsu and S.-J. Jiang, *J. Anal. At. Spectrom.*, 2002, **17**, 552.
123. E. H. Larsen, M. Hansen, T. Fau and M. Vahl, *J. Anal. At. Spectrom.*, 2001, **16**, 1403.
124. E. H. Larsen, J. J. Sloth, M. Hansen and S. Moesgaard, *J. Anal. At. Spectrom.*, 2003, **18**, 310.
125. D. E. Nixon, K. R. Neubauer, S. J. Eckdahl, J. A. Butz and M. F. Burritt, *Spectrochim. Acta, Part B*, 2003, **58**, 97.
126. J. J. Sloth and E. H. Larsen, *J. Anal. At. Spectrom.*, 2000, **15**, 669.
127. J. J. Sloth, E. H. Larsen, S. H. Bügel and S. Moesgaard, *J. Anal. At. Spectrom.*, 2003, **18**, 317.
128. K.-L. Chen and S.-J. Jiang, *Anal. Chim. Acta*, 2002, **470**, 223.
129. D. R. Bandura, V. I. Baranov and S. D. Tanner, *Anal. Chem.*, 2001, **74**, 1497.
130. V. I. Baranov, Z. A. Quinn, D. R. Bandura and S. D. Tanner, *J. Anal. At. Spectrom.*, 2002, **17**, 1148.
131. L. A. Simpson, M. Thomsen, B. J. Alloway and A. Parker, *J. Anal. At. Spectrom.*, 2001, **16**, 1375.
132. L. A. Simpson, M. Thomsen and B. J. Alloway in *Plasma Source Mass Spectrometry: the New Millennium*, eds. G. Holland and S. D. Tanner, Royal Society of Chemistry, Cambridge, UK, 2001, pp148-161.

133. M. Ben-Younes, D. C. Gregoire and C. L. Chakrabarti, *Spectrochim. Acta, Part B*, 2003, **58**, 361.
134. Note that work by the author included in Ref. 88 is reported in Chapter Four.
135. C. P. Ingle, B. L. Sharp, M. S. A. Horstwood, R. R. Parrish and D. J. Lewis, *J. Anal. At. Spectrom.*, 2003, **18**, 219.
136. J. S. Becker, G. Seifert, A. I. Saprykin and H.-J. Dietze, *J. Anal. At. Spectrom.*, 1996, **11**, 643.
137. C.-L. Liao, R. Xu, S. Nourbakhsh, G. D. Glesch, M. Baer and Y. Ng, *J. Chem. Phys.*, 1990, **93**, 4832.
138. M. Thomsen, L. A. Simpson, B. J. Alloway and J. Carter, 10th Biennial Atomic Spectroscopy Symposium, Sheffield, 17-20 July 2000 (paper C34).
139. J. A. Suarez, A. G. Espartero and M. Rodriguez, *Nucl. Instrum. Meth. Phys. Res., Sect. A*, 1996, **369**, 407.
140. M. A. Dexter, H. J. Reid and B. L. Sharp, *J. Anal. At. Spectrom.*, 2002, **17**, 676.
141. J.-M. Mermet, *Anal. Chim. Acta*, 1991, **250**, 85.
142. D. R. Bandura, V. I. Baranov and S. D. Tanner, *Fresenius' J. Anal. Chem.*, 2001, **370**, 454.
143. Y. Takaku, K. Masuda, T. Takahashi and T. Shimamura, *J. Anal. At. Spectrom.*, 1994, **9**, 1385.
144. S. Greenfield and M. Foulkes in *Inductively Coupled Plasma Spectrometry and its Applications*, ed. S. J. Hill, Sheffield Academic Press Ltd., Sheffield, 1999, pp1-34 (Chapter 1).
145. P. G. Lawrence, MSc Project Report, Loughborough University, Loughborough, 2000.
146. M. A. Hudson, BSc Project Report, Loughborough University, Loughborough, 2000.
147. B. Bernas, *Anal. Chem.*, 1968, **40**, 1682.
148. H. Agemian and A. S. Y. Chau, *Anal. Chim. Acta*, 1975, **80**, 61.
149. R. Fletcher, Personal Communication, October 2002.
150. G. K. Koyanagi and D. K. Bohme, *J. Phys. Chem. A*, 2001, **105**, 8964.
151. D. K. Bohme, York University, <http://chem.yorku.ca/profs/bohme/> (accessed June 2002).
152. D. J. Douglas and J. B. French, *J. Am. Soc. Mass Spectrom.*, 1992, **3**, 398.

153. S. Glasstone, *Textbook of Physical Chemistry*, 2nd edn., MacMillan and Co., London, 1948.
154. B. L. Sharp, *J. Anal. At. Spectrom.*, 1988, **3**, 613.
155. J. H. Batey, Personal Communication, October 2001.
156. C. N. Maréchal, P. Télouk and F. Albarède, *Chem. Geol.*, 1999, **156**, 251.
157. G. Frenking, W. Koch, D. Cremer, J. Gauss and J. F. Liebman, *J. Phys. Chem.*, 1989, **93**, 3410.

# **Appendices**



## Appendix 1 – Extracts from the “Thermoli” Ion-Molecule Reaction

### Database

See Section 2.2.2 for more information.

**Table A1.1** – Reactions between interference ions and helium, neon, argon or krypton with reaction enthalpy ( $\Delta H_r$ )  $\leq +1$  eV, rate constant ( $k$ ) quoted where available.  
(An extract from the “Thermoli” database)

Reactants		Products		$\Delta H_r$	$k$	References for:	
Ion	Gas	Ion	Neutral(s)	/eV	/cm <sup>3</sup> s <sup>-1</sup>	$\Delta H_r$	$k$
<sup>31</sup> NOH <sup>+</sup>	He	<sup>30</sup> NO <sup>+</sup>	He, H	+0.60		49	
<sup>40</sup> Ar <sup>+</sup>	He	<sup>44</sup> ArHe <sup>+</sup>		0.00		49	
<sup>41</sup> ArH <sup>+</sup>	He	<sup>1</sup> H <sup>+</sup>	He, Ar	-9.80		49	
<sup>41</sup> ArH <sup>+</sup>	He	<sup>1</sup> H <sup>+</sup>	HeAr	-9.80		49	
<sup>47</sup> HNO <sub>2</sub> <sup>+</sup>	He	<sup>1</sup> H <sup>+</sup>	He, NO <sub>2</sub>	-7.50		49	
<sup>52</sup> ArC <sup>+</sup>	He	<sup>12</sup> C <sup>+</sup>	He, Ar	+0.90		49,157	
<sup>52</sup> ArC <sup>+</sup>	He	<sup>12</sup> C <sup>+</sup>	HeAr	+0.90		49,157	
<sup>52</sup> ArC <sup>+</sup>	He	<sup>16</sup> HeC <sup>+</sup>	Ar	+0.90		49,157	
<sup>56</sup> ArO <sup>+</sup>	He	<sup>16</sup> O <sup>+</sup>	HeAr	+0.68		49,157	
<sup>56</sup> ArO <sup>+</sup>	He	<sup>16</sup> O <sup>+</sup>	He, Ar	+0.68		49,157	
<sup>56</sup> ArO <sup>+</sup>	He	<sup>20</sup> HeO <sup>+</sup>	Ar	+0.65		49,157	
<sup>31</sup> NOH <sup>+</sup>	Ne	<sup>28</sup> NO <sup>+</sup>	Ne, H	+0.57		49	
<sup>40</sup> Ar <sup>+</sup>	Ne	<sup>60</sup> ArNe <sup>+</sup>		-0.08		49	
<sup>41</sup> ArH <sup>+</sup>	Ne	<sup>1</sup> H <sup>+</sup>	Ne, Ar	-9.75		49	
<sup>41</sup> ArH <sup>+</sup>	Ne	<sup>1</sup> H <sup>+</sup>	NeAr	-9.75		49	
<sup>47</sup> HNO <sub>2</sub> <sup>+</sup>	Ne	<sup>1</sup> H <sup>+</sup>	Ne, NO <sub>2</sub>	-7.53		49	
<sup>52</sup> ArC <sup>+</sup>	Ne	<sup>12</sup> C <sup>+</sup>	NeAr	+0.94		49,157	
<sup>52</sup> ArC <sup>+</sup>	Ne	<sup>12</sup> C <sup>+</sup>	Ne, Ar	+0.94		49,157	
<sup>52</sup> ArC <sup>+</sup>	Ne	<sup>32</sup> NeC <sup>+</sup>	Ar	+0.81		49,157	
<sup>56</sup> ArO <sup>+</sup>	Ne	<sup>16</sup> O <sup>+</sup>	NeAr	+0.68		49,157	
<sup>56</sup> ArO <sup>+</sup>	Ne	<sup>16</sup> O <sup>+</sup>	Ne, Ar	+0.68		49,157	
<sup>56</sup> ArO <sup>+</sup>	Ne	<sup>36</sup> NeO <sup>+</sup>	Ar	+0.63		49,157	
<sup>15</sup> NH <sup>+</sup>	Ar	<sup>41</sup> ArH <sup>+</sup>	N	-0.48		49	
<sup>28</sup> N <sub>2</sub> <sup>+</sup>	Ar	<sup>40</sup> Ar <sup>+</sup>	N <sub>2</sub>	+0.18	2.00E-13	49	52
<sup>29</sup> COH <sup>+</sup>	Ar	<sup>41</sup> ArH <sup>+</sup>	CO	+0.88	<1.00E-12 *	49	52
<sup>31</sup> NOH <sup>+</sup>	Ar	<sup>28</sup> NO <sup>+</sup>	Ar, H	+0.57		49	
<sup>33</sup> O <sub>2</sub> H <sup>+</sup>	Ar	<sup>41</sup> ArH <sup>+</sup>	O <sub>2</sub>	+0.55	<5.00E-12	49	52
<sup>40</sup> Ar <sup>+</sup>	Ar	<sup>80</sup> Ar <sub>2</sub> <sup>+</sup>		-1.27		49	
<sup>41</sup> ArH <sup>+</sup>	Ar	<sup>1</sup> H <sup>+</sup>	Ar <sub>2</sub>	-9.75		49	
<sup>41</sup> ArH <sup>+</sup>	Ar	<sup>1</sup> H <sup>+</sup>	Ar, Ar	0.00		49	
<sup>47</sup> HNO <sub>2</sub> <sup>+</sup>	Ar	<sup>1</sup> H <sup>+</sup>	Ar, NO <sub>2</sub>	-7.53		49	
<sup>52</sup> ArC <sup>+</sup>	Ar	<sup>12</sup> C <sup>+</sup>	Ar <sub>2</sub>	+0.93		49,157	
<sup>52</sup> ArC <sup>+</sup>	Ar	<sup>12</sup> C <sup>+</sup>	Ar, Ar	+0.94		49,157	

Reactants		Products		$\Delta H_r$	$k$	References for:	
Ion	Gas	Ion	Neutral(s)	/eV	/cm <sup>3</sup> s <sup>-1</sup>	$\Delta H_r$	$k$
<sup>36</sup> ArO <sup>+</sup>	Ar	<sup>16</sup> O <sup>+</sup>	Ar <sub>2</sub>	-1.56		49,157	
<sup>36</sup> ArO <sup>+</sup>	Ar	<sup>16</sup> O <sup>+</sup>	Ar, Ar	-1.55		49,157	
<sup>36</sup> ArO <sup>+</sup>	Ar	<sup>40</sup> Ar <sup>+</sup>	Ar, O	+0.59		49,157	
<sup>36</sup> ArO <sup>+</sup>	Ar	<sup>80</sup> Ar <sub>2</sub> <sup>+</sup>	O	-0.68		49,157	
<sup>15</sup> NH <sup>+</sup>	Kr	<sup>84</sup> Kr <sup>+</sup>	NH	+0.51		49,62	
<sup>15</sup> NH <sup>+</sup>	Kr	<sup>85</sup> KrH <sup>+</sup>	N	-1.04		49,62	
<sup>17</sup> OH <sup>+</sup>	Kr	<sup>84</sup> Kr <sup>+</sup>	OH	+1.00		49,62	
<sup>17</sup> OH <sup>+</sup>	Kr	<sup>85</sup> KrH <sup>+</sup>	O	+0.63		49,62	
<sup>28</sup> N <sub>2</sub> <sup>+</sup>	Kr	<sup>84</sup> Kr <sup>+</sup>	N <sub>2</sub>	-1.58	1.00E-12	49,62	52
<sup>28</sup> CO <sup>+</sup>	Kr	<sup>84</sup> Kr <sup>+</sup>	CO	-0.02	2.20E-09	49,62	52
<sup>29</sup> COH <sup>+</sup>	Kr	<sup>85</sup> KrH <sup>+</sup>	CO	+0.32	4.00E-10	49,62	52
<sup>31</sup> NOH <sup>+</sup>	Kr	<sup>28</sup> NO <sup>+</sup>	Kr, H	+0.57		49,62	
<sup>31</sup> NOH <sup>+</sup>	Kr	<sup>85</sup> KrH <sup>+</sup>	NO	+0.51		49,62	
<sup>33</sup> O <sub>2</sub> H <sup>+</sup>	Kr	<sup>85</sup> KrH <sup>+</sup>	O <sub>2</sub>	-0.01	4.30E-10	49,62	52
<sup>40</sup> Ar <sup>+</sup>	Kr	<sup>124</sup> ArKr <sup>+</sup>		+0.49		49,62	
<sup>41</sup> ArH <sup>+</sup>	Kr	<sup>1</sup> H <sup>+</sup>	Kr, Ar	-9.75		49,62	
<sup>41</sup> ArH <sup>+</sup>	Kr	<sup>1</sup> H <sup>+</sup>	KrAr	-9.75		49,62	
<sup>44</sup> CO <sub>2</sub> <sup>+</sup>	Kr	<sup>84</sup> Kr <sup>+</sup>	CO <sub>2</sub>	+0.23		49,62	
<sup>47</sup> HNO <sub>2</sub> <sup>+</sup>	Kr	<sup>1</sup> H <sup>+</sup>	Kr, NO <sub>2</sub>	-7.53		49,62	
<sup>52</sup> ArC <sup>+</sup>	Kr	<sup>12</sup> C <sup>+</sup>	Kr, Ar	+0.94		49,62,157	
<sup>56</sup> ArO <sup>+</sup>	Kr	<sup>16</sup> O <sup>+</sup>	Kr, Ar	-0.68		49,62,157	
<sup>56</sup> ArO <sup>+</sup>	Kr	<sup>40</sup> Ar <sup>+</sup>	Kr, O	-1.55		49,62,157	
<sup>56</sup> ArO <sup>+</sup>	Kr	<sup>84</sup> Kr <sup>+</sup>	Ar, O	-1.17		49,157	
<sup>80</sup> Ar <sub>2</sub> <sup>+</sup>	Kr	<sup>40</sup> Ar <sup>+</sup>	Kr, Ar	-0.49		49,62	
<sup>80</sup> Ar <sub>2</sub> <sup>+</sup>	Kr	<sup>40</sup> Ar <sup>+</sup>	KrAr	-0.49		49,62	
<sup>80</sup> Ar <sub>2</sub> <sup>+</sup>	Kr	<sup>84</sup> Kr <sup>+</sup>	Ar <sub>2</sub>	-0.59		49,62	
<sup>80</sup> Ar <sub>2</sub> <sup>+</sup>	Kr	<sup>84</sup> Kr <sup>+</sup>	Ar, Ar	-0.49		49,62	

\* listed as 'no reaction' in Anicich<sup>52</sup>

**Table A1.2 – Reactions between interference ions and hydrogen with reaction enthalpy ( $\Delta H_r$ )  $\leq +1$  eV, rate constant ( $k$ ) quoted where available. (An extract from the “Thermoli” database)**

Reactants		Products		$\Delta H_r$	$k$	References for:	
Ion	Gas	Ion	Neutral(s)	/eV	/cm <sup>3</sup> s <sup>-1</sup>	$\Delta H_r$	$k$
<sup>13</sup> CH <sup>+</sup>	H <sub>2</sub>	<sup>14</sup> H <sub>2</sub> C <sup>+</sup>	H	−0.19	1.20E−09	49	52
<sup>13</sup> CH <sup>+</sup>	H <sub>2</sub>	<sup>15</sup> H <sub>3</sub> C <sup>+</sup>		−5.48		49	
<sup>15</sup> NH <sup>+</sup>	H <sub>2</sub>	<sup>1</sup> H <sup>+</sup>	H <sub>2</sub> N	+0.43		49	
<sup>15</sup> NH <sup>+</sup>	H <sub>2</sub>	<sup>3</sup> H <sub>3</sub> <sup>+</sup>	N	−1.02	1.23E−09	49	52
<sup>15</sup> NH <sup>+</sup>	H <sub>2</sub>	<sup>16</sup> H <sub>2</sub> N <sup>+</sup>	H	−2.03		49	
<sup>15</sup> NH <sup>+</sup>	H <sub>2</sub>	<sup>17</sup> H <sub>3</sub> N <sup>+</sup>		−7.71		49	
<sup>16</sup> NH <sub>2</sub> <sup>+</sup>	H <sub>2</sub>	<sup>17</sup> H <sub>3</sub> N <sup>+</sup>	H	−1.16	1.95E−10	49	52
<sup>16</sup> NH <sub>2</sub> <sup>+</sup>	H <sub>2</sub>	<sup>18</sup> H <sub>4</sub> N <sup>+</sup>		−6.57		49	
<sup>17</sup> OH <sup>+</sup>	H <sub>2</sub>	<sup>1</sup> H <sup>+</sup>	H <sub>2</sub> O	−0.05		49	
<sup>17</sup> OH <sup>+</sup>	H <sub>2</sub>	<sup>3</sup> H <sub>3</sub> <sup>+</sup>	O	+0.65		49	
<sup>17</sup> OH <sup>+</sup>	H <sub>2</sub>	<sup>18</sup> H <sub>2</sub> O <sup>+</sup>	H	−1.04	9.70E−10	49	52
<sup>17</sup> OH <sup>+</sup>	H <sub>2</sub>	<sup>19</sup> H <sub>3</sub> O <sup>+</sup>		−7.27		49	
<sup>18</sup> OH <sub>2</sub> <sup>+</sup>	H <sub>2</sub>	<sup>19</sup> H <sub>3</sub> O <sup>+</sup>	H	−1.71	7.60E−10	49	52
<sup>28</sup> N <sub>2</sub> <sup>+</sup>	H <sub>2</sub>	<sup>2</sup> H <sub>2</sub> <sup>+</sup>	N <sub>2</sub>	−0.16		49	
<sup>28</sup> N <sub>2</sub> <sup>+</sup>	H <sub>2</sub>	<sup>29</sup> N <sub>2</sub> H <sup>+</sup>	H	−2.59		49	
<sup>28</sup> CO <sup>+</sup>	H <sub>2</sub>	<sup>29</sup> CHO <sup>+</sup>	H	−2.05	1.40E−09	49	52
<sup>28</sup> CO <sup>+</sup>	H <sub>2</sub>	<sup>29</sup> COH <sup>+</sup>	H	−0.63		49	
<sup>28</sup> N <sub>2</sub> <sup>+</sup>	H <sub>2</sub>	<sup>30</sup> H <sub>2</sub> N <sub>2</sub> <sup>+</sup>		−3.80		49	
<sup>28</sup> CO <sup>+</sup>	H <sub>2</sub>	<sup>30</sup> H <sub>2</sub> CO <sup>+</sup>		−3.12		49	
<sup>29</sup> COH <sup>+</sup>	H <sub>2</sub>	<sup>3</sup> H <sub>3</sub> <sup>+</sup>	CO	+0.34	4.70E−10	49	52
<sup>29</sup> COH <sup>+</sup>	H <sub>2</sub>	<sup>31</sup> H <sub>2</sub> COH <sup>+</sup>		−2.69		49	
<sup>29</sup> HCO <sup>+</sup>	H <sub>2</sub>	<sup>31</sup> H <sub>3</sub> CO <sup>+</sup>		+0.17	<2.00E−14 *	49	52
<sup>30</sup> NO <sup>+</sup>	H <sub>2</sub>	<sup>32</sup> H <sub>2</sub> NO <sup>+</sup>		−0.46	<1.00E−13 *	49	52
<sup>31</sup> NOH <sup>+</sup>	H <sub>2</sub>	<sup>3</sup> H <sub>3</sub> <sup>+</sup>	NO	+0.53		49	
<sup>31</sup> NOH <sup>+</sup>	H <sub>2</sub>	<sup>17</sup> NH <sub>3</sub> <sup>+</sup>	O	+0.37		49	
<sup>31</sup> NOH <sup>+</sup>	H <sub>2</sub>	<sup>19</sup> H <sub>3</sub> O <sup>+</sup>	N	−0.86		49	
<sup>31</sup> HNO <sup>+</sup>	H <sub>2</sub>	<sup>19</sup> H <sub>3</sub> O <sup>+</sup>	N	−0.08		49	
<sup>31</sup> NOH <sup>+</sup>	H <sub>2</sub>	<sup>30</sup> NO <sup>+</sup>	H <sub>2</sub> , H	+0.57		49	
<sup>31</sup> NOH <sup>+</sup>	H <sub>2</sub>	<sup>33</sup> H <sub>2</sub> NHO <sup>+</sup>		−2.32		49	
<sup>31</sup> HNO <sup>+</sup>	H <sub>2</sub>	<sup>33</sup> H <sub>2</sub> NHO <sup>+</sup>		−1.54		49	
<sup>32</sup> O <sub>2</sub> <sup>+</sup>	H <sub>2</sub>	<sup>18</sup> H <sub>2</sub> O <sup>+</sup>	O	+0.60	<1.00E−13 *	49	52
<sup>32</sup> O <sub>2</sub> <sup>+</sup>	H <sub>2</sub>	<sup>34</sup> H <sub>2</sub> O <sub>2</sub> <sup>+</sup>		−2.95	<1.00E−13 *	49	52
<sup>33</sup> O <sub>2</sub> H <sup>+</sup>	H <sub>2</sub>	<sup>3</sup> H <sub>3</sub> <sup>+</sup>	O <sub>2</sub>	+0.01	3.30E−10	49	52
<sup>33</sup> O <sub>2</sub> H <sup>+</sup>	H <sub>2</sub>	<sup>17</sup> OH <sup>+</sup>	H <sub>2</sub> O	−0.57		49	
<sup>33</sup> O <sub>2</sub> H <sup>+</sup>	H <sub>2</sub>	<sup>18</sup> H <sub>2</sub> O <sup>+</sup>	OH	−0.96		49	
<sup>33</sup> O <sub>2</sub> H <sup>+</sup>	H <sub>2</sub>	<sup>19</sup> H <sub>3</sub> O <sup>+</sup>	O	−2.75		49	
<sup>33</sup> O <sub>2</sub> H <sup>+</sup>	H <sub>2</sub>	<sup>34</sup> H <sub>2</sub> O <sub>2</sub> <sup>+</sup>	H	−0.07		49	
<sup>33</sup> O <sub>2</sub> H <sup>+</sup>	H <sub>2</sub>	<sup>35</sup> H <sub>3</sub> O <sub>2</sub> <sup>+</sup>		−4.04		49	
<sup>35</sup> Cl <sup>+</sup>	H <sub>2</sub>	<sup>1</sup> H <sup>+</sup>	HCl	+0.68		49	
<sup>35</sup> Cl <sup>+</sup>	H <sub>2</sub>	<sup>36</sup> HCl <sup>+</sup>	H	−0.17	7.20E−10	49	52

Reactants		Products		$\Delta H_r$	$k$	References for:	
Ion	Gas	Ion	Neutral(s)	/eV	/cm <sup>3</sup> s <sup>-1</sup>	$\Delta H_r$	$k$
<sup>35</sup> Cl <sup>+</sup>	H <sub>2</sub>	<sup>37</sup> H <sub>2</sub> Cl <sup>+</sup>		-5.23		49	
<sup>36</sup> HCl <sup>+</sup>	H <sub>2</sub>	<sup>3</sup> H <sub>3</sub> <sup>+</sup>	Cl	+0.94		49	
<sup>36</sup> HCl <sup>+</sup>	H <sub>2</sub>	<sup>37</sup> H <sub>2</sub> Cl <sup>+</sup>	H	-0.54	8.20E-10	49	52
<sup>37</sup> Cl <sup>+</sup>	H <sub>2</sub>	<sup>1</sup> H <sup>+</sup>	HCl	+0.68		49	
<sup>37</sup> Cl <sup>+</sup>	H <sub>2</sub>	<sup>38</sup> HCl <sup>+</sup>	H	-0.17	7.20E-10	49	52
<sup>37</sup> Cl <sup>+</sup>	H <sub>2</sub>	<sup>39</sup> H <sub>2</sub> Cl <sup>+</sup>		-5.23		49	
<sup>38</sup> HCl <sup>+</sup>	H <sub>2</sub>	<sup>3</sup> H <sub>3</sub> <sup>+</sup>	Cl	+0.94		49	
<sup>38</sup> HCl <sup>+</sup>	H <sub>2</sub>	<sup>39</sup> H <sub>2</sub> Cl <sup>+</sup>	H	-0.54	8.20E-10	49	52
<sup>40</sup> Ar <sup>+</sup>	H <sub>2</sub>	<sup>2</sup> H <sub>2</sub> <sup>+</sup>	Ar	-0.34	8.90E-10	49	52
<sup>40</sup> Ar <sup>+</sup>	H <sub>2</sub>	<sup>41</sup> ArH <sup>+</sup>	H	-1.49		49	
<sup>41</sup> ArH <sup>+</sup>	H <sub>2</sub>	<sup>1</sup> H <sup>+</sup>	H <sub>2</sub> , Ar	-9.75		49	
<sup>41</sup> ArH <sup>+</sup>	H <sub>2</sub>	<sup>1</sup> H <sup>+</sup>	ArH <sub>2</sub>	-9.75		49	
<sup>41</sup> ArH <sup>+</sup>	H <sub>2</sub>	<sup>3</sup> H <sub>3</sub> <sup>+</sup>	Ar	-0.54	6.30E-10	49	52
<sup>44</sup> CO <sub>2</sub> <sup>+</sup>	H <sub>2</sub>	<sup>1</sup> H <sup>+</sup>	H, CO <sub>2</sub>	-0.17		49	
<sup>44</sup> N <sub>2</sub> O <sup>+</sup>	H <sub>2</sub>	<sup>16</sup> NH <sub>2</sub> <sup>+</sup>	NO	+0.31		49	
<sup>44</sup> CO <sub>2</sub> <sup>+</sup>	H <sub>2</sub>	<sup>29</sup> CHO <sup>+</sup>	OH	-0.73		49	
<sup>44</sup> CO <sub>2</sub> <sup>+</sup>	H <sub>2</sub>	<sup>29</sup> HOC <sup>+</sup>	OH	+0.69		49	
<sup>44</sup> N <sub>2</sub> O <sup>+</sup>	H <sub>2</sub>	<sup>30</sup> NO <sup>+</sup>	NH <sub>2</sub>	-1.58		49	
<sup>44</sup> N <sub>2</sub> O <sup>+</sup>	H <sub>2</sub>	<sup>30</sup> H <sub>2</sub> N <sub>2</sub> <sup>+</sup>	O	+0.62		49	
<sup>44</sup> N <sub>2</sub> O <sup>+</sup>	H <sub>2</sub>	<sup>32</sup> H <sub>2</sub> ON <sup>+</sup>	N	+0.90		49	
<sup>44</sup> CO <sub>2</sub> <sup>+</sup>	H <sub>2</sub>	<sup>46</sup> H <sub>2</sub> O <sub>2</sub> C <sup>+</sup>		-2.29		49	
<sup>47</sup> HNO <sub>2</sub> <sup>+</sup>	H <sub>2</sub>	<sup>1</sup> H <sup>+</sup>	H <sub>2</sub> , NO <sub>2</sub>	-7.53		49	
<sup>47</sup> HNO <sub>2</sub> <sup>+</sup>	H <sub>2</sub>	<sup>1</sup> H <sup>+</sup>	H <sub>2</sub> O, N, O	-2.90		49	
<sup>47</sup> HNO <sub>2</sub> <sup>+</sup>	H <sub>2</sub>	<sup>31</sup> HNO <sup>+</sup>	H <sub>2</sub> O	-1.53		49	
<sup>47</sup> HNO <sub>2</sub> <sup>+</sup>	H <sub>2</sub>	<sup>32</sup> H <sub>2</sub> NO <sup>+</sup>	OH	+0.01		49	
<sup>51</sup> ClO <sup>+</sup>	H <sub>2</sub>	<sup>1</sup> H <sup>+</sup>	ClOH	-10.55	<10E-13	49	54
<sup>51</sup> ClO <sup>+</sup>	H <sub>2</sub>	<sup>17</sup> OH <sup>+</sup>	HCl	+0.44	<10E-13	49	54
<sup>51</sup> ClO <sup>+</sup>	H <sub>2</sub>	<sup>18</sup> H <sub>2</sub> O <sup>+</sup>	Cl	-0.64	<10E-13	49	54
<sup>51</sup> ClO <sup>+</sup>	H <sub>2</sub>	<sup>35</sup> Cl <sup>+</sup>	H <sub>2</sub> O	-0.29	<10E-13	49	54
<sup>51</sup> ClO <sup>+</sup>	H <sub>2</sub>	<sup>36</sup> HCl <sup>+</sup>	OH	+0.19	<10E-13	49	54
<sup>51</sup> ClO <sup>+</sup>	H <sub>2</sub>	<sup>37</sup> H <sub>2</sub> Cl <sup>+</sup>	O	-0.43	<10E-13	49	54
<sup>51</sup> ClO <sup>+</sup>	H <sub>2</sub>	<sup>52</sup> ClOH <sup>+</sup>	H	+0.56	<10E-13	49	54
<sup>52</sup> ArC <sup>+</sup>	H <sub>2</sub>	<sup>12</sup> C <sup>+</sup>	H <sub>2</sub> , Ar	+0.94		49,157	
<sup>52</sup> ArC <sup>+</sup>	H <sub>2</sub>	<sup>14</sup> H <sub>2</sub> C <sup>+</sup>	Ar	-3.38		49,157	
<sup>52</sup> ArC <sup>+</sup>	H <sub>2</sub>	<sup>41</sup> HA <sup>+</sup>	CH	+0.44		49,157	
<sup>53</sup> ClO <sup>+</sup>	H <sub>2</sub>	<sup>1</sup> H <sup>+</sup>	ClOH	-10.55	<10E-13	49	54
<sup>53</sup> ClO <sup>+</sup>	H <sub>2</sub>	<sup>17</sup> OH <sup>+</sup>	HCl	+0.44	<10E-13	49	54
<sup>53</sup> ClO <sup>+</sup>	H <sub>2</sub>	<sup>18</sup> H <sub>2</sub> O <sup>+</sup>	Cl	-0.64	<10E-13	49	54
<sup>53</sup> ClO <sup>+</sup>	H <sub>2</sub>	<sup>37</sup> Cl <sup>+</sup>	H <sub>2</sub> O	-0.29	<10E-13	49	54
<sup>53</sup> ClO <sup>+</sup>	H <sub>2</sub>	<sup>38</sup> HCl <sup>+</sup>	OH	+0.19	<10E-13	49	54
<sup>53</sup> ClO <sup>+</sup>	H <sub>2</sub>	<sup>39</sup> H <sub>2</sub> Cl <sup>+</sup>	O	-0.43	<10E-13	49	54
<sup>53</sup> ClO <sup>+</sup>	H <sub>2</sub>	<sup>54</sup> ClOH <sup>+</sup>	H	+0.56	<10E-13	49	54
<sup>54</sup> ArN <sup>+</sup>	H <sub>2</sub>	<sup>16</sup> H <sub>2</sub> N <sup>+</sup>	Ar	-4.03		49,157	

Reactants		Products		$\Delta H_r$	$k$	References for:	
Ion	Gas	Ion	Neutral(s)	/eV	/cm <sup>3</sup> s <sup>-1</sup>	$\Delta H_r$	$k$
<sup>54</sup> ArN <sup>+</sup>	H <sub>2</sub>	<sup>40</sup> Ar <sup>+</sup>	H <sub>2</sub> N	+0.59		49,157	
<sup>54</sup> ArN <sup>+</sup>	H <sub>2</sub>	<sup>41</sup> ArH <sup>+</sup>	HN	-1.22		49,157	
<sup>56</sup> ArO <sup>+</sup>	H <sub>2</sub>	<sup>1</sup> H <sup>+</sup>	OH, Ar	+0.74		49,157	
<sup>56</sup> ArO <sup>+</sup>	H <sub>2</sub>	<sup>16</sup> O <sup>+</sup>	H <sub>2</sub> , Ar	+0.68		49,157	
<sup>56</sup> ArO <sup>+</sup>	H <sub>2</sub>	<sup>17</sup> OH <sup>+</sup>	Ar, H	+0.14		49,157	
<sup>56</sup> ArO <sup>+</sup>	H <sub>2</sub>	<sup>18</sup> H <sub>2</sub> O <sup>+</sup>	Ar	-5.42		49,157	
<sup>56</sup> ArO <sup>+</sup>	H <sub>2</sub>	<sup>40</sup> Ar <sup>+</sup>	H <sub>2</sub> O	-2.27		49,157	
<sup>56</sup> CaO <sup>+</sup>	H <sub>2</sub>	<sup>40</sup> Ca <sup>+</sup>	H <sub>2</sub> O	-1.73		49	
<sup>56</sup> ArO <sup>+</sup>	H <sub>2</sub>	<sup>41</sup> ArH <sup>+</sup>	OH	-3.11		49,157	
<sup>56</sup> CaO <sup>+</sup>	H <sub>2</sub>	<sup>57</sup> CaOH <sup>+</sup>	H	-1.07		49	
<sup>80</sup> Ar <sub>2</sub> <sup>+</sup>	H <sub>2</sub>	<sup>2</sup> H <sub>2</sub> <sup>+</sup>	Ar <sub>2</sub>	+0.84		49	
<sup>80</sup> Ar <sub>2</sub> <sup>+</sup>	H <sub>2</sub>	<sup>2</sup> H <sub>2</sub> <sup>+</sup>	Ar, Ar	+0.94		49	
<sup>80</sup> Ar <sub>2</sub> <sup>+</sup>	H <sub>2</sub>	<sup>41</sup> ArH <sup>+</sup>	Ar, H	-0.22	5.00E-10	49	52

\* listed as 'no reaction' in Anicich<sup>52</sup>

**Table A1.3 – Reactions between interference ions and water with reaction enthalpy ( $\Delta H_r$ )  $\leq +1$  eV, rate constant (k) quoted where available. (An extract from the “Thermoli” database)**

Reactants		Products		$\Delta H_r$	$k$	References for:	
Ion	Gas	Ion	Neutral(s)	/eV	/cm <sup>3</sup> s <sup>-1</sup>	$\Delta H_r$	k
<sup>13</sup> CH <sup>+</sup>	H <sub>2</sub> O	<sup>1</sup> H <sup>+</sup>	HOCH	+0.43		49	
<sup>13</sup> CH <sup>+</sup>	H <sub>2</sub> O	<sup>14</sup> CH <sub>2</sub> <sup>+</sup>	HO	+0.47		49	
<sup>13</sup> CH <sup>+</sup>	H <sub>2</sub> O	<sup>19</sup> H <sub>3</sub> O <sup>+</sup>	C	-0.74	2.90E-09	49	52
<sup>13</sup> CH <sup>+</sup>	H <sub>2</sub> O	<sup>29</sup> OCH <sup>+</sup>	H, H	-1.22		49	
<sup>13</sup> CH <sup>+</sup>	H <sub>2</sub> O	<sup>30</sup> HOCH <sup>+</sup>	H	-2.29		49	
<sup>13</sup> CH <sup>+</sup>	H <sub>2</sub> O	<sup>31</sup> H <sub>2</sub> OCH <sup>+</sup>		-7.01		49	
<sup>15</sup> NH <sup>+</sup>	H <sub>2</sub> O	<sup>16</sup> NH <sub>2</sub> <sup>+</sup>	HO	-1.38	3.50E-09	49	52
<sup>15</sup> NH <sup>+</sup>	H <sub>2</sub> O	<sup>16</sup> O <sup>+</sup>	NH <sub>3</sub>	+0.84		49	
<sup>15</sup> NH <sup>+</sup>	H <sub>2</sub> O	<sup>17</sup> NH <sub>3</sub> <sup>+</sup>	O	-2.62		49	
<sup>15</sup> NH <sup>+</sup>	H <sub>2</sub> O	<sup>17</sup> HO <sup>+</sup>	NH <sub>2</sub>	+0.48		49	
<sup>15</sup> NH <sup>+</sup>	H <sub>2</sub> O	<sup>18</sup> H <sub>2</sub> O <sup>+</sup>	NH	-0.88		49	
<sup>15</sup> NH <sup>+</sup>	H <sub>2</sub> O	<sup>19</sup> H <sub>3</sub> O <sup>+</sup>	N	-3.85		49	
<sup>15</sup> NH <sup>+</sup>	H <sub>2</sub> O	<sup>31</sup> ONH <sup>+</sup>	H, H	+0.75		49	
<sup>15</sup> NH <sup>+</sup>	H <sub>2</sub> O	<sup>32</sup> HONH <sup>+</sup>	H	-2.88		49	
<sup>16</sup> NH <sub>2</sub> <sup>+</sup>	H <sub>2</sub> O	<sup>15</sup> NH <sub>3</sub> <sup>+</sup>	OH	-0.51	2.90E-09	49	52
<sup>16</sup> NH <sub>2</sub> <sup>+</sup>	H <sub>2</sub> O	<sup>18</sup> NH <sub>4</sub> <sup>+</sup>	O	-1.48		49	
<sup>16</sup> NH <sub>2</sub> <sup>+</sup>	H <sub>2</sub> O	<sup>19</sup> H <sub>3</sub> O <sup>+</sup>	NH	-0.56		49	
<sup>17</sup> OH <sup>+</sup>	H <sub>2</sub> O	<sup>18</sup> H <sub>2</sub> O <sup>+</sup>	OH	-0.39	2.89E-09	49	52
<sup>17</sup> OH <sup>+</sup>	H <sub>2</sub> O	<sup>19</sup> H <sub>3</sub> O <sup>+</sup>	O	-2.18		49	
<sup>17</sup> OH <sup>+</sup>	H <sub>2</sub> O	<sup>34</sup> H <sub>2</sub> O <sub>2</sub> <sup>+</sup>	H	+0.50		49	
<sup>17</sup> OH <sup>+</sup>	H <sub>2</sub> O	<sup>35</sup> H <sub>3</sub> O <sub>2</sub> <sup>+</sup>		-3.47		49	
<sup>18</sup> OH <sub>2</sub> <sup>+</sup>	H <sub>2</sub> O	<sup>19</sup> H <sub>3</sub> O <sup>+</sup>	OH	-1.06	1.85E-09	49	52
<sup>24</sup> C <sub>2</sub> <sup>+</sup>	H <sub>2</sub> O	<sup>18</sup> H <sub>2</sub> O <sup>+</sup>	C <sub>2</sub>	+0.52		49	
<sup>24</sup> C <sub>2</sub> <sup>+</sup>	H <sub>2</sub> O	<sup>29</sup> COH <sup>+</sup>	CH	-2.05		49	
<sup>28</sup> N <sub>2</sub> <sup>+</sup>	H <sub>2</sub> O	<sup>18</sup> H <sub>2</sub> O <sup>+</sup>	N <sub>2</sub>	-2.97	2.40E-09	49	52
<sup>28</sup> CO <sup>+</sup>	H <sub>2</sub> O	<sup>18</sup> H <sub>2</sub> O <sup>+</sup>	CO	-1.41	2.40E-09	49	52
<sup>28</sup> N <sub>2</sub> <sup>+</sup>	H <sub>2</sub> O	<sup>29</sup> N <sub>2</sub> H <sup>+</sup>	OH	-1.94		49	
<sup>28</sup> CO <sup>+</sup>	H <sub>2</sub> O	<sup>29</sup> HCO <sup>+</sup>	OH	-1.40		49	
<sup>28</sup> CO <sup>+</sup>	H <sub>2</sub> O	<sup>29</sup> COH <sup>+</sup>	OH	+0.02		49	
<sup>28</sup> CO <sup>+</sup>	H <sub>2</sub> O	<sup>46</sup> COOH <sub>2</sub> <sup>+</sup>		-2.96		49	
<sup>29</sup> COH <sup>+</sup>	H <sub>2</sub> O	<sup>19</sup> H <sub>3</sub> O <sup>+</sup>	CO	-2.49		49	
<sup>29</sup> HCO <sup>+</sup>	H <sub>2</sub> O	<sup>19</sup> H <sub>3</sub> O <sup>+</sup>	CO	-1.07	2.60E-09	49	52
<sup>31</sup> NOH <sup>+</sup>	H <sub>2</sub> O	<sup>19</sup> H <sub>3</sub> O <sup>+</sup>	NO	-2.30		49	
<sup>31</sup> HNO <sup>+</sup>	H <sub>2</sub> O	<sup>19</sup> H <sub>3</sub> O <sup>+</sup>	NO	-1.52	2.30E-09	49	52
<sup>31</sup> NOH <sup>+</sup>	H <sub>2</sub> O	<sup>32</sup> H <sub>2</sub> NO <sup>+</sup>	OH	+0.76		49	
<sup>32</sup> O <sub>2</sub> <sup>+</sup>	H <sub>2</sub> O	<sup>18</sup> H <sub>2</sub> O <sup>+</sup>	O <sub>2</sub>	+0.53	<1.00E-12 *	49	52
<sup>33</sup> O <sub>2</sub> H <sup>+</sup>	H <sub>2</sub> O	<sup>16</sup> O <sup>+</sup>	OH, H <sub>2</sub> O	-8.48		49	
<sup>33</sup> O <sub>2</sub> H <sup>+</sup>	H <sub>2</sub> O	<sup>19</sup> H <sub>3</sub> O <sup>+</sup>	O <sub>2</sub>	-2.82		49	
<sup>33</sup> O <sub>2</sub> H <sup>+</sup>	H <sub>2</sub> O	<sup>34</sup> O <sub>2</sub> H <sub>2</sub> <sup>+</sup>	OH	+0.58		49	
<sup>34</sup> O <sub>2</sub> H <sub>2</sub> <sup>+</sup>	H <sub>2</sub> O	<sup>19</sup> H <sub>3</sub> O <sup>+</sup>	H <sub>2</sub> O	-3.00		49	

Reactants		Products		$\Delta H_r$	$k$	References for:	
Ion	Gas	Ion	Neutral(s)	/eV	/cm <sup>3</sup> s <sup>-1</sup>	$\Delta H_r$	$k$
<sup>34</sup> O <sub>2</sub> H <sub>2</sub> <sup>+</sup>	H <sub>2</sub> O	<sup>19</sup> H <sub>3</sub> O <sup>+</sup>	O <sub>2</sub> H	-0.38	1.70E-09	49	52
<sup>34</sup> O <sub>2</sub> H <sub>2</sub> <sup>+</sup>	H <sub>2</sub> O	<sup>19</sup> H <sub>3</sub> O <sup>+</sup>	O <sub>2</sub> H	-0.38		49	
<sup>35</sup> Cl <sup>+</sup>	H <sub>2</sub> O	<sup>17</sup> OH <sup>+</sup>	HCl	+0.73		49	
<sup>35</sup> Cl <sup>+</sup>	H <sub>2</sub> O	<sup>18</sup> H <sub>2</sub> O <sup>+</sup>	Cl	-0.35	5.00E-10	49	52
<sup>35</sup> Cl <sup>+</sup>	H <sub>2</sub> O	<sup>36</sup> HCl <sup>+</sup>	OH	+0.48		49	
<sup>35</sup> Cl <sup>+</sup>	H <sub>2</sub> O	<sup>37</sup> H <sub>2</sub> Cl <sup>+</sup>	O	-0.14		49	
<sup>36</sup> HCl <sup>+</sup>	H <sub>2</sub> O	<sup>18</sup> H <sub>2</sub> O <sup>+</sup>	ClH	-0.14		49	
<sup>36</sup> HCl <sup>+</sup>	H <sub>2</sub> O	<sup>19</sup> H <sub>3</sub> O <sup>+</sup>	Cl	-1.89		49	
<sup>36</sup> HCl <sup>+</sup>	H <sub>2</sub> O	<sup>37</sup> ClH <sub>2</sub> <sup>+</sup>	OH	+0.11		49	
<sup>37</sup> Cl <sup>+</sup>	H <sub>2</sub> O	<sup>17</sup> OH <sup>+</sup>	HCl	+0.73		49	
<sup>37</sup> Cl <sup>+</sup>	H <sub>2</sub> O	<sup>18</sup> H <sub>2</sub> O <sup>+</sup>	Cl	-0.35	5.00E-10	49	52
<sup>37</sup> Cl <sup>+</sup>	H <sub>2</sub> O	<sup>38</sup> HCl <sup>+</sup>	OH	+0.48		49	
<sup>37</sup> Cl <sup>+</sup>	H <sub>2</sub> O	<sup>39</sup> H <sub>2</sub> Cl <sup>+</sup>	O	-0.14		49	
<sup>38</sup> HCl <sup>+</sup>	H <sub>2</sub> O	<sup>18</sup> H <sub>2</sub> O <sup>+</sup>	ClH	-0.14		49	
<sup>38</sup> HCl <sup>+</sup>	H <sub>2</sub> O	<sup>19</sup> H <sub>3</sub> O <sup>+</sup>	Cl	-1.89		49	
<sup>38</sup> HCl <sup>+</sup>	H <sub>2</sub> O	<sup>39</sup> ClH <sub>2</sub> <sup>+</sup>	OH	+0.11		49	
<sup>40</sup> Ar <sup>+</sup>	H <sub>2</sub> O	<sup>18</sup> H <sub>2</sub> O <sup>+</sup>	Ar	-3.15	1.62E-09	49	52
<sup>40</sup> Ar <sup>+</sup>	H <sub>2</sub> O	<sup>41</sup> ArH <sup>+</sup>	OH	-0.84		49	
<sup>41</sup> ArH <sup>+</sup>	H <sub>2</sub> O	<sup>19</sup> H <sub>3</sub> O <sup>+</sup>	Ar	-3.37		49	
<sup>44</sup> CO <sub>2</sub> <sup>+</sup>	H <sub>2</sub> O	<sup>18</sup> H <sub>2</sub> O <sup>+</sup>	CO <sub>2</sub>	-1.16	2.40E-09	49	52
<sup>44</sup> N <sub>2</sub> O <sup>+</sup>	H <sub>2</sub> O	<sup>18</sup> H <sub>2</sub> O <sup>+</sup>	N <sub>2</sub> O	-0.28		49	
<sup>44</sup> N <sub>2</sub> O <sup>+</sup>	H <sub>2</sub> O	<sup>29</sup> N <sub>2</sub> H <sup>+</sup>	O <sub>2</sub> H	-0.39		49	
<sup>44</sup> N <sub>2</sub> O <sup>+</sup>	H <sub>2</sub> O	<sup>30</sup> N <sub>2</sub> H <sub>2</sub> <sup>+</sup>	O <sub>2</sub>	+0.55		49	
<sup>44</sup> N <sub>2</sub> O <sup>+</sup>	H <sub>2</sub> O	<sup>32</sup> NH <sub>2</sub> O <sup>+</sup>	NO	-0.54		49	
<sup>44</sup> N <sub>2</sub> O <sup>+</sup>	H <sub>2</sub> O	<sup>34</sup> O <sub>2</sub> H <sub>2</sub> <sup>+</sup>	N <sub>2</sub>	-2.10		49	
<sup>44</sup> CO <sub>2</sub> <sup>+</sup>	H <sub>2</sub> O	<sup>34</sup> H <sub>2</sub> O <sub>2</sub> <sup>+</sup>	CO	+0.80		49	
<sup>52</sup> ArC <sup>+</sup>	H <sub>2</sub> O	<sup>12</sup> C <sup>+</sup>	H <sub>2</sub> O, Ar	+0.94		49,157	
<sup>54</sup> ArN <sup>+</sup>	H <sub>2</sub> O	<sup>18</sup> H <sub>2</sub> O <sup>+</sup>	Ar, N	+0.38		49,157	
<sup>54</sup> ArN <sup>+</sup>	H <sub>2</sub> O	<sup>30</sup> NO <sup>+</sup>	Ar, H, H	+0.10		49,157	
<sup>54</sup> ArN <sup>+</sup>	H <sub>2</sub> O	<sup>31</sup> NOH <sup>+</sup>	Ar, H	-0.47		49,157	
<sup>54</sup> ArN <sup>+</sup>	H <sub>2</sub> O	<sup>32</sup> NOH <sub>2</sub> <sup>+</sup>	Ar	-4.88		49,157	
<sup>56</sup> CaO <sup>+</sup>	H <sub>2</sub> O	<sup>16</sup> O <sup>+</sup>	H <sub>2</sub> O, Ca	-2.75		49	
<sup>56</sup> ArO <sup>+</sup>	H <sub>2</sub> O	<sup>16</sup> O <sup>+</sup>	H <sub>2</sub> O, Ar	+0.68		49,157	
<sup>56</sup> ArO <sup>+</sup>	H <sub>2</sub> O	<sup>17</sup> OH <sup>+</sup>	OH, Ar	+0.79		49,157	
<sup>56</sup> ArO <sup>+</sup>	H <sub>2</sub> O	<sup>18</sup> H <sub>2</sub> O <sup>+</sup>	O, Ar	-0.33		49,157	
<sup>56</sup> CaO <sup>+</sup>	H <sub>2</sub> O	<sup>57</sup> CaOH <sup>+</sup>	OH	-0.42		49	
<sup>80</sup> Ar <sub>2</sub> <sup>+</sup>	H <sub>2</sub> O	<sup>18</sup> H <sub>2</sub> O <sup>+</sup>	Ar <sub>2</sub>	-1.98		49	
<sup>80</sup> Ar <sub>2</sub> <sup>+</sup>	H <sub>2</sub> O	<sup>18</sup> H <sub>2</sub> O <sup>+</sup>	Ar, Ar	-1.98		49	
<sup>80</sup> Ar <sub>2</sub> <sup>+</sup>	H <sub>2</sub> O	<sup>40</sup> Ar <sup>+</sup>	H <sub>2</sub> O, Ar	-1.88		49	
<sup>80</sup> Ar <sub>2</sub> <sup>+</sup>	H <sub>2</sub> O	<sup>41</sup> ArH <sup>+</sup>	Ar, OH	+0.43		49	

\* listed as 'no reaction' in Anicich<sup>52</sup>

## **Appendix 2 – Professional Development**

### ***Conferences Attended***

10<sup>th</sup> Biennial National Atomic Spectroscopy Symposium, Sheffield, 17-20 July 2000

*Workshop: “New Mass Spectrometries for Elemental Analysis”*

Young Scientist Atomic Spectroscopy (a meeting organised by the Atomic Spectroscopy Group of the Analytical Division of the Royal Society of Chemistry), Teddington, Middlesex, 27 February 2002.

1<sup>st</sup> Analytical Research Forum (incorporating the 38<sup>th</sup> Research and Development Topics Meeting), Norwich, Norfolk, 16-18 July 2001.

2<sup>nd</sup> Analytical Research Forum (incorporating the 39<sup>th</sup> Research and Development Topics Meeting), Kingston-upon-Thames, Surrey, 15-17 July 2002.

11<sup>th</sup> Biennial National Atomic Spectroscopy Symposium, Loughborough, 08-10 July 2002.

*Workshop: “Coupled Techniques for Speciation”*

8<sup>th</sup> International Conference on Plasma Source Mass Spectrometry, Durham, Co. Durham, 08-13 September 2002.

European Winter Conference on Plasma Spectrochemistry, Garmisch-Partenkirchen, Germany, 12-17 January 2003.

3<sup>rd</sup> Analytical Research Forum (incorporating the 40<sup>th</sup> Research and Development Topics Meeting), Sunderland, Tyne and Wear, 21-23 July 2003.



### ***University Lectures Attended***

H. Gross and B. Vale, "Induction", 04 October 2000.

M. Lansdale, "How to get the best from your supervisor", 11 October 2000.

H. Gross, "Research issues", 18 October 2000.

R. Hooper, "Ethical issues and research projects", 18 October 2000.

B. Sharp, D. Wilson and the University Fire Consultants, "fire safety and safety", 20 October 2000.

H. Gross, "Getting the message across and managing your time", 01 November, 2000.

Analytical Seminar: M. G. Tebrake, "Speed up HPLC while protecting the environment" and A. K. Al Amri, "Detection of opiate abuse using marker compounds", 11 July 2002.

RSC lecture: A. Buglass, "Sour grapes", 24 July 2003.

### ***Courses Attended***

"Teaching Skills for PGs and RAs", Staff Development, Loughborough University, 26 February, 05 & 12 March 2001.

"Graduate School", Research Councils' Graduate Schools Programme, Doncaster College, High Melton, 22-27 July 2002.

### **Appendix 3 – Publications and Conference Contributions**

#### ***Publications***

C. P. Ingle, P. K. Appelblad, M. A. Dexter, H. J. Reid and B. L. Sharp, "The use of background ions and a multivariate approach to characterise and optimise the dominant H<sub>2</sub>-based chemistries ion a hexapole collision cell used in ICP-MS", *Journal of Analytical Atomic Spectrometry*, 2001, **16**, 1076-1084.

M. A. Dexter, P. K. Appelblad, C. P. Ingle, J. H. Batey, H. J. Reid and B. L. Sharp, "The effect of adventitious water in hexapole collision cell inductively coupled plasma mass spectrometry", *Journal of Analytical Atomic Spectrometry*, 2002, **17**, 183-188.

M. A. Dexter, H. J. Reid and B. L. Sharp, "The effect of ion energy on reactivity and species selectivity in hexapole collision/reaction cell ICP-MS", *Journal of Analytical Atomic Spectrometry*, 2002, **17**, 676-681.

#### ***Conference Contributions***

##### **ORAL PRESENTATIONS:**

M. A. Dexter, H. J. Reid and B. L. Sharp, "Ion Energy Effects in Controlling Reactivity and Species Selectivity in Hexapole Collision/reaction Cell ICP-MS", *Young Scientist Atomic Spectroscopy* (a meeting organised by the Atomic Spectroscopy Group of the Analytical Division of the Royal Society of Chemistry), Teddington, Middlesex, 27 February 2002.

B. L. Sharp, M. A. Dexter and H. J. Reid, "Ion Energy Effects in Collision/Reaction Cell ICP-MS", *8<sup>th</sup> International Conference on Plasma Source Mass Spectrometry*, Durham, Co. Durham, 08-13 September 2002.

M. A. Dexter, H. J. Reid and B. L. Sharp, "Ion Energy Effects in Hexapole Collision/reaction Cell ICP-MS" *3<sup>rd</sup> Analytical Research Forum* (incorporating the *40<sup>th</sup> Research and Development Topics Meeting*), Sunderland, Tyne and Wear, 21-23 July 2003.

**POSTERS:**

M. A. Dexter, P. K. Appelblad, B. L. Sharp and H. J. Reid, "The effect of adventitious water in collision cell inductively coupled plasma mass spectrometry", *1<sup>st</sup> Analytical Research Forum* (incorporating the 38<sup>th</sup> Research and Development Topics Meeting), Norwich, Norfolk, 16-18 July 2001.

M. A. Dexter, H. J. Reid and B. L. Sharp, "Ion Energy Effects in Hexapole Collision/reaction Cell ICP-MS: Reactivity and the Control of Input Ion Energy", *11<sup>th</sup> Biennial National Atomic Spectroscopy Symposium*, Loughborough, Leicestershire, 08-10 July 2002.

M. A. Dexter, H. J. Reid and B. L. Sharp, "Ion Energy Effects in Hexapole Collision/reaction Cell ICP-MS: Reactivity and the Control of Input Ion Energy", *2<sup>nd</sup> Analytical Research Forum* (incorporating the 39<sup>th</sup> Research and Development Topics Meeting), Kingston-upon-Thames, Surrey, 15-17 July 2002.

M. A. Dexter, B. L. Sharp and H. J. Reid, "Ion Energy Effects in Hexapole Collision/reaction Cell ICP-MS: Reactivity and the Control of Input Ion Energy", *European Winter Conference on Plasma Spectrochemistry*, Garmisch-Partenkirchen, Germany, 12-17 January 2003.

